COMSAT
Technical Review

Volume 17 Number 1, Spring 1987

COMSAT TECHNICAL REVIEW is published twice a year by Communications Satellite Corporation (COMSAT). Subscriptions, which include the two issues published within a calendar year, are: one year, $15 U.S.; two years, $25; three years, $35; single copies, $10; article reprints, $2.50. Overseas air mail delivery is available at an additional cost of $18 per year. Make checks payable to COMSAT and address to Records Department, Communications Satellite Corporation, 22300 Comsat Drive, Clarksburg, MD 20871-9475, U.S.A.

ISSN 0095-9669

COMSAT TECHNICAL REVIEW

Volume 17 Number 1, Spring 1987

Index: amplifiers, integrated circuits, ion implantation, MMICs, models, transistors

Design and modeling of a GaAs monolithic 2- to 6-GHz feedback amplifier

R. K. GUPTA, J. H. REYNOLDS, M. C. FU, AND T. HEIKKILA

(Manuscript received December 3, 1986)

Abstract

The design, fabrication, and performance of a monolithic 2- to 6-GHz feedback amplifier module are described, with particular emphasis on the modeling approaches used during the design and fabrication phases. The amplifier design is based on GaAs field-effect transistor (FET) equivalent circuit parameters derived from known ion implantation profile, peak doping density, and device geometries. Measured parametric data obtained from test patterns are used to monitor and control the fabrication process. Both measured and modeled DC and RF parameters of the FETs, as well as amplifier performance results, are presented for two process wafers. Agreement between the measured and modeled gain of the feedback amplifier was within 1 dB over a broad 1- to 11-GHz frequency band.

Introduction

The use of GaAs monolithic microwave integrated circuits (MMICs) in communications systems holds great promise for enhancing system reliability while reducing mass, volume, and cost [1],[2]. However, the design and fabrication cycle for MMIC modules is relatively long and expensive compared to that of conventional hybrid circuits. In order to reduce development costs and enhance the probability of success in a single fabrication interation, a thorough understanding of field-effect transistor (FET) models, from basic

device physics through the fabrication process, design methods, and circuit modeling, is required.

This paper presents the design, fabrication, and performance of an MMIC 2- to 6-GHz feedback amplifier module developed at COMSAT Laboratories. The design strategies and modeling approaches used during various MMIC development phases are discussed. A FET equivalent circuit was first derived for a known ion implant profile, peak doping density, gate recess depth, and other fabrication parameters. The amplifier was then designed with maximum tolerance to process variations and with simple on-chip tuning to adjust for the most sensitive parameters. The modeling process described here is useful for selecting optimum FET geometries, designing the circuit for desired performance, and defining target values for critical process parameters and adjusting these values during fabrication. In addition, accurate modeling of device DC current and transfer characteristics allows *a priori* selection of device operating conditions for self-bias operation.

General design considerations

The design of broadband feedback amplifiers requires FET devices with large transconductance [3]–[6]. This can be achieved by increasing the device width and carrier concentration and decreasing the gate length. Larger device width also results in larger DC power dissipation and larger gate-to-source capacitance, C_{gs}, which tend to degrade the open-loop gain at higher frequencies. Therefore, FETs with smaller gate lengths and a higher transconductance (g_m)-to-C_{gs} ratio are desirable. Based on these considerations, a FET with a nominal gate length of 0.5 (or 0.6) μm and width of 300 μm was selected for this design. This FET geometry was consistent with other circuits on the same mask set, which included a low-noise amplifier [7], a dual-gate FET switch with a level translator, and an amplifier with passive FET switching at its input and output.

To increase the yield, the MMIC design must be tolerant to fabrication parameter variations associated with process uncertainties. Therefore, a major portion of the design effort involved developing accurate models for the active devices and the matching components, and establishing their sensitivity to process variations. Figure 1 is a flow-chart of a typical MMIC design cycle. The design begins with device selection for desired electrical performance, and includes device modeling, design of matching networks, sensitivity analysis for acceptable performance, circuit layout, and mask-making. Circuit fabrication consists of processing the various mask layers, in-line parametric testing, fabrication adjustments, DC probing, thinning, and dicing. Because of the time consumed by each mask fabrication and processing cycle, it is essential that a design be relatively insensitive to fabrication tolerances.

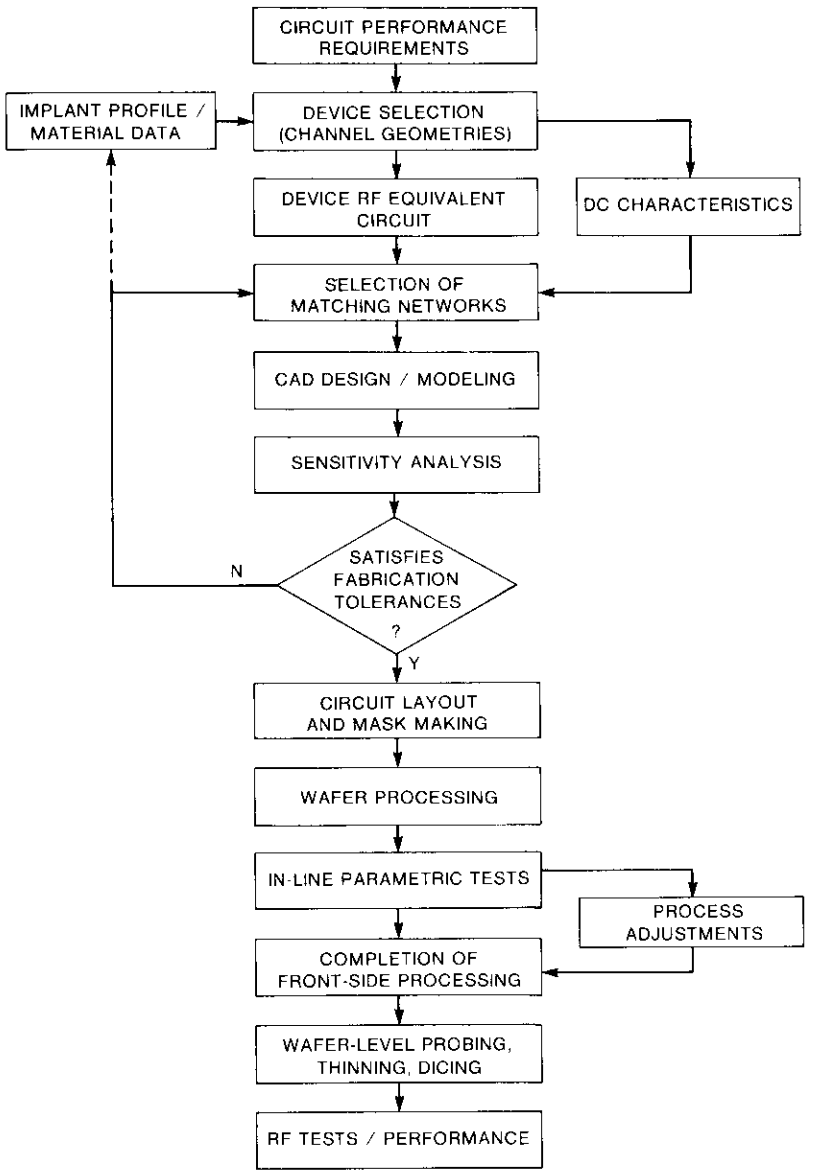

Figure 1. *Flowchart of the MMIC Design, Modeling, and Fabrication Cycle*

FET modeling

A number of models have been used at COMSAT Laboratories for the design of FETs and circuits [8],[9]. The FET model described here is based on device physics, with many refinements derived from measurements of a prototype device. For this design, the target Gaussian profile shown in Figure 2a was used with the following profile parameters:

- Peak carrier density, n_p $2.7 \times 10^{17}\ \text{cm}^{-3}$
- Peak location, d_p 0.11 μm
- Standard deviation, σ 0.065 μm

A recess depth up to the peak of the profile (0.11 μm), as shown in Figure 2b, results in a pinchoff voltage of approximately −1.5 V and makes the DC and RF device characteristics relatively insensitive to profile parameters. This profile information and measurements on the prototype device were used to obtain the device equivalent circuit shown in Figure 3. Most of the intrinsic FET elements, including junction capacitance, input resistance, and device transconductance, were computed from the basic device physics. Output resistance, parasitic capacitances, and resistances were obtained from device geometries and measurements.

Junction capacitance, C_{gs}, is modeled as the capacitance of the velocity-saturated region under the gate. Geometric inter-electrode capacitance caused by electrostatic coupling between the gate, source, and drain electrodes was computed as described by Pucel *et al.* [10]. Gate-to-N^+ and N^+-to-N^+ (rather than gate-to-ohmic and ohmic-to-ohmic) gap dimensions were used. The N^+ material is sufficiently conductive to maintain an equi-potential surface over the short distances involved. A sidewall capacitance, which accounts for the extension of the depletion region toward the source, must be added to the gate-to-source fringing capacitance. The junction sidewall capacitance computed by the model is 0.04 pF and is included in the C_g of the device equivalent circuit.

Input resistance, R_{in}, represents a charging resistance corresponding to the gate-to-source capacitance. It is usually derived from an electron transit time, τ, using resistance-capacitance (RC) time-constant relation

$$R_{in} = \tau / C_{gs} \tag{1}$$

The transit time is defined by

$$\tau = L_\tau / V_s$$

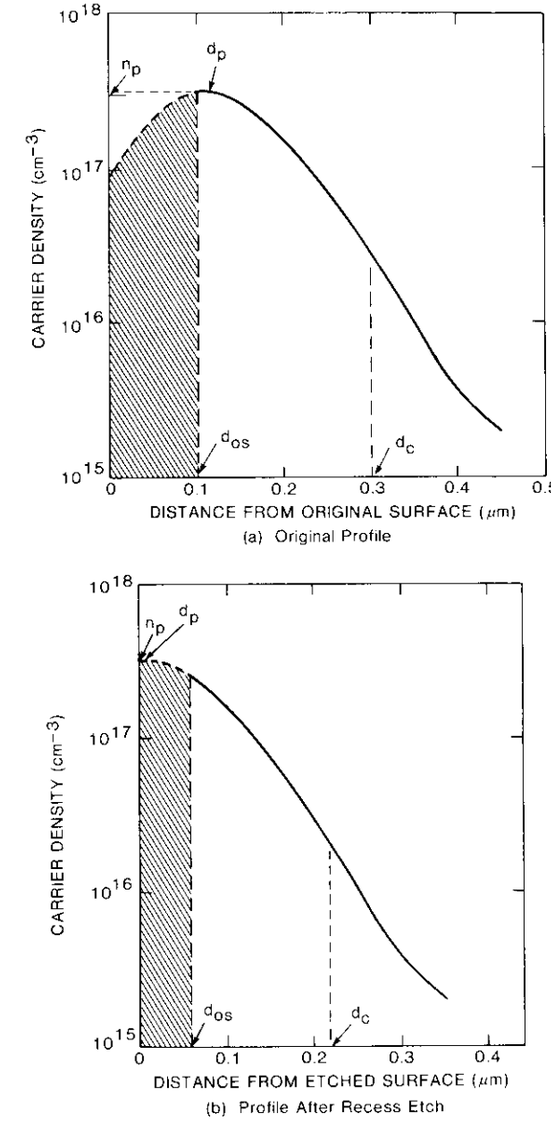

Figure 2. *Gaussian Ion Implantation Profiles for the MMIC Feedback Amplifier*

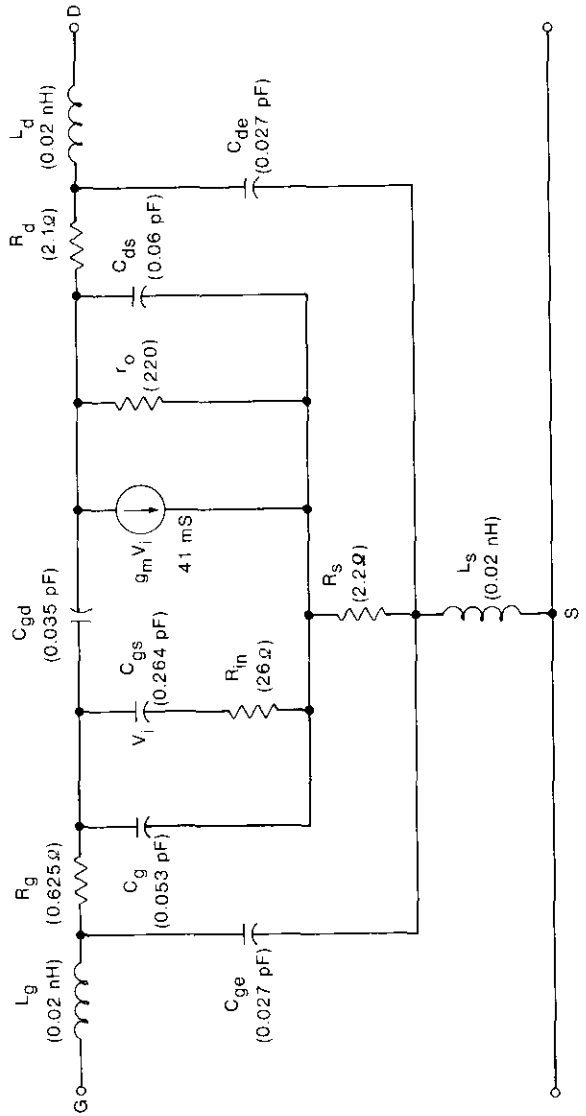

Figure 3. *Equivalent Circuit Model of a FET With 300-μm Gate Width and 0.7-μm Gate Length*

where V_s is the saturated velocity and L_τ is an empirically determined transit length. In the model, $V_s = 1.2 \times 10^7$ cm/s and $L_\tau = 0.7$ μm (geometric gate length) were used.

Transconductance, g_m, is computed from basic device physics and is dependent on carrier profile, saturation velocity, and gate width. The g_m is strongly dependent on the device operating point and is relatively sensitive to process variations. Uncertainty in computed g_m is also caused by uncertainties in saturated velocity estimates.

Extrinsic FET elements such as parasitic resistances were obtained from the parametric data measured for prototype FETs. These element values were further verified by biasing the prototype FET beyond pinchoff with no drain bias and measuring the device *S*-parameters. This bias condition essentially turns the intrinsic FET elements off, and considerably simplifies the equivalent circuit. The input and output network elements were obtained by using SUPERCOMPACT™ optimization to fit *S*-parameters to the measured data. An equivalent pad inductance of 0.02 nH and external gate-to-source pad and drain pad capacitances of 0.027 pF were included in the model.

Using the FET model, two-port *S*-parameters for the device were calculated. Also, *S*-parameters were measured for a prototype device over the 2- to 18-GHz frequency range, and an equivalent circuit was fitted to measured values using the SUPERCOMPACT optimization routine. Figures 4a (S_{11} and S_{22}) and 4b (S_{21}) show a comparison between measured, modeled, and fitted *S*-parameters of the device over the 2- to 18-GHz range. The agreement between measured and modeled values for all *S*-parameters is excellent up to 12 GHz. For higher frequencies, a larger spread is observed for the input reflection parameter (S_{11}), although the model could still be used for higher frequency designs. This model was considered suitable for the design of a 2- to 6-GHz feedback amplifier.

Amplifier design

Feedback techniques are particularly well suited for the design of general-purpose MMIC gain modules because of the achievable bandwidth and gain flatness, inherent stability, and good linearity [6]. For feedback amplifiers, loop phase shift should be minimized so that feedback does not become positive with frequency. This is easily accomplished in MMIC implementations because of their small size and circuit layout flexibility.

The design presented here is based on *S*-parameters of the device which were obtained from the device equivalent circuit of Figure 3. Figure 5 is a schematic for the two-stage feedback amplifier. Because shunt-resistive feedback is used to reduce the magnitude of reflection parameters S_{11} and

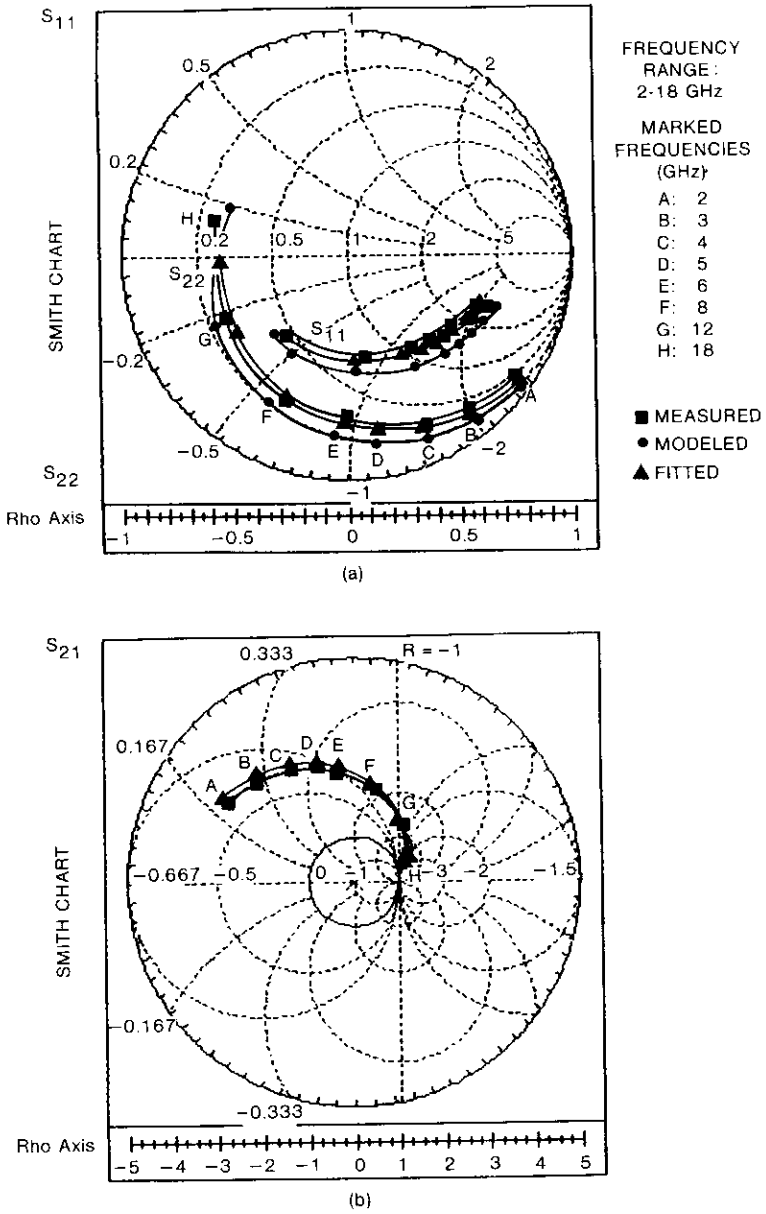

Figure 4. *Comparison of Measured, Modeled, and Fitted Device S-Parameters Over the 2- to 18-GHz Frequency Band*

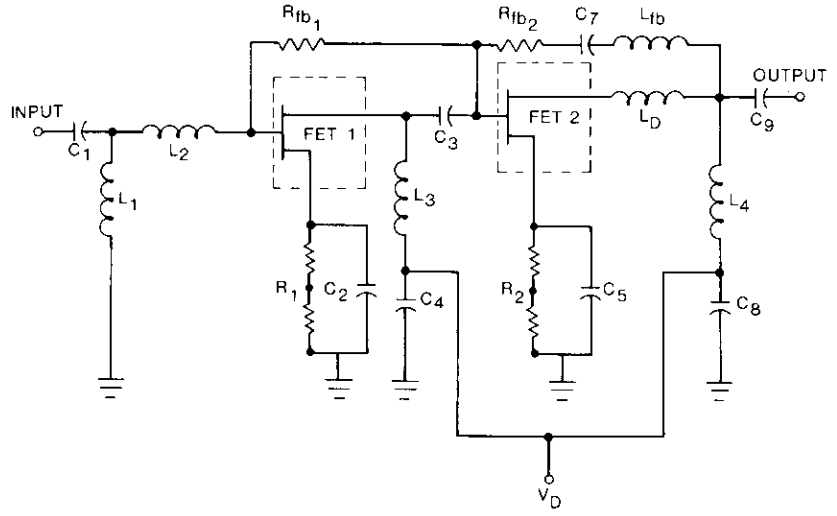

Figure 5. *Schematic of the Two-Stage Feedback Amplifier*

S_{22} at the FET gate and drain ports, transformation ratios for input/output matching networks become small and broadband matching can be accomplished by using simple matching networks. Also, parasitic elements in the device cause a gain rolloff with frequency, thus limiting the useful bandwidth.

In the feedback approach, a drain inductance (L_d) and feedback inductance (L_{fb}) can be used to extend the amplifier bandwidth. Inductance L_d compensates for the drain-to-source capacitance of the FET at higher frequencies. As frequency increases, inductance L_{fb} adjusts the S-parameters of the feedback amplifier by reducing the effectiveness of the resistance (R_{fb_2}) in the feedback loop.

The values of R_{fb_2}, L_{fb}, and L_d in the second stage of the feedback amplifier were adjusted until the maximum available gain was flat, with relatively small values of S_{11} and S_{22} over the desired frequency band of 2 to 6 GHz. The first stage (with resistive feedback) was analyzed, and the two stages were combined by using an interstage matching network having the minimum number of elements required for biasing the FETs. Capacitors C_7 and C_3 were included to isolate the drain and gate biases, and inductor L_3 and capacitor C_4 are required for drain bias to FET1. The two-stage configuration was optimized by using SUPERCOMPACT to satisfy the gain and gain flatness requirements.

The input match was achieved with one series inductor, one shunt inductor, and a series capacitor. The output could be matched with one shunt inductor and a series capacitor. The series input and output capacitors also provide

DC isolation of the input and output ports. Inductor L_4 was used for drain bias of the second FET. The parallel resistance and capacitance combination was included in the source terminals to provide self-bias for the FETs. Inductor L_1 provided the ground return for the gate terminals of both FETs. Large inductors in the bias network (L_1, L_3, and L_4) were realized as spirals and analyzed using coupled transmission line models [11]. Smaller inductor values were realized by high-impedance transmission line lengths of 15-μm width.

The overlay capacitors were realized with silicon-nitride dielectric. They were modeled as lumped capacitances and small sections of transmission lines. To minimize overall chip size, larger capacitors in the bias network were realized using thin (1,000-Å) dielectric with capacitance of 550 pF/mm^2, and smaller capacitors were realized using a relatively thick dielectric layer (5,000 Å) with capacitance of 110 pF/mm^2. Ion-implanted resistors were fabricated from N^+ regions formed in the same step as the FET N^+ contact region, which had a resistivity of 100 Ω per square.

The use of lumped elements in the design [12] resulted in reduced size, and hence more circuits per wafer. All interconnecting lines were modeled as transmission line elements with appropriate physical dimensions. The effects of discontinuities and bends in transmission lines were included in the model. The nominal gain was modeled to be greater than 10 dB, return losses to be better than 16 dB, and reverse isolation to be greater than 25 dB over the 2- to 6-GHz frequency band.

Circuit performance was analyzed to evaluate circuit sensitivity to fabrication tolerances. Variations in the device model may be caused by gate length uncertainties which affect g_m and C_{gs}, and by substrate properties which change output resistance, r_o. In addition, the resistance and capacitor values were allowed to change by ±20 and ±10 percent, respectively. Figure 6 shows the nominal amplifier gain and variations in gain response for a selected set of critical parameter variations.

Device transconductance (g_m) and output resistance (r_o) variations cause gain variations without significant change in gain flatness. Gate capacitance reduction results in improved gain slope, and vice-versa. An increase in resistances and/or reduction in capacitance in the matching circuit result in higher gain slope over the desired band. For all these variations, the input/output return loss was modeled to be better than 15 dB over the band of interest. This sensitivity analysis indicated that the design is relatively tolerant of all parameter variations except for resistance in the feedback path. Therefore, extra taps were provided in the feedback resistances so that their values could be adjusted. Adjustment capability was also provided in the self-bias resistors so that device current could be adjusted by wire-bonds.

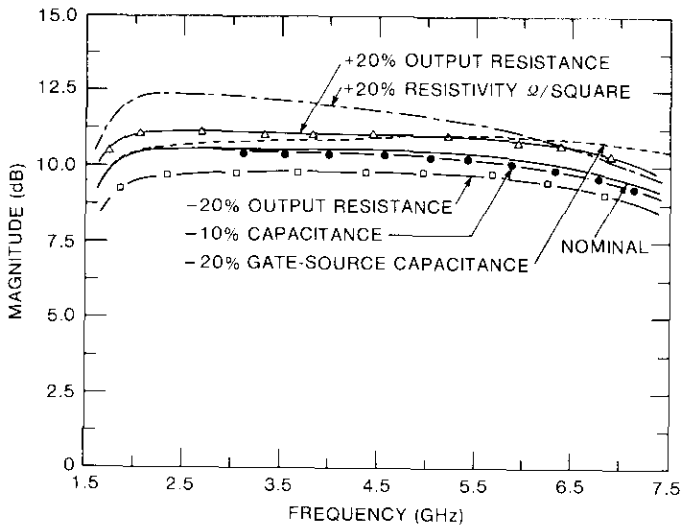

Figure 6. *Modeled 2- to 6-GHz Feedback Amplifier Gain With Parameter Variations*

Fabrication and in-line testing

Figure 7 is a photograph of the finished circuit, with overall dimensions of 60 × 100 mil (1.5 × 2.5 mm). The circuit was designed to be the same size as other circuits on the mask for dicing convenience, and could be further reduced in size. The drain biases for two stages of the amplifier were tied together for single positive-supply operation. The FETs were fabricated using selective ion implantation into liquid-encapsulated Czochralski (LEC) material. The channel was formed by a 100-keV silicon implant, and the N^+ ohmic contact area of the devices was formed by a 200-keV silicon implant with a peak carrier density of about 1×10^{18} cm^{-3}. The implanted resistors were fabricated using the same process as for the contact area. The ohmic contacts were alloyed Au/Ge/Ag/Au, and the gates were fabricated of Ti/Pt/Au approximately 0.5-μm thick and 0.5-μm (nominal) long, patterned by electron-beam lithography. All other patterning was done by near-UV optical lithography. The gate metal also formed the bottom plate of the capacitors.

The FET was designed with two parallel gate feeds. The total gate width was 300 μm, and the unit gate width was 75 μm. A dual-level (1,000- and 5,000-Å), plasma-deposited silicon nitride structure was used for the capacitor

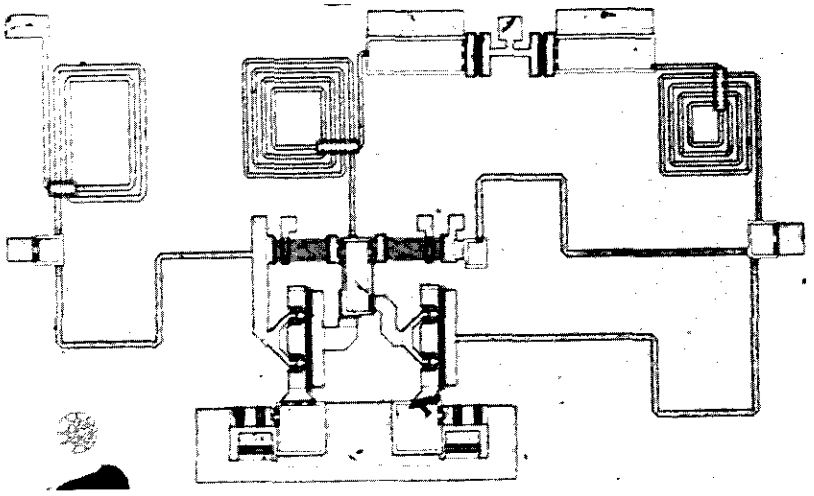

Figure 7. *The MMIC 2- to 6-GHz Feedback Amplifier Chip (dimensions: 1.5 × 2.5 mm)*

dielectric. The thicker nitride was used for glassivation of the FET channel region, while the thinner dielectric was used for high-value bypass capacitors to provide a substantial reduction in area. A 2-μm plated gold layer formed the inductors, the top plate on the capacitors, the overlay metal on the ohmic contacts, and other passive circuit metal areas. Plated gold air-bridges were used to interconnect the FET sources, to contact the top plate of the capacitors, and to form crossovers for the spiral inductors.

The data from process monitor wafers and process control monitors (PCMs) included in the mask were used to fine-tune the process parameters. The critical process step is the gate-recess etch, in which the gate is etched until the ungated saturated current (I_{dso}) in a test structure with the same channel architecture reaches a predetermined value. The value is computed from the equation

$$I_{dso} = W \int_{d_{os}}^{d_c} qnV_s dx \qquad (2)$$

where W = channel width
n = carrier density
V_s = saturated velocity
d_{os} = depth of the open-surface depletion layer.

The total channel depth, d_c, is taken for modeling purposes as the 3σ point on the trailing edge of the Gaussian carrier profile. Since the channel surface is bare GaAs, d_{os} is determined by the carrier density in the depletion layer and by the open-surface barrier height, which is 0.7 ± 0.1 V. Since the implanted carrier density is non-uniform, d_{os} is a function of recess depth.

The carrier profile is a truncated Gaussian distribution (see Figure 2) which depends on the original depth (d_p) of the implant, the width (σ) of the Gaussian distribution, the peak carrier density (n_p), and the recess depth (d_r). For a given implant profile, equation (2) is used to numerically compute I_{dso} as a fraction of the recess depth profile.

For the target profile parameters, I_{dso} as a function of recess depth is shown in Figure 8. The FET model was also used to compute the saturation current (I_{dss}) and pinchoff voltage (V_p) as a function of recess depth, as shown. The target I_{dss} was set at 40 mA for the 300-μm-wide FET (133 mA/mm). From Figure 8, the corresponding I_{dso} is observed to be 189 mA/mm. This procedure links the process parameter, I_{dso}, to the desired DC transfer characteristics. Consideration of the truncated Gaussian profile in Figure 2 shows that the parameters are insensitive to peak depth. If for example the peak is shifted to the right, then a shift in the recess depth will produce an equivalent truncated profile. A decrease in peak carrier density would require a shallower recess in order to obtain the same I_{dso}. The shallower recess also increases

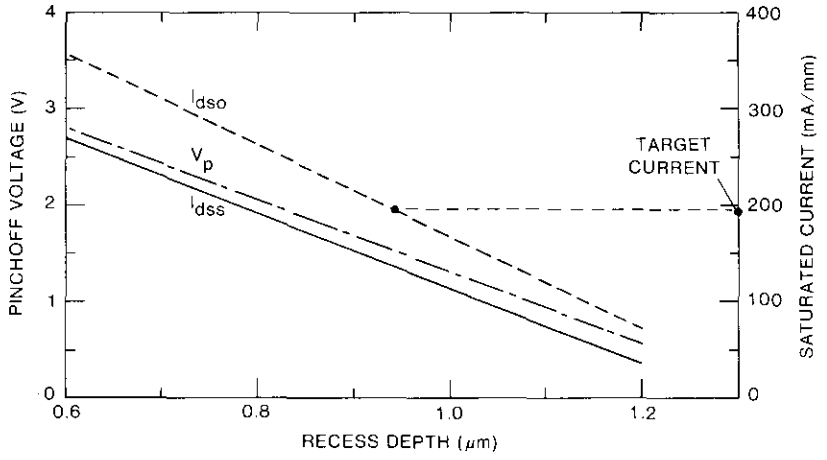

Figure 8. *Model Prediction of Saturated Current and Pinchoff Voltage for* $n_p = 2.7 \times 10^{17}\ cm^{-3}$, $d_p = 0.11$ μm, σ = 0.065 μm, *and Gate Length = 0.5* μm

I_{dss} and V_p, compensating for the reduced peak carrier density. Changes in profile width are similarly compensated.

The target I_{dso} was held fixed at the design value for the wafer runs during processing. However, in-line process data can be used to fine-tune the target value in other runs. As shown in Figure 9, device wafers are accompanied by implant process monitor wafers. The monitor wafers receive a sheet implant which can be characterized by Polaron carrier profile measurements and by contactless sheet resistance measurements. The Polaron measurement provides an estimate of the peak height and shape, as well as other information on the overall quality of the implant. The contactless resistivity measurement,

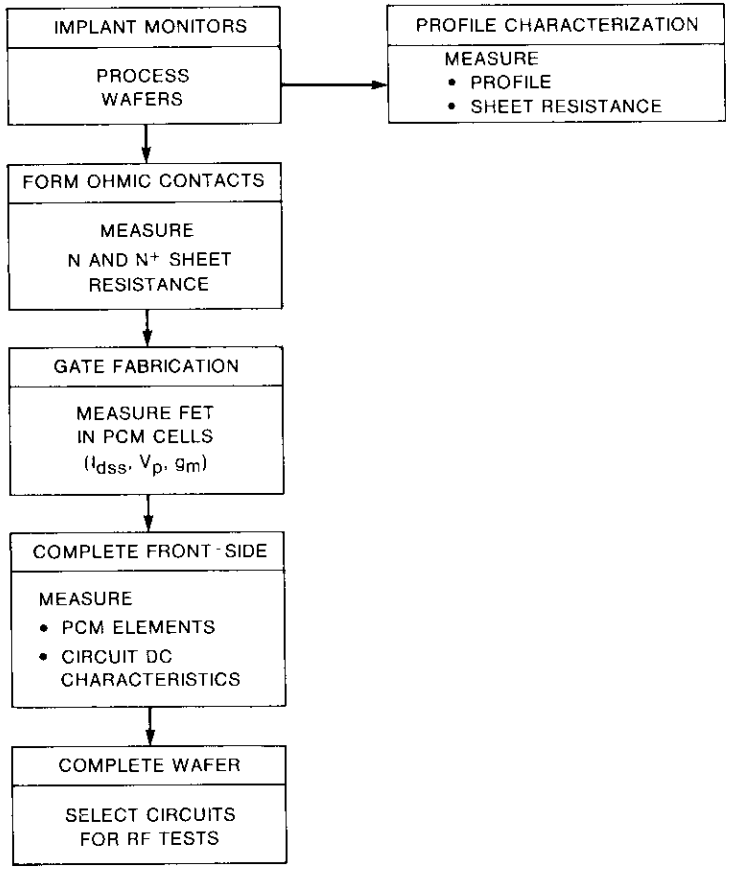

Figure 9. *In-Line Test Procedure*

calibrated by measurements on similar wafers with known profiles, provides information on the peak carrier density.

The test patterns in the PCM cells on the device wafers (Figure 10) provide additional data. The transfer length measurement pattern, which is used primarily to monitor contact resistance, also yields sheet resistance data. Additional Van der Pauw patterns provide accurate sheet resistance data, as well as information about the distribution of sheet resistance across the wafer. Since the sheet resistance of the N^+ implant formed critical resistors, it was of particular importance for this circuit. These resistance measurements, together with sensitivity analysis data from modeling, may be useful for yield predictions.

A revised estimate of the peak carrier density, based on PCM data, can be inserted into the model to establish a corrected I_{dso} before the wafers are committed to the gate deposition step. After this step, the PCMs can in principal be used to fully characterize the run. In practice, only a minimum of testing is performed before the completion of front-side wafer processing, in order to determine the basic DC FET characteristics (*e.g.*, I_{dss} and V_p) and to estimate the final wafer yield.

After completion of front-side processing, data are taken on test capacitors, resistors, and other elements. Finally, DC data on the test FETs and circuits are collected. Since the amplifier is self-biased, only the source-drain current at the operating point was measured to select chips with DC currents within the limits established by the model.

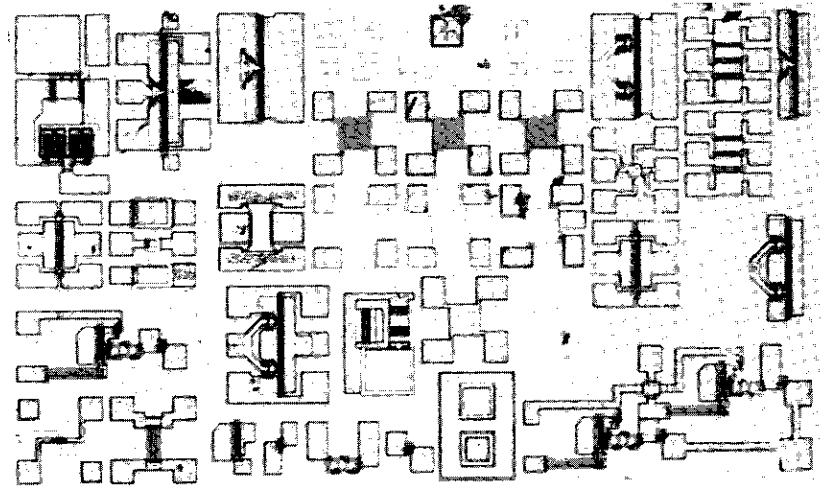

Figure 10. *Test Patterns in the PCM Cells*

Measured and modeled DC and RF results

The device model was used to compute transfer curves for two process wafer runs. Figure 11 shows the measured and modeled transfer curve and g_m for one wafer (26A/2). This transfer curve can be used to determine the device recess depth and the operating point. The values of self-bias resistors are obtained from the sheet resistivity data measured by the PCM cells. Intersection of the load line with the transfer curve gives the operating point for the amplifier chips. Thus, based on the carrier profile and other parametric data (contact resistance, sheet resistivity, capacitance, etc.) from the PCM cells, a set of input parameters needed to generate the DC and RF equivalent circuit of the device and circuit is fully defined. This information can be used to accept or reject wafers at various fabrication steps and for further processing and/or testing.

An example of this is the second wafer (27A/3), where the carrier profile was similar to target except for the peak carrier density, which was 2.1×10^{17} cm^{-3}. The measured and modeled values of g_m are shown in Figure 12. The g_m for this wafer as a function of drain-to-source current was

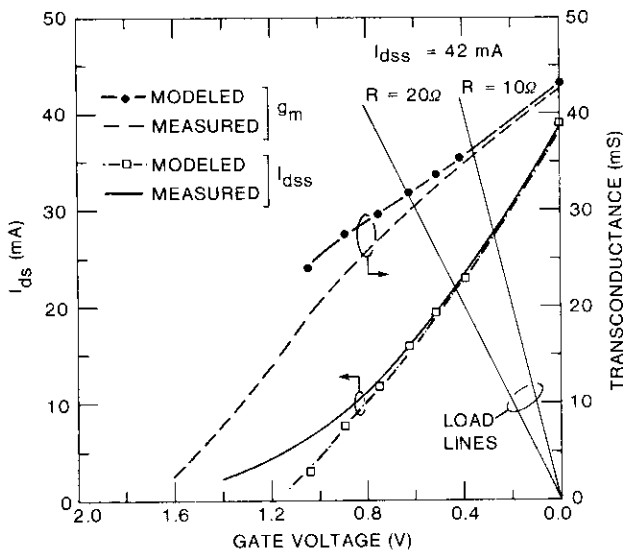

Figure 11. *Measured and Modeled Transfer Characteristics and Transconductance (g_m) for Wafer 26A/2 (profile: $n_p = 2.7 \times 10^{17}$ cm^{-3}, $d_p = 0.1$ μm, $\sigma = 0.066$ μm, $d_r = 0.084$ μm)*

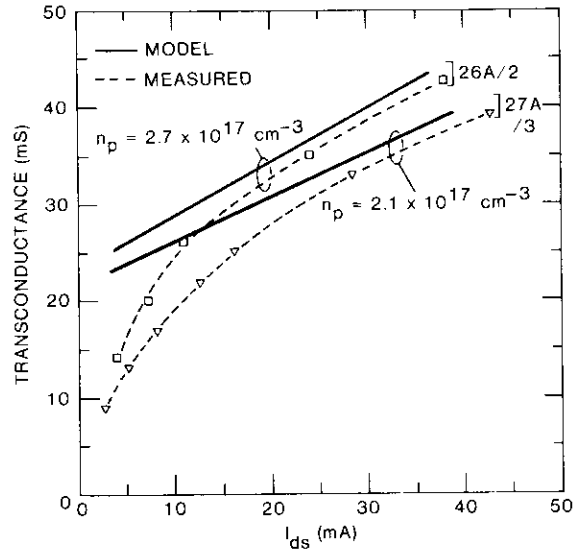

Figure 12. *Comparison of Measured and Modeled Transconductance for Two Process Wafers*

up to 15-percent lower than that of the first wafer. It is also apparent that the modeled values of g_m are close to the measured values in the region of device operation ($I_{ds} \sim 30$ mA). However, for lower values of current, the agreement between measured and modeled results degrades. This is believed to be due to the omission of parallel current paths and space-charge-limited current through the gate and substrate depletion layers [13]. The deviation is greater for the low-carrier-density wafer where these components become very significant near pinchoff.

Figure 13a shows the measured and modeled gain of the amplifiers from the two wafers, together with design gain values over the 2- to 6-GHz frequency range. The modeled values are obtained by introducing the values of g_m and C_{gs} at the operating points, as well as resistance and capacitance values obtained from measured parametric data in the original amplifier circuit model. The measured gain slope is somewhat larger than expected because the resistivity was higher and capacitance was lower than nominal design values. The measured and modeled input and output return losses of the amplifier from wafer 27A/3 are shown in Figures 13b and 13c, respectively.

Figure 14 shows the agreement between measured and modeled gain and input return loss over a broad 1- to 11-GHz frequency range. Measured and

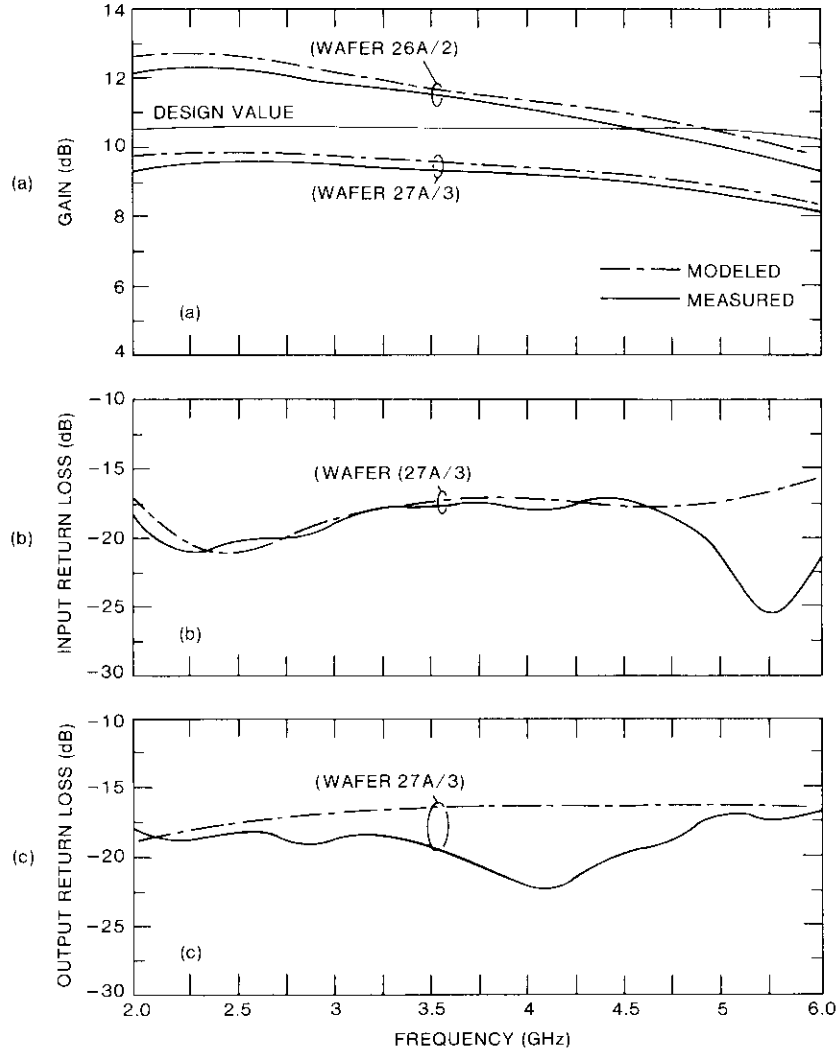

Figure 13. *Comparison of Measured and Modeled Results Over the 2- to 6-GHz Frequency Range*

modeled gains agree to within 1 dB over this range. The return loss is better than 16.5 dB over the 2- to 6-GHz frequency range of interest. The reverse isolation of the amplifiers was measured to be better than 25 dB, as modeled. The 1-dB compression point was measured to be 13.5 dBm, and the noise figure was less than 6.5 dB over the 2- to 6-GHz amplifier bandwidth.

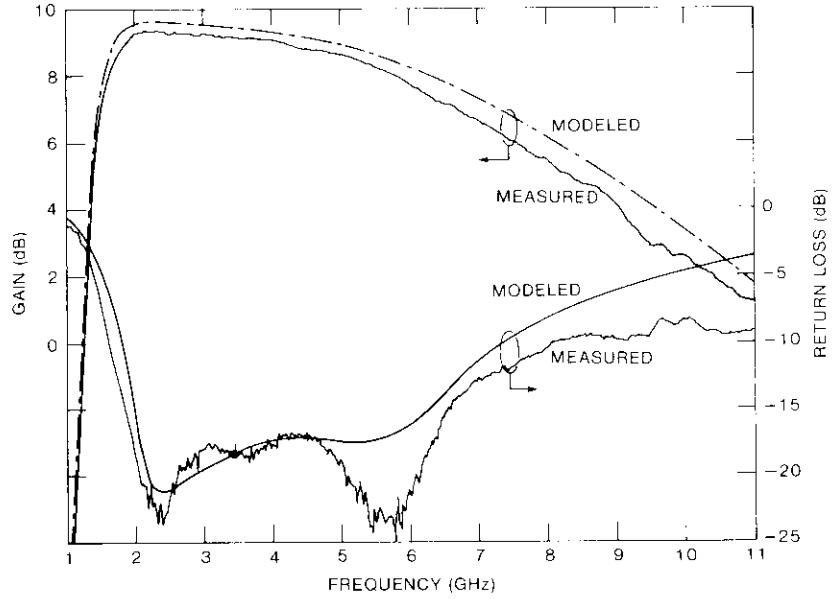

Figure 14. *Comparison of Measured and Modeled Gain and Input Return Loss Over a Broad (1- to 11-GHz) Frequency Range*

Conclusions

Design, fabrication, and performance results have been presented for an MMIC 2- to 6-GHz feedback amplifier module developed at COMSAT Laboratories. This circuit design has demonstrated that extensive use of device and circuit modeling is very useful in selecting device geometries, defining target values for critical process parameters, and making adjustments during the fabrication process. The use of PCM patterns has been particularly valuable for monitoring process parameters. Good agreement between measured and modeled results has demonstrated the validity of the device and circuit models over a broad frequency range.

Acknowledgments

The authors wish to acknowledge the efforts of J. Allison, C. Cannon, G. Carlson, R. Edwards, L. Holdeman, J. Kearney, R. Kroll, P. McNally, R. Porter, and J. Tyler during the design, CAD layout, fabrication, and test phases of this circuit development. They also wish to thank B. Geller,

R. Mott, J. Potukuchi, and T. Smith for many useful discussions. The encouragement and support provided by F. Assal, H. Huang, and C. Mahle is gratefully acknowledged.

References

[1] C. Mahle and H. C. Huang, "MMIC's in Communications," *IEEE Communications Magazine*, Vol. 23, No. 9, September 1985, pp. 8–16.

[2] J. R. Potukuchi *et al.*, "Design and Development of Monolithic 6/4-GHz Transponder Subsystems," Government Microcircuit Applications Conference, Orlando, Florida, November 1985, *Digest*, pp. 353–354.

[3] K. Niclas, "The Matched Feedback Amplifier: Ultrawide-Band Microwave Amplification With GaAs MESFETs," *IEEE Transactions on Microwave Theory and Techniques*," Vol. MTT-28, No. 4, April 1980, pp. 285–294.

[4] A. Pavio, "A Network Modeling and Design Method for a 2–18 GHz Feedback Amplifier," *IEEE Transactions on Microwave Theory and Techniques*, Vol. MTT-30, No. 12, December 1983, pp. 2212–2216.

[5] S. Moghe *et al.*, "A Wideband Two-Stage Miniature Amplifier," IEEE GaAs Integrated Circuit Symposium, Phoenix, Arizona, October 1983, *Technical Digest*, pp. 7–10.

[6] P. Rigby, J. Suffolk, and R. Pengelly, "Broadband Monolithic Low-Noise Feedback Amplifier," IEEE Microwave and Millimeter-Wave Monolithic Circuits Symposium, Boston, Massachusetts, May/June 1983, *Digest of Papers*, pp. 71–75.

[7] R. Mott, "A GaAs Monolithic 6-GHz Low-Noise Amplifier for Satellite Receivers," scheduled for presentation at the IEEE MTT-S International Microwave Symposium, Las Vegas, Nevada, June 1987.

[8] T. Smith, "A Modeling System for Simulation of GaAs FET Performance," *COMSAT Technical Review*, Vol. 15, No. 2A, Fall 1985, pp. 237–258.

[9] B. D. Geller and J. L. Abita, "A 3.7- to 4.2-GHz Monolithic Medium-Power Amplifier," *Microwave Journal*, Vol. 28, No. 9, September 1985, pp. 187–195.

[10] R. Pucel, H. Hause, and H. Statz, "Signal and Noise Properties of Gallium Arsenide Microwave Field-Effect Transistors," *Advances in Electronics and Electron Physics*, Vol. 38, New York: Academic Press, 1975, pp. 193–265.

[11] D. Cahana, "A New Transmission Line Approach for Designing Spiral Microstrip Inductors for Microwave Integrated Circuits," IEEE MTT-S International Microwave Symposium, Boston, Massachusetts, May/June 1983, *Digest*, pp. 245–247.

[12] R. K. Gupta and W. J. Getsinger, "Quasi-Lumped-Element 3- and 4-Port Networks for MIC and MMIC Applications," IEEE MTT-S International Microwave Symposium, San Francisco, California, May/June 1984, *Digest*, pp. 409–411.

[13] T. Smith, "Beyond-Punchthrough Current in GaAs MESFET's," *IEEE Electron Device Letters*, Vol. EDL-7, No. 3, March 1986, p. 188.

Ramesh K. Gupta received a B.Sc. (Honors) in electronics and communications engineering from Punjab University, Chandigarh, India, in 1974, and an M.Sc. and Ph.D. in electrical engineering from the University of Alberta, Edmonton, Canada, in 1976 and 1980, respectively. In 1976, he was awarded a 3-year Alberta Government Telephones Centennial Fellowship for graduate research in telecommunications. In 1980 he joined COMSAT Laboratories, where he is presently Associate Manager of the Microwave Systems Department. His responsibilities at COMSAT have included development of a wideband 8 × 8 microwave switch matrix for SS-TDMA applications, and design of C- *and* K_u*-band hybrid and MMIC amplifiers, switch modules, and variable gain and phase control modules. He has also contributed to the spacecraft and ground network study and support effort for the INTELSAT VI satellite program. Currently, he is involved with development of MMIC attenuators and* K_u*-band active elements for phased-array antennas. Dr. Gupta is a Senior Member of IEEE, and has served since 1985 on the Executive Committee of the Washington, D.C./Northern Virginia Chapter of the IEEE MTT Society.*

John H. Reynolds received a B.S. in physics from the Worcester Polytechnic Institute in 1962 and an M.S. in physics from Purdue University in 1964. He joined COMSAT Laboratories in 1968 and has contributed to the development of solar cells and the analysis of tunnel diodes and transfer electron devices. Recently, he has been involved with analysis and modeling of low-noise and power FETs, and GaAs MMICs. In 1986 he joined the Systems Development Division, where he is involved in software development for communications systems. Prior to joining COMSAT, Mr. Reynolds was a staff member at the Sprague Electric Research Center in North Adams, Massachusetts, where he was engaged in research on MOS transistors and other solid-state devices. He is a member of IEEE and Sigma Xi.

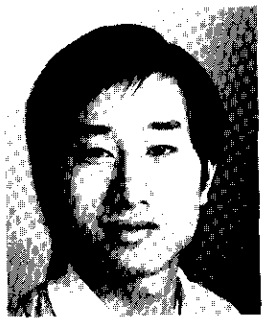

Michael C. Fu received the S.B. and S.M. degrees in electrical engineering and an S.B. in mathematics from the Massachusetts Institute of Technology, all in 1985. From 1982 to 1985, he worked in the Microwave Technology Division at COMSAT Laboratories under the MIT VI-A cooperative student program. His work involved the modeling of microwave single- and dual-gate FET devices and the design of GaAs MMIC circuits. In 1985, Mr. Fu was awarded a 3-year National Science Foundation graduate fellowship. He is currently working toward a Ph.D. in mathematics at Harvard University. He is a member of Tau Beta Pi and Eta Kappa Nu.

Tapio Heikkila received an M.Sc. in microwaves and electronics and a Licentiate of Technology degree from the Helsinki University of Technology, Finland, in 1977 and 1981, respectively. In 1977, he visited the University of Bonn, West Germany, where he was engaged in the development of an 80-GHz radio-astronomical receiver. He later worked at the VTT Telecommunications Laboratory of the Technical Research Center of Finland, where he was involved in the development of a prototype 12-GHz DBS down-converter and performed system studies on the Scandinavian Tele-x communications satellite system. From 1983 to 1985, he worked at COMSAT Laboratories as an INTELSAT assignee and was involved in the design of advanced MIC/MMIC amplifiers and circuits. In 1986, Mr. Heikkila joined Nokia Telecommunications, Espoo, Finland, where he is currently Manager of the Satellite Communications Department. Since 1985, he has served as Secretary of the National Space Technology Council of Finland.

Index: communication satellites, digital transmission, filters, synchronization, transponders, on-board data processing

A 120-Mbit/s TDMA QPSK modem for on-board applications

R. G. EGRI, K. KARIMULLAH, AND F. T. ASSAL

(Manuscript received November 24, 1986)

Abstract

The design and development of a C-band, 120-Mbit/s QPSK modem for possible on-board satellite use is presented. The modem is designed to operate in either continuous or burst mode along the INTELSAT frame-defined, time-division multiple-access (TDMA) format. The design is based on a demodulation/remodulation approach for phase-coherent carrier recovery. The demodulator detects orthogonal data streams at baseband directly from the 4-GHz QPSK signal, thereby avoiding the need for further frequency conversion. The measured modulated bit-energy to noise-power-density ratio (E_b/N_o) is within 1.2 dB of that of an ideal demodulator at a bit error rate of 10^{-6}.

The demodulator is realized in three microwave integrated circuit modules: an RF remodulation module, an emitter-coupled logic regeneration module, and a phase-locked loop. The total power consumption of the demodulator is 3.3 W. One of the most significant advantages of the design is that the hardware, which consists exclusively of microwave, digital, and DC circuits, has the potential of being realized as GaAs monolithic microwave integrated circuit (MMIC) modules, with consequent reduction of mass and power and a significant increase in reliability.

Introduction

Future satellite systems are envisioned to include on-board regeneration, which has many advantages over the conventional repeater-type transponder [1],[2]. On-board regeneration, along with processing at baseband,

provides full connectivity and substantial link budget advantages. Connectivity is achieved by a baseband switch matrix, while link performance is enhanced due to the separation of up- and down-links. This results in a significant reduction in earth station antenna size requirements and/or the need for high-power amplifiers. When the up- and down-links suffer noise degradation, bit error rate (BER) performance is considerably improved over that of a conventional transponder, as shown in Figure 1 [1].

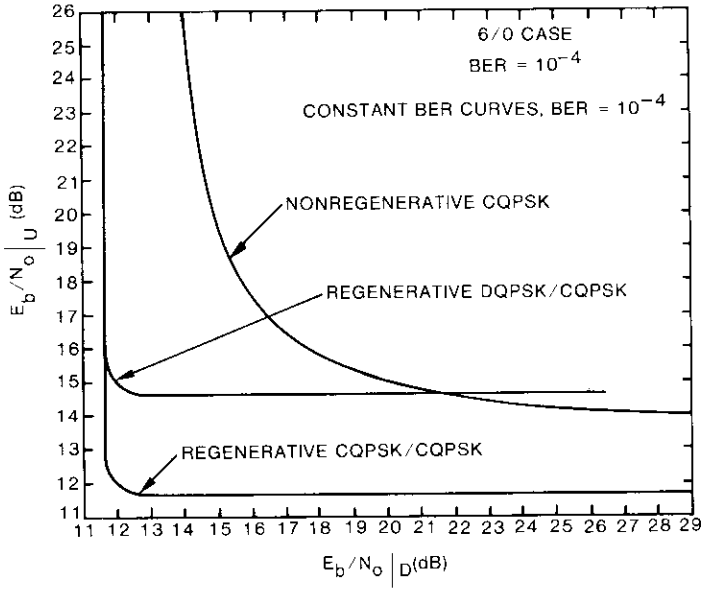

Figure 1. *ISO-BER Performance Characteristics of Three Satellite Configurations With and Without On-Board Demodulation and Remodulation [1]*

On-board regeneration of quadrature phase-shift keying (QPSK) signals will require that the coherent QPSK modem take full advantage of the available up-link e.i.r.p. Modem components must not only meet communications performance requirements, but also satisfy the specific size, weight, power, and reliability requirements of space hardware.

Figure 2 is a simplified block diagram of an on-board processing satellite for high-bit-rate time division multiple access (TDMA). In the simplest case, the up-link QPSK channels are separated by receive filters and are demodulated to yield I, Q data and the associated clock signal. Retiming buffers allow the I, Q data of each channel to be reclocked by one common reference on-board clock before being routed to various destinations by the baseband

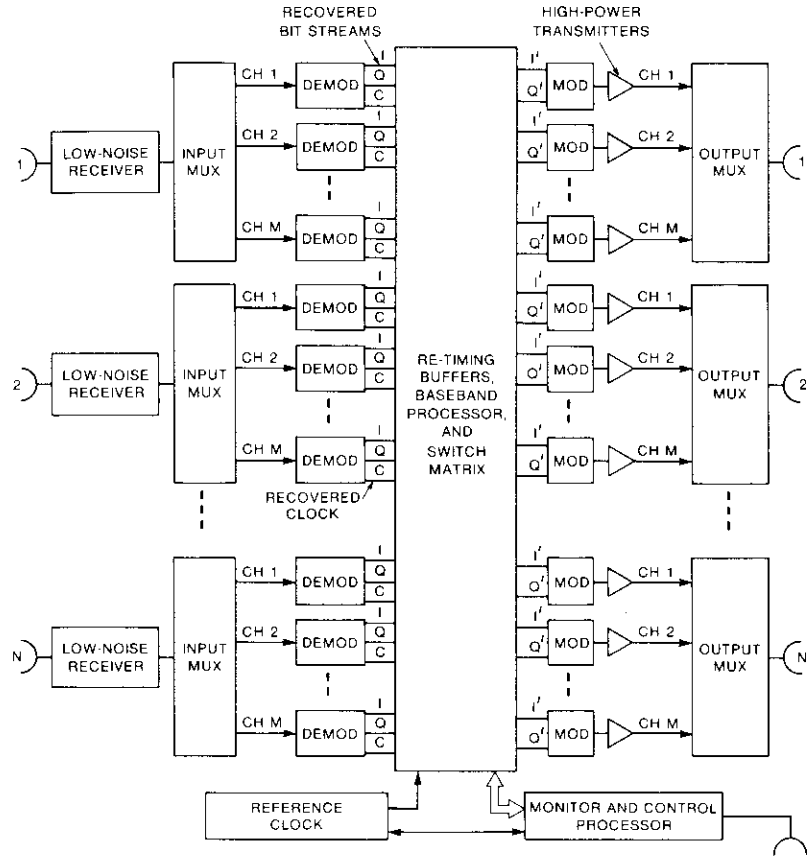

Figure 2. *Simplified Diagram of a Typical Multibeam, On-Board Processing Satellite for High-Bit-Rate TDMA Operation*

switch matrix. The output pairs of data from the switch matrix drive separate QPSK modulators. The modulated signals are then filtered, amplified, and transmitted to the respective earth stations.

The modem comprises a microwave receive filter (RXF), a QPSK demodulator, a QPSK modulator, and a microwave transmit filter (TXF). The receive filter, which could be used to demultiplex or separate the channels, is matched to the QPSK signals transmitted from the earth stations. The demodulator performs coherent detection on the incoming QPSK signal and outputs the baseband I, Q channels and symbol timing clock. The modulator produces a QPSK signal at the down-link frequency from the I, Q symbols,

while the transmit filter provides the appropriate spectral shaping for optimum BER performance and minimum adjacent channel interference (ACI).

As indicated in Table 1, the modem was designed to meet performance specifications which are compatible with the existing INTELSAT TDMA/digital speech interpolation (DSI) or satellite-switched (SS)-TDMA system specifications. The modem was developed as a proof-of-concept breadboard, with emphasis on performance and power consumption. The size, weight, reliability, and thermal stability requirements of flight hardware can also be met by specific circuit implementations, such as using GaAs monolithic microwave integrated circuits (MMICs).

TABLE 1. SPECIFICATION OF THE 120-MBIT/S QPSK ON-BOARD DEMODULATOR

Bit Rate	120-Mbit/s QPSK
Channel Spacing	80 MHz
Transmission Mode	TDMA
Frame Length	2 ms
Preamble (CW portion) (1010 . . . portion)	48 symbols 128 symbols
Receive Frequency	3.95 GHz, ±10 kHz
Receiver Dynamic Range	13 dB
RF Output (recovered carrier)	> -10 dBm
Baseband Outputs (I, Q, clock) BER (measured in a 64-symbol window after the UW) $<5 \times 10^{-3}$ $<1 \times 10^{-4}$ $<1 \times 10^{-6}$ $<1 \times 10^{-7}$ $<1 \times 10^{-8}$	ECL, rise-fall times < 2 ns at E_b/N_o = 6.5 dB 10 dB 12.9 dB 14 dB 14.5 dB
Probability of Missing UW	$<1 \times 10^{-8}$ at $E_b/N_o = 7$ dB
Probability of Carrier Cycle Slips	<1 per 10,000 at $E_b/N_o = 7$ dB
Bit-Timing Jitter	$< \pm 1$ ns
Clock Cycle Slips at $E_b/N_o = 7$ dB	<1 in 10^5
Weight	3 kg
Power	3 W
Size	5 × 5 × 5 in.
Temperature Range	10° to 40°C

Receive filter design and implementation

To satisfy interchannel spacings of 80 MHz, the earth station transmit signals must be band-limited to minimize ACI. Therefore, a square-root Nyquist filter with $x/\sin x$ compensation and 40-percent rolloff is used in earth stations ahead of the high-power amplifier (HPA). The HPA is operated nominally at 10-dB input backoff to limit spectral regrowth. In this manner, the up-link behaves approximately as a linear additive white Gaussian noise (AWGN) channel. Using the matched filter design approach [3], the on-board demodulator receive filter is required to match the up-link transmit channel, and hence have a 40-percent root Nyquist response. When filtering is performed at microwave frequencies, channel demultiplexing and matching can be accomplished simultaneously.

An eight-pole, dual-mode filter (Figure 3) with dielectrically loaded circular cavities was designed using the predistortion techniques developed by Williams *et al.* [4]. Its amplitude response approximates that of a 40-percent root Nyquist filter. By using the response characteristics of this filter in the channel simulation program [5], the BER performance curve shown in Figure 4 was obtained for the linear AWGN channel. Typical INTELSAT modulator filter response was used in the simulation [6]. From these data, it was concluded that the designed filter would perform satisfactorily as an on-board matched receive filter.

Coherent demodulator design and implementation

The demodulator is composed of circuits that are used to recover the carrier and the symbol timing clock, detect in-phase and quadrature symbols, and

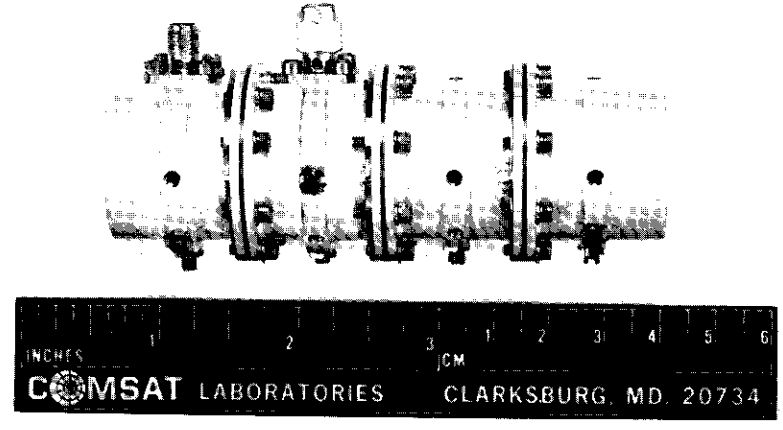

Figure 3. *8-Pole, Self-Equalized, Dielectrically Loaded Receive Filter*

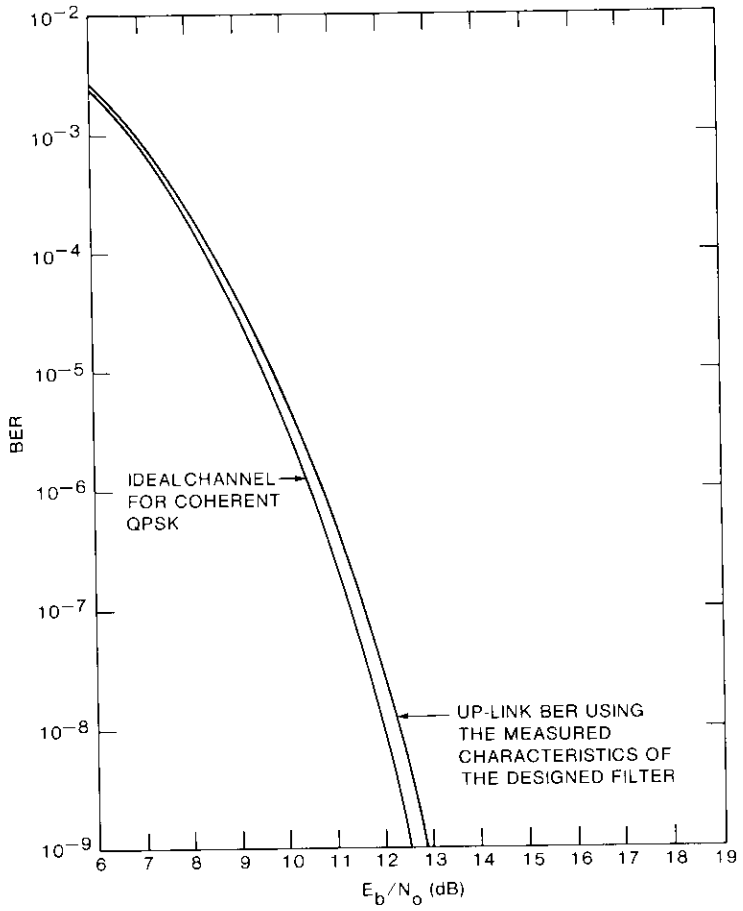

Figure 4. *Computed BER Characteristics of a CQPSK Channel Using the Receive Filter of Figure 3*

regenerate these symbols by employing mid-bit sampling. Various schemes [7], such as multiply/divide-by-4 (X4), reverse modulation loop (RML), and Costas loop, allow recovery of the carrier from a QPSK signal. In a TDMA system, carrier frequency and phase must be recovered during the preamble portion of every burst before the unique word (UW) arrives, and the carrier phase must be maintained over the entire burst duration. The former defines the phase acquisition time and the latter establishes cycle slipping requirements for the carrier. Issues related to the carrier recovery schemes for TDMA applications will be briefly reviewed.

Carrier recovery by the X4 method

In this method, the QPSK signal is applied to a nonlinear device, causing the fourth harmonic of the carrier frequency to appear at the output [8]. The carrier-to-noise ratio (C/N) at the output is degraded by approximately 12 dB from that of the input. Therefore, the variance of the phase jitter must be considerably reduced before the reconstructed carrier can be used for detection [7]. Although division by 4 will cause an improvement of 12 dB, the carrier phase noise must be reduced to a minimum prior to the division. The C/N of the recovered carrier can be improved either by employing a phase-locked loop (PLL) whose bandwidth will determine the phase jitter variance of the carrier, or by using a very narrowband filter (300 to 500 kHz) at the multiplier output. Both approaches have certain advantages and limitations.

To meet the UW-miss detection probability requirements of the TDMA system, the PLL must be designed with a much wider bandwidth so that occasional hangups can be overcome before the UW arrives [9]. Because division by 4 can be accomplished using the fourth harmonic of the voltage-controlled oscillator (VCO) at the phase detector port, this system does not necessarily require down-conversion. On the other hand, the passive bandpass filter approach requires down-conversion in order to implement submegahertz bandwidths, which are realizable in small size only at low frequencies. Furthermore, substantial gain is needed to drive the divider, since the fourth harmonic power level is generally quite low. This approach, which does not have acquisition problems, has been used (with several modifications) in earth station QPSK modems [10]. For spacecraft applications, the X4 method with down-conversion has been used along with narrowband filtering [11].

Carrier recovery by Costas loop

This approach, which incorporates a PLL whose phase error correction signal is derived from the detected bits by cross-multiplication of baseband signals [7], is best suited for continuous-mode, low-bit-rate digital modems. Although analog implementation is possible, it may require substantial hardware merely for carrier recovery [12]. From a hardware viewpoint, this scheme does not compete with either the X4 or RML methods.

Carrier recovery by RML

An RML [7],[13] operating at 4 GHz was used in the modem developed by COMSAT. Figure 5a is a block diagram of this design. Unlike the previous approaches, a quadrature phase detector (QPD), an RF QPSK modulator, and a PLL are required. The underlying principle is to detect the I and Q data streams and use this information to drive two QPSK modulators (whose other

inputs are the incoming modulated signals delayed in time) and to align this incoming RF portion with the generated bits. In this way, a continuous-wave (CW) carrier with pattern noise will appear at the output of the modulator. A VCO phase-locked to this carrier will maintain the desired coherence.

A comparison of Figures 5a and 5b reveals that the amount of hardware required for the RML is much less than for the X4 technique because there is no need for down-conversion and RF amplification. Furthermore, since the

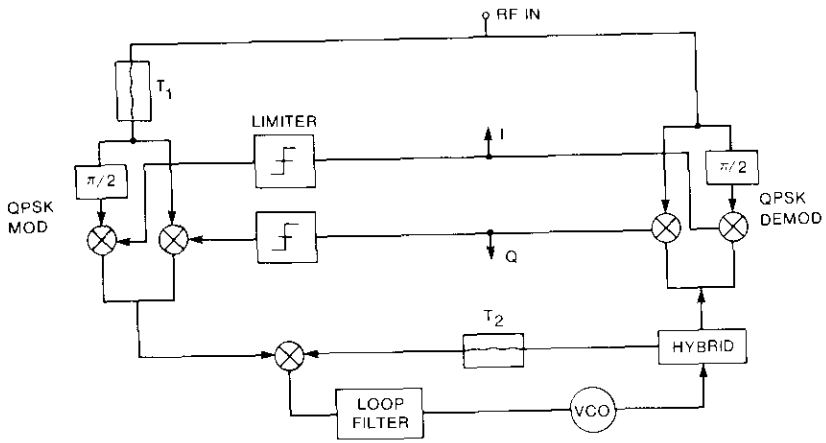

(a) Reverse Modulation Loop Carrier Recovery

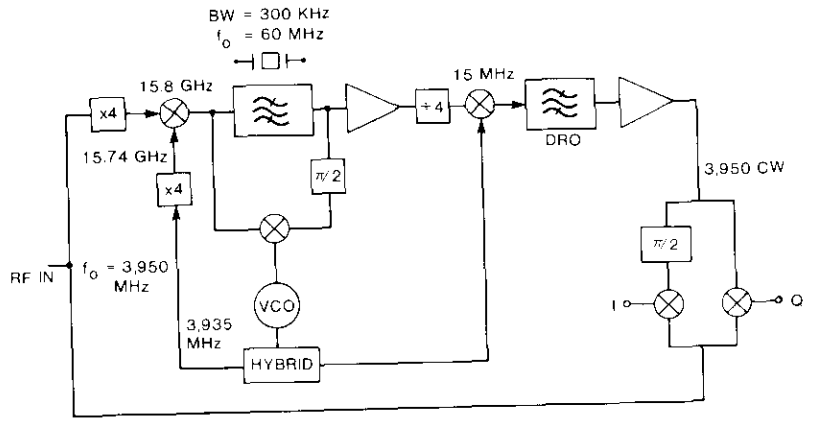

(b) Multiply-by-4, Divide-by-4 Carrier Recovery

Figure 5. *Candidate Approaches for Coherent QPSK Demodulation*

hardware consists exclusively of microwave, digital, and DC circuits, it has the potential of being realized as MMIC modules, with the consequent reduction of mass and power and a significant increase in reliability. This approach requires a very stable VCO (4×10^{-6}) and careful design of the PLL to compensate for hangup effects while meeting the cycle slipping requirements.

RML demodulator design parameters

The RML can be viewed as an ordinary PLL with a sophisticated phase detector. In Figure 6a, the RML phase detector is defined by identifying the local oscillator (LO) port, RF port, and output port. A PLL constructed as shown in Figure 6b will produce the RML. To simplify the explanation, parasitic delays due to hardware implementation (which must be balanced for satisfactory operation of the RML) have been ignored. These delays are discussed in the Appendix.

The characteristics of the RML phase detector must be deduced in order to understand the loop dynamics and the mechanism of recovering the carrier from the QPSK signal. Typically, phase detector characteristics are obtained by applying coherent CW signals to the LO and RF input ports of the detector and plotting the output voltage as a function of the phase difference between these signals. The RML phase detector characteristics are similarly determined from Figure 6a by finding $V_d = \sin(\theta + \phi)$ as a function of θ, where θ is the instantaneous phase modulation of the incoming signal, and ϕ is the detected phase at the output of the demodulator.

Variation in θ over a range of 0° to 360°, with limiters at the outputs of the QPD, generates the QPD truth table. Meanwhile, the QPSK modulator causes phase shift ϕ at the output (with reference to the inputs) according to the modulator truth table. Note that ϕ can only be 45°, 135°, −135°, or −45°. Beginning with the range $0° < \theta < 90°$, QPD outputs are $A = 1$ and $B = -1$. This combination yields a modulator phase shift $\phi = -45°$. Thus, the output signal, V_d, varies sinusoidally from $-1/\sqrt{2}$ to $1/\sqrt{2}$ V. In the next range, $90° < \theta < 180°$, QPD outputs are $A = -1$ and $B = -1$, yielding $\phi = -135°$. The voltage again varies from $-1/\sqrt{2}$ to $1/\sqrt{2}$ V, causing a discontinuity at $\theta = 90°$. The entire cycle can be completed, resulting in the characteristic shown in Figure 7.

In the event that the input is a QPSK signal and the loop has acquired, the angle θ will have values of 45°, 135°, −135°, or −45° in any symbol duration. It can be verified that for each value, the phase angle $(\theta + \phi)$ of the output signal from the modulator is 0°, which means that the modulator output is at the desired CW carrier. Thus, the remodulation process automatically strips off the modulation from the carrier. Furthermore, no additional

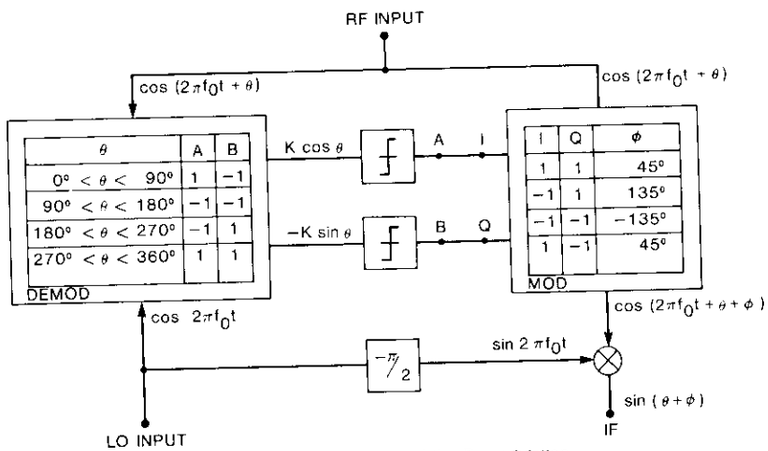

(a) Functional Diagram of the Remodulation Circuit That Yields the RML Phase Detector Characteristics of Figure 7

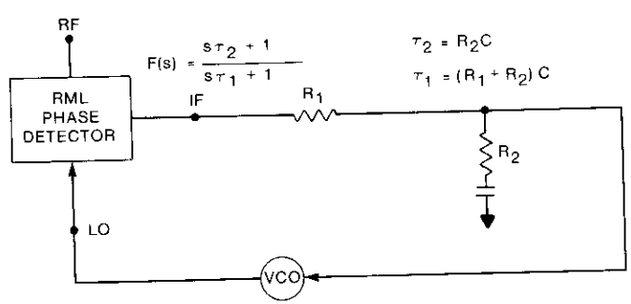

(b) Equivalent Circuit of the RML

Figure 6. *RML Demodulator—Equivalent to a PLL With a Sophisticated Phase Detector*

QPD is needed to generate the bits since they are already available in the remodulation process, in contrast to the X4 circuit where a QPD is not part of the carrier recovery circuit.

Because the characteristic of the RML phase detector has positive slopes with sharp discontinuities at 90° intervals, it is naturally resistant to hangups [9]. In the presence of noise at the phase detector input, the characteristic is smoothed out as shown by the dotted lines of Figure 7. The dotted curve

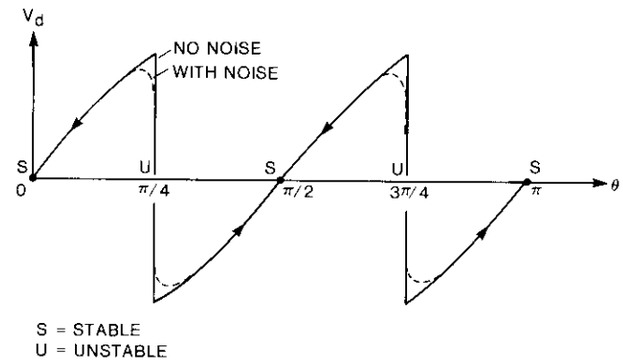

Figure 7. *Characteristics of the RML Phase Detector*

has both positive and negative slope regions. The effects of noise on the phase detector characteristic have been analyzed elsewhere [14]. Although regions with negative slopes lead to the possibility of hangup, the frequency of such events is greatly reduced compared to the case of a sinusoidal phase detector whose 0° to 360° interval contains 50-percent negative slopes.

Design of the PLL: phase acquisition and cycle slips

Three essential requirements must be satisfied by the PLL. First, the loop must acquire carrier phase before the arrival of the UW. Second, the loop should have a low frequency of slipped cycles, and third, the loop must be stable. Loop stability is related to the finite delay (<6 ns) that will exist between the input of the demodulator and the baseband outputs. The Appendix indicates that delays of such small magnitude do not pose stability problems.

It is evident from the characteristic shown in Figure 7 that the zero crossings with positive slopes ($\theta = 0°, 90°, 180°, 270°$) are the stable points of the PLL operation. For a given initial condition of phase and frequency, the loop will settle at any one of these points, thereby giving four-phase ambiguity. This ambiguity is resolved by UW comparison, as described by [15]. Moreover, the principal range ($-45° < 0 \leq 45°$) is such that the characteristic can be approximated by a sawtooth curve over 90 percent of this range, making it possible to utilize analytical results based on a linear approximation of PLL.

Open-loop gain

The BER performance of the demodulator depends on the static phase error (θ_s), which therefore must be minimized. For QPSK, this error cannot be

more than $\pm 1°$, since a $\pm 2°$ phase imbalance has already been allowed for the modulated received signal. Using a ± 10 kHz uncertainty in the received carrier and ± 20 kHz in the VCO, the net frequency offset (Δf) can be ± 30 kHz. The DC loop gain (velocity constant) K_v can be obtained by

$$K_v \triangleq \frac{2\pi\Delta f}{\theta_s} = 10.8 \text{ rad MHz} \quad . \tag{1}$$

Since a second-order PLL with lag-lead filter (shown in Figure 6b) is used, $F(0) = 1$. The open-loop gain, K, obtained from the above by $K_v = KF(0)$ is also 10.8 rad MHz/rad. Although this value does not take into account the slight gain suppression that occurs near the $\pm 45°$ edge of the phase detector characteristics, the value will be maintained for design purposes.

Noise bandwidth

The second critical parameter is the noise bandwidth of the loop, B_L. The BER degradation, cycle slipping, and acquisition time are all related to the noise bandwidth. An increase in B_L causes an increase in the occurrence of cycle slips and BER degradation, but reduces the acquisition time for a given E_b/N_o at the input. Therefore, it is necessary to select B_L such that all specifications in Table 1 are met.

Essentially, three parameters must be satisfied by the choice of the variable B_L. The initial estimate of B_L is obtained by choosing a value such that the acquisition time is much less than the duration of the total preamble. (A safety factor of 4 was chosen to accommodate the effects of hangup.) Based on the preamble format, the design value of the acquisition time [defined as the time in which the phase error will fall below 0.5° (absolute) from the instant when a frequency step is applied to the input] is 733 ns. The details of the computations and choice of damping constant (presented in the Appendix) yield the design values for the loop indicated in Table 2.

TABLE 2. DESIGN PARAMETERS OF THE PLL

Loop Bandwidth, B_L	1.50 MHz
Open-Loop Gain, K	10.8 rad MHz/rad
Natural Frequency, ω_n	24 rad kHz
Damping Constant	125
Loop Signal-to-Noise Ratio*	25 dB
rms Phase Jitter	0.063 rad
R_1	1.8 kΩ
R_2	2.2 kΩ
C	4.7 μF

* Includes the effect of pattern noise, which degrades the C/N_o at the modulator output by at most 1 dB.

The choice of 1.5 MHz for the loop bandwidth produced a negligible amount of BER degradation caused by phase noise. Because of the nature of the phase detector characteristic in the presence of noise, the cycle slipping statistics are difficult to analyze. According to the estimates given in Reference 6, the frequency of occurrence of cycle slipping should be within the specifications by a substantial margin. However, measurements indicated that this margin was only 0.3 dB at best.

Implementation of RML

The RML was implemented by using microstrip circuit design on alumina substrate. Figure 8 depicts the breadboard layout. The demodulator/remodulator unit is shown in Figure 9, and the clock recovery and sampling units are illustrated in Figure 10. The delay lines were fabricated of UT-85 semi-rigid cables, with lengths determined by actual delay measurement between the points needing compensation.

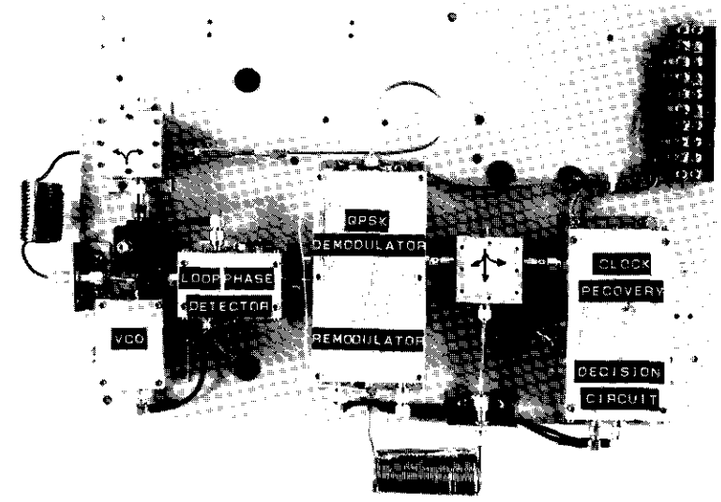

Figure 8. *Breadboard Layout of the CQPSK RML Demodulator*

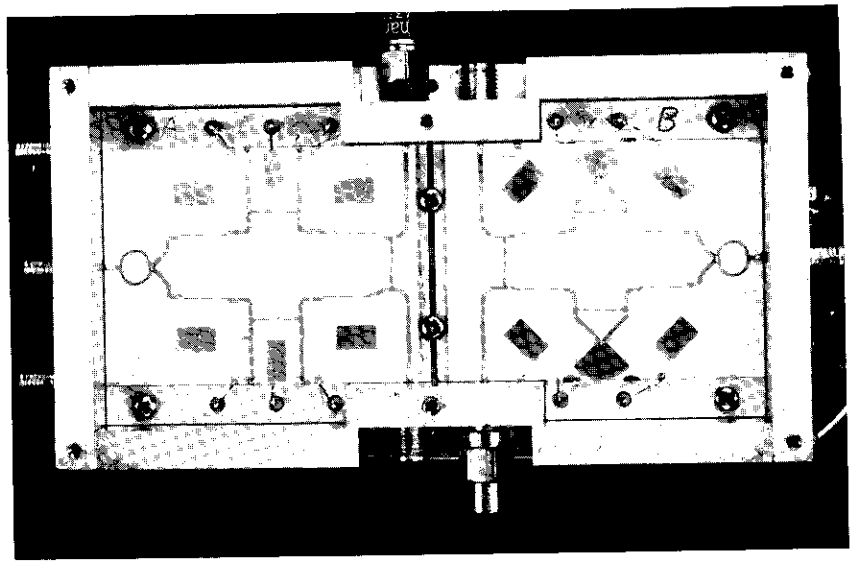

(a) Top View (RF Circuit)

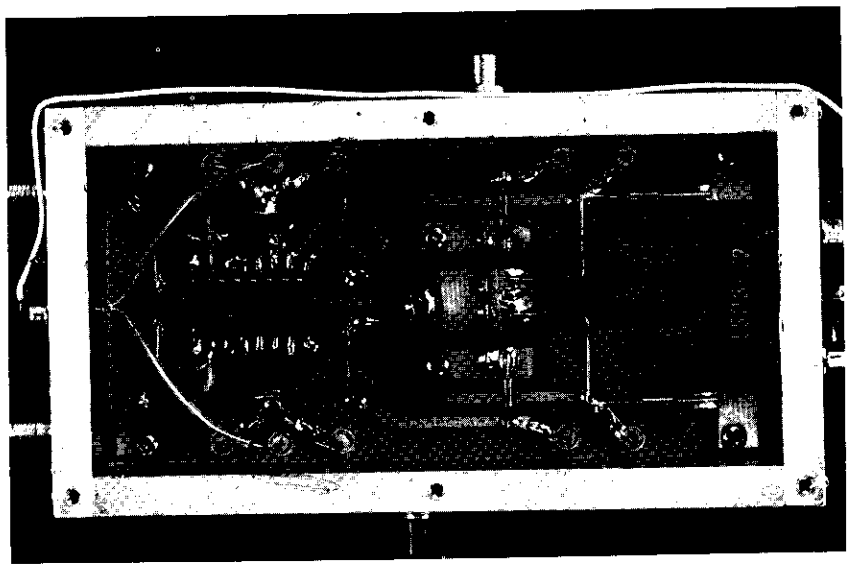

(b) Bottom View (Baseband Circuit)

Figure 9. *Demodulator/Remodulator Circuit*

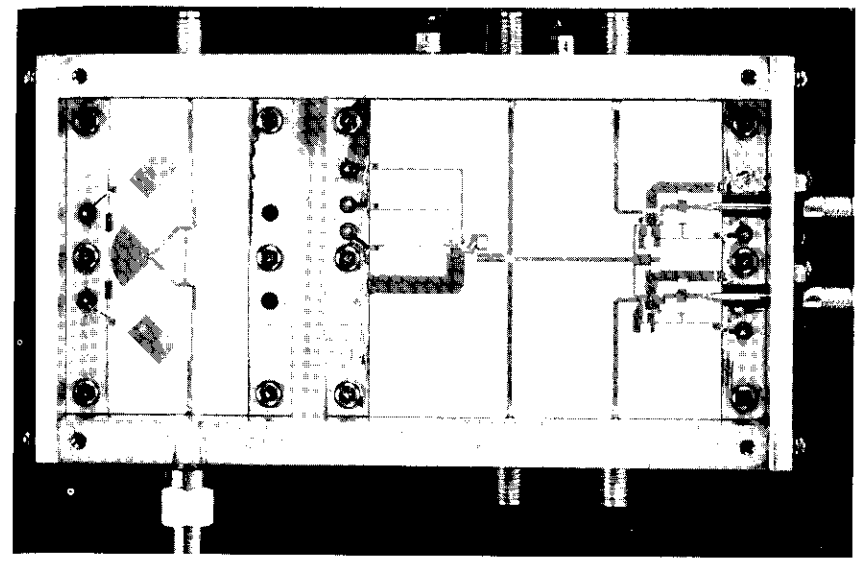

(a) Top View

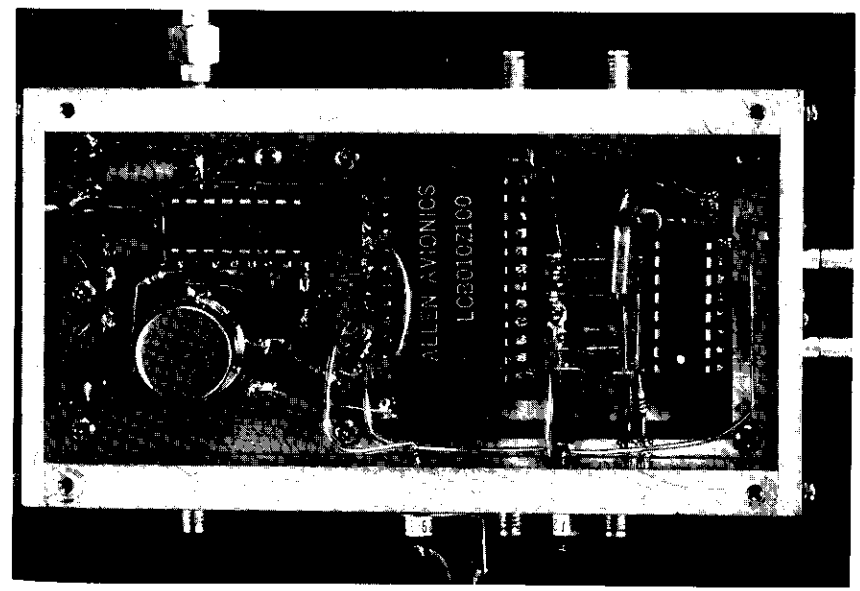

(b) Bottom View

Figure 10. *Clock Recovery and Retiming Circuit*

Initial tuning was accomplished by first driving the demodulator unit by hard-wired carrier and minimizing the BERs on both the I and Q channels. The spectrum of the modulator output (Figure 11) was observed, and the C/N_o was measured and compared to the C/N_o at the input of the demodulator. For optimum delay compensation, the C/N_o at the output of the modulator should be degraded by no more than 1 dB for an input E_b/N_o of 7 dB and a $(2^{23} - 1)$ random bit pattern.

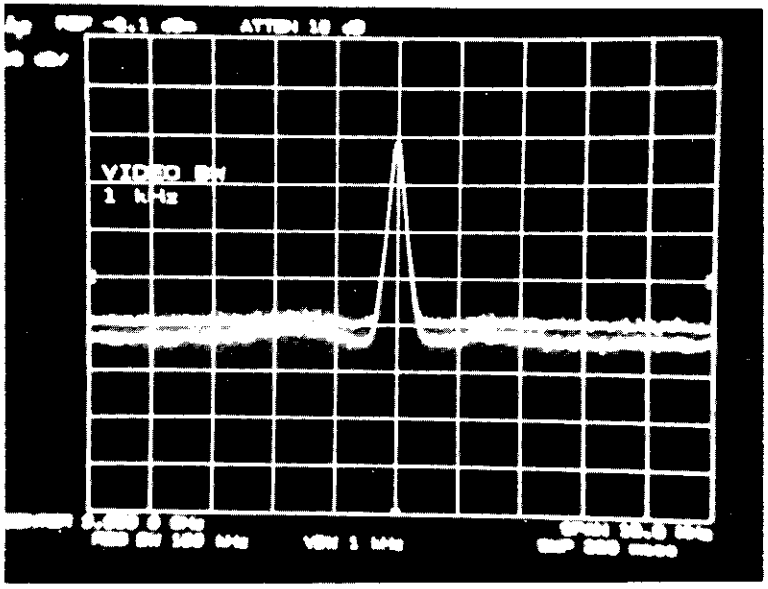

Figure 11. *Spectra of the RML Modulator Output With and Without AWGN* (E_b/N_o = *7 dB*)

Next, the PLL was implemented using a dielectrically stabilized VCO with a stability of ± 300 kHz over a 10° to 40°C temperature range. The phase detector and VCO driver amplifier were designed to give approximately $K = 12$ rad MHz/rad for an RF signal (modulator output) level between -18 and -20 dBm. The value of K is 12 instead of 10.8 to account for gain suppression in the feedback path and detector output.

The clock recovery and retiming circuit was implemented using a 60-MHz, 800-kHz bandwidth bandpass filter after an envelope detector. The output of the filter is amplified and applied to a gate oscillator operating in an injection lock mode. The output of the oscillator is then limited and used to retime the waveforms at the output of the demodulator. Figure 12 is a circuit diagram of the clock recovery unit. The circuit can successfully retime up to 30 symbols of constant phase without degradation at an E_b/N_o of 10 dB. The unit shown in Figure 8 consumes less than 3.3 W of DC power and requires 5, -5.2, and 12-V supplies.

Transmitter design and implementation

The transmitter consists of the modulator and the pulse-shaping filter. The QPSK modulator has been described elsewhere [16] and is based on a dual-BPSK, parallel implementation design. It is ECL-compatible, with an amplitude imbalance $< \pm 0.2$ dB and a phase imbalance of $< \pm 2°$.

The pulse-shaping filter that follows the modulator was principally designed for hardware simulation of a typical up-link communications channel. It was designed using the predistortion approach [4], and in this case a six-pole filter and a four-pole equalizer were selected to meet the amplitude and group delay response requirements. A single eight-pole filter was also considered; however, its group delay response and out-of-band rejection were marginal. Figure 13 shows the measured amplitude and group delay response of this filter.

Whether or not such a filter can be used on board a satellite, ahead of the TWTA, is a matter of hardware and performance tradeoff. Since the down-link is nonlinear because the TWTA operates at saturation, pulse-shaping on the transmit side does not substantially improve the performance, as demonstrated by the simulation results of Table 3.

Simulation was performed for two cases: one with INTELSAT transmit filter response (which uses $x/\sin x$ pulse shaping), and the other with a simple five-pole wideband filter. Input backoffs were adjusted to deliver the same modulated output power from the TWTA. The transponder output multiplexer filter had a 74-MHz equiripple bandwidth, and ACI effects were included in the simulation. Comparing the two columns of Table 3 reveals that pulse shaping produces a 0.4-dB improvement at BER 1×10^{-8}. From a hardware viewpoint, a viable tradeoff may lead to using a wideband filter ahead of the TWTA, instead of a more complex and group delay equalized pulse-shaping filter.

Modem performance

Figure 14 shows the measurement setup used for initial tuning and determination of BER performance and cycle slipping probability. The data generator outputs I and Q data streams that modulate a 3.95-GHz carrier.

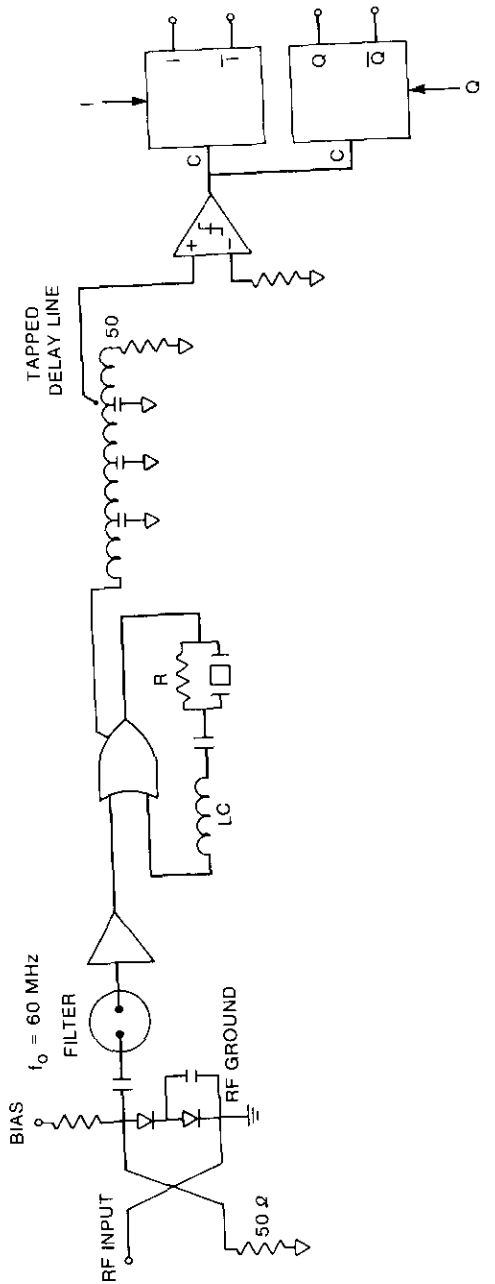

Figure 12. *Circuit Schematic of the Carrier Recovery and Retiming Unit*

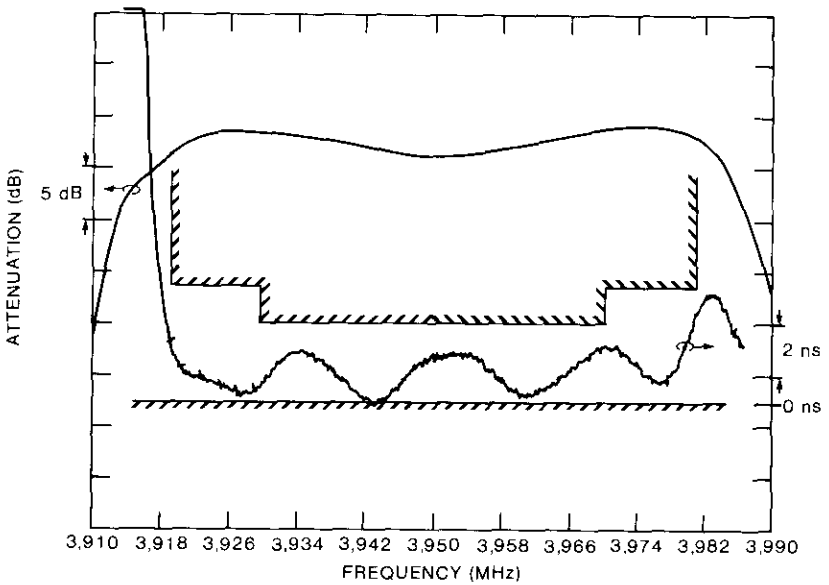

Figure 13. *Frequency Response of the Microwave Transmit Filter That Approximates* x/*sin* x *Times 40% Root Nyquist Compensation*

TABLE 3. BER PERFORMANCE OF A NONLINEAR CHANNEL

BER	DEGRADATION FROM IDEAL (dB)	
	WITH PULSE SHAPING	WITHOUT PULSE SHAPING
10^{-3}	0.4	0.5
10^{-5}	0.6	0.9
10^{-8}	0.9	1.3

The modulator output is pulse-shaped and band-limited by the transmit filter. Noise added to the signal is applied to the demodulator after linear amplification. Carrier power at the input of the demodulator is in the range of -2 to 0 dBm. The E_b/N_o is adjusted by measuring the power of the modulated signal and noise separately through a precalibrated filter of noise bandwidth 83 MHz. The BERs of the demodulated $\hat{I}$ and $\hat{Q}$ channels are

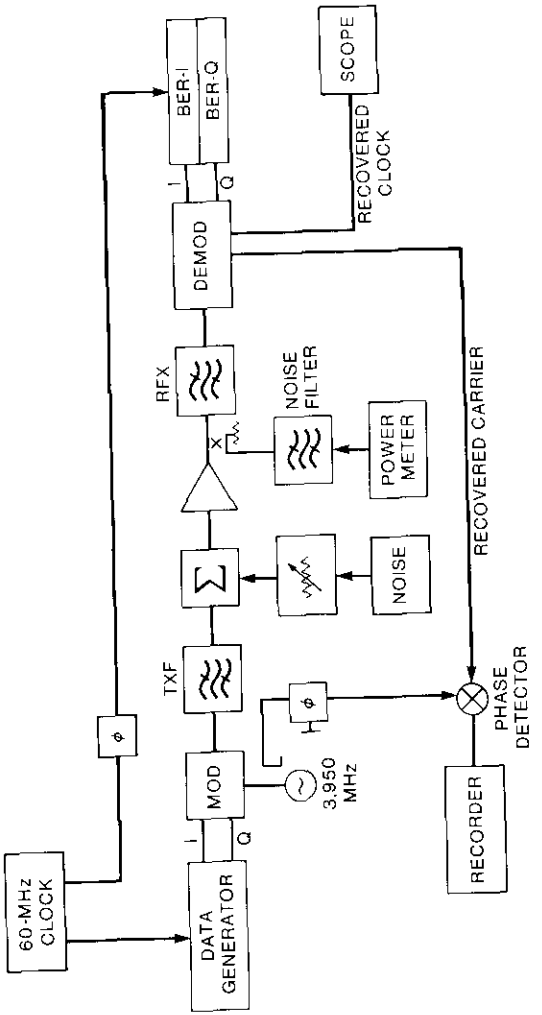

Figure 14. *Test Setup for Cycle-Slip and Continuous-Mode BER Measurements*

measured, with the average value giving the overall system BER. The recovered carrier, which is also available, is applied to a phase detector driven by the signal source. The output of the phase detector has four levels, which are recorded on a chart. Transition from one phase state to another is the cycle slip event.

Figure 15 compares the measured BER performance of the communications channel using the demodulator and the receive filter, with simulations using the TX and RX filter data and theoretically ideal QPSK. The simulated curve is for performance obtained by using the measured characteristics of the transmit and receive filters in a linear single channel model in CHAMP [5]. From these curves, it can be deduced that the channel response causes about 0.5 dB of degradation, with an additional 0.4 dB of degradation caused by the hardware of the demodulator, giving a total degradation of 0.9 dB from the ideal at a BER of 1×10^{-4}. At a BER of 1×10^{-7}, the total degradation from ideal is 1.5 dB.

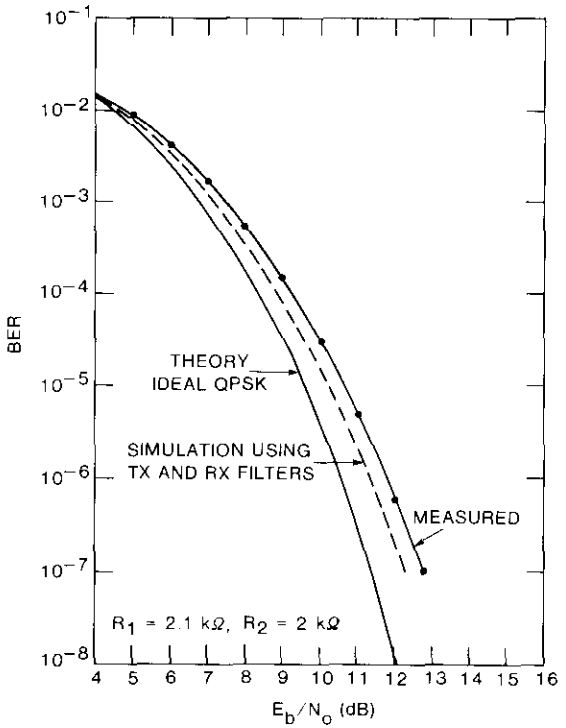

Figure 15. *Measured BER Performance of the RML Demodulator*

Next, the loop bandwidth of the filter was adjusted by varying R_1 and R_2 and observing the cycle slips. The widest loop bandwidth that would give a reasonable margin on the cycle slip was obtained at $R_1 = 2.1$ kΩ and $R_2 = 2$ kΩ. These values were held constant in all successive measurements. The VCO signal output for these values is shown in Figure 16.

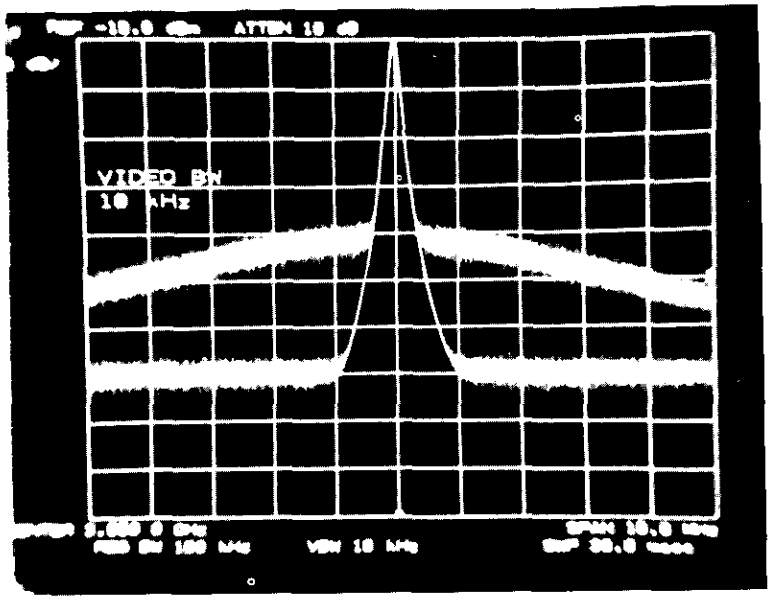

Figure 16. *Spectra of the VCO Output After Acquisition With and Without AWGN* ($E_b/N_o = 7$ *dB*)

Cycle slipping performance was plotted on a recorder over a long period of measurement time. Measurements were made up to an E_b/N_o of 7 dB, as shown in Figure 17. The statistics at $E_b/N_o = 6.5$ dB were obtained over a total measurement time of 4.2 hours, while the point at 7 dB was obtained over a total time of 20 hours.

Figure 18 depicts the measurement setup used to determine the probability of missing a UW. In this setup, the RF burst was obtained by switching between two carriers from separate sources. A specially designed burst generator was used to transmit and receive the baseband for the INTELSAT preamble and UW, to perform UW correlation, and to count the missed events by estimating the output of the correlator. The generator also outputs a start-of-burst pulse that can be used to switch the carriers.

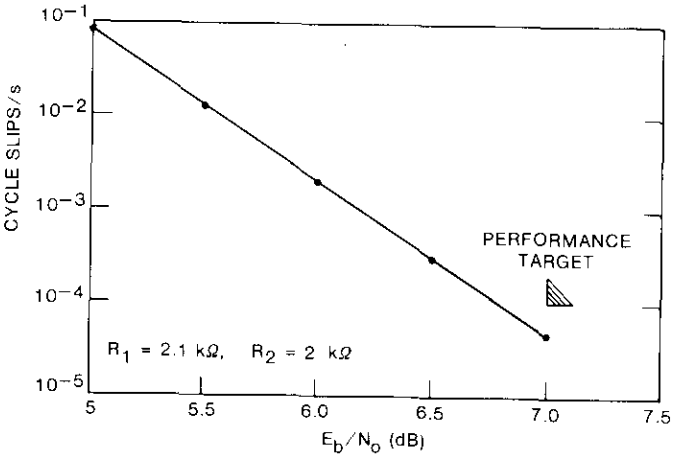

Figure 17. *Cycle Slipping Rate of the RML Demodulator Measured in a Continuous Mode*

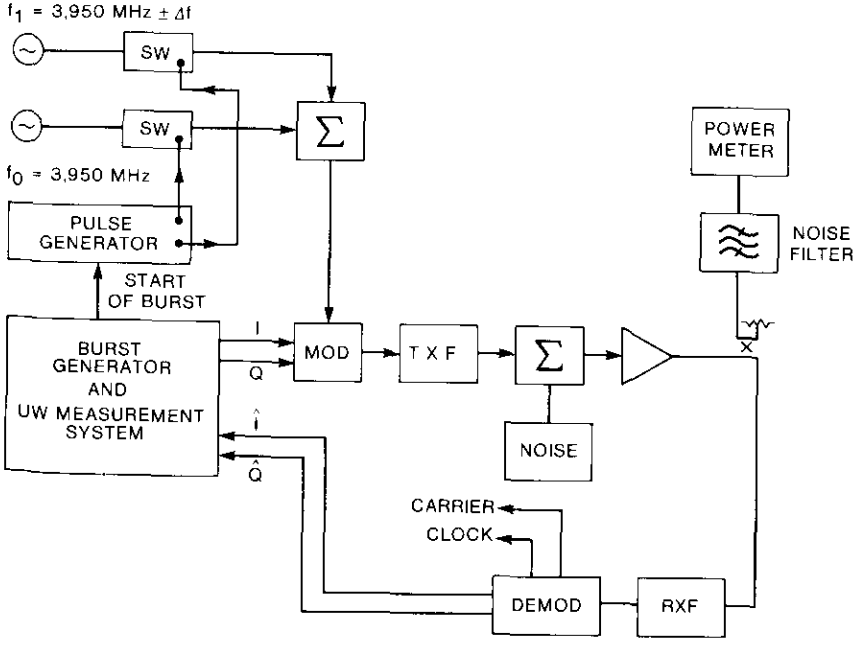

Figure 18. *Test Setup for UW-Miss Detection Measurements*

Carrier power was set constant and equal for both sources, and measurements were performed at various E_b/N_o values. The results, shown in Figure 19, reveal nearly a 0.5-dB margin in the UW-miss probability above the INTELSAT specification.

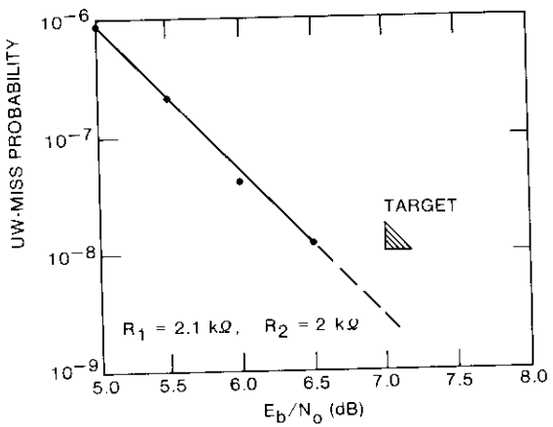

Figure 19. *Measured UW-Miss Detection Probability of the RML Demodulator*

Conclusions

A 120-Mbit/s QPSK modem for on-board satellite applications has been described, and the design criteria, circuit layout, and measured performance of the demodulator (the most critical part of the modem) have been presented. Other parts of the modem, such as the receive filter, transmit filter, and modulator, were briefly described.

By using an RML carrier recovery circuit and conventional PLL design, a simple hardware configuration was developed which meets the TDMA acquisition specifications and cycle-slip requirements. The agreement between the initial design values of R_1 and R_2 (1.8 and 2.2 kΩ, respectively) and the experimentally adjusted values of 2.1 and 2 kΩ, respectively, confirmed that the choice of noise bandwidth and damping constant could be determined by using conventional PLL design techniques based on linear models. The demodulator's low power consumption (3.3 W), coupled with the fact that most of the components can be developed using microstrip circuits which have the potential of being realized in GaAs MMIC technology, render the design feasible for spacecraft applications.

Acknowledgments

The authors wish to thank R. Bonetti for development of the microwave filters. They also wish to thank C. Mahle and P. Bargellini for their comments and critical evaluation. The hardware development skill of J. Bruno and the assistance of C. Wolejsza and G. House in the UW measurements are gratefully acknowledged.

References

[1] S. J. Campanella, F. Assal, and A. L. Berman, "On-Board Regenerative Repeater," IEEE International Conference on Communications, Chicago, Illinois, June 1977, *Conference Record*, Vol. 2, pp. 6.2-121–6.2-125.

[2] P. P. Nuspl, R. Peters, and T. Abdel-Nabi, "On-Board Processing for Communications Satellite Systems," 7th International Conference on Digital Satellite Communications, Munich, FRG, May 1986, *Proc.*, pp. 137–148.

[3] W. R. Bennett, *Introduction to Signal Transmission*, New York: McGraw Hill, 1970.

[4] A. E. Williams *et al.*, "Microwave Receive Filter for a Regenerative Repeater," 15th European Microwave Conference, Paris, France, September 1985, *Proc.*, pp. 349–354.

[5] A. Hamid, Private communication, 1982.

[6] INTELSAT, "TDMA/DSI System Specification: TDMA/DSI Traffic Terminals," Specification BG-42-65E (Rev. 1), December 17, 1981.

[7] J. J. Spilker, *Digital Communications by Satellites*, Englewood Cliffs, New Jersey: Prentice-Hall, 1977.

[8] C. J. Wolejsza and D. Chakraborty, "TDMA Modem Design Criteria," *COMSAT Technical Review*, Vol. 9, No. 2A, Fall 1979, pp. 413–464.

[9] F. M. Gardener, "Carrier and Clock Synchronization for TDMA Digital Communications," European Space Agency Document, ESA TM-19 (ESTEC), December 1976.

[10] C. J. Wolejsza, J. S. Snyder, and J. M. Kappes, "120-Mbit/s TDMA Modem and FEC Codec Performance," *COMSAT Technical Review*, Vol. 15, No. 2B, Fall 1985, pp. 423–465.

[11] K. Betaharon *et al.*, "On-Board Processing for Communication Satellite Systems," 7th International Conference on Digital Satellite Communications, Munich, FRG, May 1986, *Proc.*, pp. 421–426.

[12] G. Alletto *et al.*, Private communication, 1983.

[13] H. Yamamoto, K. Hirade, and Y. Watanabe, "Carrier Synchronization for Coherent Detection of High-Speed Four-Phase-Shift-Keyed Signals," *IEEE Transactions on Communications*, Vol. COM-20, No. 4, August 1972, pp. 803–807.

[14] A. Blanchard, *Phase-Locked Loops, Application to Coherent Receiver Design*, New York: John Wiley and Sons, 1976.

[15] S. J. Campanella and D. Schaefer, "Time-Division Multiple-Access Systems," *Digital Communications*, Chapter 8, K. Echer, ed., Englewood Cliffs, New Jersey: Prentice-Hall, 1983.

[16] K. Karimullah and R. G. Egri, "A 4-GHz QPSK Modulator for High Bit Rates," *COMSAT Technical Review*, Vol. 15, No. 2A, Fall 1985, pp. 197–210.

Appendix. Analysis for RML loop dynamics

Compensation for parasitic delays

Since real-life devices have a non-zero propagation delay through them, the proper timing of the RML is crucial for successful design. Parasitic and compensating delays for the RML (see Figure A-1) were designated as follows:

Parasitic Delays
- Demodulator-Limiter T_2
- Reverse Modulator T_3
- Phase Detector and Amplifier/Loop Filter T_4

Compensation Delays
- Transmission Line to the Reverse Modulator T_1
- Transmission Line From the VCO to the Phase Detector T_5

The signal at the input of the phase detector is

$$c(t) = \cos[\alpha(t - T_1 - T_3) + \theta(t - T_1 - T_3) + \phi(t - T_2 - T_3)] \quad \text{(A-1)}$$

where $\alpha(t) = 2\pi f_0 t$ and the input to the VCO is

$$p(t) = \sin[\alpha(t - T_1 - T_3 - T_4) + \theta(t - T_1 - T_3 - T_4) + \phi(t - T_2 - T_3 - T_4) - \psi(t - T_4 - T_5)] \quad . \quad \text{(A-2)}$$

The conditions for correct synchronization are

$$T_1 + T_3 + T_4 = T_2 + T_3 + T_4 = T_4 + T_5 \quad . \quad \text{(A-3)}$$

or

$$T_1 = T_2 \quad \text{(A-4a)}$$

$$T_5 = T_2 + T_3 \quad . \quad \text{(A-4b)}$$

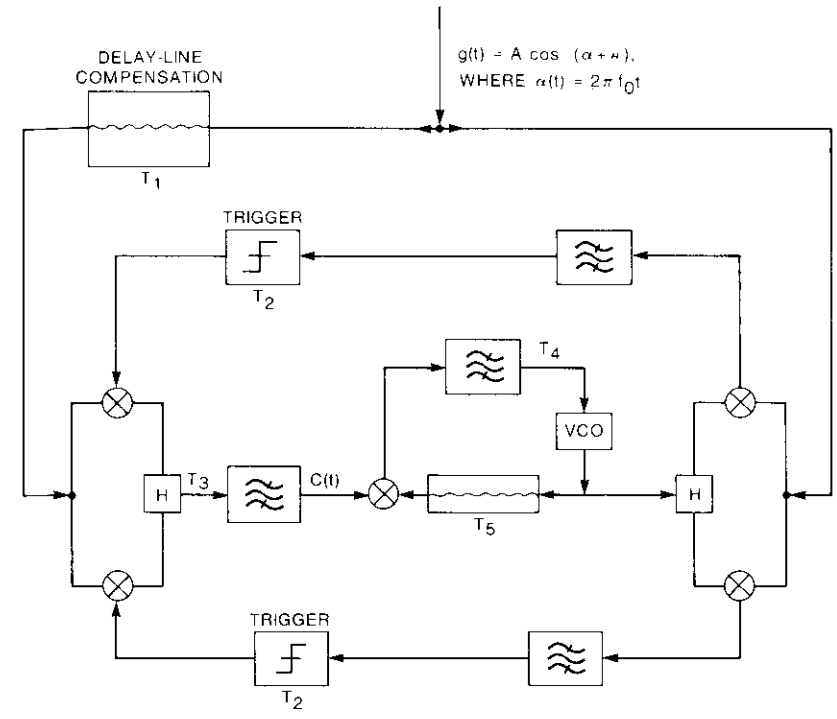

Figure A-1. *Practical Implementation of the RML Demodulator Highlighting the Delays of the Various Paths*

The delay T_4 through the phase detector/amplifier/loop filter/VCO does not affect the synchronization, but does affect through-the-loop stability. The proposed RML operates at microwave frequencies. Since microwave mixers and amplifiers are wideband circuits, their parasitic delay is much smaller than that of baseband circuits such as limiters and modulator drivers. With $T_3 << T_2$, the conditions for proper synchronization are

$$T_1 = T_2 = T_5 \quad . \quad \text{(A-5)}$$

This means that two transmission lines are needed, one at the input of the reverse modulator and the other at the input of the phase detector, to compensate for the parasitic delay (T_2) of the baseband circuits.

Estimation of acquisition time

Although the sawtooth phase detector characteristic is nonlinear, an analytical solution to the problem can be found since each continuous branch is linear. First, it is assumed that the loop does not slip cycle during acquisition. The design is based on a second-order loop with a passive lag-lead filter (shown in Figure 4b), with transfer function

$$F(s) = \frac{s\tau_2 + 1}{s\tau_1 + 1} \tag{A-6}$$

where $\tau_2 = R_2C$

$\tau_1 = (R_1 + R_2)C$.

If K denotes the open-loop gain, then the closed-loop transfer function is

$$H(s) = \frac{KF(s)}{s + KF(s)} = \frac{s(2\xi\omega_n - \omega_n^2/K) + \omega_n^2}{s^2 + 2s\xi\omega_n + \omega_n^2} \tag{A-7}$$

where $\omega_n^2 = K/\tau_1$

$2\xi\omega_n = (1 + K\tau_2)/\tau_1$.

The phase error, $E(s)$, and the phase of the incoming signal, $\Phi(s)$, are related as

$$E(s) = [1 - H(s)]\,\Phi(s) = \frac{s}{s + KF(s)}\,\Phi(s) \quad . \tag{A-8}$$

The time required for frequency and/or phase acquisition is of paramount importance. Assuming an arbitrary frequency jump (Ω) and phase jump (ϕ_o) in the incoming signal, these jumps correspond to the variation of the signal from burst to burst, or to the initial acquisition of the signal after turning on the modem. Thus,

$$\phi = \phi(t) = \Omega t + \phi_o$$

or

$$\Phi(s) = \frac{\Omega}{s^2} + \frac{\phi_o}{s} \quad . \tag{A-9}$$

From equations (A-6) and (A-8),

$$E(s) = \frac{s}{s + KF(s)}\left(\frac{\Omega}{s^2} + \frac{\phi_o}{s}\right)$$

$$= \frac{(s + \omega_n^2/K)\Omega}{s(s^2 + 2s\xi\omega_n + \omega_n^2)} + \frac{(s + \omega_n^2/K)\phi_o}{s^2 + 2s\xi\omega_n + \omega_n^2} \quad . \tag{A-10}$$

To find the inverse Laplace transform of $E(s)$, the right-hand side of equation (A-10) is expanded into partial fractions. Collecting the similar terms yields

$$E(t) = \frac{\Omega}{K}\left\{1 + \frac{1}{2\omega_n\sqrt{\xi^2 - 1}}\left[(K - p_1)\exp(-p_2t)\right.\right.$$

$$\left.\left. - (K - p_2)\exp(-p_1t)\right]\right\}$$

$$+ \frac{\phi_o}{2\omega_n\sqrt{\xi^2 - 1}}\left[\left(\frac{\omega_n^2}{K} - p_2\right)\exp(-p_2t)\right.$$

$$\left. - \left(\frac{\omega_n^2}{K} - p_1\right)\exp(-p_1t)\right] \tag{A-11}$$

where p_1 and p_2 are the roots of $s^2 + 2s\xi\omega_n + \omega_n^2 = 0$, and

$$p_{1,2} = \omega_n(\xi \pm \sqrt{\xi^2 - 1}) \quad . \tag{A-12}$$

This solution is valid whether $\xi > 1$ or $\xi < 1$. When $\xi > 1$, p_1 and p_2 are real numbers; when $\xi < 1$, they are complex. To aid in both the phase and frequency acquisitions of the loop, oscillations that might lead to cycle slippage should be avoided; hence, the loop should be such that $\xi > 1$.

If $\xi >> 1$, equation (A-11) can be simplified by using the approximations

$$\xi + \sqrt{\xi^2 - 1} \approx 2\xi$$

and

$$\xi - \sqrt{\xi^2 - 1} \approx \tfrac{1}{2}\xi \tag{A-13}$$

hence

$$E(t) \approx \frac{\Omega}{K} + \left(\frac{\Omega}{\omega_n} - \frac{\phi_o}{2\xi}\right)\left(\frac{1}{2\xi} - \frac{\omega_n}{K}\right)\exp\left(-\frac{\omega_n t}{2\xi}\right) + \left(\phi_o - \frac{\Omega}{2\xi\omega_n}\right)\left(1 - \frac{\omega_n}{2\xi K}\right)\exp\left(-2\xi\,\omega_n t\right) \quad . \qquad \text{(A-14)}$$

In equation (A-14), the first term represents the steady-state phase tracking error. Thus for a given Ω, the loop gain K should be large enough to maintain the steady-state phase error within tolerable limits. The time constants in (A-14) [*i.e.*, $(2\xi/\omega_n)$ and $(1/2\xi\omega_n)$] should be selected so that both the short-term (burst-to-burst) and long-term initial frequency offset (temperature-dependent) have a minimal effect on the phase acquisition.

Loop stability

It remains to show that the loop is stable with these parameters, even if the effective loop delay is not zero. The Bode-Nyquist criterion states that if the denominator of the transfer function is written as $1 + G(s)$, then the loop is stable as long as $|G(jw)| < 1$ whenever arc $G(jw) < -\pi$. In the present case

$$G(s) = K\frac{F(s)}{s}\exp\left(-sT_L\right) = K\frac{s\tau_2 + 1}{s(s\tau_1 + 1)}\exp\left(-sT_L\right) \quad . \qquad \text{(A-15)}$$

Now

$$|G(jw)| = K\left\{\frac{(w\tau_2)^2 + 1}{w^2[(w\tau_1)^2 + 1]}\right\}^{1/2} \qquad \text{(A-16)}$$

and since

$$K >> \frac{1}{\tau_1} \quad , \frac{1}{\tau_2}$$

the frequency point w_x where $|G(jw_x)| = 1$ must be on the order of K, as

$$1 = |G(jw_x)| \approx \frac{K}{w_x}\frac{\tau_2}{\tau_1} \quad . \qquad \text{(A-17)}$$

Thus,

$$w_x \approx K\frac{\tau_2}{\tau_1} \quad . \qquad \text{(A-18)}$$

The phase of $G(jw_x)$ can now be calculated as follows:

$$\text{arc } G(jw_x) = \text{arc tan}\,(w_x\tau_2) - \text{arc tan}\,(w_x\tau_1) - \frac{\pi}{2} - w_x T_L \quad . \qquad \text{(A-19)}$$

From equation (A-18) it is obvious that $w_x >> 1/\tau_1,\ 1/\tau_2$; therefore, both arc tangents are approximately $\pi/2$ and the phase angle of G becomes

$$\text{arc } G(jw_x) \approx -\frac{\pi}{2} - w_x T_L \approx -\frac{\pi}{2} - KT_L\frac{\tau_2}{\tau_1} \quad . \qquad \text{(A-20)}$$

Equation (A-20) gives the maximum loop delay for a given set of K, τ_1, τ_2 as

$$-K\frac{\tau_2}{\tau_1}\max\,(T_L) - \frac{\pi}{2} = -\pi$$

or

$$\max\,(T_L) \approx \frac{\pi}{2}\,\frac{\tau_1}{K\tau_2} \quad . \qquad \text{(A-21)}$$

Equation (A-21) shows that the larger the open-loop gain, K, the smaller the loop delay must be for the loop to remain stable. With $K = 10.8$ rad MHz/rad and $(\tau_1/\tau_2) \simeq 2$,

$$\max T_L = 290 \text{ ns} \quad .$$

This number is so much larger than the number being used in the design described here (*i.e.*, T_L is on the order of a few nanoseconds) that the loop is definitely stable.

Robert G. Egri received a Dipl. Eng. degree from the Budapest Technical University in 1974, and a Ph.D. from the Johns Hopkins University in 1978. From 1978 to 1986, he was a Member of the Technical Staff in the Transponders Department at COMSAT Laboratories. Since 1986, he has been a Principal Engineer with the Equipment Development Laboratories at Raytheon Company, where he is involved with the analysis and design of communications satellite systems.

Khalid Karimullah received a B.E. from Karachi Engineering University, Pakistan, in 1973, and an M.S. and Ph.D. from Michigan State University in 1976 and 1979, respectively. From 1979 to 1980, he was an Assistant Professor in the Department of Electrical Engineering at Michigan State University. He joined COMSAT Laboratories in 1980 and was a Senior Member of the Technical Staff in the Satellite Transponders Group in the Microwave Technology Division, where he was involved in the design of a differential QPSK demodulator and a coherent QPSK modem at microwave frequencies. His activities have also included the design of clock synchronization circuits, pulse-shaping channel filters, and communications channel optimization studies. In 1987 he joined M/A-COM Government Systems, where he is involved with the design of RF/IF subsystems for frequency-hopped radios.

Francois T. Assal received B.E.E. and M.E.E. degrees from the City University of New York. He is currently Associate Director of the Microwave Technology Division at COMSAT Laboratories, where he is responsible for directing research and development of earth stations, satellite payloads, state-of-the-art antennas, microwave circuits, and GaAs MMIC technology. He has written technical papers in the areas of on-board satellite regeneration of QPSK signals, network topologies to enhance the reliability of communications satellites, optimum group-delay and amplitude equalized elliptic function filters for both analog and digital transmissions, low-loss contiguous-band multiplexers, microwave switch matrices, multibeam active antennas, satellite in-orbit testing, and communications system monitoring. He also holds patents in communications satellite configurations and hardware. In 1982, he received the COMSAT Laboratories Research Award. Mr. Assal is a member of IEEE, Tau Beta Pi, and Eta Kappa Nu.

Index: communication satellites, digital transmission, distortion, modulation, demodulation, modems

An adaptive equalizer for 120-Mbit/s QPSK transmission

J. M. KAPPES

(Manuscript received June 5, 1986)

Abstract

A hardware implementation of an adaptive equalizer for use with 120-Mbit/s burst mode QPSK systems is described. Equalization is performed at IF by a three-tap transversal equalizer. Eye pattern distortion is detected at baseband and correlated with in-phase and quadrature data to determine equalizer tap weights. The ability of this equalizer to compensate for the effects of amplitude and group delay distortion on bit error rate performance was evaluated by testing with distortion present in both linear and nonlinear channel configurations. The adaptive equalizer achieved significant performance improvement for nearly all test conditions. Measurements were also performed in the burst mode using multiple distortion paths and coefficient memories to demonstrate the potential applicability of the equalizer in the INTELSAT time-division multiple-access system.

Introduction

The increased transmission of wideband digital data over satellite links has led to a need for improved channel equalization. In general, transmission bit rates have been selected to make maximum use of the channel by occupying the entire channel bandwidth. In the case of the INTELSAT V and VI transponders, the usable bandwidth is 72 MHz and a bit rate of 120 Mbit/s is being supported using QPSK modulation. Amplitude and group delay distortion requirements for this system, as specified in INTELSAT document

BG-42-65, are quite stringent. A number of elements in the transmission path, both in the earth station and in the satellite, which introduce negligible distortion when relatively narrow bandwidth frequency-division multiple-access (FDMA)/FM carriers carrying frequency-division multiplexed (FDM) voice channels are used, can cause significant degradation in wideband QPSK systems. The most straightforward technique for correcting this distortion employs fixed equalizers selected to yield a flat amplitude and group delay response over the frequency band of interest. Also, adjustable equalizers in the form of IF transversal equalizers have been used for fine-tuning the system response. Due to the nonlinear operation of the satellite traveling wave tube amplifier (TWTA), separate equalization must be provided on the up- and down-links to achieve optimal performance.

One problem associated with equalizing for flat amplitude and group delay response using currently available equipment is the necessity for placing the system being equalized in an off-line or test mode. Although this poses no problem for initial setup, once the system is operational it is undesirable to interrupt traffic for equalization changes which may be required due to equipment replacement or aging. The transversal equalizer avoids this problem because it can be adjusted without interrupting the circuit. Currently, transversal equalizers are adjusted in one of three ways: for flattest amplitude and group delay, for minimum bit error rate (BER), or for maximum eye openings of the I and Q quadrature components of the received analog data signal. The adaptive equalizer implementation was based on the latter technique, which is the only one that does not require transmission of a special test signal. This approach is equivalent to minimizing intersymbol interference (ISI).

Transversal equalizer structure and characteristics

Figure 1 is a block diagram of a three-tap transversal equalizer. The equalizer consists of two delay lines of delay T, where T is the symbol period, with taps before and after each delay. At each tap position, the signal is split and passed through an in-phase (c_j) and quadrature-phase (d_j) attenuator. By varying these attenuators, a replica of the signal present at that tap location (with variable magnitude and phase) can be obtained at the equalizer output.

Choosing the delay lines to be one symbol time enables this circuit to remove ISI which originated from adjacent symbols, as shown graphically by the signal phase diagram of Figure 2. The vector represented by R_0 corresponds to the undistorted received phase of the current symbol (0,1). The vector R_{+1} corresponds to the received phase of the preceding symbol

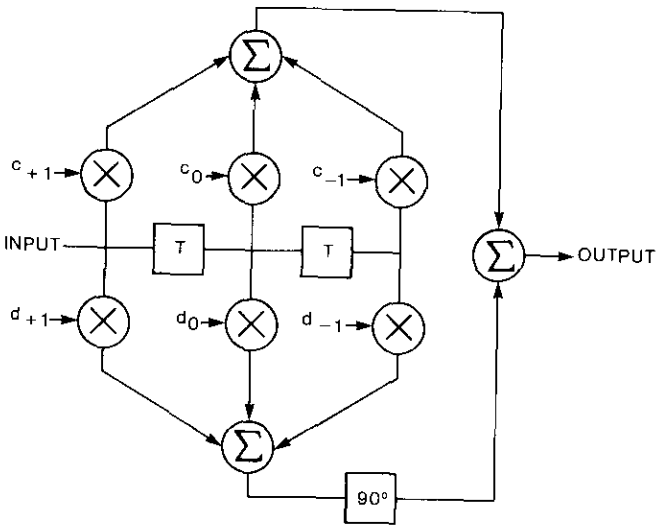

Figure 1. *IF Transversal Equalizer*

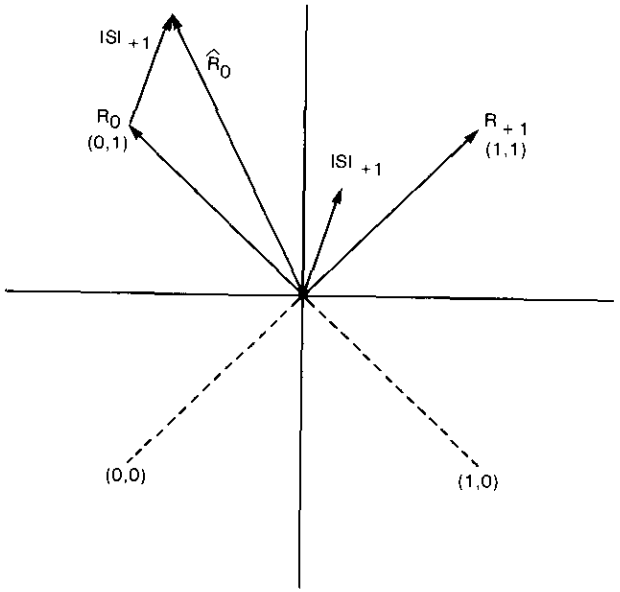

Figure 2. *Effect of ISI Due to Preceding Symbol,* R_{+1}, *on Received Symbol,* R_0

(1,1), and the vector ISI_{-1} represents the ISI to the current symbol caused by R_{+1}. Vector $\hat{R}_0$ is the received signal with the effects of ISI_{+1} shown. Vector ISI_{+1} can result from non-ideal pulse shaping at baseband or from both linear and nonlinear distortions in the transmission path. (Note that ISI_{+1} occurs one symbol time after R_{+1}, that is, at the time the decision is being made on $\hat{R}_0$.)

Reviewing the transversal structure shown in Figure 1, the signal at the output of the second delay line, R_{+1}, is available with any desired phase, depending on the values of c_{+1} and d_{+1}, and thus can be used to cancel ISI_{-1}. This is illustrated in Figure 3, which shows R_{+1} and ISI_{+1} and the vectors resulting from adjusting c_{+1} while holding d_{+1} equal to zero, and vice-versa. The c_{+1} axis is aligned with the R_{+1} vector, which simplifies the analysis as well as the hardware implementation. By proper selection of c_{+1} and d_{+1}, a vector can be generated which exactly cancels out ISI_{+1}. The adaptive equalizer uses measured ISI to obtain the optimum settings for the transversal equalizer coefficients.

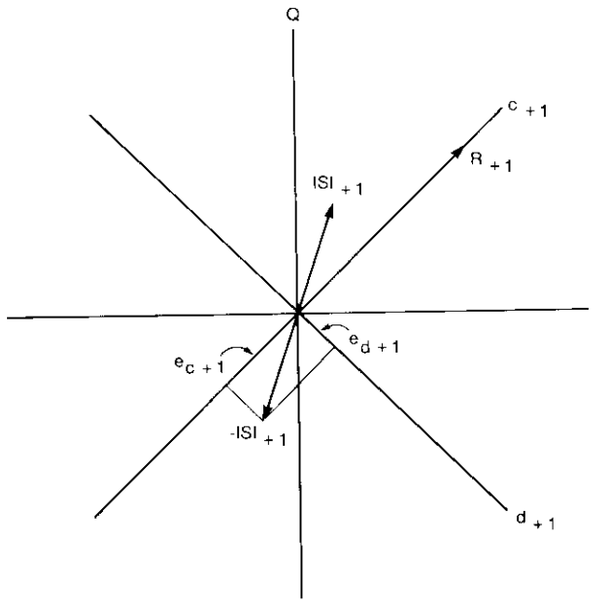

Figure 3. *Phase Relationship Between* R_{+1} *and Coordinate System* (d_{+1}, c_{+1})

Determination of IF coefficients from measured baseband ISI

Mattis, Wolcjsza, and Baker [1] have derived a set of equations and a system configuration which is capable of determining the coefficient values for the transversal equalizer from baseband distortion information. Their analysis was based on a minimum-mean-square-error approach and resulted in a system configuration which is the basis for the current development. With this work as a starting point, a realizable circuit implementation was developed and an alternate, more intuitive, approach to obtaining the equalizer tap coefficients was derived. This derivation also offers insight into the required circuit phase calibrations.

The first step in this equalization scheme is to determine the ISI present in the quadrature components of the received analog signal (I and Q). The ISI is demonstrated in Figure 4 by observing the effects of group delay distortion on the I-channel eye pattern. These eye patterns were obtained by overlapping many traces of the baseband analog waveform, first with no added distortion (Figure 4a) and then with 8-ns/72-MHz linear group delay distortion added in the IF chain (Figure 4b). The effect of this distortion on the eye pattern can be gauged by observing the increased spreading of the voltage at the sampling instant in Figure 4b. This spreading reduces the voltage difference between a one and a zero, with a resulting degradation of BER performance.

To determine the ISI present in the received analog waveforms, the quadrature components of the received analog signals were threshold-detected to obtain the expected value of the transmitted data. Figure 5 shows this process schematically. The difference between the analog data signal and the expected value is sampled at the optimum sampling point (corresponding to

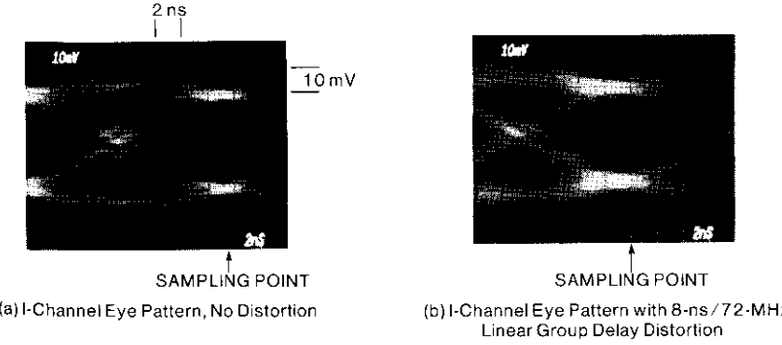

(a) I-Channel Eye Pattern, No Distortion

(b) I-Channel Eye Pattern with 8-ns/72-MHz Linear Group Delay Distortion

Figure 4. I-*Channel Eye Patterns With and Without Added Distortion*

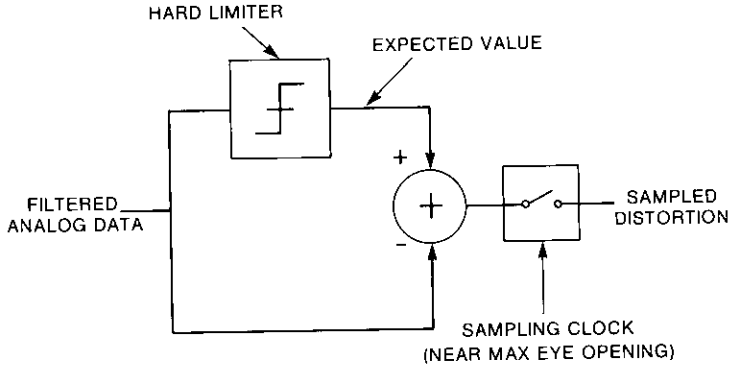

Figure 5. *Eye Pattern Distortion Detection Functional Diagram for the Baseband* I-*Channel*

the maximum eye opening) in order to derive the total ISI at the sampling instant. The result is a value of ISI in the I channel (e_I) and in the Q channel (e_Q). To illustrate these values, consider the ISI resulting from R_{+1}, labeled ISI_{+1} in Figure 6. This may be considered to be the resultant of distortion components e_I and e_Q or the desired coefficient values e_{d+1} and e_{c+1} required to cancel out ISI_{+1}. To determine the latter component values, the e_I and e_Q components must be transformed from the I, Q coordinate system to the d_{+1}, c_{+1} coordinate system. This latter system changes its orientation with respect to the I, Q system, depending on the value of R_{+1} (the last received symbol). Consequently, the transformation will not be fixed.

Referring to the notation of Figure 6,

$$e_{c+1} = r[\cos\theta] \tag{1}$$

$$e_{d+1} = -r[\sin\theta] \tag{2}$$

can be written, where e_{d+1} and e_{c+1} are the components of ISI_{+1} in the d_{+1}, c_{+1} coordinate system, r is the magnitude of ISI_{+1}, and θ is the angle of ISI_{+1} with respect to R_{+1}. Expressing e_I and e_Q, the measured values of ISI, in terms of the above variables and the angle ϕ, the angle of R_{+1} with respect to the I axis is

$$E_I = r[\cos(\theta + \phi)] = r[\cos\theta\cos\phi - \sin\theta\sin\phi] \tag{3}$$

$$E_Q = r[\sin(\theta + \phi)] = r[\sin\theta\cos\phi + \cos\theta\sin\phi] \quad . \tag{4}$$

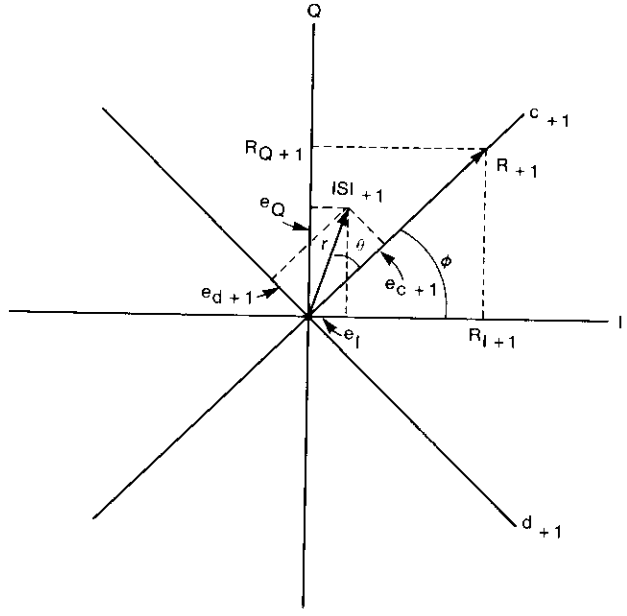

Figure 6. *Components of* ISI_{+1} *in* (I, Q) *and* (d_{+1}, c_{+1}) *Coordinate Systems*

Resolving R_{+1} into its I and Q components (which correspond to the received in-phase and quadrature bits) and defining $|R_{+1}| = 1$ yields

$$R_{I+1} = |R_{+1}|[\cos\phi] = \cos\phi \tag{5}$$

$$R_{Q+1} = |R_{+1}|[\sin\phi] = \sin\phi \quad . \tag{6}$$

Substituting equations (1), (2), (5), and (6) into equations (3) and (4) gives

$$e_I = e_{c+1}R_{I+1} + e_{d+1}R_{Q+1} \tag{7}$$

$$e_Q = e_{c+1}R_{Q+1} - e_{d+1}R_{I+1} \quad . \tag{8}$$

Solving for e_{c+1} and e_{d+1} yields

$$e_{c+1} = e_IR_{I+1} + e_QR_{Q+1} \tag{9}$$

$$e_{d+1} = e_IR_{Q+1} - e_QR_{I+1} \quad . \tag{10}$$

Equations can be derived for the other tap coefficients in the same way, resulting in the following general equations:

$$e_{cj} = e_I R_{Ij} + e_Q R_{Qj} \tag{11}$$

$$e_{dj} = e_I R_{Qj} - e_Q R_{Ij} \quad . \tag{12}$$

These values of the components along the c_j and d_j axis represent the final values which would be required to completely eliminate ISI originating from the R_j symbol. Once the attenuators of the transversal equalizer are set to these values, an evaluation of equations (11) and (12) will yield zero for e_{cj} and e_{dj}. Any further changes in transmission path distortion will result in positive or negative values for the correlation products of equations (11) and (12), which give the direction in which the coefficients should be adjusted to minimize ISI. Mattis, Wolejsza, and Baker termed these quantities *error gradients*, which gives a good intuitive indication of their role. In the actual implementation, the values of e_{cj} and e_{dj} are arrived at by a steepest-descent algorithm in which the correlation products are used to determine the direction in which the equalizer coefficients should be adjusted. Adjustments are made by adding or subtracting a fixed increment.

In practice, there is no way to separate out the ISI which originates from any given symbol. The quantities labeled e_I and e_Q actually contain the ISI from all sources. However, it is possible to determine the averages of the quantities in equations (11) and (12), such as $e_I R_{I+1}$. For example, by multiplying the measured ISI in the I channel (e_I) by the received I data bit delayed one symbol time (R_{I-1}) and averaging the resulting products, the error can effectively be correlated with the data bit from which it originated. If no component of e_I was caused by R_{I+1}, then the average of the product will be

$$\frac{1}{N}\sum_{I=1}^{N} e_I [R_{I+1}] = 0 \tag{13}$$

since the two terms are uncorrelated. Correlated products will give a nonzero average and can be combined according to equations (11) and (12) to determine values for e_{cj} and e_{dj}.

The coefficients of the transversal equalizer displaced by one delay time from the center tap are used to cancel ISI from the previous and following symbols. The center tap coefficients vary the magnitude and phase of the main IF signal. For the current implementation, the center tap coefficients were kept fixed to eliminate any rotation of the phase of the main IF signal. However, it is useful to calculate the correlation product, which corresponds to the IF signed amplitude as

$$e_{c0} = e_I R_I + e_Q R_Q \tag{14}$$

since this quantity can be used as an accurate automatic gain control (AGC) signal.

Figure 7 is a block diagram showing generation of the error gradient signals. The demodulated I and Q analog data channels are each split into two paths. In one path, the signal is threshold-detected to provide a data estimate. These data estimates are passed through the delay lines labeled T in the figure, thereby storing three successive symbols which correspond to R_{+1}, R_0, and R_{-1}. In the other path, the distortion signals e_I and e_Q are determined. As indicated, the distortion values in each channel are multiplied by the data in the same channel as well as by the data in the other channel for all three stored symbols. After multiplication and summing, as indicated in equations (11) and (12), the signals are averaged to provide the error gradients. A detailed description of the equalizer hardware follows.

Hardware implementation

Figure 8 is a block diagram showing placement of the adaptive equalizer in the earth station down-link. The transversal equalizer is placed in the down-link at IF just before the QPSK demodulator. Filtered data (eye pattern signals) and clock signals, required by the distortion detector, are obtained from the demodulator. Timing signals for burst mode operation originate from the time-division multiple-access (TDMA) terminal.

The hardware was developed in two phases. First, a continuous mode controller was constructed to demonstrate the equalizer algorithm. Second, a microprocessor-based burst mode controller was designed, built, and tested. Of the three major blocks required for coefficient generation, only the coefficient incrementer was changed for burst mode operation. The continuous mode controller will be briefly described before the changes necessary for the burst mode controller are introduced.

A detailed block diagram of the I-channel distortion detector is given in Figure 9. The incoming eye pattern signal is amplified and split into two paths. In one path, the signal is offset so that the top of the eye pattern signal (corresponding to a received 'one') is positioned at the center of the analog-to-digital (A/D) converter input signal range. Likewise, the other path is offset to position a received zero at the center of the other A/D converter's input range. At the conversion rate of 60 MHz, the highest quantization available was 6 bits.

Based on observations of eye patterns with various amounts of added distortion, it was determined that 6 bits of quantization were insufficient to resolve the resulting ISI. By using two A/D converters, one whose input range was centered at the expected value of the positive eye pattern voltage and

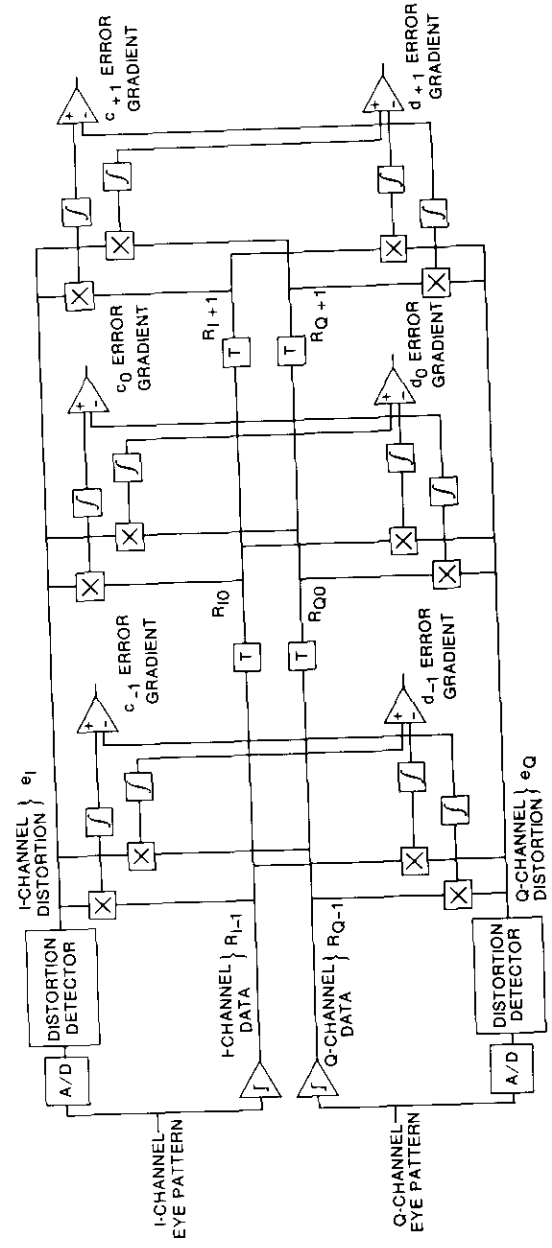

Figure 7. *Adaptive Equalizer Correlator Block Diagram*

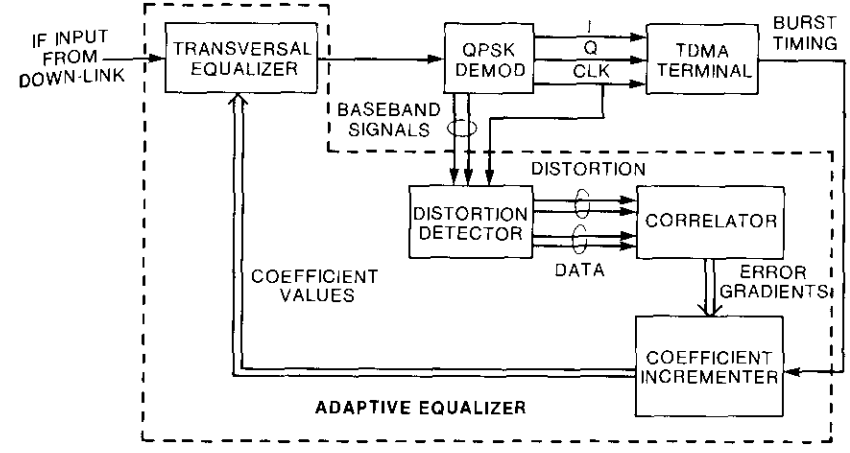

Figure 8. *Adaptive Equalizer in the TDMA Down-Link*

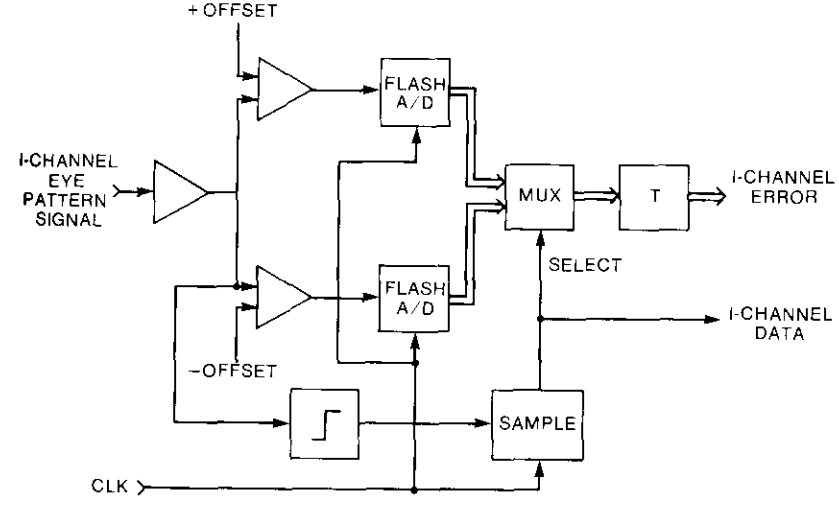

Figure 9. *Distortion Detector Block Diagram*

the other at the expected negative voltage, increased resolution was obtained. This approach has the disadvantage that certain voltages (such as values near 0 V) lie outside the range of either converter. However, for reasonable values of distortion, the voltages in the analog data signals are near the expected values at the sampling instant, and signal averaging minimizes errors due to

voltages which infrequently fall outside the range of the A/D converters. To identify which A/D converter has a valid error signal, a threshold decision is made on the corresponding eye pattern signal. This result is used as the control signal for a multiplexer which selects the 1 or 0 A/D converter. An identical circuit calculates the error and data for the Q channel.

Figure 10 depicts a typical section of the correlator used to calculate ∇_{c-1}. The error and data arrive in digital form from the distortion detector, and the data and sign-of-the-error bits are correlated by an exclusive-OR operation. The error magnitude signal, along with the modified sign bit, is then converted back to an analog signal, where it is low-pass filtered. The same process is performed for each of the cross-correlation products required by equations (11) and (12), and e_{cj} and e_{dj} are determined.

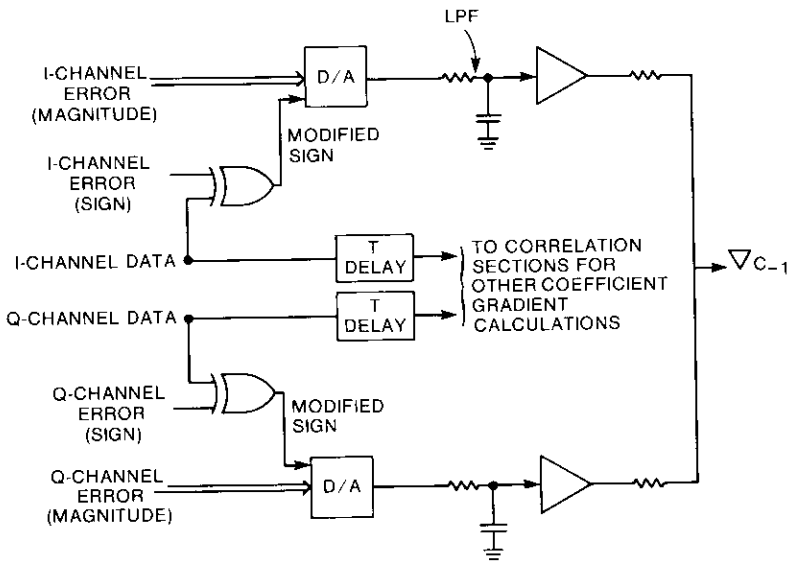

Figure 10. *Correlator Circuit*

A total of five error gradients (four to control the coefficients which reduce ISI from adjacent symbols and the fifth for AGC control) are calculated and fed to the coefficient incrementer for the continuous mode implementation. Figure 11 shows a typical section of this incrementer. Two comparators at the input of the circuit are used to compare the gradient signal with a positive and negative threshold. If either threshold is exceeded, the coefficient must be incremented; otherwise, it remains unchanged. The comparator outputs

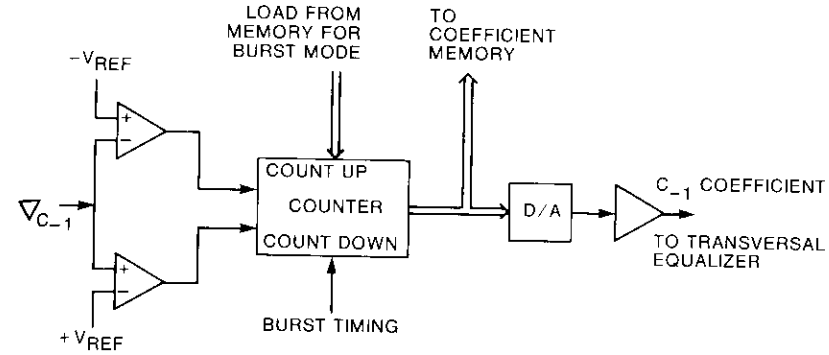

Figure 11. *Coefficient Incrementer Circuit*

are used to increment a 10-bit up/down counter. The direction of the increment is determined by which threshold was exceeded. The value in the counter is converted to an analog voltage, which is used to control the appropriate tap coefficients of the transversal equalizer.

During testing of the continuous mode adaptive equalizer, it became apparent that input signal level variations to the distortion detector circuits had to be minimized for proper operation. The AGC circuit of the modem, while perfectly acceptable for modem operation, was too coarse for the distortion detector circuits. Therefore, a new AGC circuit (Figure 12) was added just after the transversal equalizer. This improved AGC circuit uses as its control signal the average of the correlation products of equation (14). The two AGC circuits did not interact due to the large difference in their time constants. The modem AGC is capable of reacting rapidly, on the order of hundreds of nanoseconds, while the new AGC is a much slower process updated only once per millisecond.

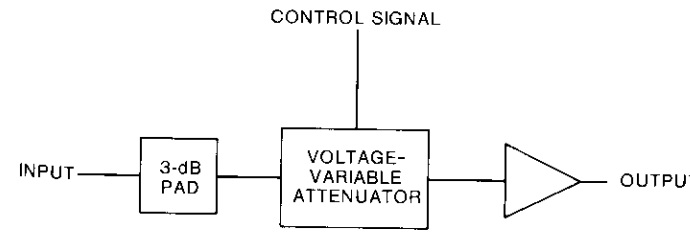

Figure 12. *Automatic Gain Control Amplifier*

Burst mode control for TDMA bursts

A burst mode controller for the adaptive equalizer was developed for use with TDMA systems. This microprocessor-based controller, which is capable of updating, storing, and loading up to 64 sets of coefficients into the equalizer, accomplishes two separate functions. First, it loads the proper coefficients from memory into the transversal equalizer at the proper time for each incoming burst. Second, the controller examines one burst per frame and updates the coefficients for that burst based on error gradient information.

Figure 13 is a block diagram of the burst mode controller. Start-of-frame and start-of-burst signals are received from the TDMA system and used by the address generator for timing synchronization. The generator retrieves coefficients from the dual-port memory which are then loaded into the input storage registers of the D/A converters. The converters have two input storage registers: one which determines the output of the converter, and another which is next in line for conversion. This arrangement is ideal for this application in which high speed is required because the coefficients can be loaded sequentially into the first set of registers and then, with a single strobe, can be loaded in parallel into the D/A converter. To update coefficients, the microprocessor examines the error gradient comparator outputs which have been stored in a latch, retrieves the coefficients from its memory, increments the coefficients if required, and stores the new values in the dual-port memory. All of this is accomplished in such a way as to avoid interfering with the ongoing process of retrieving the coefficients for the transversal equalizer. Figure 14 shows the burst timing format and indicates at what point in time various control functions are executed.

Performance measurements

The ability of the adaptive equalizer to compensate for BER degradation from known added distortions has been measured over both linear and nonlinear channels in continuous mode, and over a linear channel in burst mode.

Continuous mode—linear channel

Figure 15 depicts the linear channel continuous mode test setup. The modem used for these tests was built by COMSAT Laboratories and is nearly identical to modems which were built for and delivered to INTELSAT as part of the 120-Mbit/s TDMA Test Bed Program. The modem uses 40-percent square-root Nyquist filtering on the transmit and receive sides, and $x/\sin(x)$ compensation on the transmit side. Distortion was added by placing modules with various amounts of amplitude and group delay into the IF link. Noise

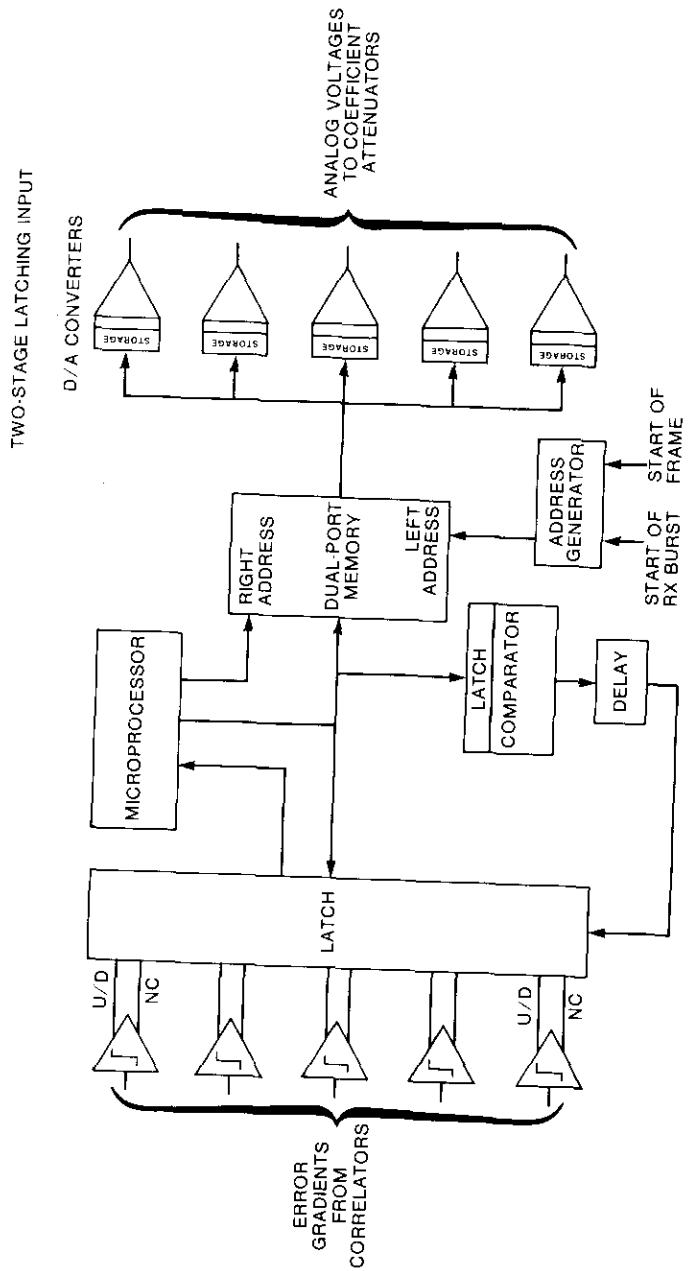

Figure 13. *Burst Mode Controller Block Diagram*

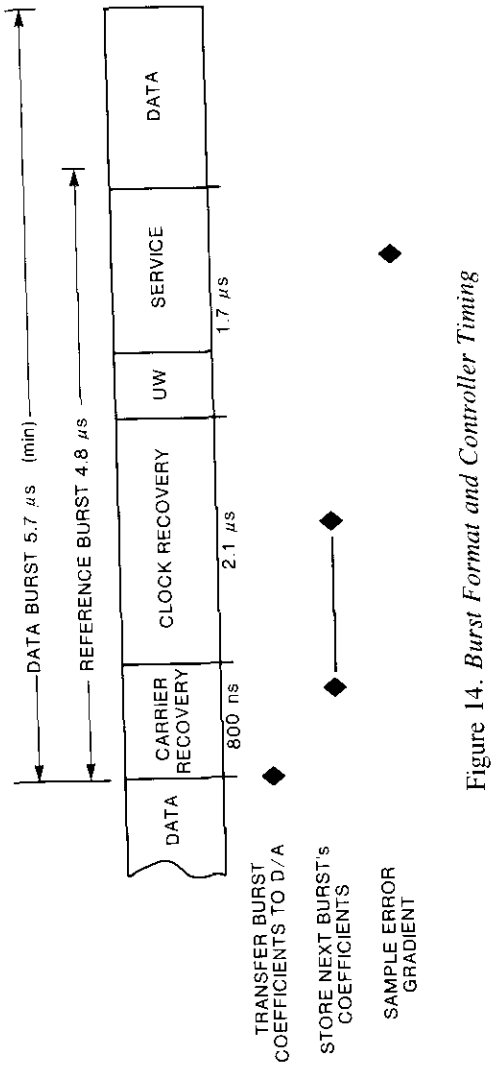

Figure 14. *Burst Format and Controller Timing*

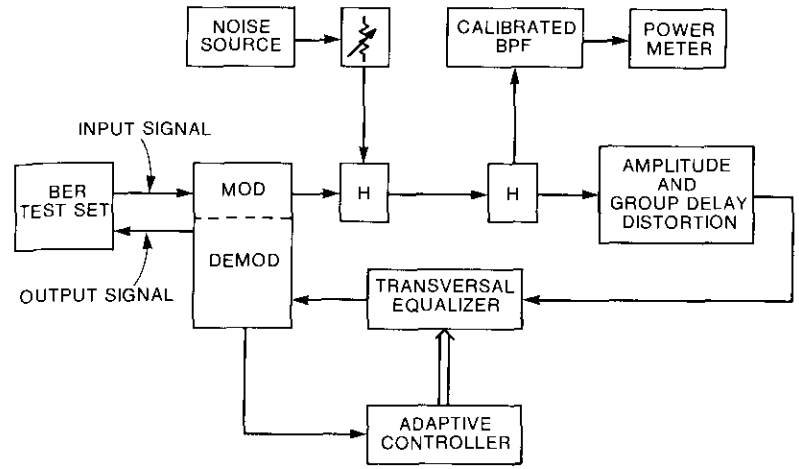

Figure 15. *Linear Channel Test Setup*

was added prior to the distortion in order to measure BER *vs* E_b/N_o. The carrier-to-noise ratio (C/N) was measured with a calibrated filter using a signal tapped off before the distortion was added. The adaptively controlled transversal equalizer was placed directly before the demodulator.

As typical examples of the effects of distortion on BER and the improvement resulting from adaptive equalization, BER *vs* E_b/N_o was measured for added linear group delay, parabolic group delay, and linear amplitude slope, both with the adaptive equalizer off (*i.e.*, transparent) and on. Figure 16 shows performance curves for the cases of 12-ns positive linear group delay, 12-ns negative coefficient parabolic group delay, and 4-dB negative linear amplitude slope. For reference, the IF loopback performance is also shown.

A summary of the equalizer performance is shown in Figure 17 for the three types of added distortion. The information for these curves was obtained from the BER *vs* E_b/N_o curves by plotting the performance degradation from ideal at a BER of 10^{-7} *vs* the amount of added distortion. These data can also be presented in a slightly different way by plotting the amount of correction provided by the adaptive equalizer *vs* added distortion (Figure 18). As can be seen from these figures, the adaptive equalizer can minimize the effects of significant amounts of added distortion.

Continuous mode—nonlinear channel

Nonlinear channel performance was measured using a 72-MHz transponder (transponder number 7-8) of the INTELSAT V satellite simulator [2]. The simulator was operated at a high-power amplifier (HPA) input backoff of 10 dB

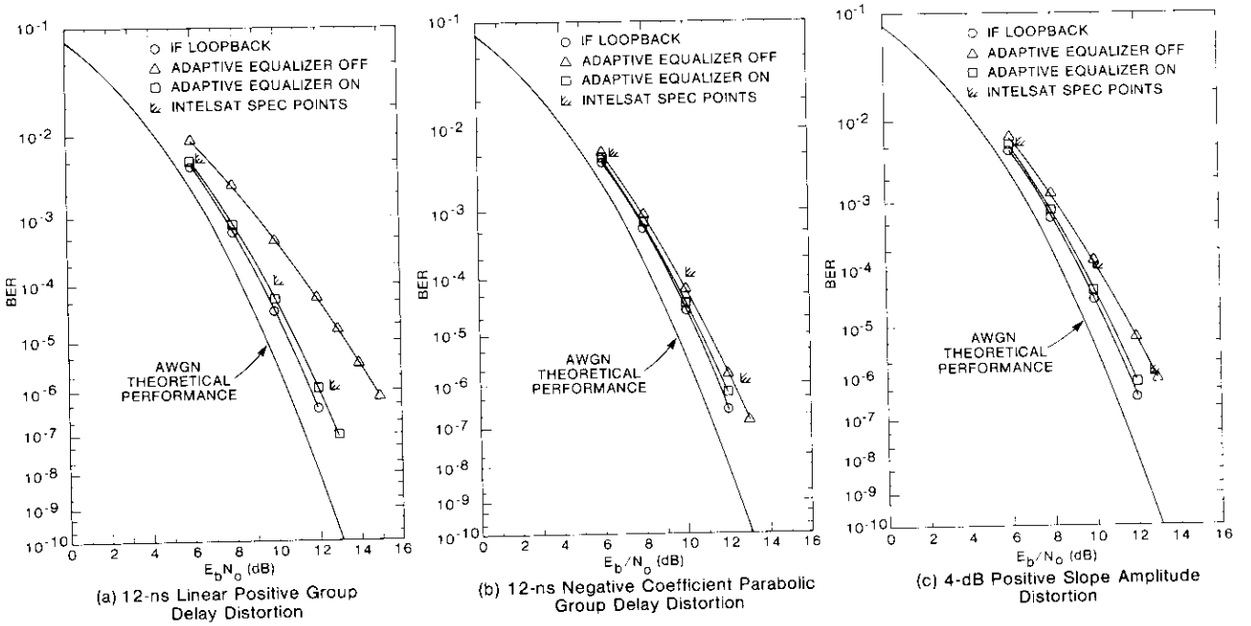

Figure 16. *Linear Channel BER* vs E_b/N_o *Performance*

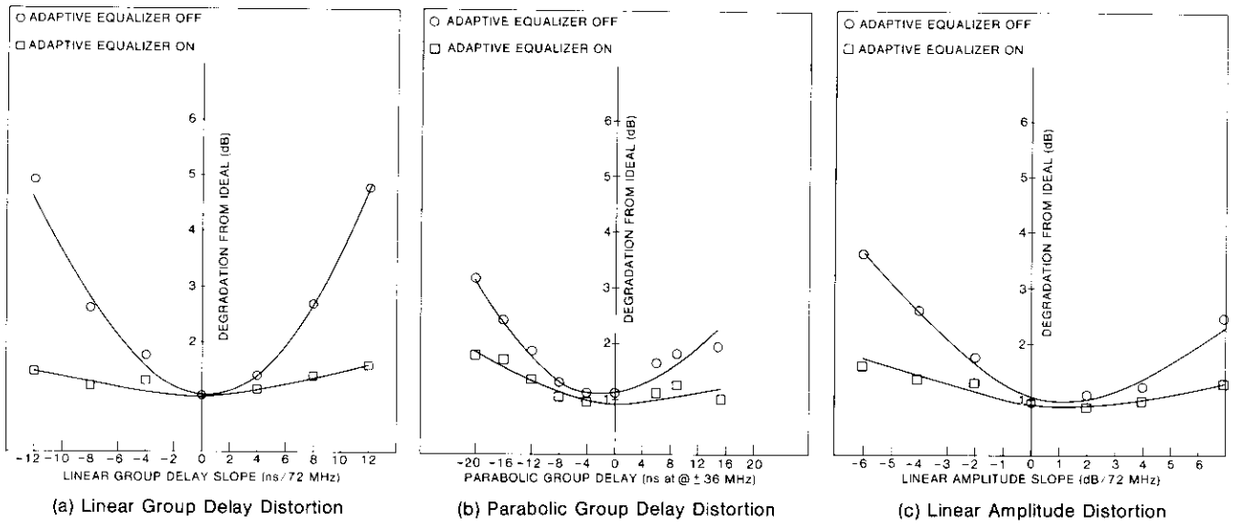

Figure 17. *Summary of Adaptive Equalizer Linear Channel Performance*

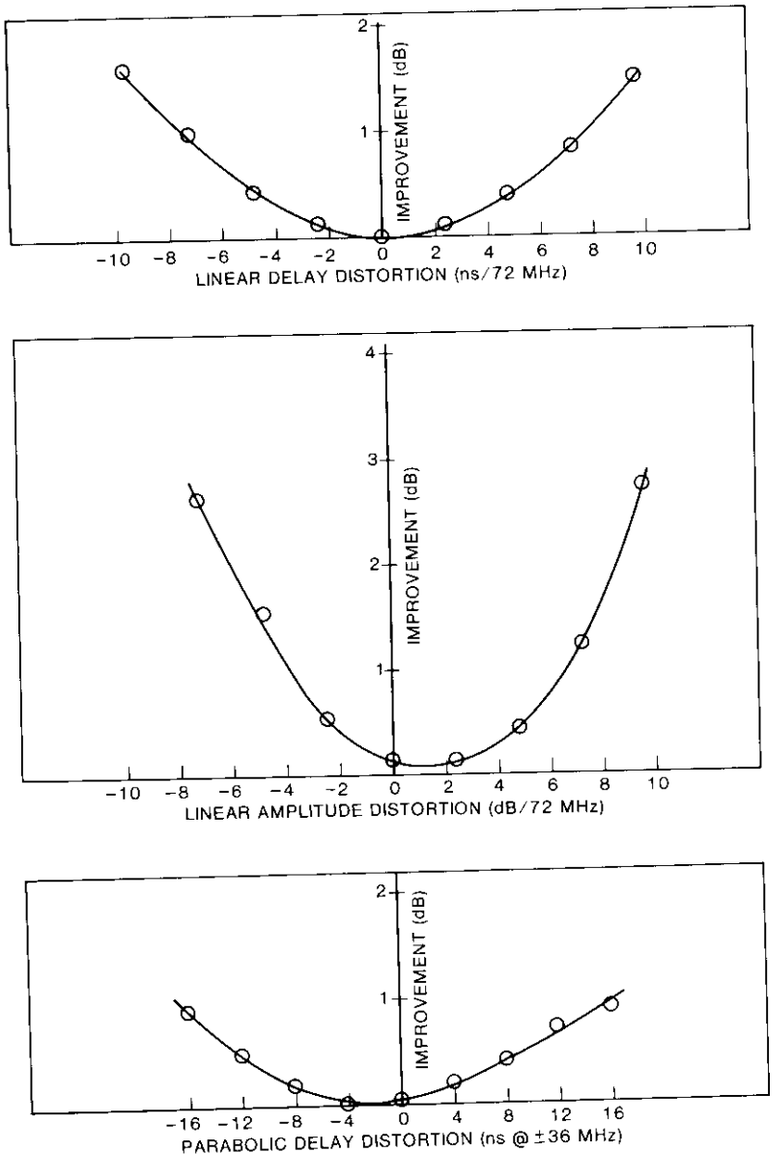

Figure 18. *Linear Channel Improvement* vs *Added Distortion Using Adaptive Equalization*

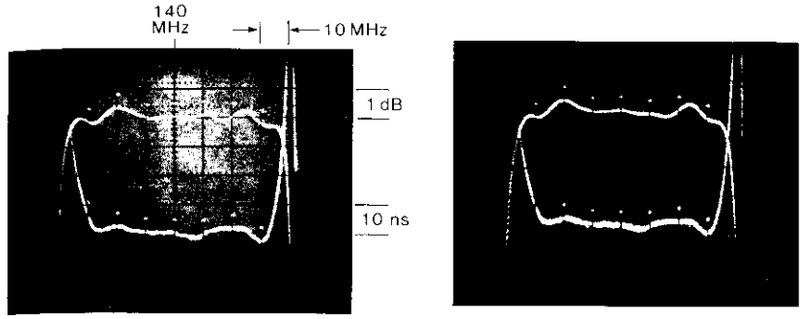

(a) HPA/TWTA Input Backoffs = 14/14 dB (b) HPA/TWTA Input Backoffs = 10/2 dB

Figure 19. *Nonlinear Channel Amplitude and Group Delay Responses*

and a satellite TWTA input backoff of 2 dB. Figures 19a and 19b show the amplitude and group delay responses of the channel with no added distortion, with the HPA and TWTA operated at input backoffs of 10/2 and 14/14 dB, respectively.

The test setup, which shows the location of the up-link and down-link added distortion, is depicted in Figure 20. During initial testing through the simulator, an inherent 2.8-dB negative slope was noted in the up-link setup, possibly with some contribution coming from the modem and IF test setup. This was observed when the addition of positive amplitude slope actually improved the BER. Therefore, a positive 2.8-dB amplitude equalizer was constructed and placed in the up-link, as shown. As in the linear channel case, the BER was measured with and without the adaptive equalizer for all types of distortion.

From the BER *vs* E_b/N_o curves described above, the performance degradation at BER = 10^{-7} for the various types of added distortion was plotted *vs* distortion added in the up-link and down-link, as shown in Figures 21 and 22, respectively. It was observed that the equalizer performs better when the distortion occurs on the down-link, and is not as effective when distortion occurs on the up-link. This is to be expected since the nonlinear TWTA, which intervenes between the up- and down-links, adds ISI distortion that cannot be removed by a linear equalizer. The one exception to this is linear group delay, for which nearly equal correction is obtained for either up-link or down-link distortion. Added up-link parabolic group delay is the least influenced by the application of equalization.

Burst mode operation

Burst mode operation requires a minimum burst length for proper adaptive equalizer performance. This minimum is determined by the time constant of

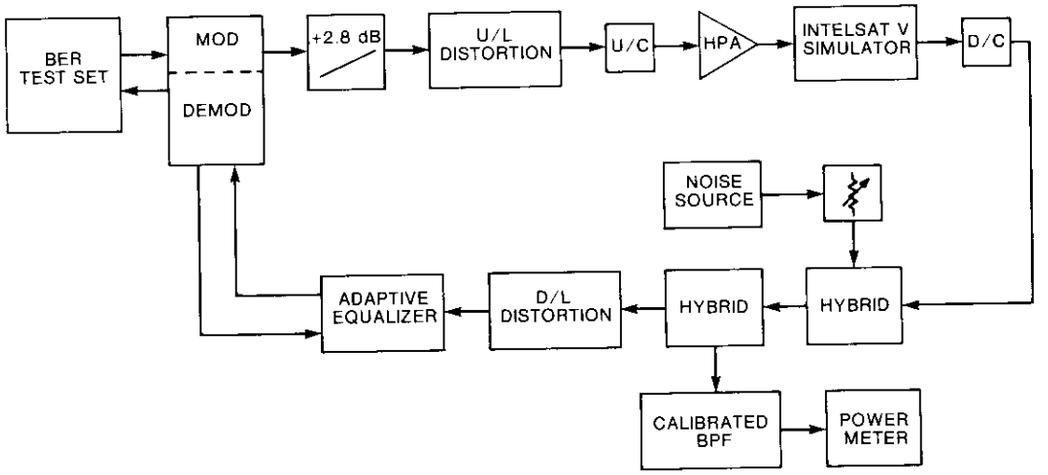

Figure 20. *Nonlinear Channel Test Setup With Added Up-Link or Down-Link Distortion*

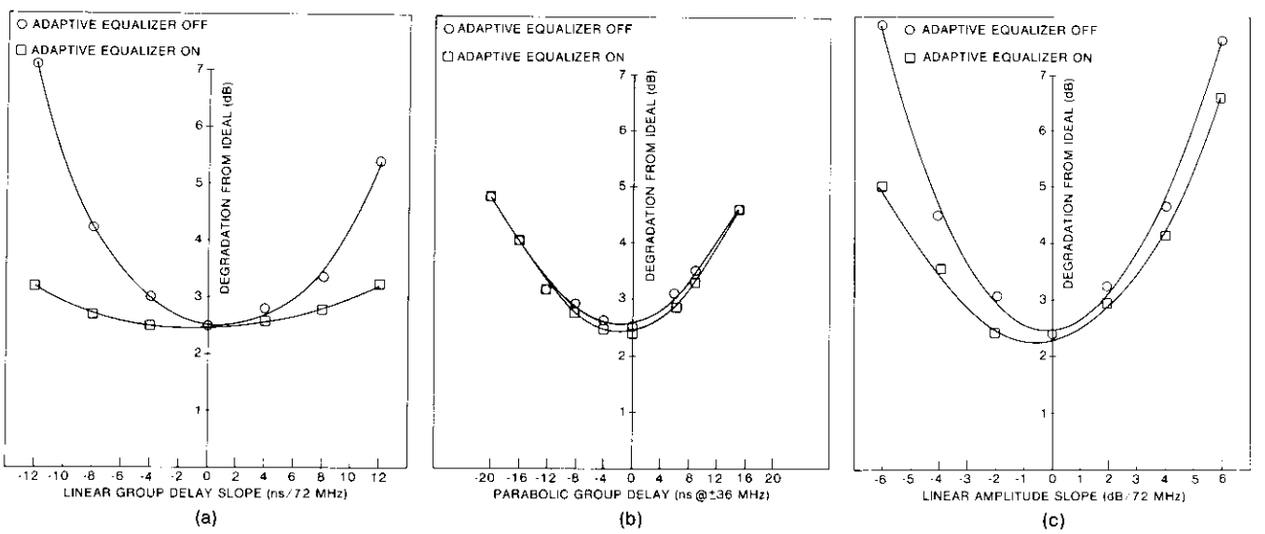

Figure 21. *Adaptive Equalizer Nonlinear Channel Performance With Distortion Added on Up-Link*

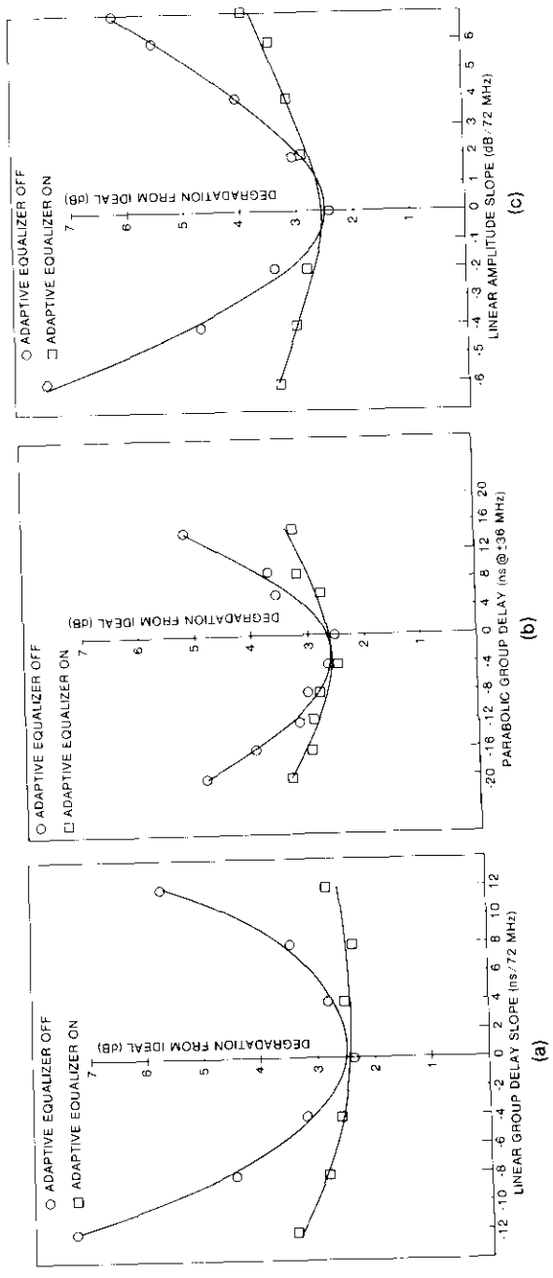

Figure 22. *Adaptive Equalizer Nonlinear Channel Performance With Distortion Added on Down-Link*

the error gradient filter. Initially, a filter with a 1-MHz bandwidth was selected for this function. Continuous mode measurements indicated that this bandwidth is sufficiently narrow to provide an adequate signal-to-noise ratio for the equalization process. Measurements were also taken to determine how many symbols were required to achieve accurate error gradient information. This was accomplished by measuring burst mode BER and sampling the error gradients for processing at various times after the preamble.

Figure 23 shows the results of the above measurements. The BER at an E_b/N_o of 12 dB is plotted *vs* the time in the burst after the end of the preamble at which the error gradient was sampled. Equalizer correction processing

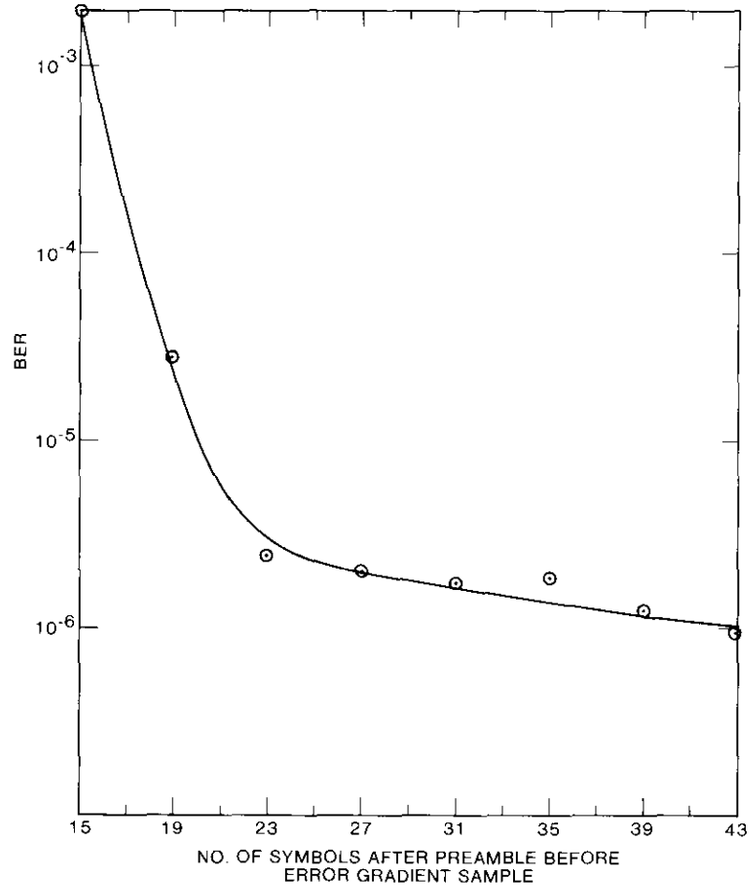

Figure 23. *Sensitivity of Adaptive Equalizer to Burst Length*

begins at this time. Time is measured in 120-Mbit/s QPSK symbols which are 16.7 ns long. After 23 symbols (0.38 μs), the BER is approximately twice its final value, and at 43 symbols (0.72 μs) the BER has essentially reached its steady-state value. These numbers indicate that the equalizer will be capable of handling the shortest bursts planned for the INTELSAT 120-Mbit/s system, which are 1.5 μs in length (not including the preamble).

Figure 24 shows the setup used for burst mode BER measurements. Two additional functions were implemented for these measurements: the timing controller and the dual-channel simulator. The timing controller supplies all timing signals, which include the following functions:

- Provide start-of-burst and start-of-frame signals for the microprocessor controller.
- Initiate data transmission from the BER test set transmit side, which in turn controls the modulator.
- Determine which of the two IF paths any given burst will be transmitted through.
- Determine during which burst BER measurements will occur.

The timing controller is meant to simulate the TDMA controller in a typical earth station application. Parameters for the controller are set up using an HP-9816 computer and the HP interface bus. Up to 32 bursts can be transmitted in one 2-ms frame, and each burst can be routed through either of the two IF paths. The BER of only one burst per frame can be measured at any one time. A number of convenience functions are also provided, such as routing all bursts through only one path for continuous mode measurements.

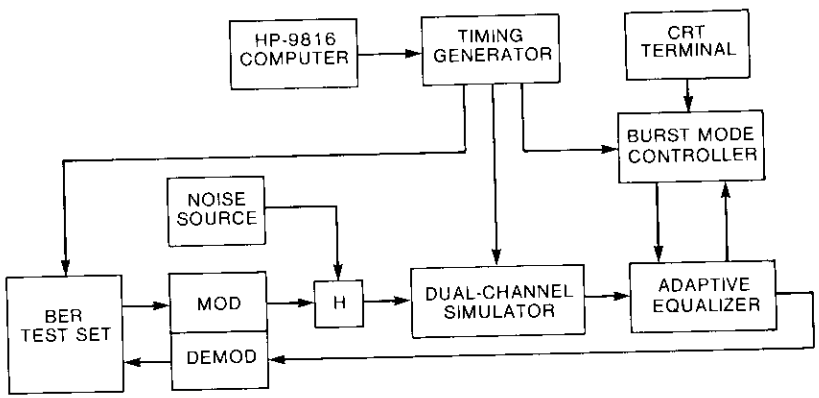

Figure 24. *Burst Mode Test Setup*

Figure 25 is a block diagram of the dual-channel simulator. The IF signal with added noise is split into three paths. One path is used as a monitor point for *C/N* measurements. The other two paths lead to diode switches, either of which can be turned on to allow the signal to pass through the selected distortion. The signal is then amplified for application to the demodulator.

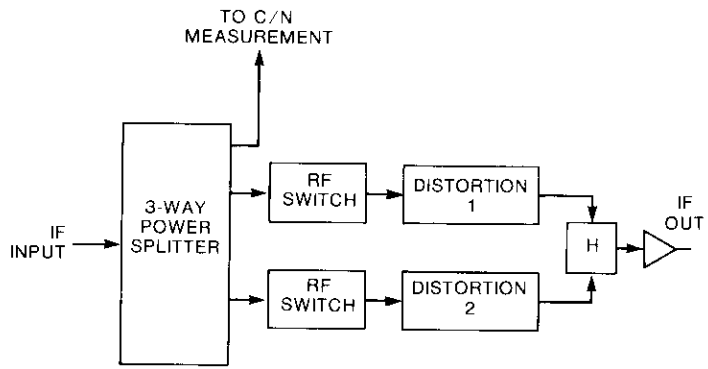

Figure 25. *Dual Channel Simulator*

Burst mode performance was measured for the following three types of distortion: 12-ns linear positive slope group delay, 12-ns negative coefficient parabolic group delay, and 4-dB negative amplitude slope. The resulting performance curves, with and without adaptive equalization, are shown in Figure 26. Continuous mode data collected using the previous continuous mode hardware are also plotted. The close agreement shown between the data indicates that the burst mode controller is performing accurately.

Additional nonlinear testing

Measurements have indicated that the adaptive equalizer is more effective at equalizing certain types of distortion, in particular parabolic delay distortion and linear amplitude slope, when it is placed on the down-link of a nonlinear channel. If the satellite TWTA could be operated in a more linear fashion, the equalizer would be more capable of correcting up-link distortions. This can be accomplished by operating the TWTA at larger input backoffs; however, the lower TWTA drive levels will result in lower satellite output power and consequently lower *C/N* at the earth station. Tests were conducted to investigate the feasibility of this approach. Since the original nonlinear channel (INTELSAT V simulator) was no longer available for these tests, a new channel was assembled, as shown in Figure 27. This test setup does not

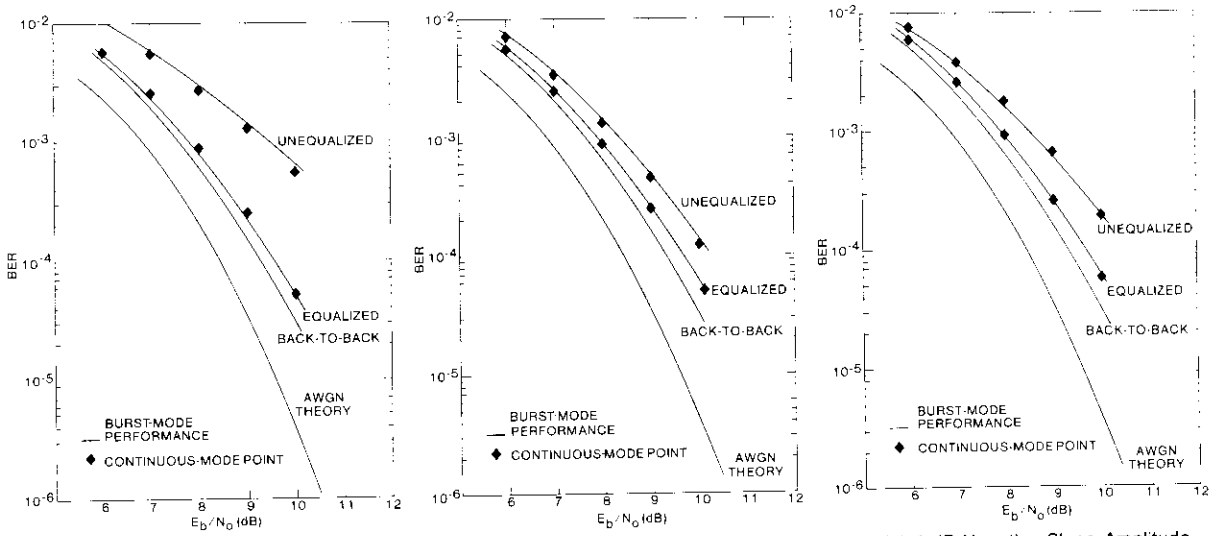

Figure 26. *Burst- and Continuous-Mode BER* vs E_b/N_o *in a Linear Channel*

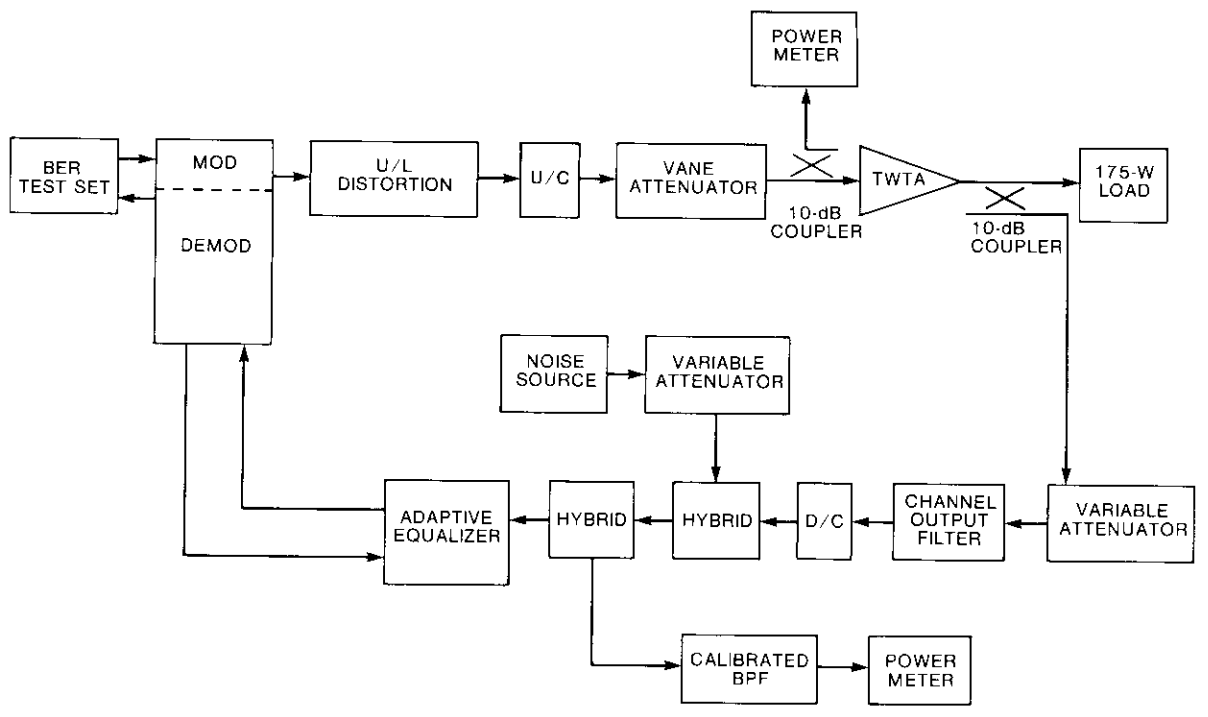

Figure 27. *Test Setup for Nonlinear Channel Backoff Measurements*

include an HPA or a satellite input multiplex filter. However, since the HPA is normally operated in a nearly linear mode (10-dB input backoff) and the input filter is very well equalized, it was felt that this channel provided a good approximation of the INTELSAT V transponder.

The BER *vs* E_b/N_o data were taken at 0-, 2-, 4-, 6-, and 8-dB TWTA input backoff. From these curves, the performance degradation at a BER of 10^{-7} with and without the adaptive equalizer was determined and is plotted in Figure 28a. To account for the loss of power due to TWTA output backoff, the TWTA transfer curve in the region of interest is plotted in Figure 28b. This loss of power translates into added degradation, which is reflected in the additional curves of Figure 28a. These data indicate that a slight performance improvement (0.35 dB) can be obtained by operating the TWTA at 4-dB input backoff. However, the amount of improvement and the optimum backoff will depend on the amount and type of added up-link distortion. Further experimental data could be taken to determine these values. However, this study has shown that significant improvement is achieved at 2-dB input backoff (even for up-link distortion) with two types of distortion commonly encountered in earth stations: linear amplitude and group delay.

To deal effectively with up-link distortion, the equalization scheme shown in Figure 29 could be employed. This setup would require a well-equalized down-converter and down-link. The demodulator could be placed near the antenna to minimize the introduction of possible distortion, such as that due to long cables.

Conclusions

Measurements have indicated that the adaptive equalizer is quite effective at minimizing ISI due to added distortion when the distortion has been added in a linear channel or on the down-link of a nonlinear channel. When the distortion has been added on the up-link of a nonlinear channel, the performance improvement gained by adaptive equalization varies with the type of added distortion. For linear group delay distortion, the adaptive equalizer performs nearly identically whether the distortion was added on the up-link or the down-link. The opposite extreme is parabolic group delay. Almost no improvement is obtained if the distortion is placed on the up-link. The situation with linear amplitude slope lies somewhere in between. Some improvement is obtained for added up-link distortion, but not as much as when the amplitude distortion is placed on the down-link.

The adaptive equalizer is capable of functioning in burst mode with a minimum of timing signals from a TDMA controller. The transversal equalizer can respond rapidly to new coefficient values and requires bursts only on the order of 1 μs in length.

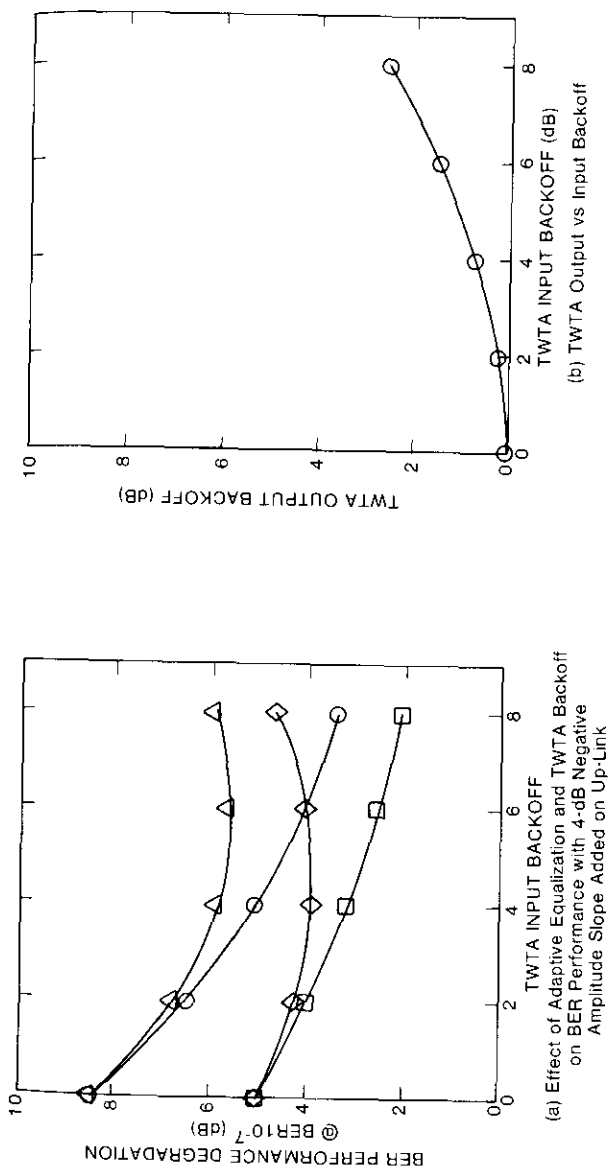

Figure 28. *Nonlinear Channel Performance*

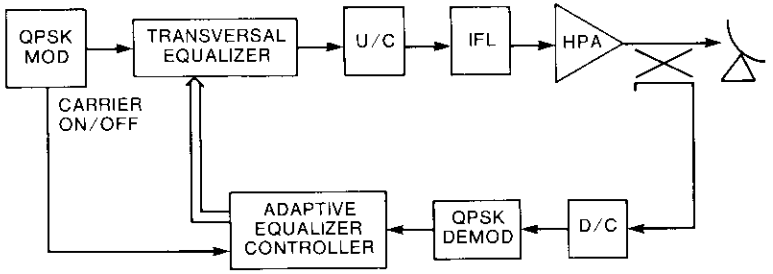

Figure 29. *Possible Setup for Up-Link Adaptive Equalization*

Acknowledgments

The efficient and timely completion of this project was due in large part to the efforts of G. House, who was responsible for all aspects of the burst mode controller, J. Miller, who breadboarded and debugged the majority of the RF circuits, and M. Hutchins, who performed the measurements and collected the data contained in this report; to C. Wolejsza, who did much of the early theoretical work and provided valuable suggestions for the hardware design; and to S. J. Campanella, who originally suggested the use of maximum-rate-of-descent linear programming for convergence and the storage of coefficients for TDMA burst mode operations.

References

[1] W. Mattis, C. Wolejsza, and S. Baker, "Digitally Controlled Transversal Equalizer," Sixth International Conference on Digital Satellite Communications, Phoenix, Arizona, September 1983, *Proc.*, pp. VI-23–VI-29.

[2] M. E. Jones, "Laboratory Hardware Simulation Measurements of 120-Mbit/s QPSK/TDMA Transmission Performance in the INTELSAT V System," Sixth International Conference on Digital Satellite Communications, Phoenix, Arizona, September 1983, *Proc.*, pp. I-A-1–I-A-8.

Mark Kappes received a B.S.E.E. and an M.S.E.E. from the University of Illinois in 1971. Since joining COMSAT Laboratories in 1979, he has been involved with the design of high-bit-rate modems and satellite link equalization equipment. As Manager of the Transmission Processing Department, he is responsible for ongoing work in satellite modem technology and associated transmission link equipment. Previously, Mr. Kappes was employed by the Watkins-Johnson Company, where he was responsible for the design of low-noise, high-dynamic-range receivers and special-purpose demodulators.

Index: communication satellites, digital transmission, small terminals, mobile communication systems, modulation, demodulation, modems

Modulation selection for the Mobile Satellite Experiment (MSAT-X)

K. M. MACKENTHUN

(Manuscript received October 16, 1985)

Abstract

The Mobile Satellite Experiment (MSAT-X) is a NASA program to determine the feasibility of a communications network in which private and commercial users send linear predictive coded voice and low-speed data via satellite, using low-cost terminals mounted in vehicles. This paper compares candidate modulation methods for MSAT-X by employing time domain simulation of a mobile-to-satellite transmission link. Binary FM with limiter-discriminator detection is shown to be the most suitable method because of its relative robustness to channel degradations such as Doppler shift, multipath noise, fading, and adjacent channel interference.

Introduction

The Mobile Satellite Experiment (MSAT-X) is a NASA program, directed by the Jet Propulsion Laboratory (JPL), to develop advanced ground segment technology for use in future land-mobile satellite systems and to experimentally verify this technology by using a first-generation commercial mobile satellite around 1988. As part of the MSAT-X program, COMSAT Laboratories is to study power-efficient modulation, an advanced linear predictive coding (LPC) vocoder, and forward error correction (FEC) coding and automatic repeat request (ARQ) for the transmission of data and near-toll-quality voice in a 5-kHz channel at a rate of 2,400 bit/s. The LPC voice transmission is to be received with a bit error rate (BER) of no worse than 10^{-3}, and the data transmission

with a BER of no worse than 10^{-6}. To make the system commercially viable, a low-cost implementation is desired.

This paper pursues the selection of a modulation technique by comparing the performance of several different modulations, using time domain simulation of a land-mobile satellite channel subject to multipath fading. The mobile satellite channel is described, modulation candidates and simulation software are discussed, and the performance of candidate modulations on the fading channel is evaluated.

Channel models

The MSAT-X channel is subject to multipath fading, shadowing, Doppler frequency shift, and adjacent channel interference (ACI). The Rice channel model is well suited for describing multipath reflections, and measurements show that a Rice factor (direct-path-to-multipath power ratio, C/I) of 10 dB is appropriate for land-mobile systems [1],[2]. The loss caused by shadowing and strong specular reflections is typically included in a "system outage" specification, since little can be done to prevent these effects. Shadowing is not expected to be a problem except in urban areas, since the elevation angle to the satellite is expected to be more than 25° for the continental U.S.

The Doppler frequency shift is given by

$$f_d = \frac{v}{\lambda} \cos \alpha$$

where v is vehicle speed, λ is the transmit or receive wavelength, and α is the elevation angle to the satellite. For the MSAT-X transmit and receive frequency band of about 840 MHz and α of 25°, f_d is about 72 Hz for a vehicle speed of 55 mph, and about 100 Hz for an assumed maximum speed of 75 mph. The mobile terminal communicates with a fixed station, which relays voice and data traffic to and from the terminal. In addition, all mobile terminals receive a common pilot beacon which allows the terminal to compensate for local oscillator instability. Therefore, transmissions from the fixed station to the mobile terminal are received at a maximum frequency offset of 100 Hz, while transmissions from the mobile terminal to the fixed station are received at a maximum offset of 200 Hz. The latter offset is twice as large because the transmission frequency of the mobile terminal is referenced to the pilot beacon.

Based on the above considerations, the following channel models were used to simulate the performance of the candidate modulations:

- an additive white Gaussian noise (AWGN) channel with frequency offset of 0 Hz;

- an AWGN channel with frequency offset of 0.1 R_b;
- an AWGN channel with frequency offset of 0.1 R_b and two adjacent channels of 10-dB greater power, offset in frequency by $\pm(5 \text{ kHz} - 0.1\ R_b)$; and
- a Rice channel with $C/I = 10$ dB.

The use of four channel models allows comparison of the relative effects of different channel degradations on modulation performance.

Simulation of the Ricean channel uses a filter to shape the in-phase and quadrature components of white Gaussian noise, which are added to the direct component of the signal. The noise-shaping filter is given by

$$H(f) = \begin{cases} (f_d^2 - f^2)^{-1/4} & , \ |f| < f_d \\ 0 & , \text{ elsewhere} \end{cases}$$

where f_d is the Doppler shift. The filter $H(f)$ corresponds to an omnidirectional antenna receiving independent signals of equal power uniformly distributed over a surrounding sphere [3]. The Ricean channel with shaping filter $H(f)$ was simulated for carrier offsets of 0, 72, and 144 Hz (see Figure 1). The first two channels (Figures 1a and 1b) model transmission from a fixed station to a mobile terminal, and the third channel (Figure 1c) models transmission

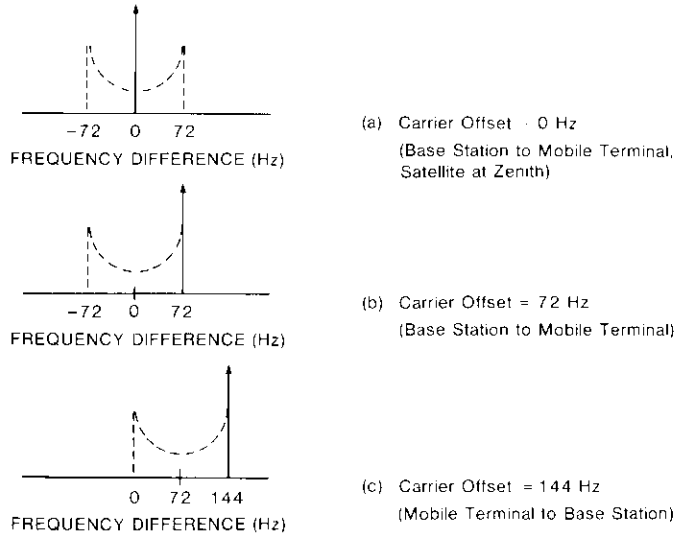

Figure 1. *Rice Channel Model Showing Rayleigh Noise Spectrum and Carrier Offset*

from a mobile terminal to a fixed station. The simulation was calibrated using a bit energy determined by the direct component alone.

Modulation candidates

The following nine modulation techniques were compared:

- minimum shift keying (MSK) with 2-bit differential detection and baseband Gaussian filtering (GMSK),
- MSK with 2-bit differential detection,
- MSK with 1-bit differential detection,
- MSK with 2-bit differential detection and a frequency-locked loop (FLL),
- binary FM with limiter-discriminator (LD) detection,
- four-level FM with LD detection,
- binary FM with noncoherent detection using $N = 3$ symbol intervals,
- duobinary FM with LD detection and a maximum-likelihood sequence estimator (MLSE), and
- differential phase-shift keying (PSK).

Except for differential PSK, the modulation methods are constant envelope and thus can be transmitted by saturated nonlinear amplifiers without spectral regrowth. The absence of regrowth is critical in the MSAT-X channel where requirements on ACI are severe.

Coherent detection was not considered because of the difficulty of maintaining phase coherence over the MSAT-X channel. To achieve significantly better performance than with differential detection, the carrier synchronization circuit should average over 10 or more symbols [4]. However, since the symbol rate is 2,400 symbol/s and the fade rate can be as high as 200 fades/s, there is a large probability of signal fade during the 10-symbol averaging time. The performance of the carrier synchronizer is also affected by phase noise arising from multipath reflections, as well as by Doppler shift and Doppler rate, which are significant compared to the symbol rate of the MSAT-X channel. Together, these effects cause coherent detection methods to exhibit worse performance than with differential detection or other noncoherent detection methods over a mobile channel [5],[6]. In particular, the error floor for coherent methods has been measured to be around 10^{-3} in a fast Rayleigh fading channel, which is the MSAT-X specification requirement for voice.

The use of GMSK with 2-bit differential detection (Figure 2) has been extensively studied for digital mobile radio applications [5]–[8]. Baseband Gaussian filtering of the input data stream on the transmit side allows a more compact RF spectrum than with MSK. In addition, the use of 2-bit rather than

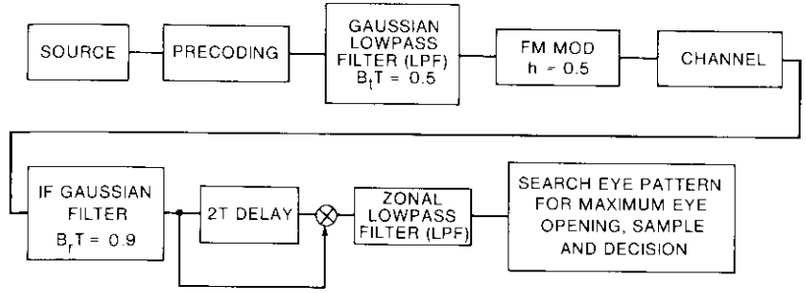

Figure 2. *MSK With 2-bit Differential Detection and Baseband Gaussian Filtering*

1-bit differential detection results in a larger eye opening, which gives improved performance especially with heavy baseband filtering. Thus, GMSK with 2-bit differential detection can be advantageous for a mobile channel that has a severe bandwidth constraint and where a relatively simple hardware implementation is desired. MSK with 2-bit differential detection and no baseband Gaussian filtering (Figure 3) was also studied because of its slight performance superiority over MSK with 1-bit differential detection (Figure 4), and because it has been emphasized by JPL.

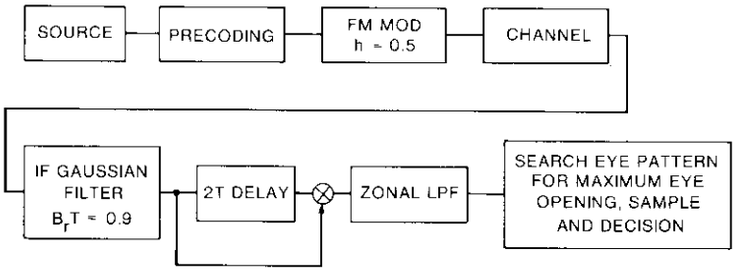

Figure 3. *MSK With 2-bit Differential Detection*

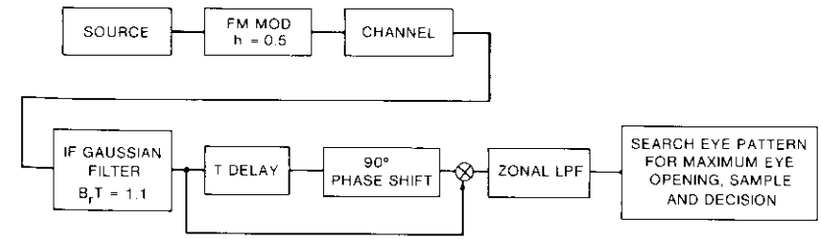

Figure 4. *MSK With 1-bit Differential Detection*

An FLL can be employed with GMSK, or with MSK with 2-bit differential detection (Figure 5), to track out channel frequency offset. An implementation of this approach by JPL using a baseband I and Q implementation of the differential detector has given good results for a channel with a frequency offset [9].

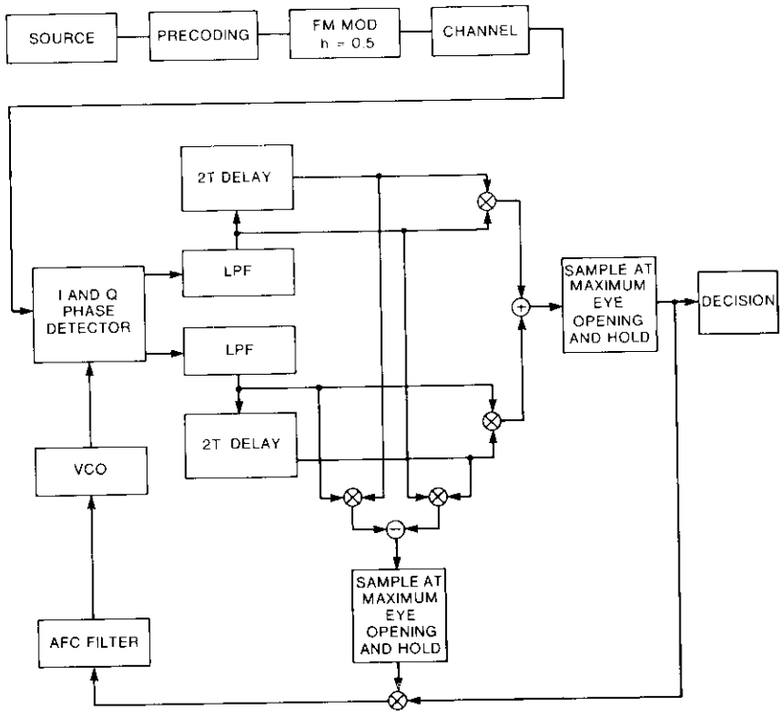

Figure 5. *MSK With 2-bit Differential Detection and FLL*

For $h = 0.5$, where h is the ratio of tone spacing to symbol rate, LD detection of binary FM has been shown analytically to be comparable in performance to 1-bit differential detection when both modulations use the same Gaussian IF filter and when an integrate-and-dump postdetection filter is used for LD detection [10] (Figure 6). The performance of LD detection can be improved by using $h > 0.5$. LD detection also is easily implemented. A significant aspect of LD detection for mobile radio applications is its relative insensitivity to frequency offset, since its primary degradation arises from offset of the signal spectrum within the IF filter.

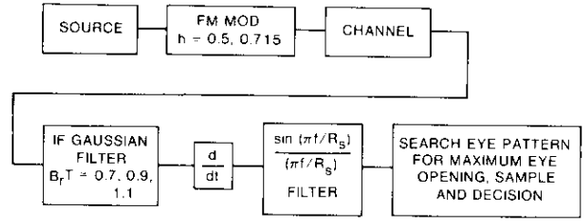

Figure 6. *Binary FM With LD Detection*

Four-level FM with $h = 0.25$ and binary FM with $h = 0.5$ have approximately the same power spectrum if the symbol rate is the same for both modulations. Since for the MSAT-X channel the symbol rate of four-level FM would be half that of binary FM, four-level FM may be better adapted to the tight bandwidth requirements of the MSAT-X channel. The suitability of four-level FM can be determined after simulation with different h values and IF filter bandwidths (Figure 7).

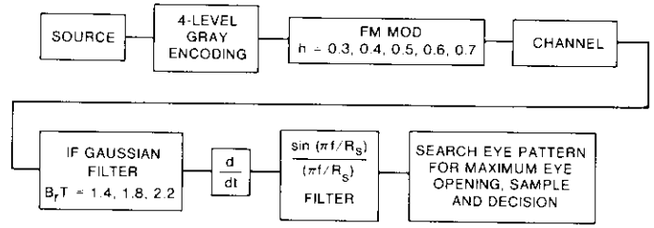

Figure 7. *Four-Level FM With LD Detection*

In noncoherent detection using $N = 3$ symbol intervals, two sets of four envelope correlations over $N = 3$ binary symbols are nonlinearly weighted in order to make a decision on the middle symbol [11] (Figure 8). Noncoherent detection uses phase trellis memory to make the detection decision, unlike the other modulations considered which employ differential phase comparisons.

Duobinary FM is generated by a partial-response baseband precoding at the transmitter, which results in a three-level baseband signal. Partial-response encoding is the same as a real-number convolutional code and can be efficiently removed by an MLSE after the LD. The MLSE is a two-state Viterbi decoder which is sufficient to remove the partial-response memory introduced by the duobinary coding. Because asymptotic performance of baseband duobinary signaling with maximum-likelihood decoding is the same as

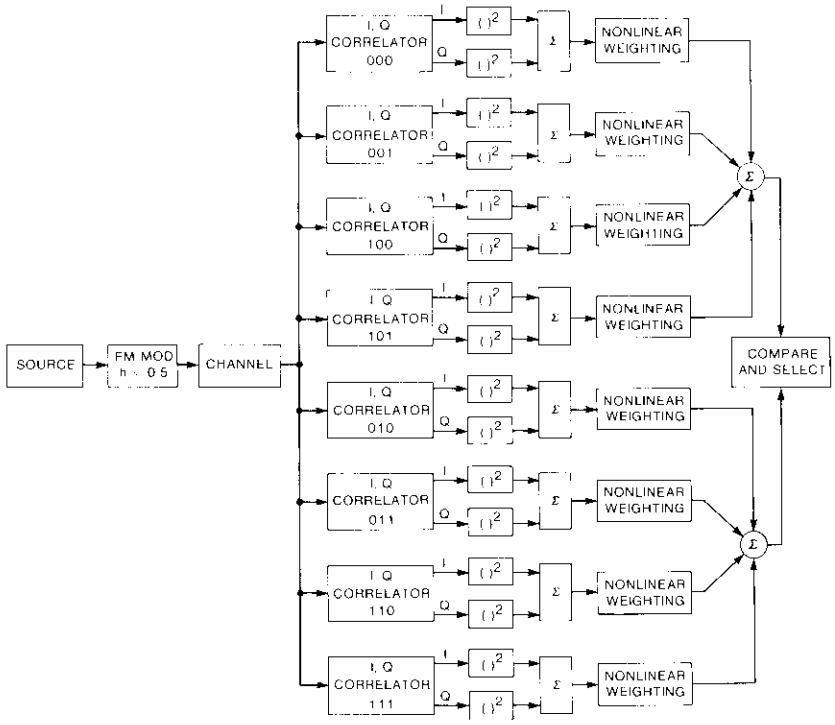

Figure 8. *Binary FM With Noncoherent Detection Over* N = *3 Channel Symbol Intervals*

baseband binary signaling [12], duobinary FM with LD detection and MLSE (Figure 9) might perform nearly as well as binary FM for large signal-to-noise ratios, while having a more compact RF spectrum.

Differential PSK (Figure 10) performs better than 1- or 2-bit differential MSK in the linear AWGN channel. However, when a nonlinear amplifier is used, power is lost because of the amplifier backoff required to limit spectral regrowth of the filtered differential PSK signal.

Simulation software

The simulation software used in this study employed basic components of the Channel Analysis and Modeling Program (CHAMP) [13], such as the filtering module, as well as new modules written to simulate the different modulations of interest and the Rice channel model. In CHAMP, the signal

$$\rho(t)e^{j\phi(t)}e^{j\omega_c t}$$

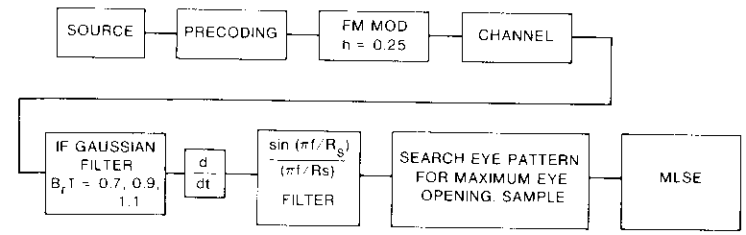

Figure 9. *Duobinary FM With LD and MLSE*

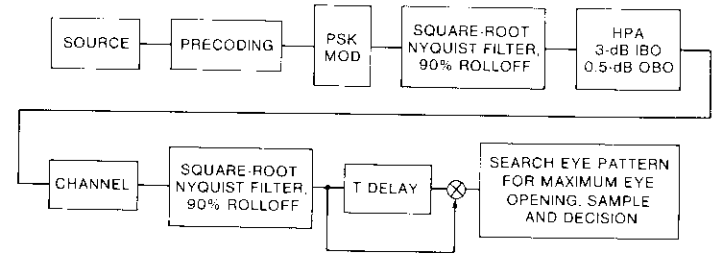

Figure 10. *Differential PSK*

is represented by a set of samples of the complex envelope

$$Re\left[\rho(t_m)e^{j\phi(t_m)}\right], \quad Im\left[\rho(t_m)e^{j\phi(t_m)}\right]$$

and an associated carrier frequency, ω_c. In simulating an AWGN channel, independent samples of a Gaussian random variable are added to the signal, based on a user-specified E_s/N_o where E_s is the energy per symbol and N_o is the one-sided noise spectral density. The peak signal power is estimated at the "calibrate" point shown in Figure 11, as

$$P = \frac{1}{n}\sum_{m=1}^{n}\left[Re\,\rho(t_m)e^{j\phi(t_m)}\right]^2 + \left[Im\,\rho(t_m)e^{j\phi(t_m)}\right]^2$$

and noise of variance σ^2 is added to both the in-phase and quadrature axes, with σ^2 adjusted so that

$$\frac{k \cdot P}{\sigma^2} = \frac{E_s}{N_o/2}$$

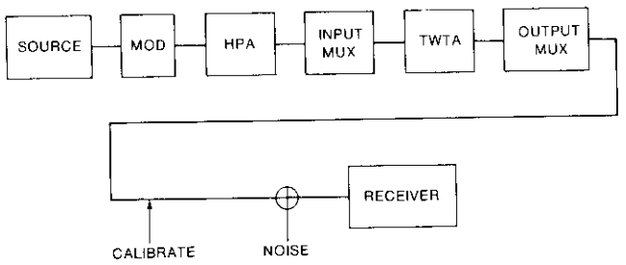

Figure 11. *Satellite Transmission Link With AWGN*

where k is the number of samples per symbol (typically 8 for binary modulations and 16 for quaternary modulations).

Using the channel model of Figure 11, the simulation program was run for values of E_s/N_o that correspond to E_b/N_o values of 6, 8, and 10 dB for each modulation. These three points allow an accurate determination of the power required to achieve a BER of 10^{-3}, the contrast-specified BER for voice transmission. Each simulation run consists of a preamble pseudonoise (PN) sequence, followed by a random data sequence. Noise (and possibly interference) is added to the random data sequence, and BER measurements are made.

The received noise-free preamble sequence is used to construct an eye diagram. The sampling time chosen is the sample point with the maximum eye opening. The decision level is taken to be the middle of the eye opening at the sampling time. For 2-bit differential detection, this decision level is nonzero. Because duobinary FM and quaternary modulations have multilevel eyes, the sampling point is the point at which the sum of the eye openings is greatest.

Performance comparison

A Gaussian IF filter was used for all modulations except noncoherent detection and differential PSK. Differential PSK used a square-root raised cosine Nyquist filter with 90-percent rolloff in order to limit ACI. MSK with 1- or 2-bit differential detection used a Gaussian IF filter of optimum bandwidth-time (BT) product, as determined by theory [8],[14],[15]. For binary FM, duobinary FM, and four-level FM, several different BT products were tried, and results are presented for the one BT value which gave the best performance for the first three channel models. For four-level FM, the deviation ratio, h, was jointly optimized with the BT product.

The performance of differential PSK was simulated for a 3-dB high-power amplifier (HPA) input backoff, or equivalently a 0.5-dB output backoff. As defined, the E_b/N_o used in simulation does not include the 0.5-dB output backoff. Therefore, when comparing the HPA power requirement of differential PSK with constant-envelope modulations, 0.5 dB should be added to the E_b/N_o requirement for differential PSK.

Additional simulation results were obtained with a Gaussian baseband filter inserted before the FM modulator for duobinary FM, noncoherent detection, LD detection, and GMSK; however, these results are not included because performance with ACI and frequency offset is worse than when no filter is used. In other words, the system is overdesigned for an assumed 10-dB adjacent channel fade if baseband Gaussian filtering is used.

Figure 12a shows the results for a single channel with no frequency offset. After allowing for the 0.5-dB HPA power loss of differential PSK, it can be seen that differential PSK, binary FM (with LD detection and $h = 0.715$), and binary FM (with noncoherent detection over $N = 3$ symbols) require similar HPA power at 10^{-3} BER and perform better than the other modulations. The good performance of noncoherent detection is expected because it involves averaging over three symbols. The curves for LD detection and noncoherent detection cross at low E_b/N_o, apparently because of an increase in the click rate for the FM modulation. This may be caused by truncation impulses which result from the relatively large deviation and narrow IF filter.

MSK with 2-bit differential detection performs next best, and shows approximately 0.5 dB of improvement over MSK with 1-bit differential detection, as predicted by theory [16]. MSK with 1-bit differential detection, and binary FM ($h = 0.5$) with LD detection, exhibit worse and almost identical performances as predicted by theory [10]. Four-level FM with LD detection performs almost as well as binary FM with LD detection.

Duobinary FM with LD and MLSE performs significantly worse than binary FM and LD detection. A possible explanation involves the importance of clicks in determining the error rate. The clicks give large noise hits, which make the observation sequence into the MLSE resemble the output of a binary symmetric (hard-decision) channel rather than an AWGN channel. For the hard-decision channel, the MLSE cannot be as effective in recovering performance lost by partial-response signaling. In addition, MLSE performance is degraded because noise at successive sampling times is correlated due to filtering and differentiation.

A frequency offset of 0.1 R_b has a marked effect on the relative ranking of the different modulations, as shown in Figure 12b. The degradation in performance of a given modulation is proportional to the length of the

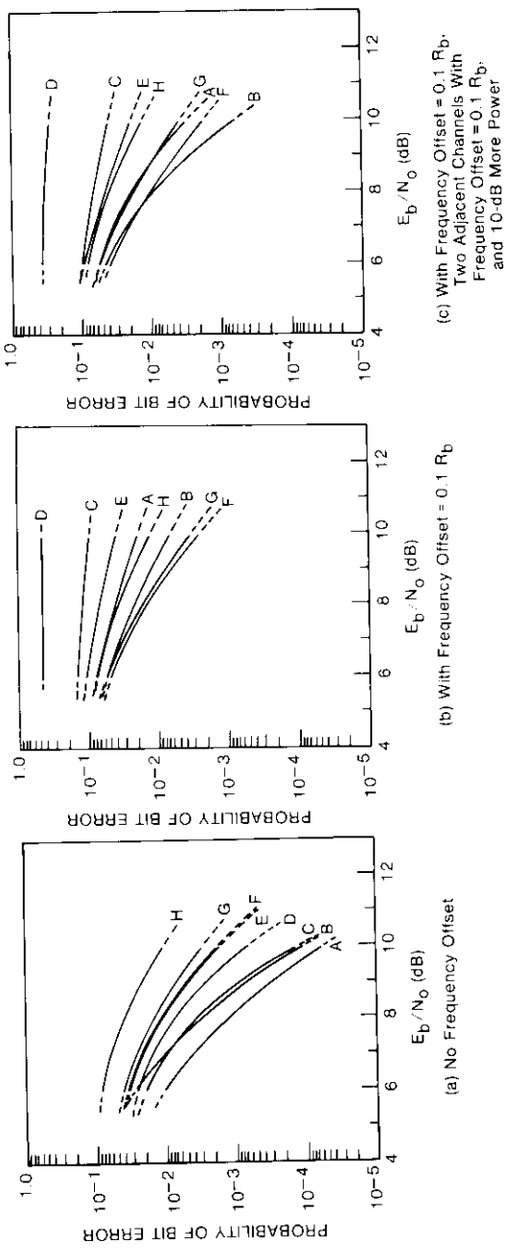

Figure 12. *Simulated Performance of Differential PSK For a Single Channel*

detection interval for that modulation, since the phase inaccuracy caused by frequency offset increases linearly with time. Thus, noncoherent detection over $N = 3$ symbols, which exhibited one of the best performances without frequency offset, now shows one of the worst performances. The degradation of MSK with 2-bit differential detection is much worse than that of MSK with 1-bit differential detection because phase is compared over a 2-bit interval rather than a 1-bit interval. In fact, for 2-bit differential detection to have an open eye at the sampling time, the receive filter BT had to be increased to 2, degrading performance significantly. Differential PSK shows almost a 3-dB degradation because of frequency offset. However, the performance of modulations using LD detection is changed very little because the main effect of frequency offset is a DC shift after the discriminator, which has little effect on the detection process. The net result is that the top three modulations employ the LD, after including the 0.5-dB power loss for differential PSK.

The results for the single channel with 10-dB fade and a frequency offset of 0.1 R_b, and for two adjacent channels with a frequency offset of 0.1 R_b, are shown in Figure 12c. The relative ranking is similar to that for the single channel with frequency offset. For the channel with interference, differential PSK is now worse than duobinary FM, so that the top four modulations all employ LD detection. The only other change in relative ranking is that binary FM with LD detection ($h = 0.715$) is moved from first to third place. Apparently, the relatively large deviation has caused the modulation to be sensitive to ACI. The performance of binary FM with $h = 0.5$ is changed only slightly when ACI is added.

JPL has implemented 2-bit differential detection of MSK with FLL to improve performance when the carrier frequency is offset [17]. A software version of this hardware was implemented, and software results agree closely with JPL hardware results for the AWGN channel and the Rice channel with and without frequency offset. The simulation results given in Figure 13 for the AWGN channel show that use of an FLL removes nearly all degradation caused by frequency offset.

Since the MSAT-X channel has a maximum fade rate of 200 Hz, and since the longest detection interval is three symbols, the channel is quasi-static over the longest detection interval. Therefore, a good approximation of performance in the Ricean channel can be obtained by averaging E_b/N_o for the AWGN channel over the first-order statistics of the Ricean density. In particular, this means that modulations will have the same relative ranking for the Ricean fading channel with frequency offset as for the AWGN channel with frequency offset, provided the BER curves do not cross for the AWGN channel. Therefore, since the two best modulations for the AWGN channel with frequency offset are binary FM with LD detection and MSK with FLL,

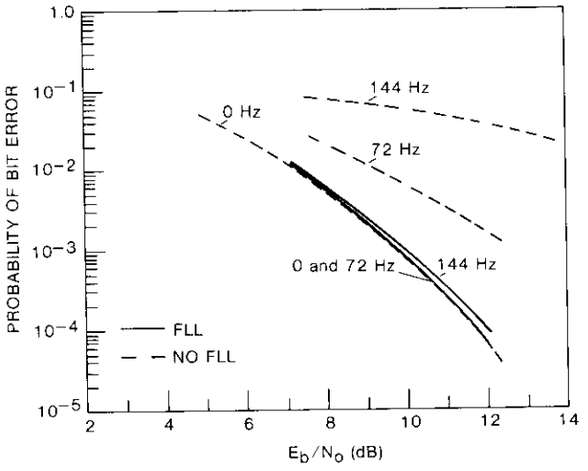

Figure 13. *Performance of Baseband Implementation of 2-bit Differential Detection of MSK* (B_rT = *0.9) With and Without FLL for AWGN Channel With Carrier Offset = 0, 72, and 144 Hz*

these modulations were selected for further study on the Ricean fading channel with and without frequency offset.

The performance of MSK with 2-bit differential detection and an FLL, and the performance of binary FM with LD detection, are compared in Figure 14 for the Rice channel with C/I = 10 dB and carrier offsets of 0, 72, and 144 Hz. The performance of MSK with FLL is slightly better at 10^{-2} BER, while binary FM with LD detection is slightly better around 10^{-3} BER. In addition, the apparent trend of the curves at 14-dB E_b/N_o indicates that binary FM with LD detection has a lower error floor than MSK with FLL. This trend is confirmed by previous experimental results [5]. It is also known that irreducible BER caused by Rayleigh noise is proportional to the length of the detection interval [17]. Because the detection interval of LD detection is half that of 2-bit differential detection, the LD error floor should be lower. The addition of Rayleigh noise to the AWGN channel causes a performance loss of 3 to 4 dB at a BER of 10^{-3} for the two modulations for C/I = 10 dB (compare Figures 12a, b, and c with Figure 14).

Binary FM with LD detection appears to be a better choice for the MSAT-X channel than MSK with 2-bit differential detection and FLL because of its slightly better performance in a Rice fading channel for 10^{-3} BER, its lower

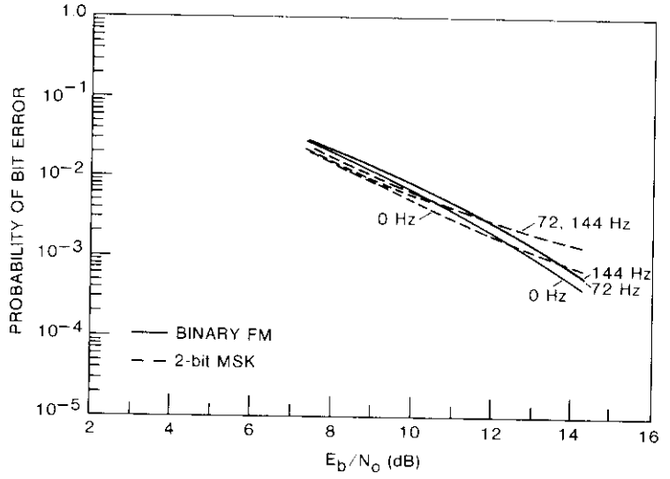

Figure 14. *Comparison of Binary FM, LD Detection,* h = *0.5, IF* B_rT = *1.1, and Baseband Implementation of 2-bit Differential Detection of MSK,* B_rT = *0.9, With FLL, for a Rice Channel With C/I = 10 dB and Carrier Offset = 0, 72, and 144 Hz*

error floor, and lower implementation complexity. In addition, binary FM with LD detection requires only symbol synchronization, while MSK with FLL requires frequency synchronization, which may be difficult to obtain in the short time allotted for the preamble.

Summary

The mobile satellite channel is subject to Doppler shift, Rayleigh noise, and ACI. Doppler shift significantly affects modulation performance because of the relatively large ratio of Doppler shift to symbol rate, and because of the use of an 800-MHz frequency band. Phase noise and fading effects result in performance degradation and a BER floor proportional to the length of the detection interval for differential and noncoherent modulations. Coherent modulations do not exhibit good performance because of the long averaging time required for the synchronizer. To limit interference to adjacent channels, a modulation with low out-of-band power and constant envelope is desirable, since constant-envelope modulations can be transmitted by saturated nonlinear amplifiers without spectral regrowth, thereby limiting interference to adjacent channels.

Simulation results have been presented which show that binary FM with LD detection exhibits better overall performance than seven other modulation types for a satellite channel degraded by Doppler shift, Rayleigh noise, and ACI. In addition, binary FM with LD detection requires only symbol synchronization (which allows the use of a short preamble) and is inexpensive to implement. For these reasons, binary FM with LD detection is suitable for use in the MSAT-X channel.

References

[1] D. J. Bell and S. A. Townes, "MSAT-X System Definition and Functional Requirements, Exhibit 1," Revision 2, prepared for NASA by JPL under contract, January 10, 1985.

[2] W. J. Vogel, "Land Mobile Satellite Transmission Measurements at 869 MHz," Electrical Engineering Research Laboratory, University of Texas at Austin, Contract Report submitted to JPL under Contract 956520, March 18, 1985.

[3] G. Pitt, III, and D. Divsalar, "Fading Channel Simulation," JPL Interoffice Memorandum MSAT-X: 331-85-180, February 6, 1985.

[4] V. K. Prabhu and J. Salz, "On the Performance of Phase-Shift-Keying Systems," *Bell System Technical Journal*, Vol. 60, No. 10, December 1981, pp. 2307–2343.

[5] K. Kinoshita *et al.*, "Evaluation of 16 kbit/s Digital Voice Transmission for Mobile Radio," *IEEE Transactions on Vehicular Technology*, Vol. VT-33, No. 4, November 1984, pp. 321–327.

[6] D. Daikoku *et al.*, "High-Speed Digital Transmission Experiments in 920 MHz Urban and Suburban Mobile Radio Channels," *IEEE Transactions on Vehicular Technology*, Vol. VT-31, No. 2, May 1982, pp. 70–75.

[7] K. Murota and K. Hirade, "GMSK Modulation for Digital Mobile Radio Telephony," *IEEE Transactions on Communications*, Vol. COM-29, No. 7, July 1981, pp. 1044–1050.

[8] M. K. Simon and C. C. Wang, "Differential Detection of Gaussian MSK in a Mobile Radio Environment," *IEEE Transactions on Vehicular Technology*, Vol. VT-33, No. 4, November 1984, pp. 307–320.

[9] F. Davarian *et al.*, Unpublished manuscript, JPL, 1985.

[10] M. K. Simon and C. C. Wang, "Differential Versus Limiter-Discriminator Detection of Narrow-Band FM," *IEEE Transactions on Communications*, Vol. COM-31, No. 11, November 1983, pp. 1227–1234.

[11] W. P. Osborne and M. B. Luntz, "Coherent and Noncoherent Detection of CPFSK," *IEEE Transactions on Communications*, Vol. COM-22, No. 8, August 1974, pp. 1023–1036.

[12] A. J. Viterbi and J. K. Omura, *Principles of Digital Communication and Coding*, New York: McGraw-Hill, 1979.

[13] A. Hamid, S. R. Baker, and W. Cook, "A Computer Program for Communications Channel Modeling and Simulation," *COMSAT Technical Review*, Vol. 13, No. 2, Fall 1983, pp. 355–383.

[14] H. Suzuki, "Optimum Gaussian Filter for Differential Detection of MSK," *IEEE Transactions on Communications*, Vol. COM-29, No. 6, June 1981, pp. 916–918.

[15] S. Ogose, "Optimum Gaussian Filter for MSK With 2-Bit Differential Detection," *Transactions of the IECE of Japan*, Vol. E-66, No. 7, July 1983, pp. 459–460.

[16] M. K. Simon and C. C. Wang, "Two Bit Differential Detection of MSK," IEEE Global Telecommunications Conference, Atlanta, Georgia, November 1984, *Digest*, pp. 740–745.

[17] W. C. Jakes, Jr., ed., *Micro Mobile Communications*, New York: Wiley, 1974, pp. 161–307.

Kenneth M. Mackenthun received a B.S.E.E. from George Washington University in 1974 and an M.S.E.E. and Ph.D. from the University of Illinois in 1976 and 1977, respectively. Since 1980, he has been in the Communications Research (formerly Communications Systems Studies) Department at COMSAT Laboratories. He is interested in modulation, synchronization, and coding for mobile terminals.

Index: filters, speech processing, adaptive filters, ADPCM

Hurwitz stability analysis of an ADPCM system

S. DIMOLITSAS AND U. BHASKAR

(Manuscript received November 24, 1986)

Abstract

The behavior of adaptive recursive filters in adaptive differential pulse-code modulation (ADPCM) applications is affected by the possibility of filter instability when the filter coefficients are adapted. Thus, in-parallel condition monitoring may be necessary to ensure that the system function poles remain bounded by the unit circle in the z-plane. These poles can be either directly monitored by reference to their z-plane geometry, or indirectly checked by satisfaction of some other condition. A method is described in which the modeled all-pole part of the decoder transfer function is approximated by a Chebychev polynomial, which in turn is decomposed into two suitably chosen functions that satisfy the Hurwitz polynomial stability constraints. The system poles can be indirectly but simply monitored and controlled so that the resulting system function remains stable.

Introduction

Adaptive recursive filters have been the object of intensive research in recent years [1]–[7], which has been motivated in applications such as adaptive differential pulse-code modulation (ADPCM) by the possible benefits of reduced complexity and improved performance, particularly when such a system is deployed in a communications network carrying nonsegregated voice and voiceband data traffic. In such cases, higher order ADPCM predictors can more accurately model (and thus represent the spectral characteristics of) voiceband data traffic, particularly at speeds of 4,800 bit/s and above.

While predictors with a higher number of poles or zeros can be relatively easily developed by including additional terms in the predictive model, monitoring the stability of such a system when the filter coefficients are adapted may be difficult. This can be demonstrated by the fact that when the 32-kbit/s ADPCM standard [8] was originally proposed it consisted of a six-zero/four-pole predictor model. However, when subsequent testing revealed that it was not possible to monitor the stability of the four-pole filter, a six-zero/two-pole model ultimately had to be adopted. Although methods have been developed for monitoring the stability (or equivalently the location of the roots) of an all-pole predictor, the feasibility of these methods for practical implementation has not been clearly shown due to the increased complexity required.

The techniques presently being studied include the lattice filter [9],[10], the adaptive recursive least mean square (RLMS) filter [2], and the hyperstable adaptive recursive family of filters [1],[5]–[7]. The stability of the lattice filter can easily be monitored by ensuring that all filter coefficients remain bounded by unity during coefficient adaptation. However, this filter involves a number of arithmetic divisions which, with today's very large-scale integration (VLSI) technology, substantially increase the total throughput filtering requirements. The adaptive RLMS filter, on the other hand, is easily implemented and adaptable, with an order of complexity equivalent to that of the stochastic gradient least mean square filter [2]. However, stability monitoring of this filter typically requires solving a nonlinear algebraic equation whose solution complexity rapidly increases with filter order. Thus, the adaptive RLMS filter has only been used in relatively low-order implementations [11] such as the CCITT G.721 algorithm [8].

The family of hyperstable filters (HARF [1], CHARF [5], and SHARF [7]) allows filter stability to be monitored by finding a polynomial which satisfies the "strictly positive real (SPR)" condition at all times. In addition to the difficulty of finding such a polynomial in the absence of specific knowledge about the source model, once found this polynomial must be updated when the source model varies with time. Consequently, the implementation feasibility of this approach has not been demonstrated.

This paper presents the mathematical formulation of an ADPCM Hurwitz-based adaptive predictor algorithm. Although results pertaining to the performance of this ADPCM system have been presented previously [12]–[19], this paper offers the first comprehensive review of its mathematical foundation.

Since with pole/zero predictors the zero part of the predictor can be assumed to be stable and independent of the stability of the pole part (other than possibly canceling individual poles), only the analysis pertaining to the all-pole predictor will be presented. Furthermore, since the focus will be on the stable adaptation of backward-type adaptive predictors (*i.e.*, encoder coefficients are not quantized or transmitted to the decoder [20]) and since the predictor reference signal is the same at both the encoder and decoder irrespective of the quantizer employed (in the absence of channel errors), quantizer modeling will not be explicitly considered. A nonadaptive, infinite-precision quantizer will thus be assumed.

First, background material will be provided on the Hurwitz and Chebychev polynomials on which this filter is based. The Hurwitz stable algorithm is then described in detail, and results are presented that indicate the stable behavior of the filter, as well as the improved performance obtained when this type of predictor is used with speech or voiceband data. From these results, it will subsequently be demonstrated that substantial performance improvement is possible when higher order stable predictors are used.

Hurwitz stability theorem for discrete systems

The Hurwitz stability approach yields a convenient method by which the stable behavior of the z-transform of an adaptive polynomial may be easily monitored, with minimal increase in complexity for higher order realizations. The Hurwitz stability criterion will only be stated here; refer to Schussler [21] for a complete proof.

Let $A(z)$ be a real polynomial of degree N given by

$$A(z) = \sum_{j=0}^{N} a_j z^j = a_N \prod_{j=1}^{N} (z - z_j) \quad . \tag{1}$$

Also let $A(z)$ be decomposed into mirror and antimirror image polynomials $F_1(z)$ and $F_2(z)$ such that

$$A(z) = F_1(z) + F_2(z) \tag{2}$$

where
$$F_1(z) = \sum_{j=0}^{N} f_{1j} z^j = f_{1N} \prod_{j=1}^{N} (z - z_{1j})$$
$$= 0.5\,[A(z) + z^N A(z^{-1})]$$
$$F_2(z) = \sum_{j=0}^{N} f_{2j} z^j = f_{2N} \prod_{j=1}^{N} (z - z_{2j})$$
$$= 0.5\,[A(z) - z^N A(z^{-1})] \quad .$$

The mirror and antimirror symmetry specifies the coefficients of $F_1(z)$ and $F_2(z)$ so that

$$f_{1j} = 0.5(a_j + a_{N-j}) \tag{3}$$

and

$$f_{2j} = 0.5(a_j - a_{N-j}) \quad . \tag{4}$$

For $A(z)$ to be a stable polynomial (or minimum phase) characterized by $|z_j| < 1$ for all $0 \leq j \leq N$, it is necessary and sufficient that the zeros (roots) of $F_1(z)$ and $F_2(z)$ be located on the unit circle; they are simple and alternate with each other. These conditions in turn imply that (see Figure 1)

$$|z_{1j}| = |z_{2j}| = 1 \quad ; \quad \text{for all } 0 \leq j \leq N \tag{5}$$

and

$$z_{1j} = z_{1k} \quad , \quad \text{iff } j = k \quad ; \quad z_{2m} = z_{2n} \quad , \quad \text{iff } m = n \tag{6}$$

and if $\arg(z_{1j}) < \arg(z_{2j})$, then

$$\arg(z_{2,j+1}) > \arg(z_{1,j+1}) > \arg(z_{2,j}) \tag{7}$$

where $\arg(z) = \arg(re^{jw}) = w$. These conditions are graphically depicted in Figure 1, which shows the location, on the z-plane, of the $F_1(z)$ polynomial and the antimirror $F_2(z)$ polynomial. The variables z_{1j} and z_{2j} denote the roots of the F_1 and F_2 polynomials, respectively. Note that the roots lie on the unit circle and interleave (separate) each other.

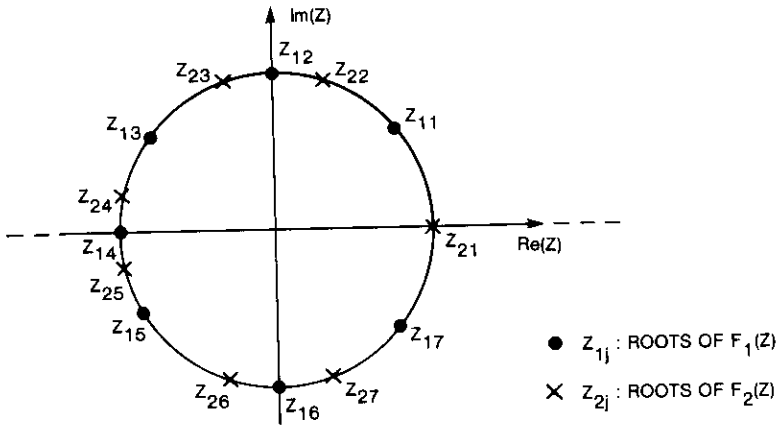

Figure 1. *Geometric Location of Roots of Mirror and Antimirror Polynomials*

This theorem is equivalent to the properties of the Hurwitz polynomial [22] where $F_1(z)$ and $F_2(z)$ correspond to the even and odd part of a Hurwitz function, respectively. To guarantee stability, a set of polynomials must be found that can represent the system function $A(z)$ so that the decomposition into $F_1(z)$ and $F_2(z)$ satisfies the above Hurwitz conditions. It will be shown that the Chebychev polynomials are a suitable set.

Chebychev polynomials

The Chebychev polynomials are a special case of the ultraspherical polynomials $P_N^a(x)$ defined by

$$P_N^a(x) = c_N(1 - x^{-2})^{-a} \frac{d^N}{dx^N}(1 - x^2)^{N-a} \tag{8}$$

where $-1 \leq a \leq \infty$.

It can be shown that $P_N^a(x)$ [23] has N distinct roots in the $[-1, 1]$ range of the x-axis and that the value of a determines the oscillatory behavior of this function in that range. In particular, if $a = -1/2$, the oscillatory behavior of $P_N^a(x)$ is equiripple. This case corresponds to the Chebychev function of order N, with $T_N(x)$ defined by

$$T_N(x) = c_N(1 - x^2)^{-1/2} \frac{d^N}{dx^N}(1 - x^2)^{N+1/2} \quad . \tag{9}$$

Another useful expression for developing an expansion of $T_N(x)$ as given by equation (9) can be derived when $x = \cos(w)$. Substituting this value of x into equation (9) yields

$$T_N(x) = T_N(\cos w) = \cos(Nw) \quad . \tag{10}$$

This expression allows the roots of $T_N(x)$ to be easily determined by evaluating $\cos(Nw_k) = 0$. Then w_k is given by

$$w_k = \frac{2k + 1}{2N}\pi \tag{11}$$

where $k = 0, 1, 2, 3, \ldots, N - 1$, and $T_N(x)$ can be written as a product of the simple factors

$$T_N(x) = \prod_{k=1}^{N} (x - \cos w_k) \tag{12}$$

with w_k given by equation (11).

Figure 2 is a schematic diagram of the real Chebychev functions of odd and even orders. In this figure, a_i represents the x-coordinate of the Chebychev function maxima and b_i represents the x-coordinate of the minima. Note that an expression similar to equation (12) can be derived if $T_N(x)$ is defined in the complex z-plane, according to the transformation $x = \cos w_i \rightarrow e^{jw} = z^{-1}$. In this case, since the coefficients of complex function $T_N(z)$ are real, its roots will be complex conjugate pairs. Thus, $T_N(z)$ can be written as

$$T_N(z) = \prod_{i=1}^{N/2} [z^{-1} - \exp(jw_i)]\,[z^{-1} - \exp(-jw_i)]$$

$$= \prod_{i=1}^{N/2} [z^{-2} - 2z^{-1}\cos(w_i) + 1] \qquad (13)$$

where $$w_i = \frac{2i+1}{2(N/2)}\pi; \quad i = 0, 1, 2, 3, \ldots, (N-1)/2 \quad .$$

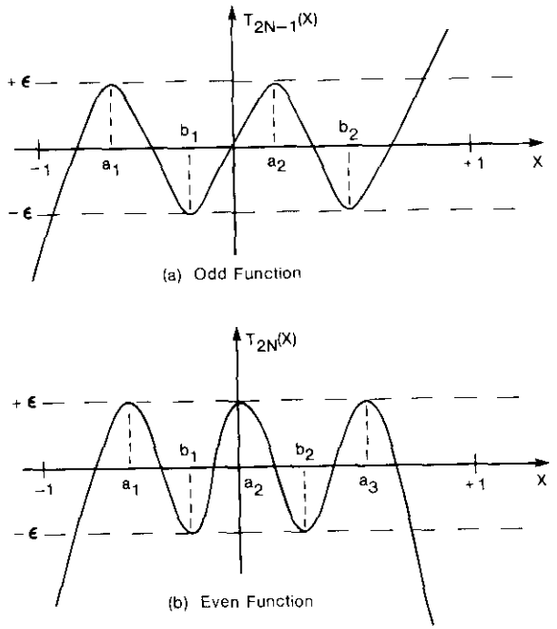

Figure 2. *Schematic Representation of Typical Antisymmetric (Odd) and Symmetric (Even) Chebychev Functions*

A system based on the Hurwitz stability conditions

Before considering the exact formulation of the Hurwitz-based ADPCM system, it is useful to briefly consider a general ADPCM coder, which is schematically illustrated in Figures 3 and 4. Figure 3 depicts the general ADPCM encoder consisting of two basic parts: an adaptive quantizer and an adaptive pole/zero predictor. The predictor estimates future values of the input digital waveform, $y(n)$, which are subsequently subtracted from the input waveform, resulting in a reduced variance signal, $d(n)$. This signal is then quantized by a quantizer whose step size can generally be adapted, depending on the variance of the output signal, $e(n)$. Signal $e(n)$ now represents differential values of the input signal $y(n)$ and is typically encoded at a substantially lower bit rate than the original waveform, before transmission to the decoder over a suitable digital channel.

The predictor will generally consist of two types of filters: an all-pole infinite impulse response (IIR) filter, and an all-zero finite impulse response

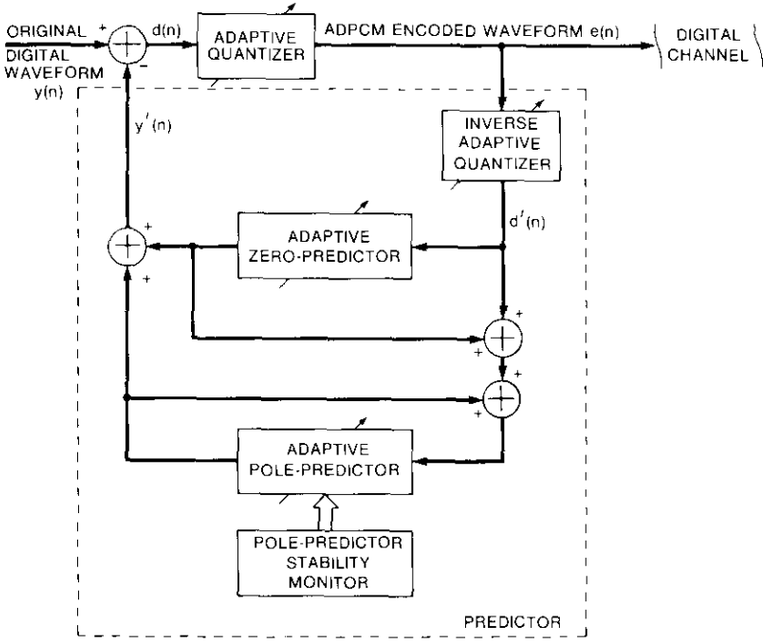

Figure 3. *ADPCM Encoder*

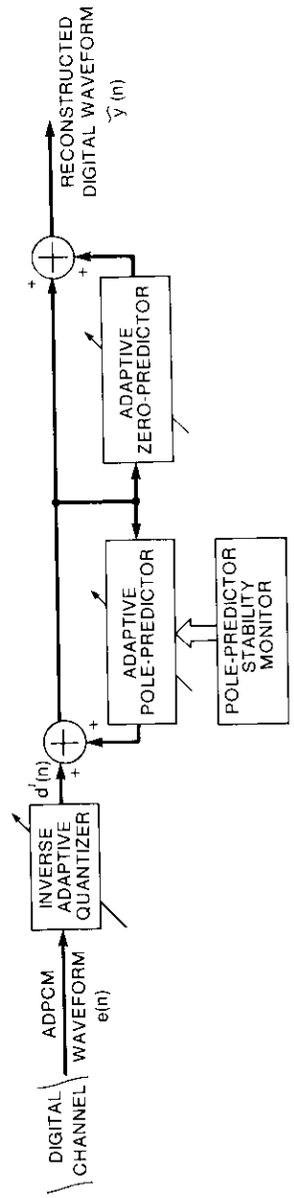

Figure 4. *ADPCM Decoder*

(FIR) filter. Because the IIR filter may be unstable when its coefficients are adapted to match the input signal statistics, it must be monitored during adaptation. The monitor is shown in Figure 3 as a separate block, which ensures that the coefficients of the all-pole filter do not lie outside a given stable range of values. Of interest here are the form and stability of this filter and the type of monitoring required. Neither the adaptive zero-predictor nor adaptive quantizer modeling are considered because these elements do not affect filter stability in general. Thus, Figure 3 can be simplified as shown in the top part of Figure 5, where the all pole-predictor is denoted by $A'(q^{-1})$ and the stability monitor is not shown. The notation q^{-1} denotes the unit delay operator [*i.e.*, $q^{-1}x(n) = x(n-1)$].

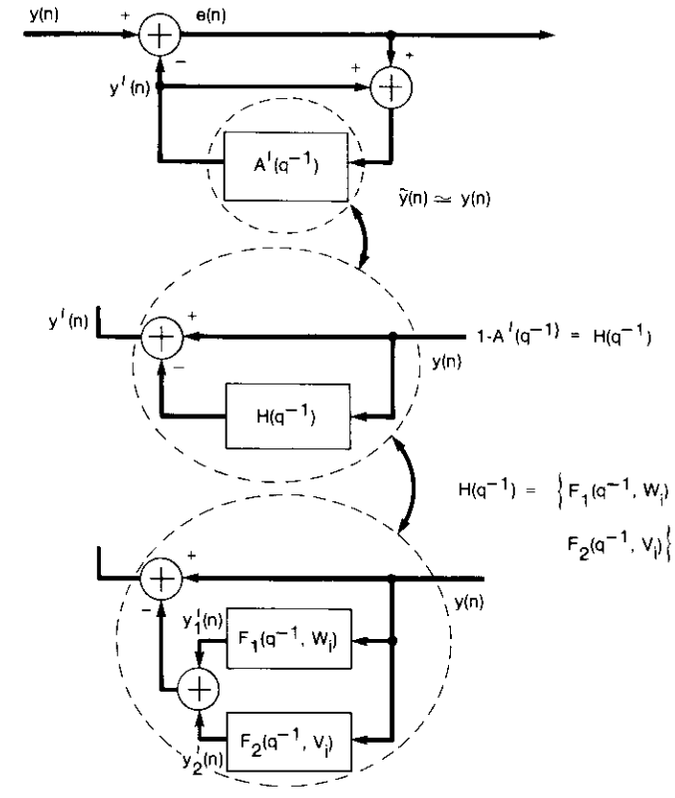

Figure 5. *Decomposition of an All-Pole ADPCM Predictor Into Mirror* (F_1) *and Antimirror* (F_2) *Functions*

The ADPCM decoder can be similarly analyzed, as shown in Figure 4. It consists of the inverse of the adaptive quantizer found in the encoder, as well as the adaptive predictor which must be identical to the one realized in the encoder in order to avoid mistracking. In this case, the decoder output $\tilde{y}(n)$ will be equal to the encoder input $y(n)$, plus some noise equal to $d'(n) - d(n)$ resulting from the quantization process. Again, neither the quantizer nor the all-zero predictor were considered. Thus, the ADPCM decoder shown in Figure 4 is equivalently reduced to the decoder shown in Figure 6.

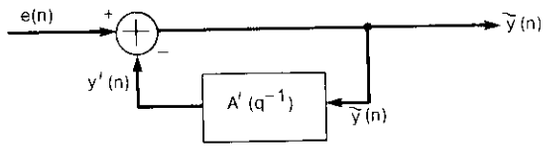

Figure 6. *ADPCM Decoder: Simplified Schematic Without Quantizer and All-Zero Predictor*

In regard to the all-pole predictor configuration, Figure 5 shows that the prediction error $e(n)$ at the encoder can be expressed as a function of the predictor input signal $\tilde{y}(n)$ as follows:

$$\begin{aligned} e(n) &= y(n) - y'(n) = y(n) - A'(q^{-1})\,\tilde{y}(n) \\ &= [1 - A'(q^{-1})]\,\tilde{y}(n) \quad . \end{aligned} \tag{14}$$

Since an infinitely fine quantizer was used, it is assumed that $y(n) = \tilde{y}(n)$. Similarly at the decoder (Figure 6), the reconstructed output $\tilde{y}(n)$ can be expressed as a function of the decoder input $e(n)$ as

$$\tilde{y}(n) = e(n)\,[1 - A'(q^{-1})]^{-1} = e(n)\,|H(q^{-1})|^{-1} \tag{15}$$

or in z-transform notation as

$$\tilde{Y}(z) = \frac{E(z)}{|1 - A'(z)|} = \frac{E(z)}{H(z)} \quad . \tag{16}$$

It is thus observed that, for bounded decoder inputs $e(n)$, the decoder-reconstructed output $\tilde{y}(n)$ will remain bounded if the roots of $[1 - A'(q^{-1})]$, or equivalently of $H(q^{-1})$, lie within the unit circle.

It can now be assumed that the estimated pole function $H(q^{-1})$ [equation (15)] can be represented by its N roots $z_1, z_2, z_3, \ldots, z_N$ as

$$H(z) = \prod_{i=1}^{N} (z^{-1} - z_i)$$

where $H(z)$ is the z-transform of the impulse response corresponding to polynomial $H(q^{-1})$. If it is also assumed that the transfer function $H(z)$ has real coefficients, then the roots of $H(z)$ will form complex conjugate pairs so that the above equation can be written as

$$\begin{aligned} H(z) &= \prod_{i=1}^{N/2} (z^{-1} - z_i)\,(z^{-1} - z_i^*) \\ &= \prod_{i=1}^{N/2} [z^{-2} - 2\,z^{-1} r_i \cos(t_i) + r_i^2] \end{aligned} \tag{17}$$

where $z_i = r_i \exp(jt_i)$ and $z_i^* = r_i \exp(-jt_i)$.

The Nth order Chebychev function $T^N(x)$ can now be considered. Since this is an equiripple function (Figure 2),

$$T^N(x) + \varepsilon = \prod_{i=1}^{N} (x - a_i) \tag{18}$$

and

$$T^N(x) - \varepsilon = \prod_{i=1}^{N} (x - b_i) \tag{19}$$

where a_i and b_i denote the x-coordinate of the Chebychev function maxima and minima, respectively.

When the x-axis is mapped onto the unit semicircle as before [equation (13)], equations (18) and (19) become

$$T^N(z) + \varepsilon = \prod_{i=1}^{N/2} (z^{-1} - e^{jw_i})\,(z^{-1} - e^{-jw_i}) \tag{20}$$

and

$$T^N(z) - \varepsilon = \prod_{i=1}^{N/2} (z^{-1} - e^{jv_i})\,(z^{-1} - e^{-jv_i}) \quad . \tag{21}$$

It is now possible to approximate the roots of $H(z)$ by the location of the roots of equations (20) and (21) so that

$$H(z) = \left[(z^{-1} - 1) \prod_{i=1}^{N/2} (z^{-1} - e^{jw_i})(z^{-1} - e^{-jw_i}) + (z^{-1} + 1) \prod_{i=1}^{N/2} (z^{-1} - e^{jv_i})(z^{-1} - e^{-jv_i}) \right] \quad (22a)$$

$$= [F_1(z) + F_2(z)] \quad . \quad (22b)$$

The transfer function $H(z)$ is now represented by a Chebychev function with two additional roots at $z^{-1} = \pm 1$, where the Hurwitz functions $F_1(z)$ and $F_2(z)$ are given by

$$F_1(z) = (z^{-1} - 1) \prod_{i=1}^{N/2} (z^{-1} - e^{jw_i})(z^{-1} - e^{-jw_i}) \quad (23)$$

and

$$F_2(z) = (z^{-1} + 1) \prod_{i=1}^{N/2} (z^{-1} - e^{jv_i})(z^{-1} - e^{-jv_i}) \quad . \quad (24)$$

Thus, the roots of $H(z)$ lie on the unit circle (by virtue of the Chebychev function real x-axis to the z-plane semicircle mapping), they alternate (since the location of a function minimum is separated by the function maxima), and are distinct. With the introduction of the two additional roots at $z^{-1} = 1$ and $z^{-1} = -1$, all of the Hurwitz stability criteria [equations (5), (6), and (7)] are met. Consequently, using equations (22a) and (17), $H(z)$ can be written as

$$H(z) = \left[(z^{-1} - 1) \prod_{i=1}^{N/2} (z^{-2} - 2z^{-1} \cos w_i + 1) + (z^{-1} + 1) \prod_{i=1}^{N/2} (z^{-2} - 2z^{-1} \cos v_i + 1) \right] \quad (25a)$$

$$= \prod_{i=1}^{N/2} (z^{-2} - 2z^{-1} r_i \cos t_i + r_i^2) \quad . \quad (25b)$$

Note that $H(z)$ will remain stable [*i.e.*, $r_i < 1$; equation (25b)] as long as $F_1(z)$and $F_2(z)$ are defined by equations (23) and (24). These conditions will not necessarily hold when $F_1(z)$ and $F_2(z)$ are adapted (by adapting the coefficients w_i and v_i), unless the Hurwitz stability criterion is maintained; coefficients w_i and v_i alternate and are distinct. In this case, no check is required for the unit circle location of the magnitude of the roots of F_1 and F_2, since only angles w_i and v_i are actually updated. The method for adapting these angles is discussed in the next section.

It should be noted that the root w_i and v_i alternating condition is very easily monitored because w_i and v_i can typically be stored sequentially, in a practical implementation, and the positiveness of the difference $(w_i - v_i)$ for $i = 0, 1, 2, \ldots, (N/2) - 1$ can easily be verified. In fact, the throughput loading for this in-line check linearly increases with the filter order. This type of system function decomposition belongs to a class of function representations that employ Chebychev-based functions to decompose the system transfer function $H(z)$ into the $F_1(z)$ and $F_2(z)$ Hurwitz polynomials. In the approach described here, a single Chebychev function is used to represent $H(z)$.

Parameter adaptation

To complete the definition of the adaptive IIR algorithm, it is next necessary to obtain an explicit relation for the adaptation of coefficients w_i and v_i [equations (23) and (24)] based on some performance criterion such as the minimization of the mean square prediction error $e(n)$ (Figures 5 and 6).

The ADPCM encoder (Figure 5) will be considered and the coefficient update expressions derived so that the decoder is stable, or equivalently so that the encoder remains minimum phase, in which case the encoder roots or the roots of $H(z)$ are bounded by the unit circle.

Consider the transfer function of the encoder of Figure 5 [assuming that $\tilde{y}(n) = y(n)$], which is given by equation (16) as

$$\frac{E(z)}{Y(z)} = [1 - A'(z)] \quad .$$

If $H(z) = 1 - A'(z)$, then $E(z)/Y(z)$ will be minimum phase (and consequently the decoder will be stable) when the roots of $H(z)$ lie within the unit circle. $H(z)$ can then be expressed according to equation (25a) or (25b), and its coefficients w_i and v_i can be adapted so that the Hurwitz stability is maintained. This can be accomplished by employing a gradient search algorithm technique so that

$$w_i(n+1) = w_i(n) - (K/2)\frac{\partial}{\partial w_i}[\langle e^2(n)\rangle]$$

and

$$v_i(n+1) = v_i(n) - (K/2)\frac{\partial}{\partial v_i}[\langle e^2(n)\rangle] \quad .$$

Substituting the stochastic estimate to the derivative in the above equations yields

$$w_i(n+1) = w_i(n) - Ke(n)\frac{\partial e(n)}{\partial w_i} \tag{26}$$

and

$$v_i(n+1) = v_i(n) - Ke(n)\frac{\partial e(n)}{\partial v_i} \tag{27}$$

where $w_i(n)$ and $v_i(n)$ are the two parameter vectors at time n, and K is a suitably chosen adaptation constant. To evaluate $e(n)$, it is convenient to employ a z-plane analysis because the Hurwitz stability has also been expressed on the same plane. Referring to Figure 5, it can be seen that $e(n) = y(n) - y'(n)$, and since the process to be predicted, $y(n)$, is independent of w_i and v_i

$$-\frac{\partial e(n)}{\partial w_i} = \frac{\partial y'(n)}{\partial w_i} \tag{28}$$

and

$$-\frac{\partial e(n)}{\partial v_i} = \frac{\partial y'(n)}{\partial v_i} \quad . \tag{29}$$

The derivation of equation (28) can now be considered, with equation (29) being similarly derived. Written in operator notation by reference to Figures 3 and 4,

$$y'(n) = H(q^{-1})\,\tilde{y}(n) \quad . \tag{30}$$

If it is assumed that the quantization noise is zero, then $\tilde{y}(n) = y(n)$ and equation (30) becomes

$$y'(n) = H(q^{-1})\,y(n) \tag{31}$$

which in z-transform notation can be written as

$$Y'(z) = H(z)\cdot Y(z) \quad . \tag{32}$$

Using equation (28),

$$\frac{\partial e(n)}{\partial w_i} = -\frac{\partial y'(n)}{\partial w_i} = -\frac{1}{2\pi j}\oint z^{n-1}\left[\frac{\partial}{\partial w_i}H(z)\,Y(z)\right]dz \tag{33}$$

where the right-hand side of equation (33) represents the inverse z-transform of the derivative of the bracketed term. However, since $Y(z)$ is not a function of w_i, equation (33) can be written as

$$\frac{\partial e(n)}{\partial w_i} = -\frac{1}{2\pi j}\oint z^{n-1}\,Y(z)\cdot\frac{\partial H(z)}{\partial w_i}\,dz \tag{34}$$

and from equations (22a) and (22b),

$$\frac{\partial e(n)}{\partial w_i} = -\frac{1}{2\pi j}\oint z^{n-1}\,Y(z)\cdot\frac{\partial F_1(z,w_i)}{\partial w_i}\,dz \tag{35}$$

since $F_2(z,v_i)$ is not a function of w_i. But

$$\begin{aligned}\frac{\partial}{\partial w_i}F_1(z,w_i) &= \frac{\partial}{\partial w_i}\left\{\prod_{i=0}^{N/2}|z^{-2} - 2z^{-1}\cos w_i + 1|\right\}\\ &= \frac{\partial}{\partial w_i}\left\{\prod_{\substack{j=0\\ j\neq i}}^{N/2}|z^{-2} - 2z^{-1}\cos w_j + 1|\right.\\ &\qquad \left.\cdot\,|z^{-2} - 2z^{-1}\cos w_i + 1|\right\}\\ &= 2z^{-1}\sin w_i\prod_{\substack{j=0\\ j\neq i}}^{N/2}|z^{-2} - 2z^{-1}\cos w_j + 1|\\ &= \frac{2z^{-1}\sin w_i}{(z^{-2} - 2z^{-1}\cos w_i + 1)}F_1(z,w_i) \quad .\end{aligned} \tag{36}$$

Thus, from equations (35) and (36)

$$\frac{\partial e(n)}{\partial w_i} = -\frac{1}{2\pi j}\oint z^{n-1}\left[\frac{2z^{-1}\sin w_i}{(z^{-2}-2z^{-1}\cos w_i+1)}\cdot F_1(z,w_i)\,Y(z)\right]dz \quad . \tag{37}$$

Note, however, that $Y(z)F_1(z,w_i) = Y_1'(z)$ has already been computed during the filtering process (Figure 5) as a result of the $H(z)$ decomposition into $F_1(z)$ and $F_2(z)$. Thus, equation (37) can now be written in terms of the already computed signal $y_1(n)$ as

$$\frac{\partial e(n)}{\partial w_i} = y_1(n) * \frac{-1}{2\pi j}\oint z^{n-1}\left[\frac{2z^{-1}\sin w_i}{(z^{-2}-2z^{-1}\cos w_i+1)}\right]dz \tag{38}$$

where * denotes the convolution operator. This can be expressed in delay operator notation as

$$\frac{\partial e(n)}{\partial w_i} = -\left[\frac{2q^{-1}\cdot\sin w_i}{(q^{-2}-2q^{-1}\cos w_i+1)}\right]y_1'(n) \quad . \tag{39}$$

Thus, the coefficient updating equation for w_i becomes

$$w_i(n+1) = w_i(n) + K\cdot e(n)\left[\frac{2q^{-1}\sin w_i}{(q^{-2}-2q^{-1}\cos w_i+1)}y_1'(n)\right] \tag{40}$$

and similarly for $v_i(n)$

$$v_i(n+1) = v_i(n) + K\cdot e(n)\left[\frac{2q^{-1}\sin w_i}{(q^{-2}-2q^{-1}\cos w_i+1)}y_2'(n)\right] \quad . \tag{41}$$

The physical significance of w_i and v_i during adaptation can be more clearly understood by referring to Figure 7, in which p_i is the actual modeled pole approximated by w_i and v_i. The Hurwitz stability separation criterion ensures that all poles are modeled by w_i on the left (or right) side and by v_i on the right (or left) side at all times. During adaptation, the w_i and v_i coefficients move closer to p_i, and hence toward each other. In this respect, the Hurwitz stability/separation conditions ensure that these w_i, v_i poles fall on the same side of the approximated poles, and thus there is no crossover between w_i and v_i during adaptation.

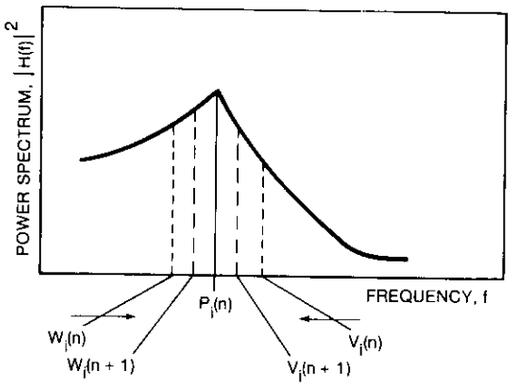

Figure 7. *Physical Significance of the Transfer Function Coefficients During Adaptation*

Experimental results

The algorithm described above has been integrated in an ADPCM coder operating at 40, 32, and 24 kbit/s [16]. In these implementations [13],[16], a 10th-order adaptive all-zero filter was realized using a sign least mean squares transversal filter. The all-pole part of the predictor was implemented using a 16th-order fixed-pole filter and a 4th-order adaptive Hurwitz-based pole filter.

Tests were conducted at COMSAT Laboratories [17] which compared such an ADPCM codec with a G.721 type of codec, both employing a 5-bit adaptive quantizer. These tests objectively measured codec performance with analog signals and voiceband data at high bit rates (9,600 and 14,400 bit/s). All of the tests were performed within the COMSAT Laboratories voiceband test facility [24] and included analog R-28 impairments [25]. Table 1 summarizes some of these measurements.

The test results show that consistently better performance was obtained with the Hurwitz-based ADPCM coder than with the G.721-based coder. With respect to modem block error rate (MBLER) measurement as a function of line signal-to-noise ratio (S/N), this difference in performance can be attributed to the implementation of higher order predictors, which is made possible by the relative ease of stability monitoring of the Hurwitz-based filter. With respect to MBLER measurements as a function of line error rate (LER), it is believed that the superior performance of the Hurwitz-based filter can be attributed to other properties of this ADPCM coder, such as the adaptive predictor gain coefficients [26].

TABLE 1. OBJECTIVE VOICEBAND DATA PERFORMANCE OF TWO CODECS*

CONDITION/CODER	HURWITZ-BASED ADPCM CODER (40 kbit/s)	G.721-BASED ADPCM CODER (40 kbit/s)
Typical V.29 Modem at 9,600 bit/s		
MBLER at S/N = 24 dBp for One Link	$(1.8 \pm 0.5) \times 10^{-1}$	$(4.8 \pm 0.8) \times 10^{-3}$
MBLER at S/N = 24 dBp for Two Asynchronous Links	$(3.9 \pm 0.9) \times 10^{-1}$	$(1.6 \pm 0.3) \times 10^{-2}$
MBLER at LER = 10^{-5} for One Link	$(8.5 \pm 1.0) \times 10^{-4}$	$(1.0 \pm 0.1) \times 10^{-2}$
Typical V.32 Modem at 9,600 bit/s		
MBLER at S/N = 21 dBp for Three Asynchronous Links	$(8 \pm 1.2) \times 10^{-5}$	$(5 \pm 1) \times 10^{-4}$
MBLER at LER = 10^{-5} for One Link	$(6.4 \pm 1.5) \times 10^{-3}$	$(8.8 \pm 1.5) \times 10^{-3}$
Typical V.33 Modem at 14,400 bit/s		
MBLER at S/N = 30.5 dBp for Two Asynchronous Links	$(5 \pm 1) \times 10^{-4}$	$(2.4 \pm 0.3) \times 10^{-2}$

* MBLER = 511 bits/block.
Figures are based on 100 errored block events, or 100,000 s of elapsed measurement time (whichever occurred first).
Confidence intervals are based on $\pm 2.\sigma$.

A series of extensive subjective evaluation tests was conducted by Bell Communications Research (U.S.) [19], and Kokusai Denshin Denwa Company, Ltd. (Japan) [18] to assess the speech quality of such ADPCM coders for the English and Japanese languages, respectively. In these tests, a 32-kbit/s Hurwitz-type algorithm was used and compared to G.721, also at 32 kbit/s. From an analysis of the results it was concluded that the Hurwitz-based algorithm gave slightly better performance than G.721 in more cases than the reverse, but the differences were within the bounds of experimental error and were not thought to be statistically significant.

Conclusions

An adaptive IIR algorithm based on the Hurwitz stability criterion has been presented that allows the stability monitoring of a pole/zero ADPCM predictor configuration. Because the algorithm is capable of easily modeling higher order processes, it would be particularly applicable in predictive encoding of processes generated by higher order source models, such as voiceband data.

Acknowledgments

The authors would like to express their gratitude to H. Suyderhoud and M. Onufry for their reviews, contributions, and encouragement in completing this work, and to F. Corcoran for providing the experimental results on voiceband data performance.

References

[1] C. R. Johnson, Jr., "Adaptive IIR Filtering: Current Results and Open Issues," *IEEE Transactions on Information Theory*, Vol. IT-30, No. 2, March 1984, pp. 237–250.

[2] S. Horvath, Jr., "A New Adaptive Recursive LMS Filter," *Digital Signal Processing*, E. V. Cappellini and A. G. Constadinides, eds., New York: Academic Press, 1980, pp. 21–26.

[3] L. Ljung, "Analysis of Recursive Stochastic Algorithms," *IEEE Transactions on Automatic Control*, Vol. AC-22, No. 4, August 1977, pp. 551–575.

[4] B. Friedlander, "System Identification Techniques for Adaptive Signal Processing," *IEEE Transactions on Acoustics, Speech, and Signal Processing*, Vol. ASSP-30, No. 2, April 1972, pp. 240–246.

[5] C. R. Johnson, Jr., "CHARF Convergence Studies," 13th Asilomar Conference on Circuits, Systems, and Computers, Pacific Grove, California, November 1979, *Proc.*, pp. 403–407.

[6] C. R. Johnson, Jr., "A Convergence Proof for a Hyperstable Adaptive Recursive Filter," *IEEE Transaction on Information Theory*, Vol. IT-25, No. 6, November 1979, pp. 745–749.

[7] M. G. Larimore, J. R. Treichler, and C. R. Johnson, Jr., "SHARF: An Algorithm for Adapting IIR Digital Filters," *IEEE Transactions on Acoustics, Speech, and Signal Processing*, Vol. ASSP-28, No. 4, August 1980, pp. 428–440.

[8] CCITT, "32 kbit/s Adaptive Differential Pulse Code Modulation (ADPCM)," Recommendation G.721, Fascicle III.3, Malaga-Torremolinos, 1984.

[9] M. L. Honig, *Adaptive Filters-Structures, Algorithms and Applications*, The Netherlands: Kluwer Academic, 1984.

[10] B. Friedlander, "Lattice Filters for Adaptive Processing," *Proc. IEEE*, Vol. 70, No. 8, August 1982, pp. 829–867.

[11] D. Millar and P. Mermelstein, "Prevention of Mistracking in ADPCM Coders," International Conference on Communications, Amsterdam, The Netherlands, May 1984, *Proc.*, Vol. 3, pp. 1508–1512.

[12] K. Hosoda *et al.*, "A New Adaptive Digital Echo Canceller," 35th IEEE Vehicular Technology Conference, May 1985, Boulder, Colorado, *Proc.*, pp. 310–313.

[13] A. Fukasawa *et al.*, "Analysis and Performance of a New Iteratively Controlled Digital Prediction Filter," *Proc. ICC*, May 1984, pp. 1500–1503.

[14] K. Hosoda and A. Fukasawa, "32 kbps ADPCM Codec Composed by the Prediction Filter Including Poles and Zeros," European Signal Processing Conference, Erlangen, W. Germany, September 1983, *Proc.*, pp. 391–394.

[15] A. Fukasawa *et al.*, "An Advanced 32 kbit/s ADPCM Coding to Transmit Speech and High Speed Voiceband Data," IEEE International Conference on Acoustics, Speech, and Signal Processing, Tokyo, Japan, April 1986, *Proc.*, pp. 821–824.

[16] CCITT, "High-Level Description of Advanced 32 kbit/s ADPCM," Q25/XVIII Ad Hoc Group, Contribution No. 27, September 1986.

[17] CCITT, "Testing/Phase I: Results of an Objective Performance Evaluation of ADPCM Coders for DCME Voiceband Data Transparency," Q25/XVIII Ad Hoc Group, Contribution No. 74, January 1987.

[18] CCITT, "Comparative Study of Subjective Quality of Advanced 32 kbit/s ADPCM for Japanese Speech," Q25/XVIII Ad Hoc Group, Contribution No. 64, January 1987.

[19] CCITT, "Subjective Evaluation of Speech Quality for G.721 and KDD/OKI Advanced 32 kbit/s ADPCM Coders," Q25/XVIII Ad Hoc Group, Contribution No. 57, January 1987.

[20] N. S. Jayant and P. Noll, *Digital Coding of Waveforms*, Chapter 6, Englewood Cliffs, New Jersey: Prentice Hall, 1984.

[21] H. W. Schussler, "A Stability Theorem for Discrete Systems," *IEEE Transactions on Acoustics, Speech, and Signal Processing*, Vol. ASSP-24, No. 1, February 1976, pp. 87–89.

[22] E. A. Guillemin, *The Mathematics of Circuit Analysis*, New York: Wiley-Interscience, 1962.

[23] M. A. Snyder, *Chebychev Methods in Numerical Approximation*, New York: Prentice Hall, 1966.

[24] CCITT, "The COMSAT Laboratories Data Modem/Voice Codec Test (DMVCT) Facility for DCME 32 kbit/s ADPCM Codecs," Q25/XVIII Ad Hoc Group, Contribution No. 18, September 1986.

[25] CCITT, "Report of the Meeting of Working Party XVIII/2 (Speech Processing)," COM XVIII R-28, Geneva, December 1983.

[26] S. Dimolitsas, "A Comparison of the Channel Noise Immunity Between the CCITT G.721 and the OKI 32 kbit/s ADPCM Codecs During Voice Band Data Transmission," *COMSAT Data Catalog*, Update 10, December 1986, Accession No. 86DC056.

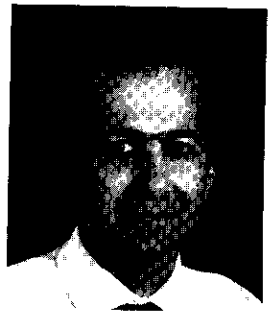

Spiros Dimolitsas received a B.Sc. (with Honors) in physics and mathematics from Sussex University, Great Britain, in 1977; an M.Sc. and Dipl. Eng. Q.M.C. in nuclear reactor engineering from London University in 1979; and a D.Phil. in computer engineering and digital signal processing from Sussex University in 1982. From 1982 to 1983, he worked for High Energy and Nuclear Equipment S. A. in Geneva, Switzerland, and later for the Mayo Clinic and for MOSTEK Corporation, where he was involved in digital image processing (CT) and modem design (V.32), respectively. He joined COMSAT Laboratories in 1986 and has been involved in studies of linear and nonlinear voice processing systems, with special emphasis on adaptive IIR filters, coder stability, and noise cancellation techniques. He is presently a Member of the Technical Staff in the Communications Techniques Division. Recently, he has been COMSAT's representative to the CCITT experts' group on ADPCM voiceband data transparency for digital circuit multiplication equipment. Dr. Dimolitsas is a member of the IEEE Communications Society; the IEEE Acoustics, Speech, and Signal Processing Society; the European Association for Signal Processing (EURASIP); and the technical committee of the ASME Society on Active Noise Control.

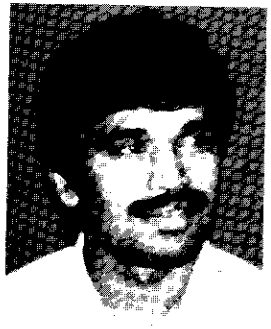

Udaya Bhaskar received a Ph.D. in electrical engineering from Rensselaer Polytechnic Institute in 1985. Since then, he has been a Member of the Technical Staff in the Communications Techniques Division at COMSAT Laboratories working on the development of low- and medium-bit-rate speech coding techniques. He is a member of IEEE.

Index: digital transmission, filters, modulation, demodulation, modems

Pole-zero approximations for the raised cosine filter family

J. J. POKLEMBA

(Manuscript received October 7, 1986)

Abstract

Normalized pole and zero locations that approximate the full and square-root raised cosine families of frequency responses are presented. The normalized roots are particularly useful in modem designs that realize Nyquist data shaping with analog filter implementations. However, they could also be used with an infinite impulse response digital design.

Pole and zero values are tabulated in 10-percent rolloff rate increments from 10 through 100 percent for the full cosine, and 20 through 100 percent for the square-root cosine. The pole and zero locations are arrived at through separate computer optimization of the magnitude and group delay responses. The resulting approximation families exhibit negligible intersymbol interference and greater than 40 dB of stopband rejection. The typical degradation in computer-simulated bit error rate is on the order of 0.02 dB.

Introduction

This paper develops approximations for the raised cosine filter family that can be used to band-limit digital data transmission without producing intersymbol interference (ISI). The filters are specified in terms of poles and zeros that are normalized to a 1-Hz low-pass bandwidth. In the background section, the need to precisely regulate the spectral shape when band-limiting digital data is discussed. Moreover, Nyquist has defined the required spectral characteristics in a very general way, such that numerous families of functions

satisfy the band-limiting constraint and exhibit no ISI at the detection sampling instants [1]. A widely used subset of these Nyquist functions is the raised cosine family, which is specified in terms of its rolloff factor.

In a strict sense, Nyquist spectral shapes are not physically realizable. The particular features of the raised cosine that render it unrealizable are its perfectly flat passband and its infinite attenuation stopband. These two requirements led to the establishment of error ripple constraints as guidelines in approximating the raised cosine magnitude sections. The specific guidelines selected were 0.5-percent root mean square (rms) passband ripple and $\geq$40 dB of stopband attenuation. Group delay equalization was effected by cascading first- and second-order compensation sections until the degradation in computer-simulated bit error rate (BER) for quaternary phase-shift keyed (QPSK) modulation with perfect synchronization was on the order of 0.02 dB. These results should also be valid for binary phase-shift keying (BPSK).

Intermediate rolloff full and square-root 50-percent raised cosine approximations were developed first. Candidate root selection did not prove effective, primarily because the resultant bell-shaped pole clusters are completely unlike that of any well-known filter family. Hence, initial estimates for subsequent family members were obtained by extrapolation. Both the full and square-root 50-percent raised cosine approximations were group-delay equalized with one second-order section. The overall delay through each of these 50-percent composite filters corresponded to a duration of about 2.5 data symbols.

Next, a complete family of full and square-root raised cosine approximations was computed in 10-percent rolloff rate increments. The range was 10 through 100 percent for the full raised cosine, and 20 through 100 percent for the square-root raised cosine, where the 20-percent square root response is roughly equivalent in transition band shape factor and implementation complexity to a 10-percent full raised cosine response. With a nominal rms error ripple of 0.5 percent and better than 40 dB of stopband rejection, both the full and square-root approximations resulted in negligible BER degradation over the entire rolloff range. The required amount of group delay equalization varied from one first-order section for the full 100-percent raised cosine to five second-order sections for the full 10-percent raised cosine. These had delays ranging from 1.35 to 13.5 data symbols, respectively.

In the overview section, the importance of group delay compensation is illustrated by plotting the BER for the raised cosine family's magnitude approximation alone. To summarize the performance and put the approximation results into perspective, magnitude and group delay frequency responses and eye patterns are given for 20-, 50-, and 100-percent rolloff rates.

Background

Nyquist has shown that it is possible to transmit sequences of digital data without ISI. To do this, the transmission path must possess a vestigial type of symmetry about its half-amplitude point, as well as linear phase or equivalently flat group delay [1]–[4]. Other more general frequency domain characteristics which inhibit ISI have also been defined [5]; however, they typically yield asymmetrical impulse responses and are difficult to implement with analog hardware.

Figure 1 shows specific Nyquist amplitude shapes. The best known is the ideal rectangular frequency characteristic. Its impulse response is

$$h(t) = \frac{\sin(\pi t/T)}{(\pi t/T)} \tag{1}$$

where $T = 1/R$ is the data symbol duration in seconds, and R is the data rate in baud. The zero crossings of $h(t)$ occur at uniformly spaced time instants of $t = T, 2T, 3T, \ldots$. Hence, if adjacent responses are superimposed (such as when a sequence of data symbols is transmitted), the adjacent responses do not interfere at the detection sampling points.

As with the ideal rectangular filter characteristic, it is well known that the raised cosine shape also exhibits equally spaced axis crossings with no ISI at

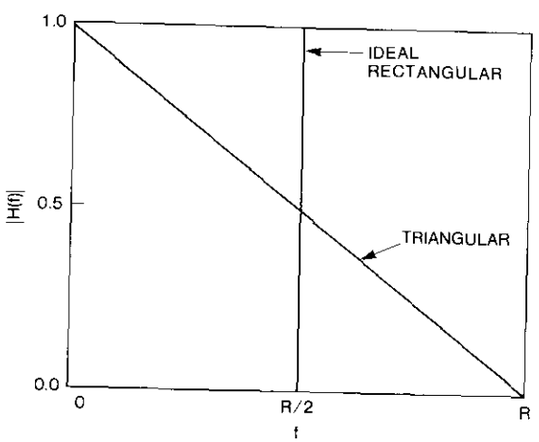

Figure 1. *Nyquist Magnitude Shapes*

the detection sampling instants. The magnitude response of the raised cosine function is defined by

$$|H(f)| = \begin{cases} 1 & f \leq f_1 \triangleq (1 - r) f_h \\ \frac{1}{2}\left\{1 - \sin\left[\frac{\pi}{2r}\left(\frac{f}{f_h} - 1\right)\right]\right\}, & f_1 \leq f \leq f_0 \\ 0 & f \geq f_0 \triangleq (1 + r) f_h \end{cases} \qquad (2)$$

where r = rolloff factor
f_h = half-amplitude frequency
f_1 = maximum unity transmission frequency
f_0 = minimum zero transmission frequency.

For illustration, a representative sample of raised cosine filters with rolloff rates of 20, 50, and 100 percent are plotted in Figure 2. The filters can be described as having a perfectly flat amplitude response up to f_1, a cosine-shaped transition band, and no transmission above f_0. Implicit in this discussion is the assumption of linear phase. This is usually brought about in practice by cascading all-pass group delay equalization networks. Without linear phase in the frequency domain, the transformed impulse response would not have an even time symmetry.

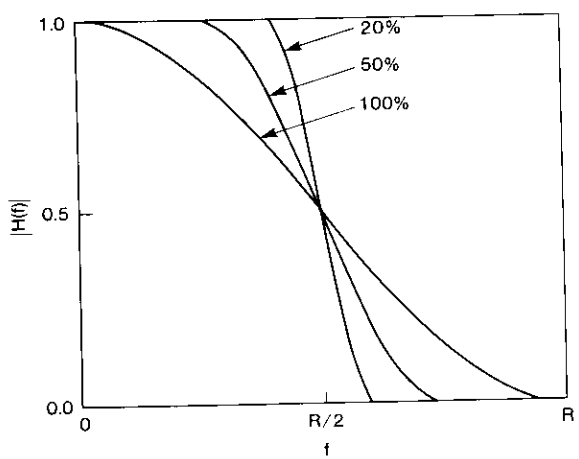

Figure 2. *Raised Cosine Magnitude Shapes*

Equation (2) is a lowpass representation. An analogous definition at bandpass requires arithmetic symmetry about some center frequency. Unfortunately, the two definitions are not equivalent because the classical lowpass-to-bandpass transformation exhibits geometric symmetry, except when the percent bandwidth $\triangleq 2\Delta f/f_c$ (double-sided bandwidth divided by center frequency) is relatively small, such that $(1 - \Delta f/f_c)^{-1} \simeq 1 + \Delta f/f_c$. Thus, the development of a bandpass prototype raised cosine rolloff filter is a separate issue, and only the lowpass representation will be dealt with here.

References 6 and 7 document previous attempts at approximating the raised cosine characteristic. Nader and Lind [6] develop an analytic theory for the design of an optimal analog data transmission filter. Theirs is primarily a time domain technique, which is based on minimizing the ISI at the detection sampling points. An interesting facet of their solution is that it does not require group delay equalization. As a result, the impulse response does not exhibit an even time symmetry, although it does have very good ISI performance. The disadvantage of this technique is that the filter selectivity and stopband attenuation cannot be easily specified or controlled.

Kesler and Taylor [7] use an all-pole Butterworth filter whose 3-dB bandwidth and a portion of its attenuation slope are matched to the desired raised cosine rolloff magnitude characteristic. For group delay equalization, they employ a power series expansion technique that yields maximally flat delay. The advantage of their method is its simplicity. The disadvantage is that the magnitude response is not a precise match because of the Butterworth constraint and the incumbent omission of complex zeros.

The approach employed in this paper is based on a minimum mean square error (MMSE) computer optimization of a candidate pole and zero set, to the exact frequency domain symmetry criteria defined by Nyquist. The merit of the solution was determined from its impact on the channel BER. Moreover, familiarity with filter theory was exercised, both in selecting the candidate roots and in interacting with the optimization routine.

Approximating the raised cosine characteristic

An ideal raised cosine rolloff filter is not realizable because of two fundamental discrepancies: a perfectly flat passband and a stopband with zero transmission, or equivalently, infinite attenuation. In the transition band, cosine shaping does not present any fundamental problems, although it is quite unlike that of any common generic filter such as Butterworth, Chebychev, or Cauer.

The pole-zero approximations for the raised cosine filter family were determined through separate computer optimizations of the magnitude and

group delay responses. The routines, described in detail in the Appendix, may be characterized here simply as a straightforward application of an MMSE convergence constraint. The MMSE constraint typically gives rise to an error ripple. In the passband, the approximation generally exhibits a nearly equiripple error; whereas in the stopband, the error manifests itself as attenuation ripple and notches.

The effects of passband ripple error and finite stopband attenuation were evaluated by using a computer-simulated BER of a 50-percent raised cosine filtered data channel. COMSAT's communications channel modeling program (CHAMP) was used for this purpose [8]. Because of its widespread utility, QPSK was the selected modulation technique. To facilitate an ideal matched filtered Nyquist channel, square-root 50-percent raised cosine filtering was used on both the transmit and receive sides [9]–[12]. The filters were defined by 41 frequency domain points spaced equally from zero to $R = 1/T$ (Hz). To isolate the effects of passband amplitude ripple, the stopband attenuation in the simulation was set to 90 dB and the group delay variation was set to zero. An equiripple passband was then simulated by alternating the sign of the error added to successive data points. As a result, five equiripple cycles occurred in the unity transmission portion of the passband. Table 1 lists the results for the transmit and receive filters.

TABLE 1. COMPUTER-SIMULATED SQUARE-ROOT 50-PERCENT COSINE ERROR RIPPLE DEGRADATION

PEAK AMPLITUDE ERROR (%)	DEGRADATION IN E_b/N_o FOR BER = 10^{-6} (dB)
TRANSMIT FILTER	
±5	0.060
±2	0.015
±1	0.009
±0.5	0.005
RECEIVE FILTER	
±5	0.090
±2	0.021
±1	0.011
±0.5	0.008

The degradation for a maximum stopband attenuation limit on the transmit and receive filters is summarized in Table 2. In practice, a transmit filter must typically have greater than 40 dB of stopband attenuation to limit out-

of-band (OOB) spurious response. This value corresponds to a BER degradation for a single filter of about 0.005 dB. For a comparable amount of degradation, a peak error ripple of no more than 0.5 percent in the passband is allowed. Hence, a 40-dB stopband and a 0.5-percent passband were chosen as tentative approximation guidelines, such that they could be compromised later as a function of the resulting performance and filter complexity.

TABLE 2. COMPUTER-SIMULATED SQUARE-ROOT 50-PERCENT RAISED COSINE ATTENUATION LIMIT DEGRADATION

STOPBAND ATTENUATION LIMIT (dB)	DEGRADATION IN E_b/N_o FOR BER = 10^{-6} (dB)
TRANSMIT FILTER	
−50	0.004
−40	0.004
−30	0.008
−20	0.029
RECEIVE FILTER	
−50	0.004
−40	0.005
−30	0.013
−20	0.092

The degree of phase equalization required was also determined on the basis of BER. That is, phase compensation was achieved through a cascade of first- and second-order all-pass networks. Hence, sections were added until the cumulative degradation in error rate from all sources was on the order of 0.01 dB. Although this appears to be a rather stringent requirement, the resultant filter complexity is not at all severe.

50-percent raised cosine candidate root selection and results

In Figure 3, the magnitude-squared frequency responses for the full and square-root 50-percent raised cosine transfer functions are plotted on a semilog scale. As the zero transmission frequency (f_0) is approached, the slope of the attenuation increases sharply, particularly for the square-root filter. To realize this type of response, a function with attenuation poles or notches in the stopband is necessary. For the full cosine, a single notch was sufficient.

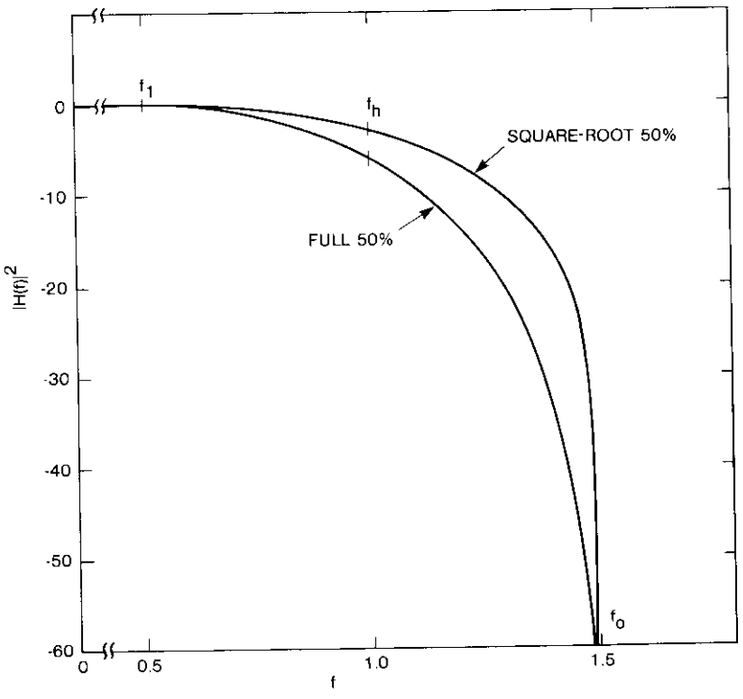

Figure 3. *Full and Square-Root Raised Cosine Magnitude Response*

With the square-root response, two notches were necessary. Moreover, analogous increases in attenuation notch complexity prevail with sharper rolloff elliptic filters [13].

It is well known that, for linear additive white Gaussian noise (AWGN) channels, using a square-root Nyquist response for both the transmit and receive filters yields ideal BER performance. In contrast, the full cosine response was also considered because of its utility in nonlinear channel applications. In particular, the transmit/receive filter apportionment of an elliptic (which is relatively transparent over the Nyquist bandwidth) with a full raised cosine has proven effective for nonlinear operation [14]–[17].

The behavior of the raised cosine passband below f_h is not unlike that of a maximally flat Butterworth response. For the full 50-percent raised cosine, the ratio of the 10- to 1-dB bandwidth is about 1.6, which corresponds to a five-pole Butterworth filter [18],[19]. Moreover, a fifth-order Butterworth filter with a complex-zero notch positioned at $f = 1.5$ Hz was selected as

the starting point for optimization. After a few cycles, it became clear that the five-pole solution could not satisfy the 40-dB OOB constraint, so a sixth pole was added. Table 3 lists the full 50-percent raised cosine results. The poles and zeros have been normalized such that the Nyquist half-amplitude bandwidth (6-dB down point) occurs at unity, which corresponds to operation at $R = 2$ symbol/s. The maximum peak-to-peak (p-p) error ripple variation and the minimum stopband attenuation are the worst-case points, whereas the rms error is an average taken over the entire frequency response. Both the rms error and stopband attenuation are consistent with the approximation goals of 0.5 percent and 40 dB, respectively. To achieve nearly equiripple stopband behavior, a constant error-weighting multiplier with adjustable frequency limits was employed.

TABLE 3. FULL 50-PERCENT RAISED COSINE MAGNITUDE APPROXIMATION

Magnitude Response				Error Parameters		
Zeros (Hz)		Poles (Hz)		Maximum p-p (s)	rms Error (s)	Minimum Stopband Attenuation (dB)
Real	Imaginary	Real	Imaginary			
0.0	±1.5777	−0.6031	±0.3177	0.0228	0.0053	41.6
		−0.3219	±0.7591			
		−0.2000	±1.1538			

An additional complex pole and zero pair was required to adequately approximate the square-root 50-percent raised cosine. The results are summarized in Table 4. Again, the approximation errors are compatible with the desired guidelines.

TABLE 4. SQUARE-ROOT 50-PERCENT RAISED COSINE MAGNITUDE APPROXIMATION

Magnitude Response				Error Parameters		
Zeros (Hz)		Poles (Hz)		Maximum p-p (s)	rms Error (s)	Minimum Stopband Attenuation (dB)
Real	Imaginary	Real	Imaginary			
0.0	±1.5167	−0.7108	±0.3584	0.0186	0.0050	41.7
0.0	±1.6819	−0.4025	±0.8417			
		−0.2076	±1.2498			
		−0.0562	±1.4456			

The migration of the roots from initial estimates to their final optimization values is depicted in Figures 4a and 4b for the full and square-root 50-percent raised cosine responses, respectively. The final pole locations are arranged in a bell-shaped pattern which is unlike the elliptical patterns of such generic filter families as Cauer, Chebychev, inverse Chebychev, and Butterworth. Also, the final complex pole clusters are predominantly underdamped.

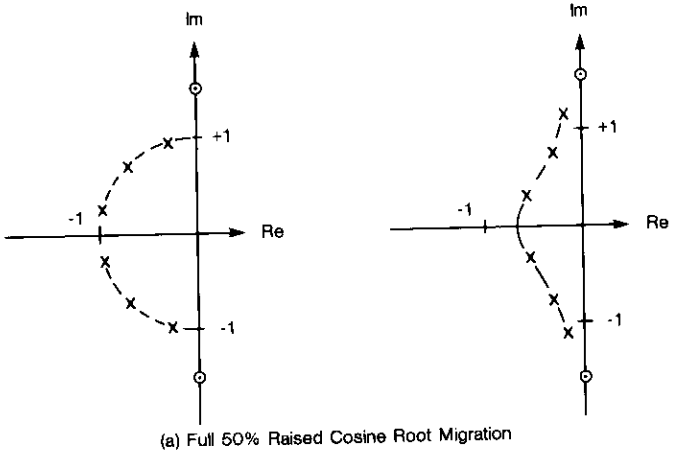

(a) Full 50% Raised Cosine Root Migration

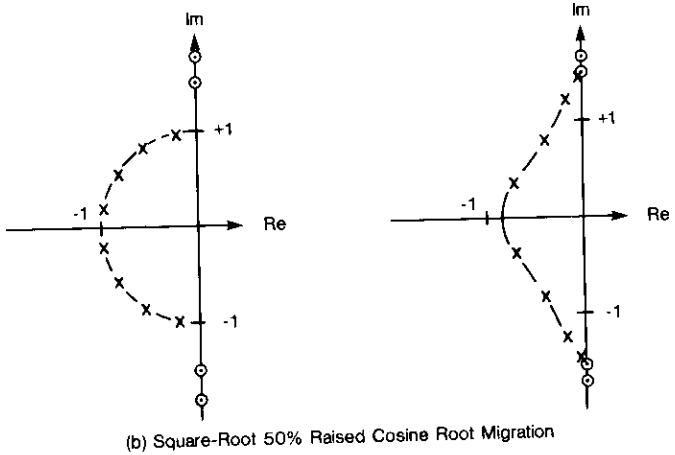

(b) Square-Root 50% Raised Cosine Root Migration

Figure 4. *50% Raised Cosine Root Migration*

The zeros were constrained to be purely imaginary during optimization in order to conform with conventional filter notation. As expected, their final locations are just above the Nyquist stopband frequency limit, f_0.

As explained previously, the number of first- and/or second-order group delay equalizer sections were determined by the minimum amount required to achieve negligible degradation in BER (~0.01 dB). Table 5 lists the results for the full 50-percent raised cosine approximation with the 6-dB bandwidth normalized to 1 Hz, which corresponds to operation at $R = 2$ symbol/s.

TABLE 5. FULL 50-PERCENT RAISED COSINE GROUP DELAY EQUALIZATION

Group Delay Equalizer Roots	
Real	±0.8070 Hz
Imaginary	±0.2364 Hz
Error Parameters	
Average Delay	1.3283 s
Maximum p-p	0.0606 s
Percent p-p	4.56%
Normalized rms	0.0124 s
Equalization Bandwidth	1 Hz
$\Delta E_b/N_o$	Negligible

The error parameters consist of the average delay, the maximum absolute and percent peak-to-peak delay, and the rms delay normalized by the average. These parameters are representative of the overall filter response, not just the group delay compensation. The equalization bandwidth is the frequency range over which group delay optimization was performed, and $\Delta E_b/N_o$ is the BER degradation determined by computer simulation. For the full 50-percent raised cosine approximation, one second-order equalizer section was sufficient. Its roots are a pair of complex poles in the left half of the s-plane, and a set of mirror image complex zeros in the right half-plane. For operation at the Nyquist rate [lowpass bandwidth-symbol time product (BT) = 0.5], the delay through the full 50-percent raised cosine filter is approximately 2.65 data symbols, or $2.65T$. Note that about a 5-percent peak-to-peak delay ripple over the Nyquist bandwidth was sufficient to yield negligible degradation in BER.

Table 6 gives the group delay parameters for the square-root 50-percent raised cosine approximation with the filter 3-dB bandwidth normalized to 1 Hz ($R = 2$ symbol/s). Again, one second-order equalizer section was adequate. The overall filter delay was approximately $2.53T$ with about an 8-percent peak-to-peak ripple.

TABLE 6. SQUARE-ROOT 50-PERCENT RAISED COSINE GROUP DELAY EQUALIZATION

Group Delay Equalizer Roots	
Real	±0.6921 Hz
Imaginary	±0.3846 Hz
Error Parameters	
Average Delay	1.2649 s
Maximum p-p	0.0984 s
Percent p-p	7.78%
Normalized rms	0.0143 s
Equalization Bandwidth	1.1 Hz
$\Delta E_b/N_o$	0.027 dB

The eye patterns for the full, square-root, and cascaded square-root 50-percent raised cosine filters are shown in Figure 5. The responses exhibit an even time symmetry, and the ISI at the detection sampling point is negligible for the full cosine; whereas, it is just noticeable with the cascaded square-root approximations. In particular, the BER degradation corresponding to the latter case is 0.07 dB. This is more than twice the degradation of a single square-root filter (0.027 dB) because the magnitude and delay errors reinforce perfectly in the simulation, and BER is a nonlinear function of these parameters. However, the net degradation is still less than 0.1 dB, which is virtually negligible in practice.

A family of full and square-root raised cosine filters

Once the 50-percent raised cosine poles and zeros were obtained, initial estimates for adjacent family members were extrapolated from these, until the entire family was resolved. Depending on the rolloff factor, poles were added or deleted to maintain the consistency of the error parameters. For the full raised cosine, one complex zero pair was always sufficient to achieve the desired transition band shape factor.

Full raised cosine magnitude approximation

The full raised cosine family magnitude results, listed in Table 7, are normalized to a 6-dB bandwidth of 1 Hz for operation at 2 symbol/s. The rms error is typically around 0.5 percent and the minimum stopband attenuation is greater than 40 dB. Adding additional poles and zeros can improve the ripple and attenuation parameters; however, such endeavors did not yield a

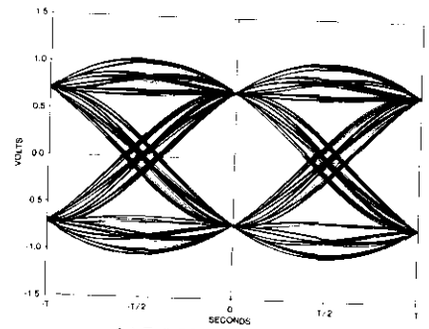

(a) Full 50% Raised Cosine

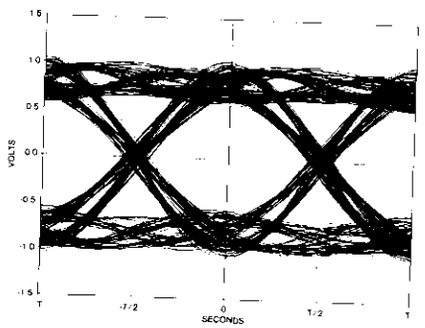

(b) Square-Root 50% Raised Cosine

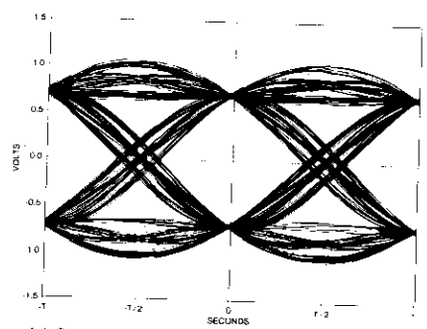

(c) Cascaded Square-Root 50% Raised Cosine

Figure 5. *50% Raised Cosine Eye Patterns*

return-to-scale improvement in computer-simulated BER. Furthermore, increasing the stopband attenuation degraded the group delay so that it required more sections to be equalized.

TABLE 7. FULL RAISED COSINE MAGNITUDE APPROXIMATION

Rolloff Rate	Magnitude Response: Zeros (Hz) Real	Zeros (Hz) Imaginary	Poles (Hz) Real	Poles (Hz) Imaginary	Error Parameters: Maximum p-p (s)	rms Error (s)	Minimum Stopband Attenuation (dB)
100	0.0	±2.1321	−0.6614	0.0	0.0165	0.0045	43.1
			−0.5842	±0.7211			
			−0.3804	±1.3878			
90	0.0	±2.0365	−0.7573	0.0	0.0202	0.0057	41.7
			−0.5506	±0.6570			
			−0.3543	±1.3109			
80	0.0	±1.9156	−0.8194	0.0	0.0210	0.0063	41.5
			−0.5019	±0.6260			
			−0.3244	±1.2487			
70	0.0	±1.7839	−0.5409	±0.4114	0.0141	0.0038	44.0
			−0.4649	±0.8572			
			−0.2813	±1.2969			
60	0.0	±1.6900	−0.6440	±0.3755	0.0190	0.0048	42.1
			−0.4011	±0.7598			
			−0.2395	±1.2101			
50	0.0	±1.5777	−0.6031	±0.3177	0.0228	0.0053	41.6
			−0.3219	±0.7591			
			−0.2000	±1.1538			
40	0.0	±1.4578	−0.5471	0.0	0.0181	0.0044	42.4
			−0.4879	±0.5605			
			−0.2679	±0.8359			
			−0.1606	±1.1436			
30	0.0	±1.3446	−0.5256	0.0	0.0221	0.0048	41.4
			−0.4337	±0.4907			
			−0.2004	±0.8376			
			−0.1256	±1.0847			
20	0.0	±1.2308	−0.5753	0.0	0.0214	0.0042	41.0
			−0.7136	±0.3443			
			−0.3610	±0.6070			
			−0.1421	±0.8858			
			−0.0879	±1.0533			
10	0.0	±1.1152	−0.5934	±0.1456	0.0217	0.0034	41.1
			−0.4334	±0.2826			
			−0.2906	±0.5909			
			−0.1811	±0.8116			
			−0.0722	±0.9439			
			−0.0444	±1.0267			

Full raised cosine group delay equalization

Table 8 catalogs the group delay compensation results for the full raised cosine family. The number of group delay equalizer sections required was basically that amount which rendered the computer-simulated BER degradation negligible. Examination of the list reveals that a single first-order section was necessary for rolloff rates from 100 percent down through 60 percent, a second-order section was used for 50 and 40 percent, and cascaded sections were required at 30 percent and below. The average delay through the composite filter ranged from approximately $1.37T$ (where $T = 1/R = 0.5$ s) to $13.5T$ for 100- through 10-percent rolloffs, respectively. It was generally only necessary to equalize the peak-to-peak ripple to a value of about 5 percent of the average delay over 1 to 1.2 times the Nyquist bandwidth.

TABLE 8. FULL RAISED COSINE GROUP DELAY EQUALIZATION

Rolloff Rate	Group Delay Equalizer Roots (Hz) Real	Group Delay Equalizer Roots (Hz) Imaginary	Error Parameters: Average Delay (s)	Maximum p-p (s)	Percent p-p (%)	Normalized rms (s)	Equal Band (Hz)	$\Delta E_b/N_o$ (dB)
100	±1.8210	0.0	0.6851	0.0366	5.34	0.0108	1.2	0.015
90	±1.4586	0.0	0.7370	0.0310	4.21	0.0136	1.1	0.02
80	±1.1320	0.0	0.7991	0.0486	6.08	0.0193	1.1	0.025
70	±0.8834	0.0	0.9522	0.0261	2.74	0.0095	1.0	0.00
60	±0.7364	0.0	1.0194	0.0314	3.08	0.0084	1.0	0.00
50	±0.8070	±0.2364	1.3283	0.0606	4.56	0.0124	1.0	0.00
40	±0.5248	±0.3336	1.5934	0.0522	3.28	0.0083	1.0	0.00
30	±0.4415	0.0	2.0696	0.0898	4.34	0.0104	1.0	0.01
	±0.4060	±0.5044						
20	±0.3158	0.0	3.2398	0.1300	4.01	0.0080	1.0	0.015
	±0.3013	±0.3282						
	±0.2666	±0.6703						
10	±0.1566	±0.0884	6.2574	0.3172	5.07	0.0110	1.0	0.02
	±0.1541	±0.2690						
	±0.1501	±0.4492						
	±0.1427	±0.6324						
	±0.1284	±0.8185						

Square-root raised cosine magnitude approximation

Table 9 presents data for the square-root raised cosine magnitude response, with the 3-dB bandwidth normalized to 1 Hz for operation at $R = 2$ symbol/s. Two complex zero pairs were required in order to approximate each member of the square-root cosine family because of the sharper transition attenuation relative to the full cosine. Also, more poles were typically needed for a given rolloff rate. As before, the rms error was about 0.5 percent and the minimum stopband attenuation was greater than 40 dB.

Square-root raised cosine group delay equalization

Table 10 lists the group delay equalization results for the square-root raised cosine family. Scanning the table reveals that one second-order section was sufficient for the 100- through 50-percent rolloff rates, while cascaded sections were necessary for sharper rolloffs. The composite filter delay ranged from $1.65T$ at 100 percent to $6.36T$ at 20 percent. Peak-to-peak group delay ripples as large as 10 percent did not significantly degrade the BER, and the equalization bandwidth again ranged between 1 and 1.2 times the Nyquist bandwidth.

Overview of the results

The BERs for the raised cosine family approximations of Table 9 are plotted in Figure 6, with identical square-root responses allocated to the transmit and receive sides. These BERs represent the performance attainable by approximating the Nyquist magnitude criterion alone; that is, no effort was made to equalize the group delay response. It is apparent that the error rate degrades dramatically for the sharper rolloff filters. The modulation technique used in the simulation was QPSK. Multilevel signaling schemes would probably suffer more degradation because they exhibit greater sensitivity to ISI. BER curves for the group delay equalized cases were not plotted because they would virtually be superimposed on the ideal BPSK/QPSK curve.

To give an overview of the results, the full raised cosine magnitude and group delay responses for rolloff rates of 20, 50, and 100 percent are depicted in Figure 7. The corresponding square-root raised cosine responses are plotted in Figure 8. These figures show that it was unnecessary to equalize the group delay out to its peak, because the peak occurs substantially beyond the 3-dB frequency and little output power is passed at those frequencies. Also, the group delay characteristic has a plateau below its peak. This is caused by soft rolloff in the low-frequency portion of the transition band; whereas, the peak results from the excessively sharp attenuation near the cutoff frequency,

TABLE 9. SQUARE-ROOT RAISED COSINE MAGNITUDE APPROXIMATION

Rolloff Rate	Magnitude Response: Zeros (Hz) Real	Zeros (Hz) Imaginary	Poles (Hz) Real	Poles (Hz) Imaginary	Error Parameters: Maximum p-p (s)	Error Parameters: rms Error (s)	Minimum Stopband Attenuation (dB)
100	0.0	±2.0399	−0.7522	±0.4858	0.0381	0.0067	42.4
	0.0	±2.5863	−0.4761	±1.3331			
			−0.1417	±1.8013			
90	0.0	±1.9389	−0.6876	±0.4970	0.0388	0.0069	42.1
	0.0	±2.4402	−0.4425	±1.2815			
			−0.1327	±1.7157			
80	0.0	±1.8379	−0.6229	±0.5081	0.0400	0.0068	41.3
	0.0	±2.2940	−0.4089	±1.2298			
			−0.1236	±1.6299			
70	0.0	±1.7304	−0.9141	0.0	0.0293	0.0056	42.6
	0.0	±2.0169	−0.5588	±0.6988			
			−0.3190	±1.2822			
			−0.0901	±1.5765			
60	0.0	±1.6286	−0.7402	0.0	0.0297	0.0054	41.3
	0.0	±1.8754	−0.4741	±0.7252			
			−0.2807	±1.2390			
			−0.0812	1.4960			
50	0.0	±1.5167	−0.7108	±0.3584	0.0186	0.0050	41.7
	0.0	±1.6819	−0.4025	±0.8417			
			−0.2076	±1.2498			
			−0.0562	1.4456			
40	0.0	±1.4100	−0.5518	±0.3326	0.0193	0.0047	42.4
	0.0	±1.5692	−0.3095	±0.8394			
			−0.1687	±1.1806			
			−0.0438	±1.3479			
30	0.0	±1.3080	−0.5052	±0.3139	0.0409	0.0059	41.6
	0.0	±1.4457	−0.2750	±0.8289			
			−0.1561	±1.1037			
			−0.0388	±1.2459			
20	0.0	±1.2052	−0.5119	±0.0	0.0257	0.0055	40.4
	0.0	±1.2990	−0.4104	±0.5007			
			−0.1984	±0.8855			
			−0.1110	±1.0738			
			−0.0291	±1.1677			

TABLE 10. SQUARE-ROOT RAISED COSINE GROUP DELAY EQUALIZATION

Rolloff Rate	Group Delay Equalizer Roots (Hz)		Error Parameters					
	Real	Imaginary	Average Delay (s)	Maximum p-p (s)	Percent p-p (%)	Normalized rms (s)	Equal Band (Hz)	$\Delta E_b/N_o$ (dB)
100	±1.0804	±0.6625	0.8252	0.0253	3.07	0.0091	1.2	0.023
90	±1.0898	±0.5900	0.8573	0.0329	3.83	0.0111	1.15	0.028
80	±1.1265	±0.4797	0.8893	0.0420	4.72	0.0131	1.1	0.026
70	±1.0740	±0.3662	1.0017	0.0560	5.59	0.0117	1.1	0.021
60	±0.8664	±0.3823	1.1000	0.0780	7.09	0.0140	1.1	0.021
50	±0.6921	±0.3846	1.2649	0.0984	7.78	0.0143	1.1	0.027
40	±0.5507 ±0.5334	0.0 ±0.5885	1.7022	0.1724	10.13	0.0182	1.1	0.013
30	±0.4045 ±0.3857	±0.2309 ±0.6841	2.2220	0.2216	9.93	0.0197	1.1	0.012
20	±0.3387 ±0.3490 ±0.3226	±0.1640 ±0.4881 ±0.7629	3.1822	0.1019	3.20	0.0058	1.0	0.016

f_0. Such behavior is a consequence of the well-known relationship between magnitude and phase for linear minimum phase networks.

Eye patterns for the square-root and full raised cosine responses with rolloff rates of 20, 50, and 100 percent are shown in Figure 9. They correspond to a time-synchronous overlay of the filtered responses from all possible digital input data sequences, viewed over a one-symbol aperture. The sharper rolloff filters exhibit more ringing and overshoot in their responses, and their zero crossings are more broadly distributed. This zero-crossing dispersion gives rise to pattern jitter in a modem's symbol timing recovery circuit. Note that the eye patterns for the 100-percent raised cosine have negligible zero-crossing dispersion. The dispersion has effectively been traded for softer rolloff and greater spectral occupancy.

Conclusions

A broad range of full and square-root raised cosine family magnitude responses have been approximated with a modest number of poles and zeros, and equalization of the group delay response has entailed relatively little

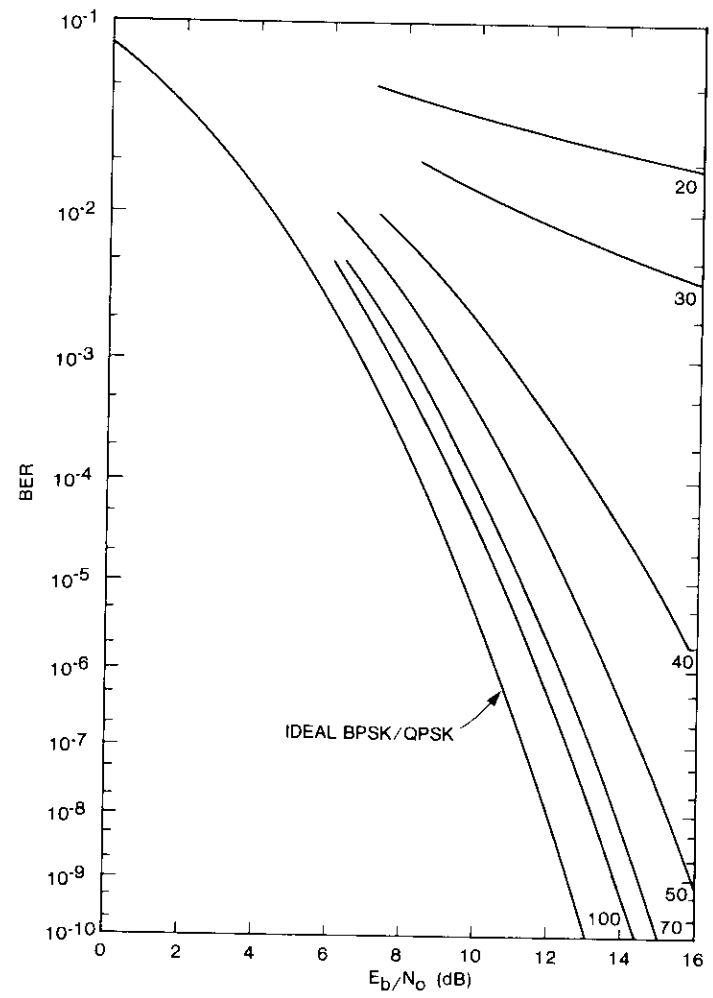

Figure 6. *BERs for the Raised Cosine Magnitude Approximation*

additional complexity. In particular, a full 50-percent rolloff group delay equalized filter required only two complex-zero and four complex-pole pairs; whereas, a 50-percent square-root response used three zero and five pole pairs. The QPSK BER degradation for operation at the Nyquist rate was nominally on the order of 0.02 dB for both the full and square-root cosine families of filters, although when two square-root responses were cascaded the BER degradation approached 0.1 dB. The rms magnitude and group delay

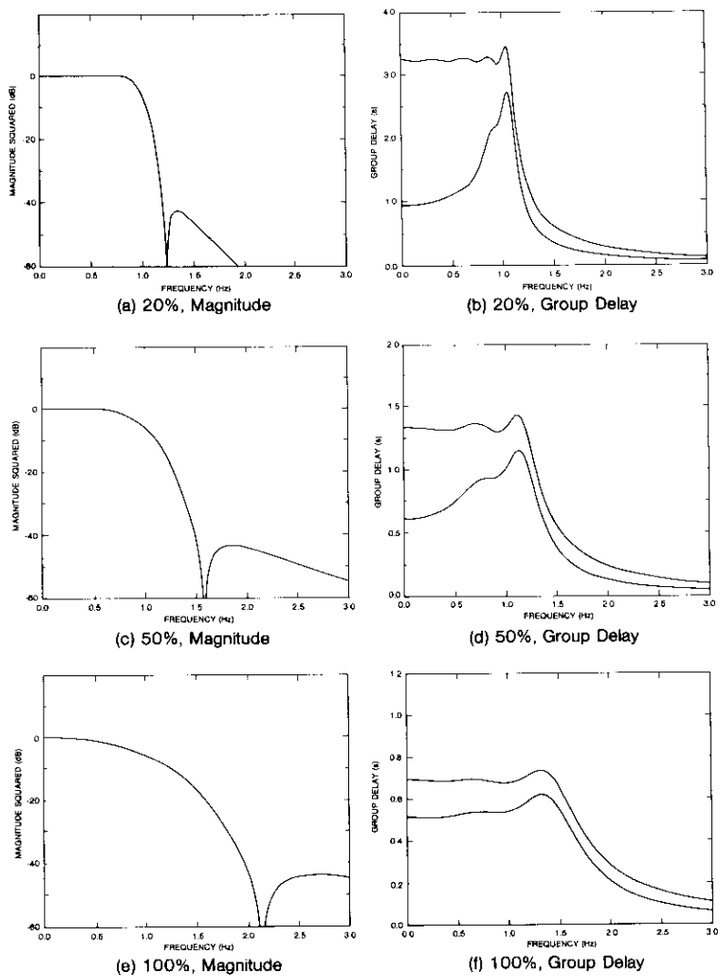

Figure 7. *Full Cosine Magnitude and Group Delay*

error ripples were typically 0.5 and 1.5 percent, respectively, and the minimum OOB rejection was greater than 40 dB. Moreover, solutions of lower implementation complexity could be traded for greater ripple error, poorer OOB response, and increased BER degradation. In particular, the raised cosine approximation appeared very sensitive to the magnitude of stopband attenuation. That is, more pole-zero complexity is required in the magnitude

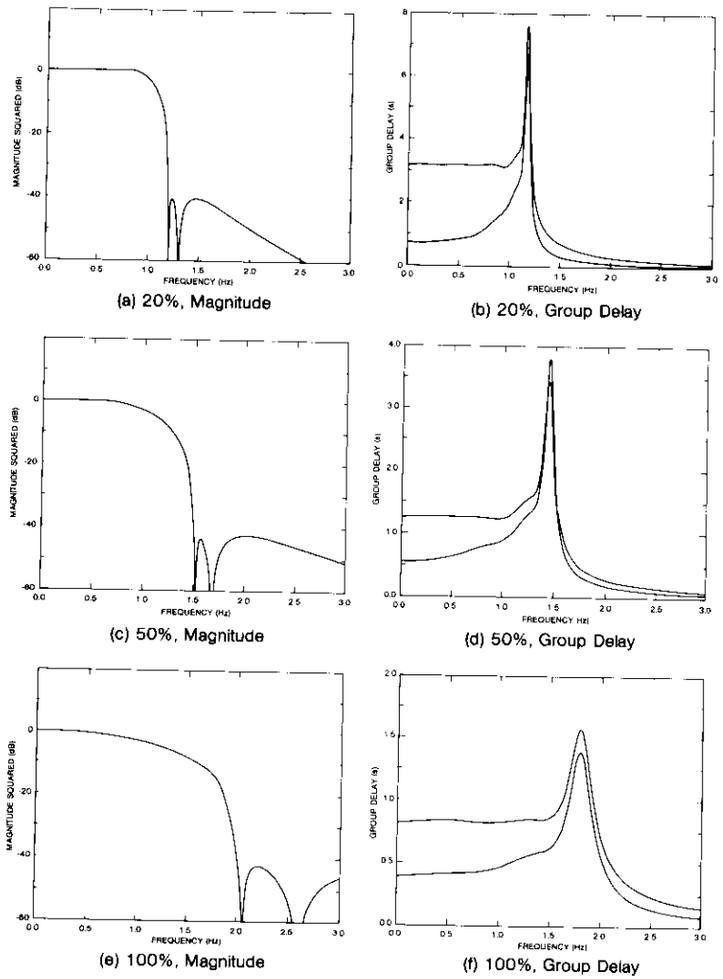

Figure 8. *Square-Root Cosine Magnitude and Group Delay*

response to achieve a sharper attenuation characteristic. This in turn causes greater group delay dispersion, which necessitates a more complex equalizer.

When rectangular digital data pulses drive the transmit filter, $x/\sin(x)$ aperture compensation is necessary to minimize ISI, as described in Reference 12. More specifically, the full or square-root transmit raised cosine filter must be cascaded with a network that resembles the $x/\sin(x)$ response. Hence,

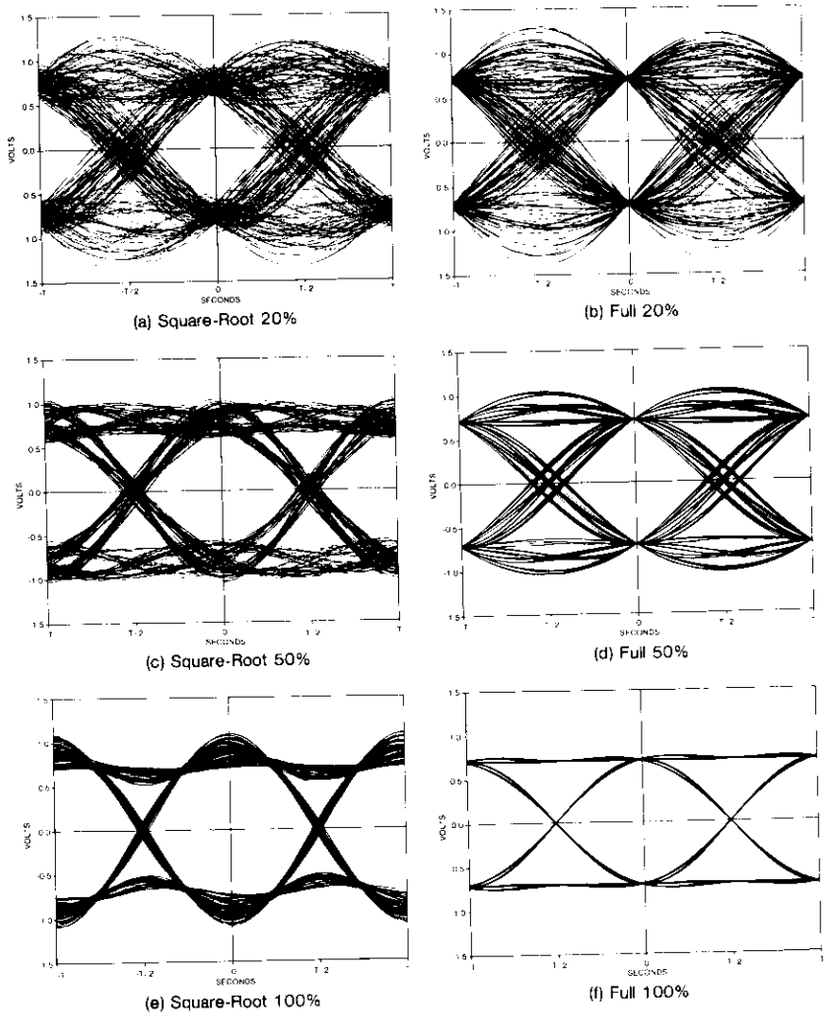

Figure 9. *Square-Root and Full Cosine Eye Patterns*

separate families of raised cosine approximations could be generated for the combined response. It should be possible to develop such an approximation with little or no increase in complexity relative to the raised cosine alone. However, for the softer rolloff filters, the $x/\sin(x)$ aperture peaking is quite abrupt, which can result in a filter with a large net gain over a broad region in the transition band. Consequently, aperture compensation peaking constraints are necessary to approximate the aggregate response. This would be an interesting topic for follow-up work.

Group delay equalization had a substantial impact on BER performance because it is the primary contributor in facilitating an even time symmetry to suppress ISI in the impulse response. The surprising result was that relatively coarse equalization could yield such exceptional BER performance. In particular, it was found that (depending on the rolloff rate) a 5- to 10-percent peak-to-peak group delay error optimized at over 1.0 to 1.2 times the Nyquist bandwidth was sufficient to achieve negligible BER degradation. To explain this, it could be speculated that beyond the Nyquist half-amplitude frequency, where the energy distribution of the data spectrum falls off, the group delay variation has proportionally less impact. Moreover, the consistent 5- to 10-percent equalized group delay variation was achieved by normalizing relative to the average delay rather than to the data pulse interval. If the latter normalization had been used, the peak-to-peak group delay variation for the 10-percent full cosine rolloff filter would be more than 60 percent of a symbol duration. Hence it appears that, as the average equalized filter delay increases, there is less sensitivity to delay dispersion, possibly because the impulse response energy is more spread out for the sharper rolloff filters.

The amplitude and group delay computer optimization routines generally converged well, although occasionally they settled on local minimums. Premature convergence was easily detected and redirected through user interaction. A Fletcher-Powell convergence algorithm was also tried, but it did not converge as rapidly or to as small an error.

References

[1] H. Nyquist, "Certain Topics in Telegraph Transmission Theory," *AIEE Transactions*, Vol. 47, April 1928, pp. 617–644.

[2] E. D. Sunde, "Theoretical Fundamentals of Pulse Transmission," *Bell System Technical Journal*, Vol. 33, Part I, May 1954, pp. 721–788; Part II, July 1954, pp. 987–1010.

[3] E. D. Sunde, "Ideal Binary Pulse Transmission by AM and FM," *Bell System Technical Journal*, Vol. 38, November 1959, pp. 1357–1426.

[4] W. R. Bennett and J. R. Davey, *Data Transmission*, New York: McGraw-Hill, 1965.

[5] R. A. Gibby and J. W. Smith, "Some Extensions of Nyquist's Telegraph Transmission Theory," *Bell System Technical Journal*, Vol. 44, September 1965, pp. 1487–1510.

[6] S. Nader and L. Lind, "Optimal Data Transmission Filters," *IEEE Transactions on Circuits and Systems*, Vol. CAS-26, No. 1, January 1979, pp. 36–45.

[7] S. Kesler and D. Taylor, "Research and Evaluation of the Performance of Digital Modulations in Satellite Communications Systems," Internal Report CRL92, Communications Research Laboratory, McMaster University, Hamilton, Ontario, Canada, October 1981.

[8] L. C. Palmer and S. Lebowitz, "Including Synchronization in Time-Domain Channel Simulations," *COMSAT Technical Review*, Vol. 7, No. 2, Fall 1977, pp. 475–526.

[9] D. W. Tufts, "Nyquist's Problem—The Joint Optimization of Transmitter and Receiver in Pulse Amplitude Modulation," *Proc. IEEE*, March 1965, pp. 248–259.

[10] M. R. Aaron and D. W. Tufts, "Intersymbol Interference and Error Probability," *IEEE Transactions on Information Theory*, Vol. IT-12, No. 1, January 1966, pp. 26–34.

[11] I. Korn, "Error Probability and Bandwidth of Digital Modulation," *IEEE Transactions on Communications*, Vol. COM-28, No. 2, February 1980, pp. 287–290.

[12] J. Poklemba, "An Approximation Technique for Realizing the Reciprocal sin $(x)/(x)$ Frequency Response," *COMSAT Technical Review*, Vol. 12, No. 1, Spring 1982, pp. 121–156.

[13] R. Saal, *The Design of Filters Using the Catalogue of Normalized Low-Pass Filters*, Telefunken, GMBH, Backnang, West Germany, 1963.

[14] L. Lundquist, M. Lopriore, and F. M. Gardner, "Transmission of 4ϕ-Phase-Shift-Keyed Time Division Multiple Access Over Satellite Channel," *IEEE Transactions on Communications*, Vol. COM-22, No. 9, September 1974, pp. 1354–1360.

[15] D. Chakraborty and T. Noguchi, "Effects of Bandlimiting in Nonlinear Digital Satellite Links," International Conference on Communications, Seattle, Washington, June 8–12, 1980, *Conference Record*, Paper 62.3.

[16] S. Murakami *et al.*, "Optimum Filters and Their Tolerance for Nonlinear Satellite Channels," Fifth International Conference on Digital Satellite Communications, Genoa, Italy, March 1981, *Proc.*, pp. 69–75.

[17] D. Chakraborty and C. J. Wolejsza, "A Survey of Modem Design and Performance in Digital Satellite Communications," *IEEE Journal on Selected Areas in Communications*, Vol. SAC-1, No. 1, January 1983, pp. 5–20.

[18] E. Christian and E. Eisenmann, *Filter Design Tables and Graphs*, New York: John Wiley, 1966.

[19] A. Zverev, *Handbook of Filter Synthesis*, New York: John Wiley, 1967, pp. 142–143, 245.

Appendix. Optimization routines

Amplitude matching

A Fortran computer program, AMATCH, was developed to match a candidate set of poles and zeros to a desired amplitude response. In carrying out the matching, poles and zeros are perturbed in small increments to minimize a mean-square error (MSE) cost function. Optimization is not terminated until a maximum peak-to-peak amplitude error ripple is either met or determined to be unreachable. Hence, termination is effected when successive root perturbations cease to lower the MSE.

Figures A-1 and A-2 are simplified functional flow charts outlining the AMATCH main program and its optimization routine, respectively. The variable names are defined in Table A-1. Program operation is described as follows. In the main program, pertinent reference data such as the frequency range of computation, number of data points, and predistortion mode, are read in. This information is used to compute a composite reference function, which may be predistorted. Additional approximation data such as the frequency range for matching, error weighting, and candidate poles and zeros must then be input to calculate the approximating function and error parameters. If a complete listing of the frequency response is not desired, the user can proceed directly to the optimization, or select the same or new functions or stop modes.

TABLE A-1. COMPUTER OPTIMIZATION VARIABLE NAMES

APTP	Maximum peak-to-peak amplitude variation specified for convergence
I	Total number of composite optimization cycles
J	$-\log_2$ (step-size increment) that led to termination
K	Total number of root passes that led to termination
L	Total number of iterations
M	Number of consecutive iterations of the same root
MSE	Mean-square error
MSELST	Last MSE
MSENEW	New MSE
MSEOLD	Old MSE
RPL	Maximum peak-to-peak amplitude or group delay variation computed for candidate root locations
TPTP	Maximum peak-to-peak group delay variation specified for convergence

The optimization routine consists of four nested DO-loops, as shown in Figure A-2. Beginning at statement 410, a convergence specification is read in for the desired peak-to-peak amplitude ripple variation (APTP). Although the program's convergence is based on an MSE cost function, termination is

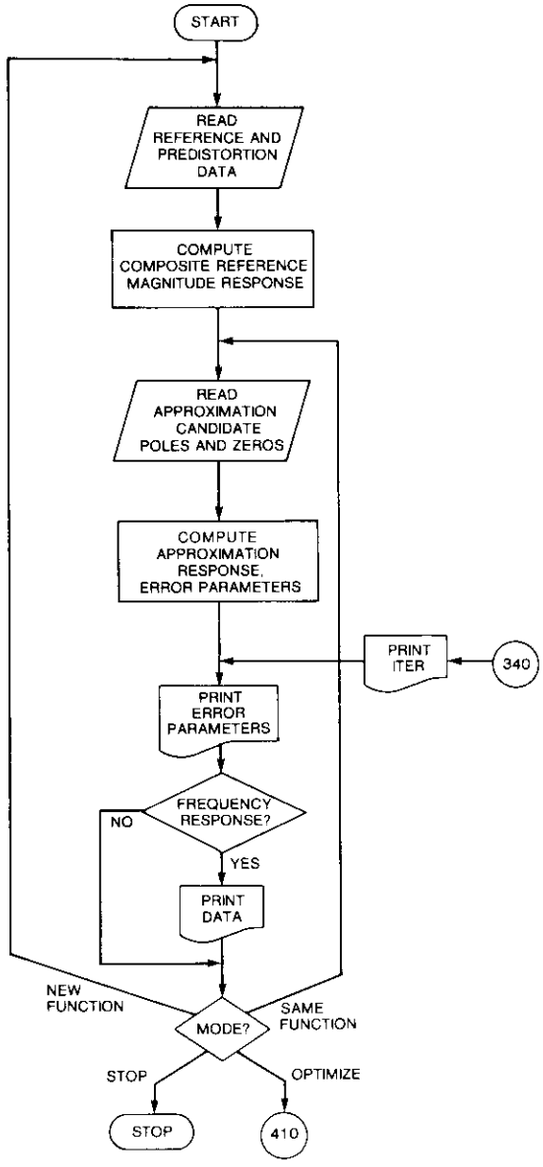

Figure A-1. *AMATCH Main Program*

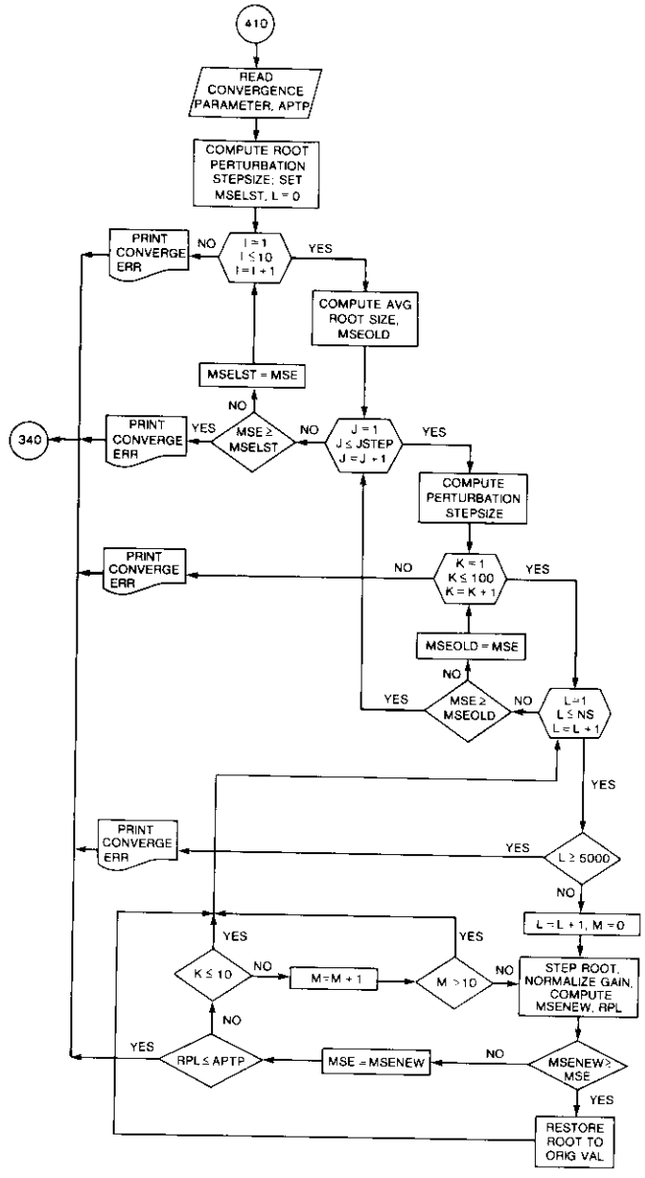

Figure A-2. *AMATCH Optimization Routine*

resolved only when the error ripple is less than or equal to APTP. From the relative magnitude of APTP, the number of perturbation step sizes is computed. Also, the minimum MSE is set equal to MSELST, and the total number of iterations, L, is initialized.

The outermost of the nested DO-loops allows the subsequent optimization procedures to be cycled as many as 10 times. In this loop, the average value of the real and imaginary parts of the candidate roots is determined. Then, in the second loop, a nominal value for the root perturbation step size is calculated and this value is reduced by a factor of 2 with each ensuing pass through the loop. In the third nested loop, the real and imaginary parts of each pole and zero are perturbed in turn, for as many as 100 passes. Each time the innermost loop is engaged, the total number of iterations is increased. After the perturbation value is added to or subtracted from the real or imaginary part of a root, a new MSE and its associated error parameters are computed. If MSENEW $\geq$ MSE, the root is restored to its original value and the next perturbation trial is summoned. Otherwise, MSE is set equal to MSENEW, and the peak-to-peak ripple is checked for convergence. If RPL $>$ APTP, optimization continues. For the first 10 root passes ($K \leq 10$), no individual root may be perturbed successively. This is to prevent any one root from wandering away from a contributory location or locking on to a local minimum. After 10 complete root passes, an individual root may be perturbed successively as many as 10 times in the same direction ($M \leq 10$).

The nested iterations discussed above are repeated until either normal termination is concluded or a convergence restriction has been triggered. To prevent excessively long run times, optimization will cease when $L = 5{,}000$ total iterations are completed. The routine will also end if $K = 100$ root passes are encountered. Finally, if no further improvement in MSE is possible for any step size (or when $I = 10$ overall cycles are concluded), optimization will also terminate.

Group delay equalization

A completely analogous program (GRDLOP) to that described for the amplitude response was used to equalize the group delay. Figures A-3 and A-4 are simplified flow charts for the main program and optimization routine, respectively. Pertinent differences relative to the amplitude optimization routine can be described as follows. Rather than having a reference group delay function, a constant reference value is computed after the number of equalizer sections has been determined and the composite average delay has been established. The reference group delay value is not normalized, as is the gain in the amplitude matching routine. The composite average is calculated from the pre-equalized response cascaded with the equalizer. The

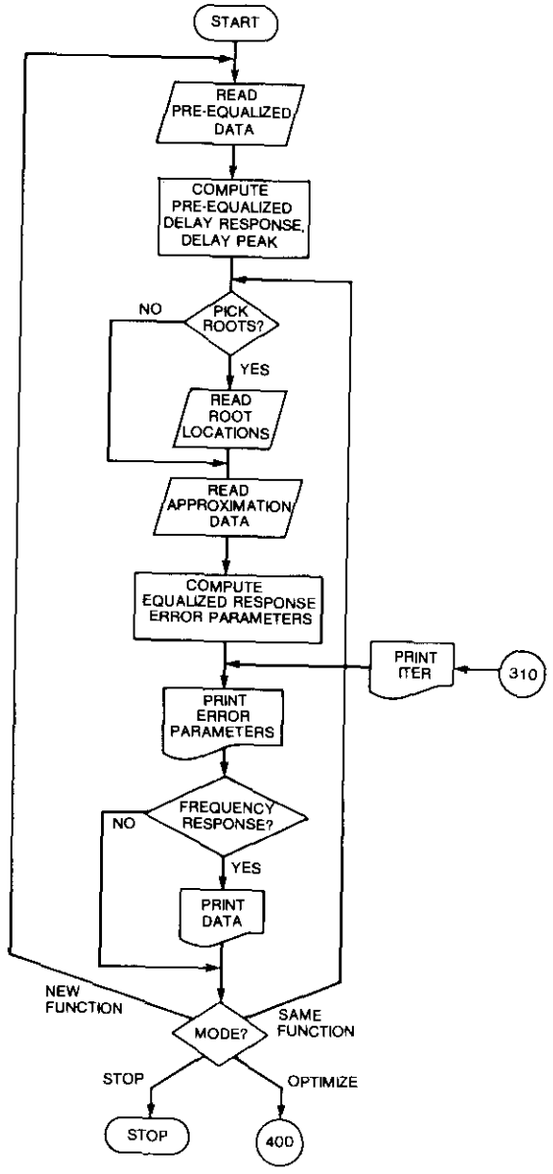

Figure A-3. *GRDLOP Main Program*

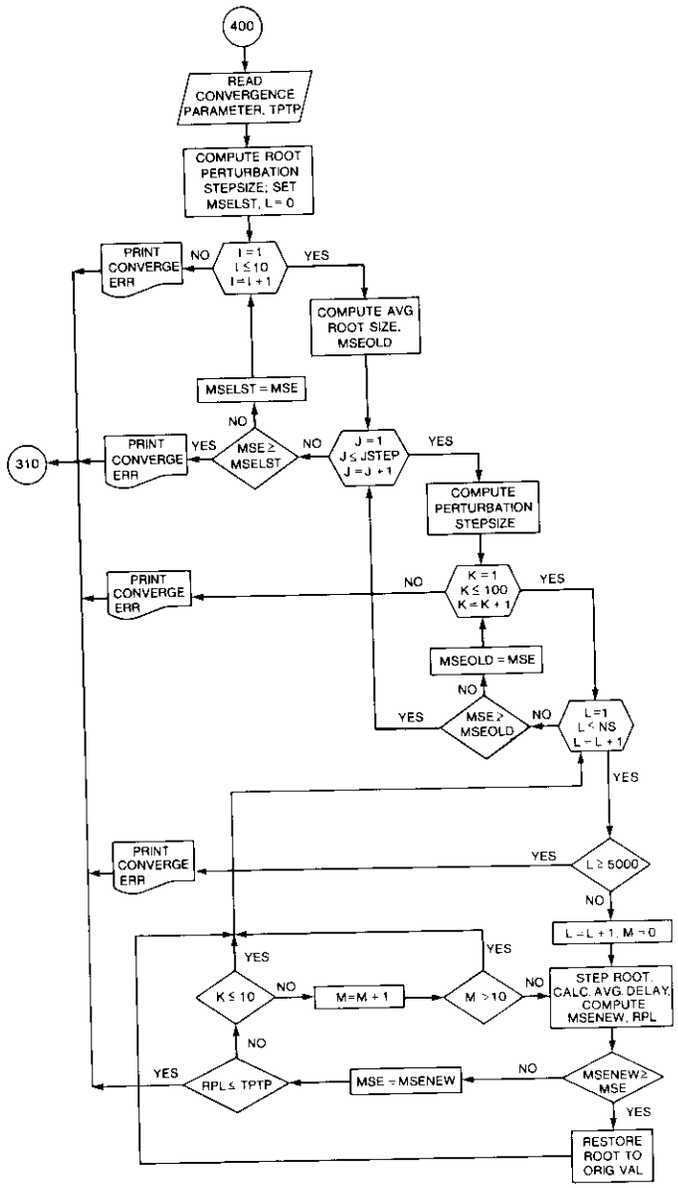

Figure A-4. *GRDLOP Optimization Routine*

pre-equalized group delay characteristic is computed from the poles and zeros that determine the magnitude response. Candidate equalizer root locations can be input, or they may be selected internally by the program. With regard to convergence, the peak-to-peak ripple termination parameter (TPTP) and the MSE cost function are still in effect.

John J. Poklemba received a B.S.E.E. from Drexel University in 1972, and the M.S.E.E. and E.E. degrees, concurrently, from the Massachusetts Institute of Technology in 1974. He is currently Associate Manager of the Transmission Processing Department at COMSAT Laboratories, where his principal interests are the application of detection and estimation theory to practical receiver structures, and the development of various types of filtering relevant to information transmission. At COMSAT, he originated the Concurrent Carrier and Clock Synchronization (CCCS) concept in 1978 and holds two patents on its implementation. In 1983, together with J. Thomas of COMSAT Laboratories, he developed the Digitally Implemented Modem (DIM), which is programmable in terms of data rate, spectral shaping, and modulation technique. Prior to joining COMSAT, Mr. Poklemba spent 2 years working with high-frequency receivers and high-resolution laser video signal processing.

A simulation study of rain attenuation and diversity effects on satellite links

J. MASS

(Manuscript received October 23, 1986)

Abstract

Rain cell shapes and sizes influence single path and diversity path attenuation statistics. A simplified model is proposed which simulates the three-dimensional structure of rain based on circularly cylindrical rain cells of constant rain rate having a lognormal distribution of cell diameters and a linear distribution of cell heights. The characteristics of these distributions depend on rain rate, and were originally established from radar-derived and other experimental data. Subsequent model adjustments were made to fit the experimental rain attenuation curves.

The simulation model requires earth station rain statistics either from meteorological models or from actual rain measurements. Attenuation distributions are computed along both single and diversity paths for a given frequency, elevation angle, and station separation, and results are given for transverse and longitudinal orientations of the diversity baseline. Model predictions are compared with experimental results at 24 stations having different frequencies, climates, elevation angles, and diversity spacings, and in most cases show discrepancies of less than 1 dB.

Introduction

Planning an earth station for satellite communications requires an estimate of the attenuation due to rain, especially in the frequency bands above 10 GHz. When attenuation becomes unacceptably high for a given grade of service, site diversity may be employed such that two interconnected earth stations at some distance from each other are operated simultaneously. In

the simplest configuration, only the path which experiences less attenuation at any instant is used. The need for diversity becomes increasingly important at higher frequencies and with stricter requirements for availability.

An estimate of attenuation statistics requires a good estimate of rain statistics. For most locales, good rain accumulation data are available for 25 years or more. However, these data must be converted to rain-rate distribution curves and then to single path attenuation distributions and diversity path attenuation distributions as required by systems engineers.

Existing models

Many attempts have been reported in the literature to relate path attenuation to rain measurements [1]–[4]. CCIR reports [5] have recommended the use of "effective path lengths" to convert from point rain distributions to path rain attenuation distributions, using computations of attenuation per kilometer of path length at constant rain rate [6],[7]. The specific attenuation is of the form α (dB/km) = aR^b, where a and b are constants depending upon frequency and rain type, and R is the rain rate in mm/hr. The effective path lengths depend on elevation angle, and change with rain rate to account for the variable spatial extent of the rain. The effective-path-length method, which is fairly simple to use, is based on regression analysis of experimental results; however, it may become inaccurate when applied to situations other than those verified experimentally because it is not based on a physical model of rain. Furthermore, it is not well adapted to estimating diversity performance.

As reviewed by Rogers [8], some attempts to estimate rain attenuation by modeling the spatial structure of rain cells have been reported. Zintsmaster and Hodge [9] assumed circularly cylindrical rain cells of constant height, relating cell diameter to rain rate in different ways. Misme and Fimbel [10] employed circularly cylindrical rain cells embedded in a pedestal of residual rain for terrestrial paths. Fimbel [11] applied the same method to slant paths with a constant 3-km rain cell height. Misme and Waldteufel [12] modeled rain attenuation on slant paths in the same manner, taking into account rain cell sizes as functions of high and low rain rates (convective rain and widespread rain, respectively). However, this method will probably not account for diversity effects because it does not allow for cell size variability at fixed rain rates. Rogers [13] used conically shaped cells of specified heights, with base diameters varying according to a probability law. Because he did not use cells of known rainfall, but rather cells causing a certain attenuation for which statistical information was available from radar measurements, it is difficult to apply this model when only rain statistics are available.

Allnutt and Rogers [14] proposed a simple site diversity model based on estimating the "knee" in the curve describing the diversity gain (in dB) *vs* the single path attenuation, as well as the diversity offset from the ideal diversity gain. This model, which is applicable only to relatively large site separations, assumes that the single path attenuation statistics are known or obtained from the rain statistics by CCIR-recommended or other methods.

By applying Crane's two-component rain model [15], Shieh [16] recently proposed a method which estimates diversity gain based on the spatial characteristics of rain. This method uses spatial correlation techniques with radar measurement results for convective (high-rain-rate) cells and the associated widespread "debris" rain [17]. Climatic zones are defined in terms of rain-rate exceedance statistics for convective rain and the mean and standard deviation of the lognormal rain rates for debris rain, as well as the relative contributions of convective and widespread rain.

Fedi and Paraboni [18] have recently proposed a radar-derived model to predict path attenuation from rain statistics. Their model assumes cylindrical cells of elliptical cross section with rain rate decreasing exponentially from the center. The parameters for the cell distribution (peak rain intensity, radii of cells) are taken from analysis of radar data collected in Italy, and the density of cells is fitted to the given rain exceedance statistics for the locality of interest.

Proposed model

The present study is based on a rain cell model previously developed at COMSAT Laboratories [19] which attempted to estimate not only rain attenuation from the geometric modeling of rain cells, but also diversity performance which depends on the spatial characteristics of the rain cells. The basic approach was similar to Fimbel's [11] in that it used the ratio of the locus of "possible areas" for the (circular) rain cell centers that cause a certain attenuation on a defined path, to the possible areas causing certain rain rates at a point. These ratios provide the link between the readily available point rain statistics and the required attenuation statistics.

To obtain results for diversity attenuation, larger diameter cells had to be admitted. Therefore, instead of using a definite relationship between the rain rate and the cell diameter, a lognormal cell-size distribution with a common variance was assumed, with the mean value depending on rain rate. Thus, larger rain cells are possible at a reduced probability. The need for many cell sizes for each constant rain rate, as well as a more accurate calculation of path length inside the cells, requires considerable computer time but should cause no undue problems in any laboratory or technical institution. In this study, an Amdahl 5860 computer was used with FORTRAN 77 programs.

This method is still largely artificial in that it assumes cylindrical cells of constant rain rate; however, it is believed that as the effects of horizontal and vertical extent are taken into account, the difference between the model and real rain cells would largely average out over longer time spans. The parameters describing the cells (diameter and height as a function of rain rate) were originally estimated from radar measurements of rain cells [20]–[22] and were then adjusted to improve the model.

The required rainfall inputs to the model are either Rice-Holmberg [23] parameters in the form of total yearly rainfall and thunderstorm–rain ratio, or rain rate values exceeded as measured or estimated at the site. As more experimental results have become available, it has been possible to test the model in different climates for attenuation statistics on single paths and diversity paths, with satisfactory results. The modeling also makes it possible to investigate to a first approximation the elevation angle dependence of single path and diversity path attenuations, as well as the effect of the separation distance between diversity stations.

The proposed method could be extended to different cell shapes, especially to the shape recently proposed by Capsoni *et al.* [24] (*i.e.*, cylindrical cells with rain rates exponentially decreasing with the radius), or to elliptically shaped cells that embody information obtained locally from meteorological radars. The proposed method assumes equal probability for rain cells to be anywhere in the area around the paths, which precludes orographic effects caused by such features as mountain ranges, lakes, and shorelines. Future extension of the rain cell modeling could take some of these effects into account by using different rain rate statistics for different areas around the station.

Model description

The rain cell model used in this study is based on the following assumptions:

a. Rain cells are circularly cylindrical and of constant rain rate.

b. Rain cell diameters are lognormally distributed, with the median depending on rain rate. The standard deviation of the lognormal distribution was taken as 1.1 for all cell sizes.

c. Rain cell height (thickness) is given by four values of equal probability. These heights are not necessarily measured from the ground, but from the horizontal base of the cylinder to the horizontal top. Rain in the process of falling but which has not yet reached the ground, or rain which has reached the ground but is about to end, accounts for the smaller heights. The cell heights also depend in some measure on the type of rain or on the rain rate, the maximum corresponding approximately to the height of the freezing layer above the ground.

d. Rain cells are equally distributed horizontally, implying that orographic effects are ignored.

For every sample rain cell taken from the population defined above, the modeling program calculates the probability that the rain cells cover more than a certain critical length, L_C, of a single path and of two paths simultaneously. The variable L_C is the length of the path in the rain cell of rain rate R that produces attenuation A, as given by $L_C = A/aR^b$. These probabilities are calculated relative to the probability that the rain cells in question cover a point. Summing all the weighted possible areas for all the cells of the chosen population of rain rate R and dividing by the weighted possible areas for rain rate R at a point yields the ratio of the probability of attenuation on a path exceeding A (due to rain cells of rate R) to the probability of the rain rate R itself at a point.

The cumulative rain rate distribution curve is arbitrarily divided into 13 intervals for which the rain rate is assumed to be constant and equal to the value at the center, as illustrated in Figure 1. Thus it is assumed that for a certain percentage of the year (*i.e.*, for a certain number of minutes every year as defined by the width of the percentage interval), all rainfall is of a fixed intensity and equal to the rain rate at the linear midpoint of the percentage scale (*e.g.*, 0.0075 percent for the interval from 0.005 to 0.01 percent). By summing these properly weighted contributions for all intervals of R, the probability that A will be exceeded on one path or on two paths simultaneously is given relative to the probability that R is exceeded at a point.

To calculate the above probability ratios for path lengths in excess of L_C, a simple approach was chosen. The length of the rain-covered part of the path, L_W, was calculated by simple geometry (Figure 2). Then, the center of the circular rain cell was translated in the horizontal plane to establish the boundaries of the area within which the center of the rain cell must be located in order to cover more than L_C ($L_W \geq L_C$) of one or both paths. This approach was chosen to avoid solving the rather cumbersome explicit formulas for the possible areas of the cell centers as a function of L, L_C, and r (see Figure 2), as used by Zintsmaster and Hodge [9]. This direct approach could easily be extended to differently shaped rain cells (elliptical, spherical, conical, etc.). Note that the path within the cell L_C is not always the horizontal projection L on the circular base divided by $\cos(E)$, where E is path elevation angle. In some cases, the path cuts through the upper base of the cell and is therefore shorter.

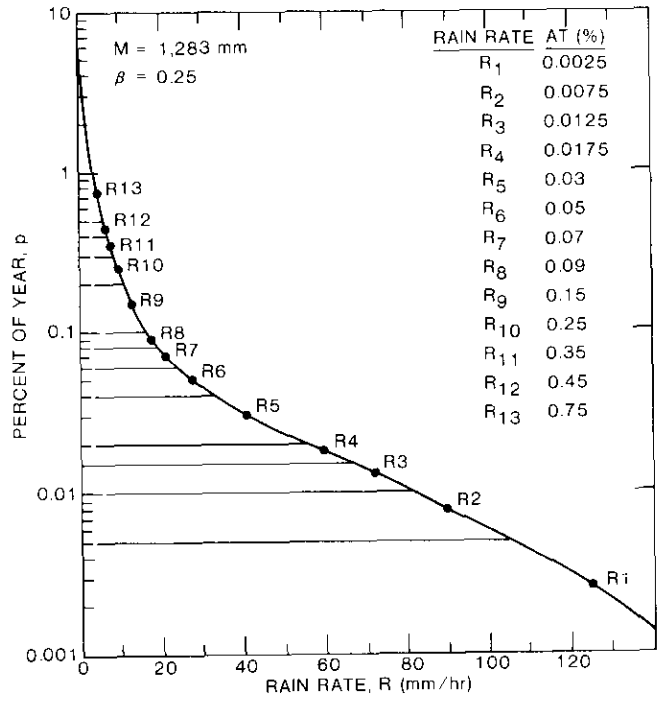

Figure 1. *Cumulative Rain Rate Distribution at Clarksburg, Maryland, October 1974 through September 1975*

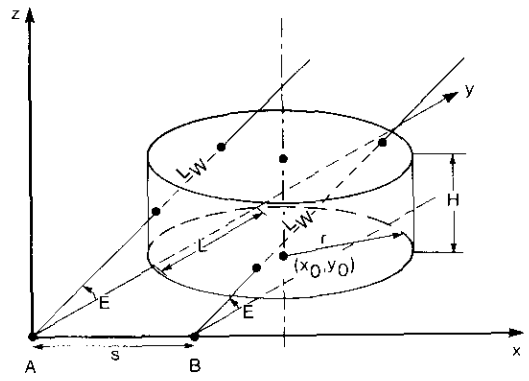

Figure 2. *Geometry for Two Paths From* A *and* B *Intersecting a Cylindrical Rain Cell*

To cover a point, the corresponding area of the cell center must be πr^2. Figure 3 illustrates the method for a certain radius r and covered length L_C, yielding the possible areas a_1, a_{12}, a_p for a single path, diversity paths, and point rain, respectively. By moving the circle of radius r, it can be verified that whenever the center is inside shaded area a_1, the circle will cover more than L_C on the path from B; whenever it is in area a_{12}, it will cover more than L_C on both paths; and whenever it is within a_p, it will cover point A. Assuming that the cell could be anywhere with equal probability, it follows that a_1/a_p is the ratio of the probability of a cell of radius r covering more than L_C of a path to the probability of its covering a point. This is a purely geometrical consideration and will be similar for slant paths, except that L_C (Figure 3) will then be the projection of the real L_C onto the ground plane.

The simulation program establishes areas a_1 and a_{12} by moving x_0, y_0 (Figure 2) to establish their boundaries. The possible area for rain cell centers in the transverse case is a_{12T} for the case where the two diversity stations are on an azimuth perpendicular to the satellite path azimuth, and a_{12L} for the longitudinal case in which the diversity stations are parallel to the satellite azimuth.

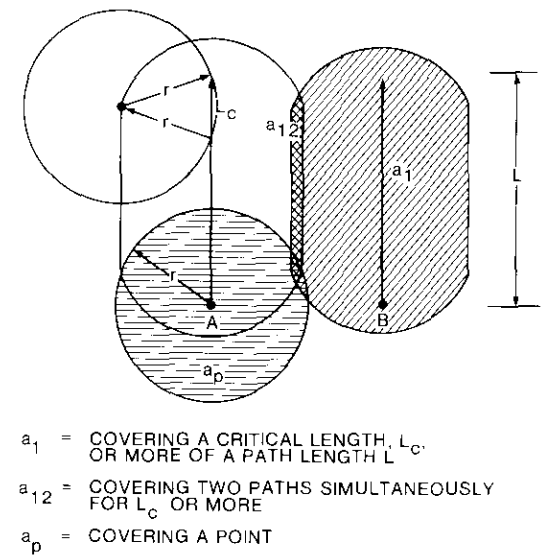

Figure 3. *Locus Areas or Possible Areas for Centers of Circular Rain Cells of Radius* r

Attenuation distributions from rain rate distributions

Performing the following steps, in sequence, will yield the attenuation distributions:

a. Obtain a rain rate distribution, $P(R)$, where P denotes probability.

b. Divide the rain rate cumulative distribution curve into 13 time-percentage intervals of different widths, Δp_i, where p denotes percentage.

c. For each time-percentage interval, take the center value and assume that all rain cells in this interval have the same constant rain rate, R_i, but a lognormal distribution of diameters and a height distribution approximated by four values (h_1, h_2, h_3, h_4) equally spaced for uniform distribution.

d. For each value of attenuation A_j from 1 to 14 dB (for $j = 1$ to $j = 14$), calculate the L_C required in a rain cell of rain rate R_i as follows: $L_C = A_j/aR_i^b$, where a and b depend on frequency, as in the formulas given by Olsen, Rogers, and Hodge [7].

e. For each value of R_i, assume 40 cells of height h_1 with diameters from 1 to 40 km, each having a relative probability of occurrence according to the lognormal distribution

$$P(D) = \frac{1}{\sqrt{2\pi}\, D \cdot \sigma} \exp\left[-\frac{ln(D/D_m)^2}{2\sigma^2} \right]$$

where D_m is the median value of D for the rain rate R_i and σ is the standard deviation of the distribution of $ln(D)$.* Also assume 40 cells of height h_2 with similar weights $P(D)$, and the same for heights h_3 and h_4. Altogether, 160 cells of constant rain rate R_i will be involved in the computation of the probability ratios for the percentage interval i.

f. For each of the cells of diameter D, calculate the areas a_1, a_{12T}, a_{12L}, and a_p. This requires L_C (from step *d*), L_W (from the geometry of the case), and S (separation between stations).

g. From the weighted ratios for each A_j (*i.e.*, for each value of attenuation), and for each rain rate interval around R_i, compute the following quantities:

* The value lnD_m is the mean of the variable lnD, which is normally distributed. This normal distribution has a median at lnD_m. Therefore, the median of the distribution of lnD is also at $D = D_m$. The mean of the distribution of lnD is at a higher value of D. See, for instance, Reference 25.

$$F_{ji} = \frac{\sum_{D,h} P_i(D) \cdot a_{1ji}(D,h)}{4 \sum_{D} P_i(D) \cdot a_{pi}(D)} = \frac{\text{probability that path attenuation exceeds } A_j, \text{ due to rain } R_i}{\text{probability that rain rate covers a point}}$$

For transverse orientation of diversity stations, denoted by T:

$$d_{Tji} = \frac{\sum_{D,h} P(D) \cdot a_{1ji}(D,h)}{\sum_{D,h} P(D) \cdot a_{12Tji}(D,h)} = \frac{\text{probability that path attenuation exceeds } A_j, \text{ due to } R_i}{\text{probability that both path attenuations exceed } A_j, \text{ due to } R_i}$$

For longitudinal orientation of diversity stations, denoted by L:

$$d_{Lji} = \frac{\sum_{D,h} P_i(D) \cdot a_{1ji}(D,h)}{\sum_{D,h} P_i(D) \cdot a_{12Lji}(D,h)} = \frac{\text{probability that path attenuation exceeds } A_j, \text{ due to } R_i}{\text{probability that both path attenuations exceed } A_j, \text{ due to } R_i}$$

The factor 4 in the denominator of F_{ji} is required because the sum $\Sigma\, P_i(D) \cdot a_{1ji}(D, h)$ was taken four times, once for each height. (For the case where a_{1ji} is always equal to a_{pi}, the result must be $F_{ji} = 1$.)

h. For the same percentage interval (with R_i at center), calculate F_{ji}, d_{Tji}, and d_{Lji} for all j (say, for A_j from 1 to 14 dB).

i. Repeat steps (*c*) through (*h*) for each percentage interval i of width Δp_i.

k. Form the following sums to give the cumulative distributions of A_j on single and diversity paths:

$$P(A_j) = \sum_i \Delta p_i F_{ji} = \left\{ \begin{array}{l} \text{probability of attenuation} \\ A_j \text{ being exceeded for a} \\ \text{single path} \end{array} \right.$$

$$P(DAT)_j = \sum_i \frac{\Delta p_i F_{ji}}{d_{Tji}} = \left\{ \begin{array}{l} \text{probability of attenuation } A_j \text{ being} \\ \text{exceeded for transverse diversity} \\ \text{paths due to single rain cells} \end{array} \right.$$

$$P(DAL)_j = \sum_i \frac{\Delta p_i F_{ji}}{d_{Lji}} = \left\{ \begin{array}{l} \text{probability of attenuation } A_j \text{ being} \\ \text{exceeded for longitudinal diversity} \\ \text{paths due to single rain cells} \end{array} \right.$$

Corrected diversity attenuation distributions are obtained by adding to the probability calculated for single rain cells the probability of rain attenuation (A_j) caused on the second path by other cells, which is nearly equal to the probability of both paths being covered by rain independently. This correction is the diversity attenuation conditional probability (conditioned to total rain time) for mutually independent single-site statistics and is obtained by squaring the conditional probability that rain attenuation exceeds A_j on one path. This rain condition amounts to approximately 4 percent of the year on the U.S. East Coast. (Changing this value to 3 or 5 percent would not produce very different results.) The corrected distributions are then given by the sums of probability for two conditions: that a single cell caused the indicated attenuation (A_j), and that two different cells caused the attenuation, as

$$P(DATC)_j = P(DAT)_j + P(IND)_j$$

for transverse diversity, and

$$P(DALC)_j = P(DAL)_j + P(IND)_j$$

for longitudinal diversity, where

$$P(IND)_j = 0.04 \left\{ \frac{P(A_j)}{0.04} \right\}^2$$

is the diversity attenuation distribution for stations in the same weather area that have independent rain rates (spacing greater than about 40 km). As the largest rain cell assumed for the model had a diameter of 40 km, it is assumed that for stations separated by more than 40 km, all diversity attenuation is caused by different rain cells.

Discussion of assumptions

In the simulation program described above, the 1-minute averaged rain rate distribution for step (a) is usually obtained from the Rice and Holmberg [23] model. Only the total yearly rainfall, M (mm), and the thunderstorm rain ratio, β, need be specified. The percentage of the year for which the rain rate, R, is exceeded is given by [23]

$$p(R) = (M/8.76) \cdot \{0.03\,\beta \exp(0.03R) + 0.2\,(1 - \beta) \cdot [\exp(-0.258R) + 1.86 \exp(-1.63R)]\}$$

in which only the first term in the main brackets is relevant for $R > 40$ mm/hr. The M in the U.S. East Coast area is approximately 800–1,300 mm, while β is typically between 0.08 and 0.3.

Usually, M is known from long-term meteorological data and β can be obtained from published values [23] or can be estimated from regularly reported "excessive short duration rainfalls" by drawing a line through the median values for many years of recorded 5-, 10-, 15-, and 20-minute "excessive precipitation" values [26].

If measured rain rate data are available, the 13 rain rate values needed for modeling (see Figure 1) can be directly specified. Figure 1 shows the rain rate distribution for Clarksburg, Maryland (October 1974 through September 1975) arbitrarily divided into 13 intervals. Rain rates below 2 mm/hr do not contribute significantly to the attenuation distribution. For example, a 15.2-km path covered by rain at an intensity of 2 mm/hr would cause only 1 dB of attenuation at 14.2 GHz.

The parameters D_m and σ of the lognormal distribution, and the heights, h, of the rain cells of step (e), will to some extent control the shape of the distribution curves for single and diversity paths. These parameters can be modified in order to fit the model to experimental data for a particular climate, and the model can then be extrapolated to other frequencies, elevation angles, separations, or orientations of the diversity stations in that climate.

The values of D_m, σ, and h used in the program were originally based on radar measurements of rain cell size distributions as given by Strickland [20], Katz [21], and Konrad and Kropfli [22]. For all of the measurements, the lognormal distribution of rain cell sizes was found to be applicable, as is often the case in nature when many multiplying random factors influence a variable. However, because of the way the data are presented, there is only an approximate correspondence between the model parameters and the radar-derived diameters and heights. The radar-derived values had to be adjusted to fit the experimental data, since real rain cells are not circular and not of uniform rain rate. In particular, the median diameters of the distribution, D_m, had to be increased considerably for the very low rain rates in order to obtain the smaller experimental diversity improvements at the lower attenuations.

It is evident from radar pictures that the contours of low rain rates (5 or 10 mm/hr) are noncircular, while intense rain rates tend to have more circular contours. For a randomly shaped contour, the mean path length would be greater and the diversity advantage would be less than for a circular cell of equal area (as can easily be verified graphically). Therefore, the program must use larger than equal-area diameters for D_m at low rain rates.

Table 1 was used to specify rain conditions in the U.S. East Coast area, in Europe, and in East Asia by fitting to experimental data. The same table

was also applied to attenuation simulations in all these areas after some adjustment to enable the use of a single table for all climates.

TABLE 1. PARAMETERS OF SPATIAL STRUCTURE OF RAINFALL FOR MODEL USE

RAIN RATE, R (mm/hr)	MEDIAN DIAMETER, D_m (km)	HEIGHTS, h (km)	STANDARD DEVIATION, $\sigma(\ell n\, D)$
>50	1.2	1, 2, 3, 4	1.1
30–50	2	1, 2, 3, 4	1.1
20–30	4	1, 2, 3, 4	1.1
14–20	8	2, 2.7, 3.3, 4	1.1
8–14	12	3, 3.7, 4.3, 5	1.1
0–8	20	4, 4.3, 4.7, 5	1.1

The intervals of the rain distribution curve (Figure 1) for which $R > 30$ mm/hr influence the higher attenuation values (above 6 dB at 11 GHz), while those for which $R < 14$ mm/hr influence most strongly the 1- to 3-dB values on the attenuation distribution. It has been found that single path attenuation distributions are influenced mainly by the heights of the cells, while diversity gains are governed by the median cell diameters, D_m. Attenuation distributions are insensitive to changes in σ of about 0.9 to 1.3, which is the approximate range of variability of the parameter according to radar measurements [20],[21] and rain gauge measurements, with time variations converted to spatial variations [27].

A good check on the D_m and σ values of the table would be obtained by comparing calculated and experimental diversity rain rate distributions for two points at various distances such as 10, 20, and 30 km. Unfortunately, few such experiments are available. Comparison with Japanese rain diversity data given by Yokoi, Yamada, and Ogawa [28] would confirm the D_m of Table 1. Point rain diversity results for New Jersey, as given by Freeny and Gabbe [29] for higher rain rates, are also consistent with the D_m used in the table for values of $R > 30$ mm/hr.

The rain cell heights used in Table 1 are actually instantaneous thicknesses and not necessarily altitudes above ground. Rain cells having a cylindrical structure in which the rain has not reached the ground or does not extend to the clouds are accommodated by the program, as can be seen from the geometry of the calculation. From geometrical considerations, it is clear that a circular cylindrical rain cell of any thickness based at some altitude will have the same ratio of probabilities F, d_t, and d_L as one based on the ground.

The instantaneous heights of rain cells are normally not reported because radar returns are usually averaged over long periods in order to obtain the altitude dependence of reflectivity, which is fairly constant up to the melting layer. Crane [30] reports an average vertical extent of rain cells of between 1 and 2.5 km, which is reflected in the vertical extents assumed in Table 1.

The parameters a and b required in step (d) where

$$A[\text{dB/km}] = aR[\text{mm/hr}]^b$$

were taken from the Olsen, Rogers, and Hodge [7] formula as follows:

For $f = 2.9$ to 54 GHz	$a = 4.21 \cdot 10^{-5} \cdot f^{2.42}$
For $f \leq 8.5$ GHz	$b = 0.851 \cdot f^{0.158}$
For f between 8.5 and 25 GHz	$b = 1.41 \cdot f^{-0.0779}$
For $f \geq 25$ GHz	$b = 2.63 \cdot f^{-0.272}$

Values are given in Table 2 for several sample frequencies.

TABLE 2. VALUES OF a AND b FOR DIFFERENT FREQUENCIES

PARAMETER	FREQUENCY (GHz)					
	11.2	11.6	13.6	17.8	19.5	30.0
a	0.01457	0.01586	0.02330	0.04470	0.05574	0.15810
b	1.168	1.165	1.151	1.127	1.119	1.043

As noted earlier, the independent diversity attenuation distribution caused by two rain cells had to be added to the geometrically calculated distributions based on single rain cells. The probability of a certain attenuation being exceeded at any two independent stations in the same weather area (same rainy days) is about one-fourth of the probability that this attenuation is exceeded at two stations separated by about 16 km for the case where only a single rain cell affects both stations. The probabilities $P(OPT)$ and $P(DAT)$ at $A = 6$ dB may be compared in the computer printout given in the Appendix. [Note that $P(IND)$ was called $P(OPT)$ in the computer program.]

The addition of the independent diversity, based on squaring the conditional probability that a single station will exceed a certain attenuation, is equivalent to adding the cases where the two paths are affected by different rain cells. This approach may be somewhat pessimistic, especially at very small spacings,

because the probability of different cells affecting both stations would become smaller and tend toward zero for $S = 0$. However, for small spacing, the addition of $P(IND)$ is insignificant because of the much larger contribution of the geometrical effect.

Comparison with experimental results

When the simulation program was originally developed, few diversity results were available. The model was adjusted to fit data from three experiments conducted in New Jersey using radiometers at 15.5 GHz, as measured by Gray (reported by Hogg and Chu [31]), and radiometer data obtained at Clarksburg by COMSAT at 11.6 GHz, as well as data for Boston obtained from ground-to-satellite 17.8-GHz transmissions with the ATS-6 satellite [32], including diversity results for an 11-km spacing. The fitting consisted of varying the entries in the rain table that specify the diameters and heights of rain cells as a function of rain rates, as in Table 1.

Subsequently, experimental data have become available and, in an attempt to specify a unique rain structure table for all climates, the cell heights had to be increased for the lower rain rates (below 20 mm/hr). Table 1, a compromise to fit the different climates, is applied to all comparisons between experiment and model for the various stations. Recently, Crane has pointed out that radar measurements of the geometrical structure of rain tend to confirm that a basically similar structure may be ascribed to rain worldwide, especially at high rain rates [33].

Table 1 is based on comparisons with many experimental measurements and could certainly be refined as more data become available. Alternatively, different rain tables could be adopted for different rain climates. This subsection compares the model results and experimental measurements of the exceedance statistics of single path attenuations and diversity path attenuations. The single path and diversity paths of 13 stations were compared, and single path data were compared at another 11 stations. The data were chosen to represent a wide range of climates, frequencies, elevation angles, and diversity separation distances.

In many cases, concurrent rain data were available and were used in the simulation; in other cases, meteorological data as available were used for the station. A list of stations in North America, Europe, and East Asia for which those comparisons were made is given in Tables 3 and 4 for diversity path and single path attenuation experiments, respectively. Most data were collected at frequencies near 11.6 GHz (mainly radiometric), with some collected at 17.8 and 19, 20, or 30 GHz (satellite sources).

TABLE 3. DIVERSITY PATH ATTENUATION EXPERIMENTS*

LOCATION	TYPE**	FREQUENCY (GHz)	ELEVATION (deg)	DIVERSITY SEPARATION (km)	RAIN DATA	DATES	REFERENCE	REMARKS
Albertslund, Denmark	B-OTS	11.8	26.5	15	215, 0.06	1979, 1980	2	p. 206 M, β fit to measured data
Austin, TX	R	13.6	30	16	m	1979, 1980	34	—
Boston, MA	B-ATS-6	17.8	35.8	11	m	5/74–5/75	35	Beacon up-link
Blacksburg, VA	B-Sirio	11.6	10.7	7.3	m	7/80–6/81	36	—
Cobb County, GA	R	12	20	37.5	m	4/79–10/80	37	—
Etam, WV	R	11.6	18	35	1260, 0.2	10/77–10/80	38	M, β from meteorological estimates
Ontario, Canada	R	13	15.5	27.4	820, 0.13	1980	39	M, β from meteorological data [40],[23]
New Jersey	R	15.5	32	19 27 33	1125, 0.09	11/71–11/72	41	M, β from meteorological data [40],[23]
Palmetto, GA	R	17.8	38.2	16 31	m	6/73–6/75	41	Rain measurements not overlapping
Slough, U.K.	B-ATS-6	30	22.4	12.3	Zone E	7/75–8/76	42	Model fit to CCIR Zone E, [43]

TABLE 3 (continued). DIVERSITY PATH ATTENUATION EXPERIMENTS*

LOCATION	TYPE**	FREQUENCY (GHz)	ELEVATION (deg)	DIVERSITY SEPARATION (km)	RAIN DATA	DATES	REFERENCE	REMARKS
Slough, U.K.	R	11.6	29.5	16.4 23.6	785, 0.03	1973–75	44	From meteorological data [40],[23]
Quebec, Canada	R	13	18	18.6 22.7 31.8	Zone E	1980	39	Model fit to CCIR Zone E [43]
Yokosuka, Japan	B-CS	19.5	48	19	1563, 0.12	3/75–8/77	45	M from meteorological data [40], β from fit to measurements

* Rain data are measured (m), derived from (M, β) parameters shown, or fit to designated CCIR rain zones.
** B = beacon; R = radiometer.

TABLE 4. SINGLE PATH ATTENUATION EXPERIMENTS

LOCATION	TYPE*	FREQUENCY (GHz)	ELEVATION (deg)	RAIN DATA**	DATES	REFERENCE	REMARKS
Bringelly, Australia	R	11.6	43	m	5/76–3/77	46	—
Clarksburg, MD	R	11.6	42	m	10/74–9/75	47	—
Cobb County, GA	R	20	20	m	4/79–11/80	37	—
	R	30	20	m	4/79–11/80	37	—
Fucino, Italy	B-Sirio	11.6	31	m	78–81	2	p. 142
Fucino, Italy	B-Sirio	12.8	31	m	78–81	2	p. 124
Gometz, France	B-Sirio	11.6	32	m	1978	2	p. 124, problems with rain data
Harwell, U.K.	R	11.6	28	m	11/75–11/76	46	—
Lario, Italy	B-Sirio	11.6	32	m	78–82	2	p. 124, model gives lower attenuation
Lario, Italy	R	11.7	25	1412, 0.06	3/77–6/78	47	Rain data
Lustbühl, Austria	B-OTS	11.6	35.2	m	1979–82	2	p. 124
Michelbachberg, Germany	R	11.6	33	m	5/76–6/77	46	—
Nederhorst, Netherlands	B-OTS	11.6	30	m	1979–81	2	p. 124
Singapore	R	11.7	41	m	1/76–2/77	46	—

* R = radiometer; B = beacon.
** m = measured rain data.

Figures 4 and 5 show data comparisons chosen to represent the different climatic zones, frequencies, and elevation angles. Rain data were gathered from three possible sources: published concurrent measurements, estimates taken from M and β tables (if possible, using M for the experiment time period), or from fitting the 13 time percentages of the model to CCIR rain zone data [43].

Figures 6 and 7 summarize the differences between experiment and predictions for all stations. The differences are shown at yearly time percentages of 0.1, 0.01, and 0.001 percent. In some cases where the experimental data did not cover the low percentages, values for slightly higher percentages were used. Figure 6 shows single path attenuation differences only. Except for a few extreme cases, the errors are within ± 1 dB. Since the simulation program simulates rain attenuation only, another few tenths of a dB of attenuation are probably due to clouds, fog, and other non-rain effects. For comparison, this would shift the 0-dB line by a few tenths of a dB below the 0-dB line of Figure 6, as implied by the -0.5 ± 1 dB band. The same shift occurs in Figure 7, which summarizes the diversity difference measurements.

In both Figures 6 and 7, the differences for 0.001 percent of the year are sometimes considerable. At such low time percentages, the experimental measurements tend to be less reliable due to instrumentation effects and data processing procedures. In the simulation model, the decrease in accuracy is mainly due to the artificiality becoming more evident because of less statistical averaging at the high rain rates.

Baseline orientation is addressed by the model in the two limiting cases: transverse and longitudinal orientations. As the thicknesses of the circular cells assumed in this model are comparable to their diameters, there appears to be no pronounced difference between these two extreme cases so that normally no preference exists. This characteristic was examined in a previous paper [19] and examples were given. In Figures 4b and 4d, the slight differences between the longitudinal and transverse diversity attenuation results seem contradictory to intuition, as it would be expected that longitudinally oriented stations with both paths in the same vertical plane would have a greater chance of passing through the same rain cell, resulting in a smaller diversity effect. However, this is apparently not so at the distances, angles, and limited cell thicknesses considered here. For instance, at a diversity separation of 15 km and an elevation angle of only 20°, the vertical distance between the paths is over 5 km, more than the thickness of most rain cells. No distinction was made between the different polarizations of the signal because the differences in rain attenuation due to polarization are small and probably negligible in the context of this model.

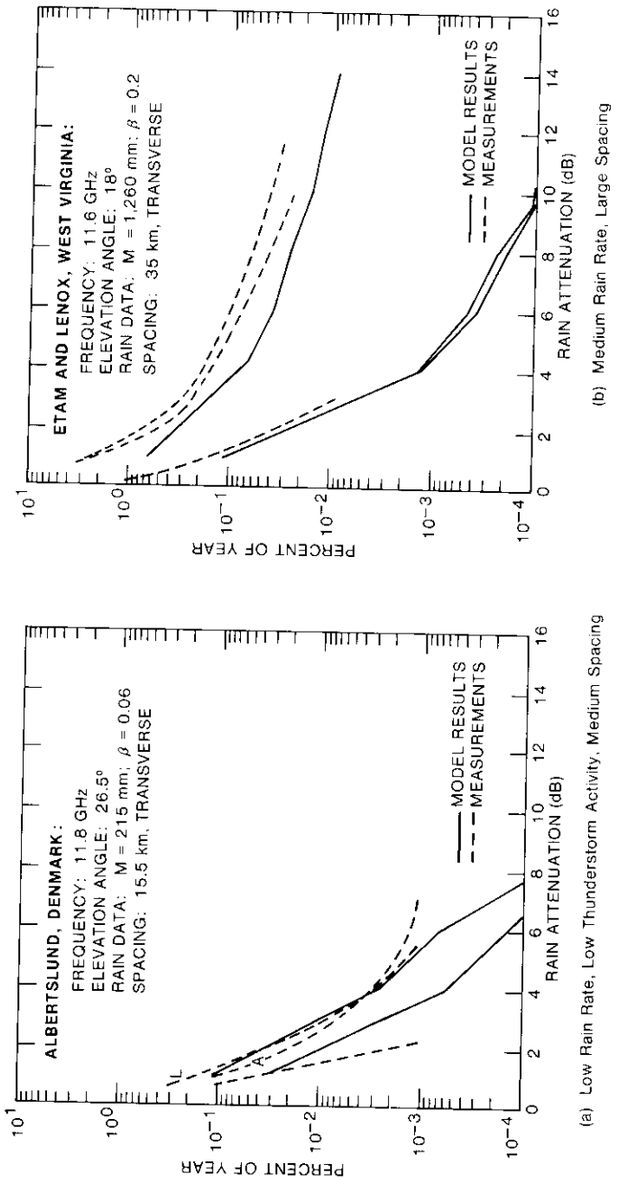

(b) Medium Rain Rate, Large Spacing

(a) Low Rain Rate, Low Thunderstorm Activity, Medium Spacing

Figure 4. *Comparison of Model and Measurements for Single Path and Diversity Path Attenuations*

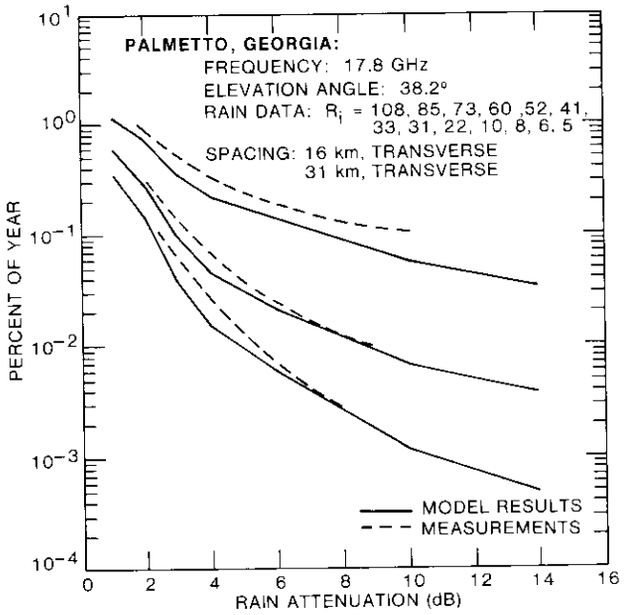

(c) High Rain Rate, High Frequency, Two Spacings

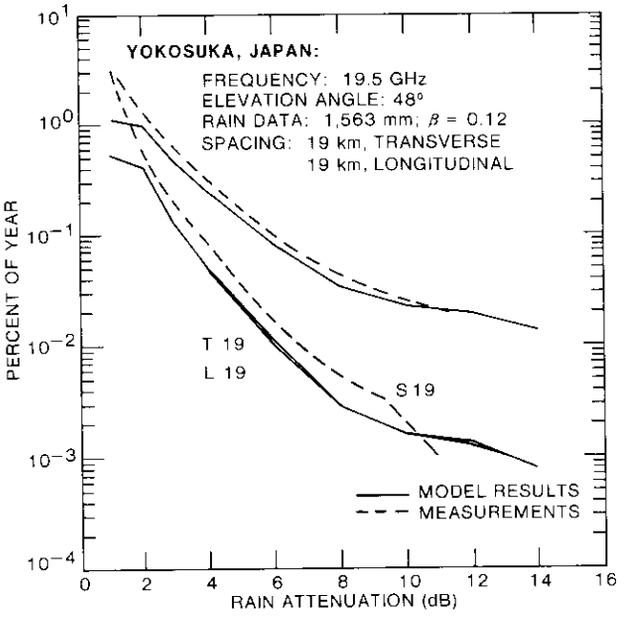

(d) High Rain Rate, High Frequency

Figure 4. (continued) Comparison of Model and Measurements for Single Path and Diversity Path Attenuations

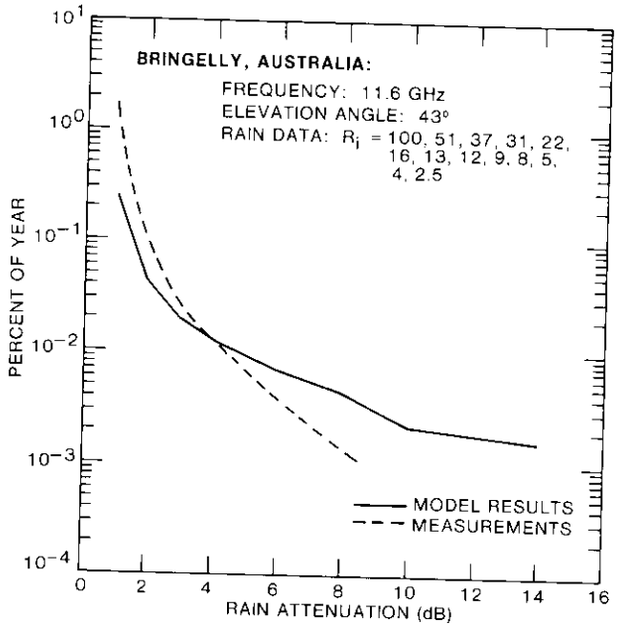

(a) High Rain Rate

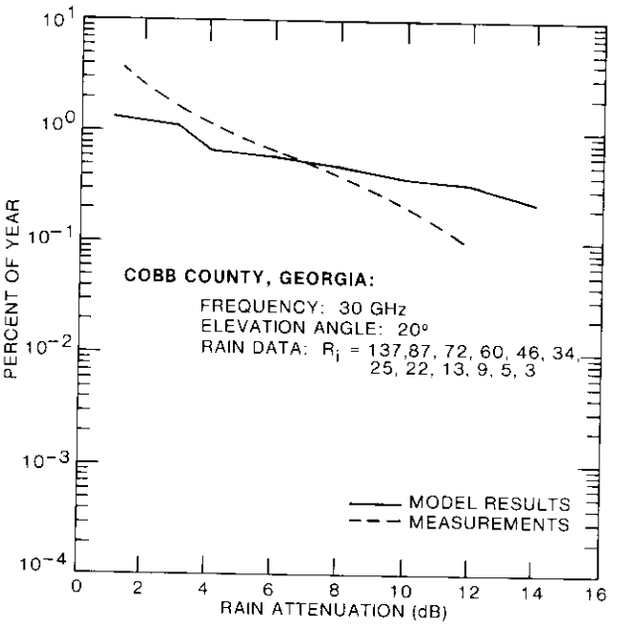

(b) High Rain Rate, High Frequency

Figure 5. *Comparison of Model and Measurements for Single Path Attenuations*

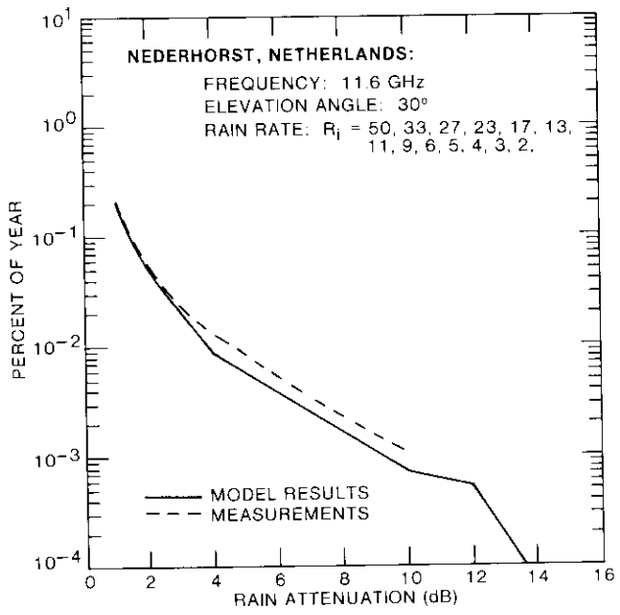

(c) Low Rain Rate

Figure 5. (continued) *Comparison of Model and Measurements for Single Path Attenuations*

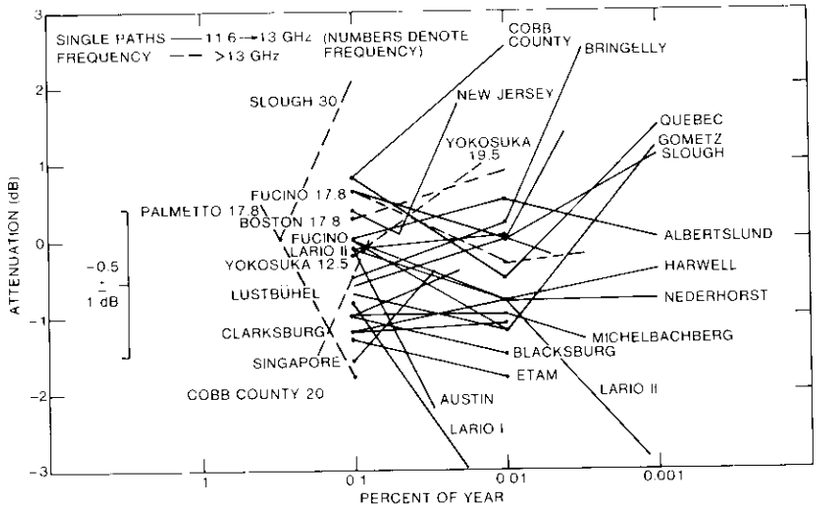

Figure 6. *Attenuation Differences Between Model Results and Measurements for 25 Single Path Experiments*

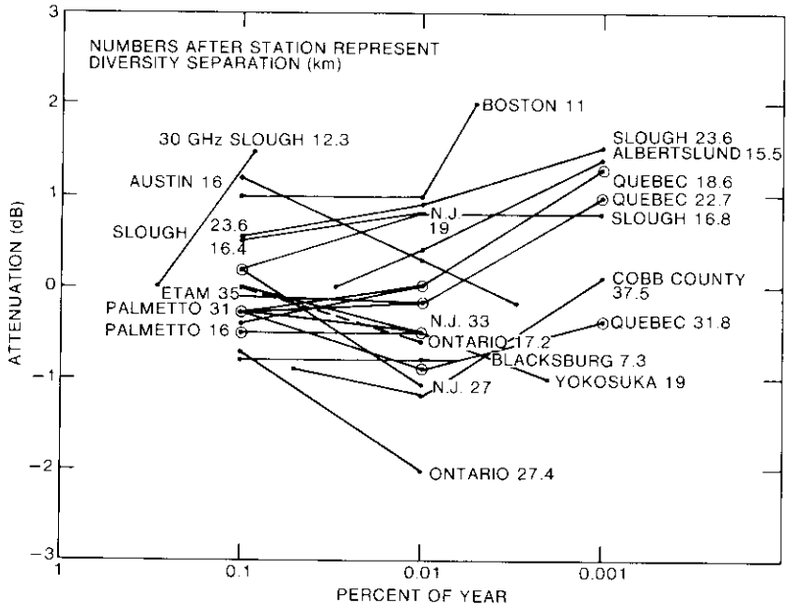

Figure 7. *Attenuation Differences Between Modeled and Experimental Results for Diversity Stations*

Effects of site separation distance

The effectiveness of increasing the site separation between diversity stations is under study using the rain structure model. First, results for the rain climate of the U.S. East Coast could be compared to experimental results obtained by Goldhirsh and Robison [48] using radar measurements, and by Hodge [49] using attenuation measurements and radiometer results. The influence of lower elevation angles on the effectiveness of site separation could then be modeled and compared with experimental measurements as they become available.

The solid lines of Figure 8 show the diversity gain measured or inferred from measurements as a function of site separation for single path attenuations of 10 dB and 6 dB. Goldhirsh's radar measurements were taken at 18 GHz and at an elevation angle of 45°, while Hodge's data refer to 15.3 GHz and 16 GHz at an elevation angle of 38°. These data were collected in Virginia, New Jersey, and Ohio, respectively.

The model simulation results, shown as broken lines in Figure 8, are for 10-dB and 6-dB single path attenuation. The results of the model simulation for an elevation angle of 40°, a frequency of 11.2 GHz, and a rain climate

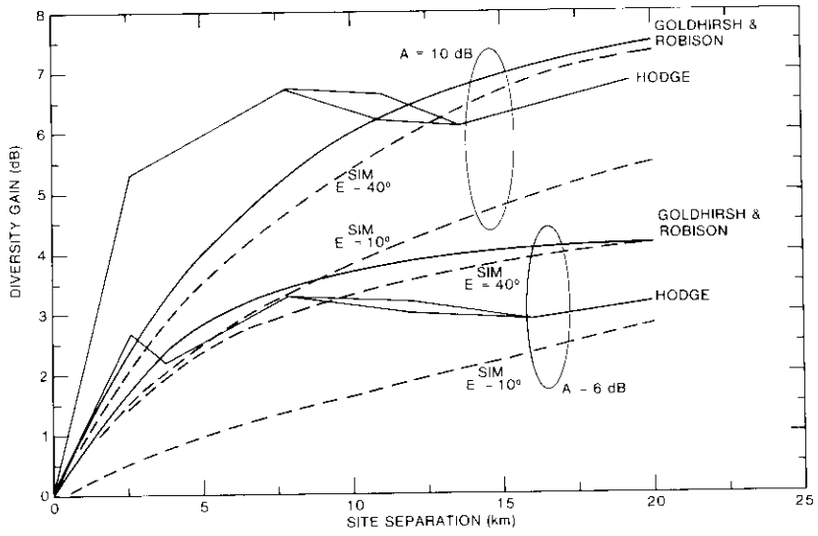

Figure 8. *Diversity Gain as a Function of Site Separation for Single Site Attenuations of 10 and 6 dB*

defined by a total annual rainfall of $M = 990$ mm and a thunderstorm ratio of $\beta = 0.11$, show a good fit with the experimental results. The decrease of diversity effectiveness with elevation angle is also shown.

Diversity gains for an elevation angle of 10° are shown to be rather small at site separations of up to 20 km. The following is a possible physical explanation for the small gain. For higher elevation angles, cells of high rain rate must account for the 10-dB single-path attenuation because the path length inside the cell is limited mainly by cell height rather than cell diameter. For lower elevation paths, lower rain-rate cells having larger diameters can account for the high attenuation, and therefore site separation must be larger to obtain the same effect.

Studies are under way using the described model to estimate the influence of frequency, rain climate, elevation angle, and site separation on diversity gain.

Conclusions

A relatively simple model of cylindrical cells of constant rain rate with varying diameters and heights (thicknesses) has been presented which seems to give usable results, not only for single ground-satellite paths, but also for estimating diversity effectiveness, even for such diverse climates as those of the U.S. East Coast, Europe, and East Asia. Unfortunately, no tropical rain measurements are available to test and adjust the model.

In its present form, the model does not include orographic effects. These could possibly be included in future work if the different rain statistics in the various directions from the stations are known. In some cases, due to local climatic effects, rain cells tend to be more elliptical or to appear in squall lines of known azimuth, and future studies could model elliptical cells with a specified orientation. If the model is found to give a fairly accurate picture of attenuation caused by rain on ground-satellite paths, the dependence of diversity gain and single path attenuation on frequency, elevation, separation distance, and rain climate could be simulated.

Acknowledgments

The constructive criticism of D. Fang, R. Taur, and J. Harris is acknowledged. Special appreciation is due to programmers F. Lee and J. Jih. G. Hyde and L. Pollack encouraged the study and supported the program development, and D. Rogers supported the evaluation phase and contributed to it in many ways.

References

[1] G. Brussaard, "Prediction of Attenuation due to Rainfall on Earth Space Links," *Radio Science*, Vol. 16, No. 5, September–October 1981, pp. 745–760.

[2] F. Fedi, *ed.*, "Prediction of Rain Attenuation Statistics From Point Rainfall Intensity Data," *Alta Frequenza*, May 1985, pp. 140–156.

[3] L. J. Ippolito, "Radio Propagation for Space Communication Systems," *Proc. IEEE*, Vol. 69, No. 6, June 1981, pp. 697–727.

[4] R. K. Crane, "Prediction of Attenuation by Rain," *IEEE Transactions on Communications*, Vol. COM-28, No. 9, September 1980, pp. 1717–1733.

[5] CCIR, "Propagation Data and Prediction Methods Required for Earth-Space Telecommunication Systems," Report 564-3, *Recommendations and Reports of the CCIR*, Vol. 5, Geneva, 1986, pp. 389–431.

[6] R. G. Medhurst, "Rainfall Attenuation of Centimeter Waves: Comparison of Theory and Measurement," *IEEE Transactions on Antennas and Propagation*, Vol. AP-13, No. 4, July 1965, pp. 550–564.

[7] R. L. Olsen, D. V. Rogers, and D. B. Hodge, "The aR^b Relation in the Calculation of Rain Attenuation," *IEEE Transactions on Antennas and Propagation*, Vol. AP-26, No. 2, March 1978, pp. 318–329.

[8] R. R. Rogers, "Statistical Rainstorm Models: Their Theoretical and Physical Foundations," *IEEE Transactions on Antennas and Propagation*, Vol. AP-24, No. 4, July 1976, pp. 547–566.

[9] L. R. Zintsmaster and D. B. Hodge, "The Prediction of Millimeter Wavelength Precipitation Attenuation Using a Cylindrical Storm Cell Model," NASA-CR-122445, Ohio State University, Columbus, June 1972.

[10] P. Misme and J. Fimbel, "Détermination Théorique et Expérimentale de l'Affaiblissement par la Pluie sur un Trajêt Radioeléctrique," *Annales des Telecommunications*, May–June 1975, pp. 149–158.

[11] J. Fimbel, "Affaiblissement Terre-Satellite Geostationnaire à partir de Mésures Radio-metriques a 20 GHz," *Annales des Telecommunications*, May–June 1975, pp. 159–162.

[12] P. Misme and P. Waldteufel, "A Model for Attenuation by Precipitation on a Microwave Earth-Space Link," *Radio Science*, Vol. 15, No. 3, May–June 1980, pp. 655–665.

[13] R. R. Rogers, "Radar Derived Statistics on Slant-Path Attenuation at 10 GHz," *Radio Science*, Vol. 7, No. 6, June 1972, pp. 631–643.

[14] J. E. Allnutt and D. V. Rogers, "Novel Method for Predicting Site Diversity Gain on Satellite-to-Ground Radio Paths," *Electronics Letters*, Vol. 18, No. 5, March 1982, pp. 233–235.

[15] R. K. Crane, "Two-Component Rain Model for the Prediction of Attenuation Statistics," *Radio Science*, Vol. 17, No. 6, November–December 1982, pp. 1371–1387.

[16] H. C. Shieh, "A Statistical Model for the Estimation of Satellite System Performance When Site Diversity is Employed," Thayer School of Engineering, Dartmouth College, Hanover, New Hampshire, Radio-Wave Propagation Report RWP-3, June 1984.

[17] R. K. Crane and K. R. Hardy, "The HIPLEX Program in Colby-Goodland, Kansas; 1976–1980," Environmental Research and Technology, Inc., Concord, Massachusetts, Report P-1552-F, 1981.

[18] F. Fedi and A. Paraboni, "A New Prediction Method for Attenuation Beyond 10 GHz Based on a Model of Raincells Characterized by Exponential Shape," URSI Commission-F Symposium on Wave Propagation and Remote Sensing, University of New Hampshire, July–August 1986, *Preprint Volume*, pp. 9.5.1–9.5.5.

[19] J. Mass, "Diversity and Baseline Orientation," *IEEE Transactions on Antennas and Propagation*, Vol. AP-27, No. 1, January 1979, pp. 27–30.

[20] J. L. Strickland, "Radar Measurements of Site-Diversity Improvement During Precipitation," *J. Recherche Atmospheriques*, January–June 1974, pp. 451–464.

[21] I. Katz, "A Rain Cell Model," 17th Conference on Radar Meteorology, American Meteorology Society, Seattle, Washington, October 1976, *Proc.*, pp. 442–447.

[22] T. G. Konrad and R. A. Kropfli, "Radar Derived Spatial Statistics of Summer Rain," NASA CR-2592, September 1975.

[23] P. L. Rice and N. R. Holmberg, "Cumulative Time Statistics of Surface-Point Rainfall Rates," *IEEE Transactions on Communications*, Vol. COM-21, No. 10, October 1973, pp. 1131–1136.

[24] C. Capsoni, A. Paraboni, and A. Pawlina, "A Realistic Model of the Horizontal Structure of Rain Cells," International Symposium on Satellite Telecommunication, Graz, Austria, September 1985, ESA SP-245.

[25] A. Hald, *Statistical Theory With Engineering Applications*, New York: John Wiley and Sons, 1962, p. 161.

[26] J. Mass, Unpublished work, 1976.

[27] G. Drufuca, "Rain Attenuation Studies," McGill University, Montreal, Quebec, Canada, Report MW-77, March 1973.

[28] H. Yokoi, M. Yamada, and A. Ogawa, "Measurement of Precipitation Attenuation for Satellite Communications at Low Elevation Angles," *J. Recherche Atmospheriques*, January–June 1974, pp. 329–346.

[29] A. E. Freeny and T. D. Gabbe, "A Statistical Description of Intense Rainfall," *Bell System Technical Journal*, Vol. 48, No. 4, July–August 1969, pp. 1789–1851.

[30] R. K. Crane, "An Analysis of Radar Data to Obtain Storm Cell Sizes, Shapes and Spacings," Thayer School of Engineering, Dartmouth College, Hanover, New Hampshire, Radio Wave Propagation Report RWP-1, April 1983.

[31] D. C. Hogg and T. Chu, "The Role of Rain in Satellite Communications," *Proc. IEEE*, Vol. 63, No. 9, September 1975, pp. 1308–1331.

[32] G. Hyde, "ATS-6 Preliminary Results from the 13/18-GHz COMSAT Propagation Experiment," *IEEE Transactions on Aerospace and Electronic Systems*, Vol. AES-11, No. 6, November 1975, pp. 1084–1094.

[33] R. K. Crane, "The Spatial Structure of Rain as Observed by Radar," URSI Commission-F Symposium on Wave Propagation and Remote Sensing, University of New Hampshire, July–August 1986, *Preprint Volume*, pp. 5.3.1–5.3.4.

[34] W. J. Vogel, "Measurement of Satellite Beacon Attenuation at 11.7, 19.04 and 28.56 GHz and Radiometric Site Diversity at 13.6 GHz," *Radio Science*, Vol. 17, No. 6, November–December 1982, pp. 1511–1520.

[35] "ATS-F COMSAT MM-Wave Propagation Experiment," Part II, Final Report for NASA Contract NAS5-2166, November 1976.

[36] G. C. Towner *et al.*, "Initial Results from the VPI and SU Sirio Diversity Experiment," *Radio Science*, Vol. 17, No. 6, November–December 1982, pp. 1489–1494.

[37] D. V. Rogers, Private communication, 1983.

[38] D. V. Rogers and G. Hyde, "Diversity Measurements of 11.6-GHz Rain Attenuation at Etam and Lenox, West Virginia," *COMSAT Technical Review*, Vol. 9, No. 1, Spring 1979, pp. 243–254.

[39] J. Schlesak and J. Strickland, "Measurement of Precipitation Attenuation, Depolarization and Site Diversity Improvement in Canada," Preparatory Seminar for 1983 RARC, Ottawa, Canada, May 4, 1981.

[40] J. A. Ruffner and F. E. Bair, *The Weather Almanac*, Detroit: Gale Research Co., 1977.

[41] S. H. Lin, H. J. Bergmann, and M. V. Pursley, "Rain Attenuation on Earth-Satellite Paths—Summary of 10-Year Experiments and Studies," *Bell System Technical Journal*, Vol. 59, No. 2, February 1980, pp. 183–228.

[42] J. E. Allnutt and P. F. Shutie, "Space Diversity Results at 30 GHz," URSI Commission-F Open Symposium, LaBaule, France, April 28–May 6, 1977, *Proc.*, pp. 371–374.

[43] CCIR, "Radiometeorological Data," Report 563-3, *Recommendations and Reports of the CCIR*, Vol. 5, Geneva, 1986, pp. 108–142.

[44] J. E. Allnutt, "Slant-Path Attenuation and Space-Diversity Results Using 11.6 GHz Radiometers," *Proc. IEE*, Vol. 123, No. 11, 1976, pp. 1197–1200.

[45] Y. Hosaya, K. Sato, and T. Nagatsu, "Propagation Characteristics on Slant Path in 20 and 30 GHz Bands," *Review of the Electrical Communication Laboratories* (Japan), Vol. 28, Nos. 7–8, 1980, pp. 588–603.

[46] J. E. Allnutt, "The INTELSAT Propagation Measurements Programme," IEE Conference Publication No. 195, Pt. 2, April 1981, pp. 46–53.

[47] D. J. Fang and J. M. Harris, "Precipitation-Attenuation Studies Based on Measurements of ATS-6 20/30 GHz Beacon Signals at Clarksburg, Maryland," Report prepared by COMSAT under NASA Contract NAS5-20740, August 1976.

[48] J. Goldhirsh and F. L. Robison, "Attenuation and Space Diversity Statistics Calculated From Radar Reflectivity Data of Rain," *IEEE Transactions on Antennas and Propagation*, Vol. AP-23, No. 2, March 1975, pp. 221–227.

[49] D. B. Hodge, "Space Diversity for Reception of Satellite Signals," Ohio State University, Columbus, Technical Report 2374-16, October 1974.

Appendix. Sample computer printouts of attenuation data for a single path and diversity paths

*** STATION: PALMETTO TIME: 08/14/86
E=38.20 FREQ=17.80
(P IN UNITS OF 10**-6 OF YEAR)

S(KM)		A=1DB	A=2DB	A=3DB	A=4DB	A=6DB	A=8DB	A=10DB	A=12DB	A=14DB
	P(A)=	0.12E+05	0.73E+04	0.36E+04	0.23E+04	0.14E+04	0.98E+03	0.58E+03	0.44E+03	0.34E+03
	P(OPT)=	0.33E+04	0.13E+04	0.33E+03	0.13E+03	0.48E+02	0.20E+02	0.84E+01	0.49E+01	0.29E+01
16.0	P(DAT)=	0.27E+04	0.16E+04	0.64E+03	0.32E+03	0.16E+03	0.10E+03	0.58E+02	0.45E+02	0.35E+02
	P(DATC)=	0.60E+04	0.29E+04	0.97E+03	0.45E+03	0.21E+03	0.12E+03	0.66E+02	0.49E+02	0.37E+02
	P(DAL)=	0.30E+04	0.15E+04	0.61E+03	0.32E+03	0.16E+03	0.99E+02	0.57E+02	0.42E+02	0.32E+02
	P(DALC)=	0.63E+04	0.28E+04	0.94E+03	0.45E+03	0.21E+03	0.12E+03	0.65E+02	0.47E+02	0.35E+02
31.0	P(DAT)=	0.23E+03	0.12E+03	0.47E+02	0.22E+02	0.10E+02	0.63E+01	0.33E+01	0.25E+0*	0.19E+01
	P(DATC)=	0.35E+04	0.15E+04	0.37E+03	0.15E+03	0.58E+02	0.27E+02	0.12E+02	0.75E+01	0.48E+01
	P(DAL)=	0.31E+03	0.94E+02	0.38E+02	0.20E+02	0.10E+02	0.56E+01	0.32E+01	0.23E+01	0.16E+0*
	P(DALC)=	0.36E+04	0.14E+04	0.36E+03	0.15E+03	0.58E+02	0.26E+02	0.12E+02	0.72E+01	0.45E+01

ATTENUATION FORMULA A * (RI) ** B
WHERE A = 0.4470E-01 B = 0.1127E+01

TABLE OF RM AND H NUMBER 31

RI(MM/HR)	RM (KM)	H (KM)
> 50.	0.6	1.00,2.00,3.00,4.00
30. - 50.	1.0	1.00,2.00,3.00,4.00
20. - 30.	2.0	1.00,2.00,3.00,4.00
14. - 20.	4.0	2.00,2.67,3.33,4.00
8. - 14.	6.0	3.00,3.67,4.33,5.00
0. - 8.	10.0	4.00,4.33,4.67,5.00

RAIN FALL STATISTIC AS SPECIFIED OR FROM EXPERIMENT

INTERVAL	RANGE PERCENT	WIDTH-UNITS 10**-6	RAIN-RATE CENTER MM/HR	RM KM	H KM
1	0.000 - 0.005	50.	108.00	0.6	1.00,2.00,3.00,4.00
2	0.005 - 0.010	50.	85.00	0.6	1.00,2.00,3.00,4.00
3	0.010 - 0.015	50.	73.00	0.6	1.00,2.00,3.00,4.00
4	0.015 - 0.020	50.	60.00	0.6	1.00,2.00,3.00,4.00
5	0.020 - 0.040	200.	52.00	0.6	1.00,2.00,3.00,4.00
6	0.040 - 0.060	200.	41.00	1.0	1.00,2.00,3.00,4.00
7	0.060 - 0.080	200.	33.00	1.0	1.00,2.00,3.00,4.00
8	0.080 - 0.100	200.	31.00	1.0	1.00,2.00,3.00,4.00
9	0.100 - 0.200	1000.	22.00	2.0	1.00,2.00,3.00,4.00
10	0.200 - 0.300	1000.	10.00	6.0	3.00,3.67,4.33,5.00
11	0.300 - 0.400	1000.	8.00	10.0	4.00,4.33,4.67,5.00
12	0.400 - 0.500	1000.	6.00	10.0	4.00,4.33,4.67,5.00
13	0.500 - 1.000	5000.	5.00	10.0	4.00,4.33,4.67,5.00

Jonathan Mass received the Engineering Degree from the Haifa Technion in 1944 and the Docteur-Ingenieur Degree from Paris University in 1963. In 1964, he founded the Haifa Radio Observatory and served as its Director, and later Staff Member, until 1986. He was on sabbatical leave at COMSAT Laboratories from 1975 to 1976, and served as Deputy Director for Research and Development at RAFAEL (Armament Development Authority, Israel) from 1977 to 1980. In 1986, he was again on sabbatical leave at COMSAT Laboratories from the Israeli National Committee for Space Research. He is currently on sabbatical leave at ESA/ESTEC in Holland. Dr. Mass has authored more than 25 published papers in the areas of radio propagation and satellites. He is a Member, Plenary of the Israel Space Agency.

Index: coding, digital transmission, time division multiple access, error control, error correcting codes

Programmable convolutional encoder and threshold decoder

J. S. SNYDER

(Manuscript received March 12, 1987)

Abstract

A novel error-correction encoder/decoder architecture is presented which employs random-access memory (RAM) data storage and programmable read-only memory (PROM) control signal generation instead of the traditional shift-register structure. The threshold decoder also uses programmable logic devices to generate the syndrome pattern and error-correction signals. The programmable codec features reduced implementation complexity, standardized design, and the ability to change code parameters and interface conditions by merely changing the programmable components.

An experimental application is described in which the programmable codec improves the bit error rate of 64-kbit/s pulse-code modulation (PCM) channels in the INTELSAT 120-Mbit/s time-division multiple access (TDMA) system by efficiently implementing an unequal-error-protection coding scheme. This application provides differing degrees of error correction to the bits within a PCM byte in order to permit reliable transmission of digital data over the PCM voice channels.

Introduction

Convolutional encoders and threshold decoders [1] have typically been implemented with shift registers and exclusive-OR gates [2], [3]. While this is suitable for simple codes, such an approach results in complex designs requiring many integrated circuits for high-rate codes (particularly those which correct two or more errors) or when interleaving is employed. Moreover, each such code requires a unique codec design. The structure of the

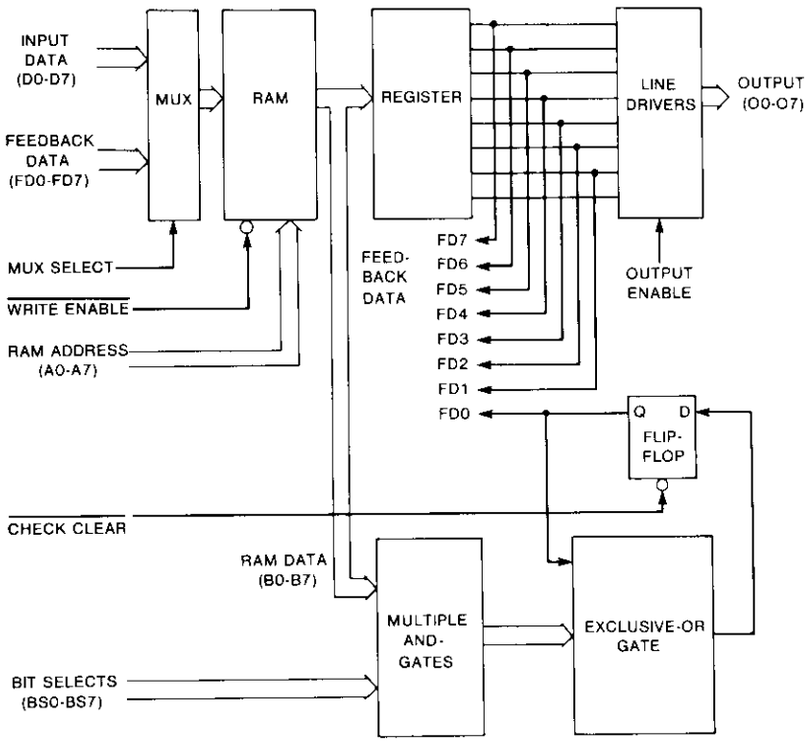

Figure 2. *Encoder Memory and Check-Bit Computation*

shift register encoder implementation, data are not shifted through the RAM. Instead, the RAM address is sequentially incremented until the memory is full, at which time new data are written over the oldest stored data. The address counter specifies the oldest memory location involved in a given encoding cycle, and is incremented under PROM control when the address counter enable signal is asserted. Various relative offset values (which depend on the specific code being used) are added to the address counter value to obtain the actual read and write addresses for the RAM during any encoding cycle.

The decoder memory may be implemented (Figure 4) in much the same manner as the encoder memory. The essential difference is that feedback data in the decoder pass through individual exclusive-OR gates before being written back into memory, in order to provide a means for the corresponding error-correction signals to complement erroneous information bits.

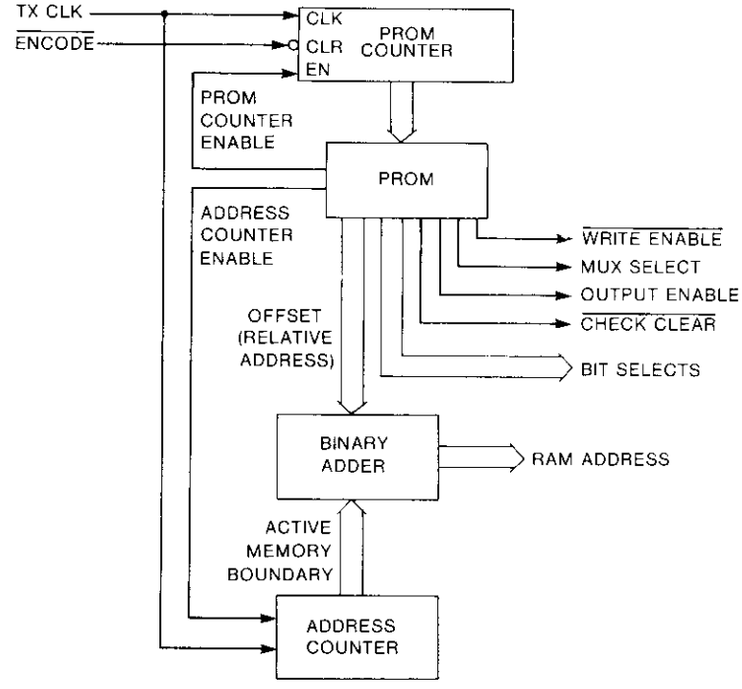

Figure 3. *Encoder Control*

The decoder error-correction function (Figure 5) employs an exclusive-OR operation with an accumulator, similar to that used in the encoder check-bit computation, to calculate syndrome bits. While these syndrome bits could be stored in the RAM, the speed of subsequent processing is significantly increased by storing them in a separate syndrome register. Selected bits from the syndrome register, as determined by the particular code employed, are fed to majority decision functions, each of which generates a correction signal if a majority of its inputs are 1s. The syndrome register and majority decision functions are implemented using PAL devices to minimize circuit complexity and provide programmable generality. Omitted for clarity are the multiple feedback connections from each majority function to specific syndrome register bits to eliminate the effects of detected errors from subsequent decisions.

Decoder control and address signals are generated by a counter-driven PROM in the same manner as for the encoder. Decoder control function operation is initiated by a decoding command pulse.

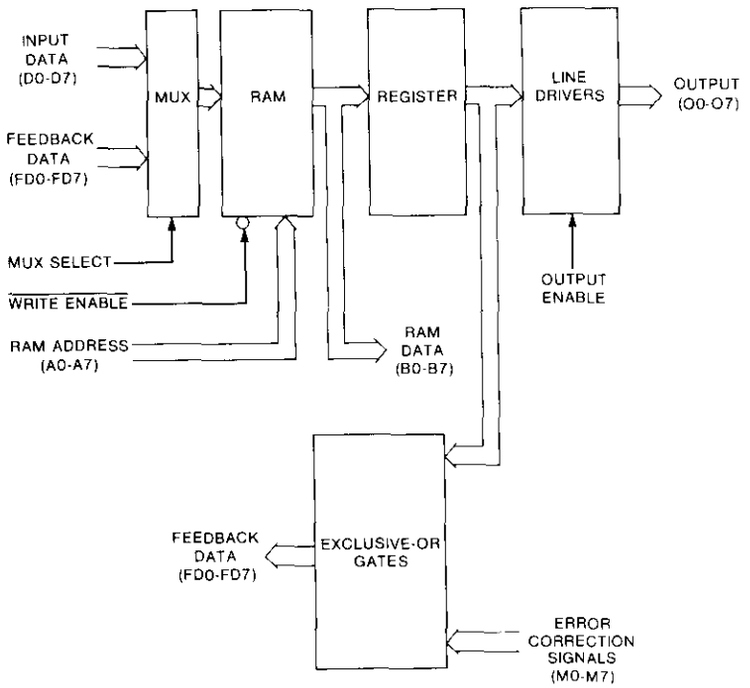

Figure 4. *Decoder Memory*

Implementation variations

With the generalized 8-bit architecture presented (Figures 2 through 5), code rate k/n is readily programmable for any value for which $1 \leq k \leq n$ and $1 \leq n \leq 8$. For example, a rate 3/4 code could easily be implemented by accepting information input in 3-bit groupings and combining each grouping of three information bits with one check bit. Alternatively, a rate 3/4 code could be implemented with a 6-bit input byte and an 8-bit output byte containing two check bits. Code rate is readily extendable to values of n greater than 8 by either encoding over more than one byte or by extending the byte width through additional RAM devices. For example, a rate 15/16 code could be implemented by accepting an 8-bit input byte followed by a 7-bit input byte. Each encoder output byte would contain eight bits, with the eighth bit in alternate bytes being a check bit.

Likewise, virtually any practical code length can be accommodated, including those of interleaved codes. Code performance (e.g., single-, double-, or triple-error correction) is also programmable.

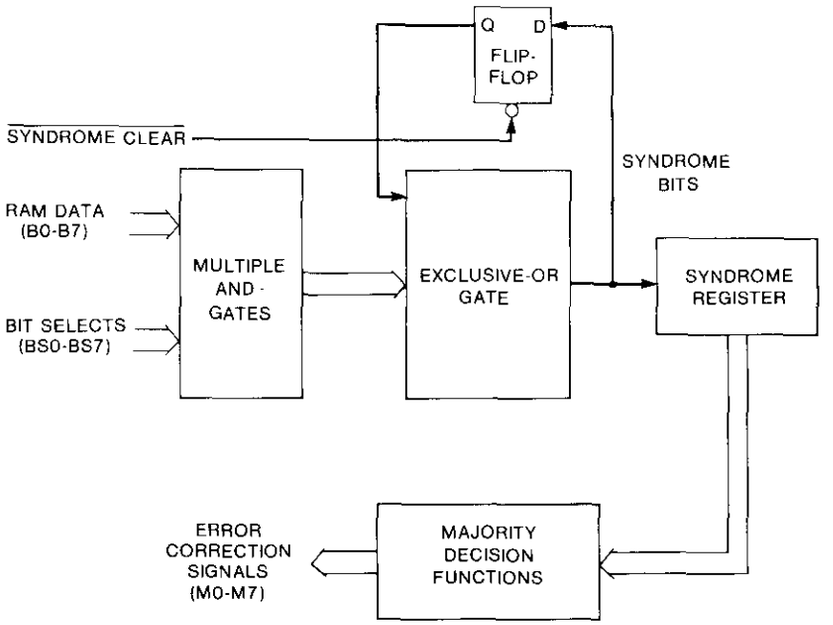

Figure 5. *Decoder Error Correction*

The codec input/output interfaces are also programmable. Data stored in the RAM may be written in and read out when convenient, and computations may be made between read/write cycles. In general, input/output data transfer could be programmed to take place one byte at a time or N bytes at a time, the limitation being the number of clock periods between read/write cycles needed to perform the calculations required by the particular code. Furthermore, the read and write operations could be programmed to occur at different times within the encoding cycle. Serial data interfaces could easily be accommodated by adding serial-to-parallel conversions at the codec inputs and parallel-to-serial conversions at the codec outputs.

While the programmable codec has been conceived and developed for use with systematic convolutional codes in which unaltered information bits are transmitted along with additional check bits, the concept may be extended to other codes as well. For example, the programmable encoder can readily generate a nonsystematic code containing only check bits, although some changes in the programmable decoder structure would be required. Moreover, the basic encoder architecture may also be applied to block codes, although again the programmable decoder would require changes in structure.

Error correction of PCM data

The programmable codec was experimentally applied to improving the bit error rate (BER) of 64-kbit/s pulse-code modulated (PCM) channels within the INTELSAT 120-Mbit/s time-division multiple access/digital speech interpolation (TDMA/DSI) system to permit reliable transmission of 9.6 kbit/s digital data over the PCM voice channels. For this application, previous experiments [7] have found that errors in the most-significant PCM bits are the greatest cause of errors in the 9.6-kbit/s digital data, while errors in the least-significant PCM bit positions have virtually no effect on 9.6-kbit/s data errors. The empirical results show that the BER of the 9.6-kbit/s modem is given by a weighted sum of the error rates of the individual PCM bits times an error multiplication factor, and may be expressed as

$$\mathrm{BER}_M \simeq 14.2\,(0.369\,\mathrm{BER}_7 + 0.357\,\mathrm{BER}_6 + 0.235\,\mathrm{BER}_5 + 0.036\,\mathrm{BER}_4 + 0.003\,\mathrm{BER}_3) \quad (1)$$

where BER_M is the BER at the output of the 9.6-kbit/s demodulator, and BER_i (for $i = 3$ through 7) is the BER of the i-th bit in each PCM sample, with $i = 7$ denoting the most-significant bit (MSB).

The objective in this application is to achieve a BER of 1×10^{-6} or less at the output of the 9.6-kbit/s demodulator, for a BER in the 64-kbit/s channel of 1×10^{-4}. From equation (1), this objective may be met by reducing the PCM error rate of 1×10^{-4} to 5×10^{-8} or less for the four MSBs in each PCM sample (bits 7, 6, 5, and 4), and to 5×10^{-6} or less for bit 3. Such performance is readily achievable with threshold decoding. Moreover, the lack of soft-decision capability in the system reduces the potential improvement of Viterbi decoding by 2 dB. Finally, the continuous nature of the data and the need to minimize system changes make convolutional coding more attractive than block coding.

Based on the above considerations, a systematic self-orthogonal convolutional code which unequally protects the various bits in a PCM byte was chosen. This UEP code provides double-error correction for the four MSBs of each 8-bit PCM sample, and single-error correction for the next-most-significant bit. The following two PCM bits are unprotected, while the least-significant bit (LSB) in each PCM sample is replaced by a check bit. After threshold decoding, the LSB is reset to a zero at the decoder output.

Code parameters

The selected code may be specified by the following five sets of integers:

(0, 14, 17, 26)
(0, 11, 18, 24)
(0, 16, 20, 21)
(0, 2, 10, 25)
(0, 19).

These integers denote the delays, relative to the current byte, of the information bits which are exclusive-ORed to generate the current check bit. Thus, the current check bit is formed by exclusive-ORing the current value of bit 7; the 14th, 17th, and 26th previous values of bit 7; the current value of bit 6; the 11th, 18th, and 24th previous values of bit 6; and so forth.

This special UEP code is created from a standard rate 4/5 double-eror correcting code [8] by adding the fifth set of integers (0, 19), which adds single-error correction to the fifth PCM bit. To maintain the self-orthogonal property of the parent code, the difference between any two elements of the fifth set must not be the same as the difference between any two elements of any other set [2], [3]. [This criterion could also be met by selecting (0, 22) for the fifth set.] The resulting special code has a rate of 5/6. When the two unprotected bits are included, the overall code rate becomes 7/8.

Codec input and output

Because of system considerations, it is desirable in this application for one programmable codec to bulk-process six PCM channels. Six 8-bit bytes enter the encoder in a burst every 125 μs, and six 8-bit coded bytes simultaneously leave the encoder. Each byte represents one PCM sample from one of six adjacent 64-kbit/s speech channels within the 30-channel INTELSAT TDMA/DSI system [9]. Each bit within a byte is transferred simultaneously in parallel by a 2.048-MHz byte clock. The six PCM bytes entering the encoder during one 125-μs frame leave the encoder during the following frame with each LSB replaced by a check bit.

Decoder input and output also occur simultaneously in six 8-bit bytes per 125-μs frame, with data transferred by a 2.048-MHz byte clock. Corrected data leave the decoder six frames after entering, with each LSB set to a zero.

Hardware performance and implementation complexity

To verify the desired unequal-error-correction capability, codec performance was independently measured for the most-significant PCM bits, the

next-most-significant PCM bits, and so forth. Measured data (Figure 6) confirmed that the greatest BER improvement is associated with the four MSBs in each PCM sample (bits 7, 6, 5, and 4), which receive double-error correction. Bit 3 attains the intermediate improvement of single-error correction, while bits 1 and 2, being uncoded, exhibit a decoder output BER equal to the decoder input BER. The complete UEP codec requires only 55 standard integrated circuits, including all bus interface, timing and control functions. This is far fewer components than would be necessary for a conventional shift-register implementation.

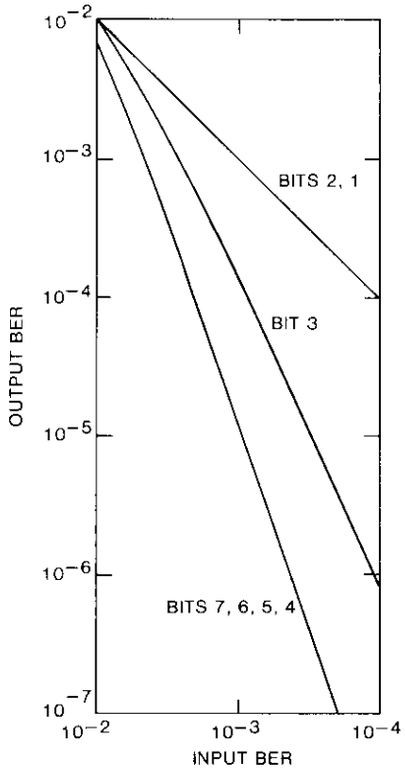

Figure 6. *Codec Performance*

The selected UEP code is an optimum choice for this specific application in terms of both complexity and BER performance. If double-error correction were extended to the remaining PCM bits, a longer code would be required. In addition to somewhat increasing the codec hardware complexity, overall system performance would actually suffer for several reasons. First, the double-error correction capability of the most-significant four bits would be spread over a longer constraint length. Second, the increased number of bits entering into the check bit calculation would increase the probability of a syndrome 1 for any given channel BER, thereby reducing the ability to correct errors in the four MSBs. Finally, the improvement in output BER in the less-significant bits would be more than counteracted by degradation in the output BER of the four MSBs because of the relatively greater influence of the more-significant PCM bits on the BER of the 9.6-kbit/s data.

Conclusions

The programmable codec combines the use of RAM data storage (rather than the more conventional shift-register codec structure) with PROM generation of control signals to achieve a universal architecture which accommodates a wide variety of codes and interface conditions. The codec is particularly well-suited for modern, bus-oriented digital communications systems. The decoder also employs programmable logic devices to enhance decoding speed while minimizing circuit complexity and maintaining programmability.

The flexibility of the programmable structure has been demonstrated by an application which provides unequal error-correction capability to the various bits within a message byte. This application illustrates the features of the programmable codec, which include reduced implementation complexity, standardized design suitable for a variety of applications, and the ability to change code parameters and/or interface characteristics by merely changing the programmable components.

Acknowledgments

The author greatly appreciates many helpful discussions with K. Mackenthun on code selecton, and especially his suggestion to create the rate 5/6 UEP code. The author also acknowledges the significant contributions of K. Boehm in constructing, debugging, and testing the codec, and of J. Phipps in generating the schematics.

References

[1] J. L. Massey, *Threshold Decoding*, Cambridge, Massachusetts: The MIT Press, 1963.

[2] W. W. Peterson and E. J. Weldon, *Error-Correcting Codes*, Cambridge, Massachusetts: The MIT Press, 1972.

[3] G. C. Clark, Jr., and J. B. Cain, *Error-Correction Coding for Digital Communications*, New York: Plenum Press, 1981.
[4] B. Masnick and J. Wolf, "On Unequal Error Protection Codes," *IEEE Transactions on Information Theory*, Vol. IT-13, No. 4, October 1967, pp. 600–607.
[5] D. Mandelbaum, "Unequal-Error-Protection Codes Derived From Difference Sets," *IEEE Transactions on Information Theory*, Vol. IT-18, No. 5, September 1972, pp. 686–687.
[6] C. C. Kilgus and W. C. Gore, "A Class of Cyclic Unequal-Error Protection Codes," *IEEE Transactions on Information Theory*, Vol. IT-18, No. 5, September 1972, pp. 687–690.
[7] F. Corcoran, Private communication.
[8] J. P. Robinson and A. J. Bernstein, "A Class of Binary Recurrent Codes With Limited Error Propagation," *IEEE Transactions on Information Theory*, Vol. IT-13, No. 1, January 1967, pp. 106–113.
[9] INTELSAT, "TDMA/DSI System Specification: TDMA/DSI Traffic Terminals," Specification BG-42-65E (Rev. 1), June 25, 1981.

John S. Snyder received a B.S.E.E. from Rochester Institute of Technology in 1965 and an M.S.E.E. from the University of Rochester in 1973. He joined COMSAT Laboratories in 1973 and is presently a Staff Scientist in the Image Processing and Digital Techniques Department, where he is engaged in the research and development of error-correction coding and other digital signal processing techniques applied to satellite communications. Previously, with Taylor Instrument Company and the Department of Defense, he was involved in research and development in the areas of analog and digital signal processing and CRT display systems. Mr. Snyder is a member of the IEEE and holds a number of patents in the areas of error-correction coding and signal processing. He has written several technical papers for international satellite communications conferences, and has authored a variety of papers appearing in technical publications.

CTR Note

Geostationary satellite log for year end 1986

C. H. SCHMITT

(Manuscript received March 31, 1987)

This note provides lists of current and planned geostationary satellites for the Fixed-Satellite Service (FSS), the Broadcasting-Satellite Service (BSS), the Radiodetermination-Satellite Service (RDSS), the Aeronautical Mobile-Satellite Service (AMSS), the Maritime Mobile-Satellite Service (MMSS), the Land Mobile-Satellite Service (LMSS), and the Space Research Service (SRS). The lists are ordered by increasing East longitude orbit position and update the previously published material [1] through December 1986.

Table 1 lists the satellites that are operating as of late December 1986, or satellites that are in orbit and are capable of operating. Satellites being moved to new orbital positions are shown at their planned final positions for 1987, unless another satellite at the same frequencies occupies the position. Refer to the Remarks column for further information.

Table 2 lists newly proposed and replacement satellites and their currently planned orbital positions. Planned satellites are listed when information has been published by the International Frequency Registration Board (IFRB), or when it has been learned that satellite construction has commenced. Additional technical characteristics may be obtained from the author, from the country or organization listed in the table, or from the referenced IFRB Circulars, as published weekly in the circular's special sections [2].

Table 3 gives the codes used in Tables 1 and 2 that correspond to the frequency bands allocated to the space services listed. Allocated bands include the following services: fixed, maritime mobile, broadcasting (including community reception), aeronautical mobile, land mobile, and mobile satellites. Other space services, such as the Meteorological-Satellite Service and the Earth Exploration-Satellite Service, appear only when needed to document a satellite network shown in Tables 1 and 2.

Carl H. Schmitt, formerly with COMSAT, is Principal Engineer and President of Satellite Communications (SatCom) Consultants, Inc., 1629 K Street, N.W., Suite 600, Washington, DC 20006, (202) 223-4884.

Exact satellite operating frequencies cannot be shown here due to space constraints. Regions given are defined by ITU Radio Regulations, Article 8, and are summarized as follows:

- *Region 1:* Africa, Europe, Mongolia, and the USSR
- *Region 2:* North and South America and Greenland
- *Region 3:* Asia (except for Mongolia and the USSR) and Australia

Information on exact frequencies and additional information on technical parameters is available and is updated regularly. The author invites inquiries and comments, and would appreciate receiving information on newly planned satellite networks as they become available.

Acknowledgments

Special thanks are due to E. Reinhart for his invaluable assistance in reviewing the author's work, and for defining a new format for the frequency codes. The author also wishes to thank R. Krishna for her contributions to this research, for her dedication in data acquisition, and for the revision and application of the new codes. In addition, the author wishes to thank D. Ledbetter for his contributions to this project.

References

[1] C. H. Schmitt, "Geostationary Satellite Log," *COMSAT Technical Review*, Vol. 16, No. 1, Spring 1986, pp. 253–298.

[2] *IFRB Circulars*, AR11/A/ . . . (refers to Article 11, Section 1, which contains advanced publication requirements) and AR11/C/ . . . (refers to Article 11, Section 2, which contains coordination requirements), and SPA/AA/ . . . or /AJ/ . . . These special sections may be obtained from International Telecommunications Union IFRB, CH 1211, Geneva 20, Switzerland.

TABLE 1. IN-ORBIT GEOSTATIONARY COMMUNICATIONS SATELLITES FOR YEAR END 1986

Subsatellite Longitude[a]	Launch Date Object/Catalog Number[b]	Satellite Designation	Country or Organization	Service	Frequency Up/Down-Link (GHz)	Remarks
0.0°E	19 Jun 1981 12544	METEOSAT 2	ESA (F)	MetSat	UHF/UHF,2	SPA-AA/43/1157/IFRB: 0°E AR11/A/43
5.7°E	11 May 1978 10855	OTS 2	ESA	FSS, BSS	14a/11	Experimental IFRB: 5°E AR11/A/90 AR11/C/ADD-1'66
7.0°E	04 Aug 1984 15158	EUTELSAT II-7E (ECS-2)	EUTELSAT-ESA	FSS STS	14a/11	IFRB: 7°E EUTELSAT 1-3 in coordination AR11/A/305/1732 AR11/C/446
12.9°E	16 Jun 1983 14128	EUTELSAT I (ECS-1)	EUTELSAT-ESA	FSS	14a/11	Designated ECS 1 before acceptance by EUTELSAT IFRB: 13°E EUTELSAT 1-2
19.0°E	08 Feb 1985 15560	ARABSAT 1-A	Arab League	FSS, BSS	6/4, 2.6b,2.6c	IFRB: 19°E AR11/A/278 AR11/C/330 AR11/A/7/1347 AR11/C/1/1597

TABLE 1 (continued). IN-ORBIT GEOSTATIONARY COMMUNICATIONS SATELLITES FOR YEAR END 1986

Subsatellite Longitude[a]	Launch Date Object/Catalog Number[b]	Satellite Designation	Country or Organization	Service	Frequency Up/Down-Link (GHz)	Remarks
26.0°E	18 Jun 1985 15825	ARABSAT 1-B	Arab League	FSS, BSS	6/4, 2.6b,2.6c	IFRB: (ARABSAT 1D) AR11/A/211/1347 AR11/C/173/1388
34.0°E	26 Nov 1982 13669	RADUGA 11	USSR	FSS	6/4	IFRB: 35°E (STATSIONAR 2)
35.0°E	15 Sep 1985 16250	RADUGA 17	USSR	FSS	6/4	IFRB: 35°E (STATSIONAR 2) SPA-AA/76/1179 AR11/C/26/1251
39.4°E	28 Dec 1979 11648	GORIZONT 3	USSR	FSS	6,8/4,7	IFRB: 40°E (STATSIONAR 12) AR11/C/878/1737; incl. 5.4°
44.0°E	25 Aug 1983 14307	RADUGA 13	USSR	FSS	6/4	
45.0°	25 Oct 1986 17046	RADUGA 19	USSR	FSS	6/4	IFRB: 45°E (STATSIONAR D-4) AR11/A/196/1675
45.0°E	08 Aug 1985 15946	RADUGA 16	USSR	FSS	6/4	IFRB: 45°E (STATSIONAR 9) SPA-A5/51/1276 APA-A5/63/1280
52.0°E	26 Jun 1984 14940	GORIZONT 9	USSR	FSS	6/4	
53.0°E	15 Mar 1982 13092	GORIZONT 5	USSR	FSS	6,8/4,7	IFRB: 53° (STATSIONAR 5)
57.0°E	31 Mar 1978 10778	INTELSAT IV-A (F-6)	INTELSAT	FSS	6/4	AR11/C/876/1737 Arrives Second Quarter 1987
60.0°E	Unknown	DSCS 11	U.S.-G	FSS	UHF,8/UHF,7	IFRB: 60°E SPA A5/211/1418 (USGCSS 2 IND)
60.0°E	14 Dec 1978 11145	DSCS 10	U.S.-G	FSS, MMSS	8/7	IFRB: 60°E (USGCSS 3 IND)
60.6°E	28 Sept 1985 16101	INTELSAT V-A (F-12)	INTELSAT	FSS	6,14a/4,11	IFRB: 60°E (INTELSAT VA IND 1) AR/11/A167/1580
61.2°E	26 Dec 1980 12/20	EKRAN 6	USSR	BSS	6/UHF	Incl. 5°
62.9°E	28 Sept 1982 13595	INTELSAT V (F-5) MCS A	INTELSAT INMARSAT Lease	FSS MMSS	6,14a/4,11 1.6b,6/4, 1.5a	IFRB: 63°E (INTELSAT V, IND 1) IFRB: 63°E MCS IND A Maritime Package
65.9°E	19 Oct 1983 14421	INTELSAT V (F-7) MCS C	INTELSAT INMARSAT Lease	FSS MMSS	6,14a/4,11 1.6b,6 1.5a,4	IFRB: 66°E IFRB: 66°E MCS IND D INMARSAT Spare

TABLE 1 (continued). IN-ORBIT GEOSTATIONARY COMMUNICATIONS SATELLITES FOR YEAR END 1986

Subsatellite Longitude[a]	Launch Date Object/Catalog Number[b]	Satellite Designation	Country or Organization	Service	Frequency Up/Down-Link (GHz)	Remarks
67.4°E	08 Apr 1983 13974	RADUGA 12	USSR	FSS	6/4	Incl. 2.28°
71.6°E	18 Jul 1978 10987	RADUGA 4	USSR	FSS	6/4	Incl. 3.33°
72.5°E	10 Jun 1976 8882	MARISAT F-2	US-COMSAT General	MMSS	UHF 1.6b,6/4 UHF 1.5a	Spare, but unused except for UHF transponder IFRB: 72.5°E
74.0°E	3 Aug 1983 14318	INSAT 1B	India	FSS	6/4	AR11/A/131 AR11/C/57/1277 AR11/A/208/1344 AR11/C/231/1429
75.0°E	May 1979 11353	FLTSATCOM 2	US-Government	FSS	UHF,8/UHF,7	IFRB: 75°E (FLT SATCOM IND) AR11/A/87 AR11/C/169
77.0°E	13 Mar 1977 09862	PALAPA A-2	INDONESIA	FSS	6/4	Backup for PALAPA B-1 IFRB: 77°E PALAPA-2 AR11/A/45/1338
80.0°E	01 Aug 1984 15144	GORIZONT 10	USSR	FSS	6,8/4,7	IFRB: 80°E (STATSIONAR 13) AR11/C/598/1737
83.0°E	08 Jul 1976 09009	PALAPA A-1	INDONESIA	FSS	6/4	Near retirement IFRB: 83°E AR11/A/45/1339
85.0°E	15 Feb 1984 14725	RADUGA 14	USSR	FSS	6/4	IFRB: 85°E (STATSIONAR 3)
85.0°E	09 Oct 1981 12897	RADUGA 10	USSR	FSS	6/4	
89.9°E	18 Nov 1986 17083	GORIZONT 13	USSR	FSS	14/11	IFRB: 90°E (LOUTCH-3)
90.0°E	30 Nov 1983 14532	GORIZONT 8	USSR	FSS	6,8/4,7	IFRB: 90°E (STATSIONAR 6) AR11/C/770
95.4°E	26 Jun 1981 12564	EKRAN 7	USSR	BSS	6/UHF	AR11/A/151 AR11/C/86 Incl. 4.62°
96.4°E	15 Dec 1977 10516	SAKURA (CS)	Japan-NTT	FSS	6,30a/4,20a	Experimental Incl. 4.52°
98.0°E	22 Mar 1985 15626	EKRAN 14	USSR	BSS	6/UHF	
99.0°E	30 Sep 1983 14377	EKRAN 11	USSR	BSS	6/UHF	IFRB: 99°E (STATSIONAR T2) SPA 2-3-AA SPA 2-3-AJ
101.0°E	16 Mar 1984 14821	EKRAN 12	USSR	BSS	6/UHF	

TABLE 1 (continued). IN-ORBIT GEOSTATIONARY COMMUNICATIONS SATELLITES FOR YEAR END 1986

Subsatellite Longitude[a]	Launch Date Object/Catalog Number[b]	Satellite Designation	Country or Organization	Service	Frequency Up/Down-Link (GHz)	Remarks
103.4	20 Feb 1980 11708	RADUGA 6	USSR	FSS	6/4	Incl. 5.6°
107.5°E	23 Jan 1984 14659	BS-2A	Japan	BSS	2,14a/12a,2	
108.0°E	18 Jun 1983 14134	PALAPA B-1	INDONESIA	FSS	6/4	Domestic and regional IFRB: 108°E ARII/A/197 ARII/C/18.5
110.0°E	12 Feb 1986 16597	BS-2B	Japan	FSS	2,14a/12a,12b,2	IFRB: 110°E (BS-2) ARII/A/305 ARII/C/10
113.0°E	21 Mar 1987 17706	PALAPA B-2 B	Indonesia			ARII/A/305 ARII/C/10
127.8°E	22 Jun 1984 15057	RADUGA 15	USSR	FSS	6/4	IFRB: 128° (STATSIONAR 15) SPA-AJ/312/1469 APA-AJ/317/1473 Incl. 1.22°
131.6°E	04 Feb 1983 13782	CS-2A	Japan	FSS	6,30a/4,20a	IFRB: 132°E
135.0°E	Nov 1979 05587	DSCS II	US-Government	FSS	UHF,8/UHF,7	
136.1°E	5 Aug 1983 14248	CS-2B/SAKURA 2B	Japan	FSS, STS	6/4	IFRB: 135.0°E
135.0°E	Sep 1982	DSCS III	US-Government	FSS	UHF,8/UHF,7	
135.0°E	1983/4	CSE-A	Japan	FSS	20a/11	ARII/C/178-179/1606
135.6°E	05 Aug 1983 14248	CS-2B	Japan	FSS	6,30a/4,20a	IFRB: 136°E
140.0°E	20 Oct 1982 13624	GORIZONT 6	USSR	FSS	6,8/4,7	
140.0°E	18 Jan 1985 15484	GORIZONT II	USSR	FSS	6,8/4,7	IFRB: 140°E (STATSIONAR 7)
156.0°E	27 Aug 1985 15993	AUSSAT 1 K-1	Australia	FSS	14a,12b,12c	IFRB: 156°E Incl. 0.019° ARII/A/299 ARII/C/296
164.0°E	28 Nov 1985 16275	AUSSAT 2 K-2	Australia	FSS	14a,12b,12c	IFRB: 160°E Incl. 0.018° ARII/A/300 ARII/C/305

TABLE 1 (continued). IN-ORBIT GEOSTATIONARY COMMUNICATIONS SATELLITES FOR YEAR END 1986

Subsatellite Longitude[a]	Launch Date Object/Catalog Number[b]	Satellite Designation	Country or Organization	Service	Frequency Up/Down-Link (GHz)	Remarks
172.0°E	31 Oct 1980 12046	FLTSATCOM 4 (WPAC)	US-Government	FSS	UHF,8/UHF,7	IFRB: 172°E (FLTSATCOM W PAC)
174.0°E	23 May 1981 12474	INTELSAT V (F-1)	INTELSAT	FSS	6,14a/4,11	IFRB: 57°E (INTELSAT V, IND 3) SPA-A5/376/1511
175.0°E	Sep 1984	DSCS III	US-Government	FSS	UHF,8/UHF,7	IFRB: 175°E (USGCSS III W PAC)
176.1°E	14 Oct 1976 9478	MARISAT F-3	US-COMSAT General	MMSS	UHF,1.6b,6/ UHF,1.5a,4	Spare but unused except for UHF transponder IFRB: 176.5°E (MARISAT-PAC) AR11/A/6 AR11/C/25
177.0°E	Jan 1978 10557	INTELSAT IV-A (F-3)	INTELSAT	FSS	6/4	IFRB: 177.0°E (INTELSAT 4A PAC2) AR11/A/332 AR11/C/692
177.5°E	12 April 1985 15643	LEASESAT F-3	USA-GOVERNMENT			AR11/A/222 AR11/C/242
177.9°E	13010	MARECS A	ESA-INMARSAT	MMSS	1.6b/6 1.5a,4	Spare (MARECS PAC 1) IFRB: 177.5°E
178.0°E	Dec 1978	DSCS II	US-Government	FSS	UHF 8/UHF 7	IFRB: 175°E
179.9°E (180.0°W)	20 Dec 1985 14786	INTELSAT V (F-8)	INTELSAT	FSS	6,14a/4,11	IFRB: 180°E (INTELSAT V PAC 3) IFRB: 180°E (MCS PAC A)
		MCS D	INMARSAT Lease	MMSS	1.6b,6/ 1.5a,4	A11/A/255 A11/C/682
194.7°E	24 Aug 1984 15219	EKRAN 13	USSR	BSS	6/UHF	Incl. 3.94°
211.0°E (149.0°W)	7 Dec 1966 02608	ATS-1	USA	FSS	6/4	Incl. 12.3°
217.1°E (142.9°W)	28 Oct 1982 13631	SATCOM V (F-5)	US-Alascom, Inc.	FSS	6/4	IFRB: 143°W in coordination AR11/A/7 AR11/C/414
220.0°E (139.1°W)	11 Apr 1983 13984	SATCOM I-R	US-RCA	FSS	6/4	IFRB: 139°W in coordination AR11/4/6 AR11/C/337
221.0°E (139.0°W)	1987 13984	SATCOM VI	US-RCA	FSS	6/4	IFRB: 136°W

TABLE 1 (continued). IN-ORBIT GEOSTATIONARY COMMUNICATIONS SATELLITES FOR YEAR END 1986

Subsatellite Longitude[a]	Launch Date Object/Catalog Number[b]	Satellite Designation	Country or Organization	Service	Frequency Up/Down-Link (GHz)	Remarks
223.9°E (136.0°W)	13637	PSCS-16	US-Government	FSS	--	IFRB: 135.0°W (USGCSS 2 E PAC) ARII/A/139 Incl. 0.051°
225.0°E (135.0°W)	June 1975 08366	GOES West	USA	FSS	6/4	SPA-A5/367/1508 Incl. 6.9°
226.0°E (134.0°W)	28 Jun 1983 14158	GALAXY I (USASAT II-D)	US-Hughes Comm.	FSS	6/4	IFRB: 134°W in coordination
229.0°E (131.0°W)	21 Nov 1981 12967	SATCOM III-R	US-RCA	FSS	6/4	IFRB: 131°W in coordination ARII/A/329 ARII/C/347
232.0°E (128.0°W)	27 Aug 1985 15994	ASC1	US-Amer. SAT CO.	FSS	6/4	IFRB: 128°W Adv. Publication ARII/A/202/1676 Incl. 0.01°
235.0°E (125.0°W)		TELSTAR 303	US-AT/T	FSS	6/4	
237.5°E (122.5°W)	09 Jun 1982 13269	WESTAR 5	US-Western Union	FSS	6/4	IFRB: 123°W in coordination ARII/A/5 ARII/C/284
240.0°E (120.0°W)	23 May 1984 14985	SPACENET I	US-GTE Spacenet	FSS	6/14a/4,12a	IFRB: 120°W in coordination ARII/A/10 ARII/C/833/1699 ARII/C/166/ ADD-1/1682
242.5°E (117.5°W)	12 Nov 1982 13652	ANIK C3 (E)	Canada-TELESAT	FSS	14a/12a	IFRB: 117.5°W ARII/A/138 ARII/C/69
243.1°E (116.3°W)	27 Nov 1985 16274	MORELOS B	Mexico	FSS	6,14a/4,12a	IFRB: 116.5°W ARII/A/30 ARII/C/387
247.0°E (113.0°W)	17 Jun 1985 15824	MORELOS A	Mexico	FSS	6,14a/4,12a	IFRB: 113.5°W ARII/A/28 ARII/C/386
249.0°E (111.0°W)	Oct 1985 15383	ANIK D2	Canada-TELESAT	FSS	14a/12a	ARII/A/358/1500 ARII/C/716/1673
250.0°E (110.0°W)	18 Jun 1983 14133	ANIK C2	Canada-TELESAT	FSS	14a/12a	IFRB: 110°W in coordination ARII/A/137/1500 ARII/C/129/1533

TABLE 1 (continued). IN-ORBIT GEOSTATIONARY COMMUNICATIONS SATELLITES FOR YEAR END 1986

Subsatellite Longitude[a]	Launch Date Object/Catalog Number[b]	Satellite Designation	Country or Organization	Service	Frequency Up/Down-Link (GHz)	Remarks
251.0°E (109.0°W)	16 Dec 1978 11153	ANIK B1 (4)	Canada-TELESAT	FSS	6,14a/4,12a	IFRB: 109°W ARII/A/136/1551 ARII/C/136/1567
252.2°E (107.5°W)	13 Apr 1985 15642	ANIK C1	Canada-TELESAT	FSS	14a/12a	IFRB: 107.5°W in coordination ARII/A/357/1500 ARII/C/569/1516 ARII/C/728/1674
257.0°E (103.0°W)	May 1985 15677	G-STAR 1	US-GTE	FSS	14a/12a	IFRB: 106.5°W (GSTAR) ARII/A/14/1525
254.0°E (106.0°W)	May 1978 8747	LES 9	US-Government	EXPER	6/UHF,7,4	IFRB: 106.0°W SPA-AA/207
254.7°E (105.3°W)	12 Aug 1969 04068	ATS 5	US-NASA	Experi-mental	UHF,6/UHF,7,4	IFRB: 105°W
255.0°E (105.0°W)	31 Aug 1984 15236	LEASESAT F-2	US-Government		UHF	
255.5°E (104.5°W)	26 Aug 1982 13431	ANIK D1	Canada-TELESAT	FSS	6/4	IFRB: 104.5°W ARII/A/279/1682 ARII/C/465/1724
255.0°E (105.0°W)	08 May 1985 16649	G-STAR 2	US-GTE	FSS	14a/12a	IFRB: 103°W *Adv. Publication AR/4/15/1525*
260.0°E (100.0°W)	09 Feb 1978 10669	FLTSATCOM	US-Government	FSS	UHF,8/UHF,7	IFRB: 100°W SP4-AJ/166/1382
261.0°E (99.0°W)	26 Feb 1982 13069	WESTAR 4	US-Western Union	FSS	6/4	IFRB: 99°W in coordination ARII/C/272/1623
261.0°E (99.0°W)	11 Nov 1982 13651	SBS 3 (USASAT 6B)	US-Satellite Business Systems	FSS	14a/12a	IFRB: 99°W SPA-A3/61/1280
263.0°E (97.0°W)	15 Nov 1980 12065	SBS 1 (USASAT 6A)	US-Satellite Business Systems	FSS	14a/12a	IFRB: 97°W in coordination ARII/C/325/1624 ARII/A/34/1553
264.0°E (96.0°W)	28 Jul 1983 14234	TELSTAR 301 (3A)	US-AT&T	FSS	6/4	IFRB: 97°W ARII/A/8/1524 ARII/C/879/1738
265.0°E (95.0°W)	24 Sep 1981 12855	SBS 2 (USASAT 6C)	US-Satellite Business Systems	FSS	14a/12a	IFRB: 95°W in coordination ARII/C/331/1624 ARII/C/332-336/1624
266.5°E (93.5°W)	21 Sep 1984 15308	GALAXY III (USASAT 12B)	US-Hughes Comm.	FSS	6/4	IFRB: 93.5°W in coordination ARII/A/22/1687 ARII/C/824/1615
268.8°E (91.2°W)	30 Aug 1984 15235	SBS 4 (USASAT 9A)	US-Satellite Business Systems	FSS	14a/12a	IFRB: 91°W in coordination ARII/A/10/1609 ARII/C/818/1696

TABLE 1 (continued). IN-ORBIT GEOSTATIONARY COMMUNICATIONS SATELLITES FOR YEAR END 1986

Subsatellite Longitude[a]	Launch Date Object/Catalog Number[b]	Satellite Designation	Country or Organization	Service	Frequency Up/Down-Link (GHz)	Remarks
269.0°E (91.0°W)	10 Aug 1979 11484	WESTAR 3	US-Western Union	FSS	6/4	IFRB: 91°W ARII/A/37 ARII/C/197 To be replaced by WESTAR VI-S in 1988
274.0°E (86.0°W)	01 Sep 1984 15237	TELSTAR 302 (USASAT 3C)	US-AT&T	FSS	6/4	IFRB: 86°W in coordination ARII/C/246/1620 ARII/C/247-256/1620
277.0°E (83.0°W)	16 Jan 1982 13035	SATCOM IV (USASAT 7B)	US-RCA	FSS	6/4	IFRB: 83°W ARII/C/188/1612
283.8°E (76.2°W)	21 Feb 1981 12309	COMSTAR D4 (USASAT 12C)	US-COMSAT General	FSS	6/4	Incl. 1.09° Colocated with COMSTAR D-2
284.2°E (76.0°W)	22 Jul 1976 09047	COMSTAR D2 (USASAT 12C)	US-COMSAT General	FSS	6/4	IFRB: 76°W ARII/C/907/1748 ARII/C/908-909/1748 Colocated with COMSTAR D-4
285.0°E (75.0°W)	May 1974 12472	GOES 5	US	FSS	6/4	IFRB: 75°W (GOES EAST) ARII/A/28
286.0°E (74.0°W)	22 Sep 1983 14365	GALAXY 2 (USASAT 7A)	US-Hughes Comm.	FSS	6/4	IFRB: 74°W in coordination ARII/A/312 ARII/C/812
288.0°E (72.0°W)	08 Sep 1983 14328	SATCOM II-R (VII) (USASAT 8B)	US-RCA	FSS	6/4	IFRB: 72°W in coordination ARII/A/37 ARII/C/221
291.0°E (69.0°W)	23 May 1984 15385	SPACENET II	US-GTE Spacenet	FSS	6,14a/4,12a	IFRB: 69°W in coordination USASAT 7C ARII/A/11 ARII/C/835
291.0°E	Feb 1986 16650	SBTS-2	Brazil	FSS	6/4	IFRB: 70.0°W (SBTS A1) ARII/A/16 ARIi/C/94
295.0°E (65.0°W)	08 Feb 1985 15561	SBTS-1	Brazil	FSS	6/4	IFRB: 65°W (SBTS A2) ARII/A/17 ARII/C/99
307.5°E (52.5°W)	15 Dec 1981 12994	INTELSAT V (F-3)	INTELSAT	FSS	6,14a/4,11	Manuevered from 27°W during Sep 1985 IFRB: 53°W, (INTELSAT V Continental I) ARII/A/82/1588 ARII/C/591
310.0°E (50.0°W)	22 May 1975 7815	INTELSAT IV (F-1)	INTELSAT	FSS	6/4	IFRB: 50.0°W, (INTELSAT IV ATL I) ARII/A/75 ARII/C/592

TABLE 1 (continued). IN-ORBIT GEOSTATIONARY COMMUNICATIONS SATELLITES FOR YEAR END 1986

Subsatellite Longitude[a]	Launch Date Object/Catalog Number[b]	Satellite Designation	Country or Organization	Service	Frequency Up/Down-Link (GHz)	Remarks
318.0°E (42.0°W)	05 Apr 1983 13969	TDRS East	US-NASA US-Systematics Gen.	SRSS FSS	1,14d/2,13 6/4	IFRB: 41.0°W Incl. 1.51°
319.0°E (41.0°W)	1983 13969	TDRS 1	US	FSS	6/4	IFRB: 41.0°W (TDRS EAST) ARII/A/231 ARII/C/46
325.5°E (34.5°W)	05 Mar 1982 13083	INTELSAT V (F-4)	INTELSAT	FSS	6,14a/4,11	IFRB: 34.5°W, (INTELSAT V ATL 4) ARII/A/121 AR/II/C/220
329.0°E (31.0°W)	26 Sep 1975 08330	INTELSAT IV-A (F-1)	INTELSAT	FSS	6/4	Incl. of 1.7° on 12/26/85 IFRB: 31°W (INTELSAT IVA ATL 6) ARII/A/68 ARII/C/215
331.5°E (18.5°W)	19 May 1983 14077	INTELSAT V (F-6) MCS B	INTELSAT INMARSAT Lease	FSS MMSS	6,14a/4,11 1,6b,6 1.5a,4	IFRB: 18.5°W, MCS ATL A is a spare for MARECS B2 IFRB: 18.5°W (INTELSAT V ATL 2)
332.5°E (27.5°W)	29 Jun 1985 15873	INTELSAT V-A (F-11)	INTELSAT	FSS	6,14a/4,11	IFRB: 27.5°W (INTELSAT VA ATL 2) ARII/A/335 ARII/C/123
334.0°E (26.0°W)	10 Nov 1984 15386	MARECS B2	ESA-leased to INMARSAT	MMSS	1.6b,6b 1.5a,4	Operational 1 Jan 1985 as Pacific Ocean Maritime Satellite IFRB: 177.5°E
335.0°E (25.0°W)		VOLNA 1	USSR	AMSS	UHF,1.6e/UHF, 1.5c	(MARECS PAC 1)
335.0°E (25.0°W)	16497	RADUGA 18	USSR	FSS	6/4	IFRB: 25.0°W (STATSIONAR 8) ARII/A/95 ARII/C/50
335.4°E (24.5°W)	22 Mar 1985 15629	INTELSAT V-A (F-10)	INTELSAT	FSS	6,14a/4,11	IFRB: 24.5°W (INTELSAT VA ATL 1)
335.7°E (24.3°W)	05 Oct 1980 12003	RADUGA 7	USSR	FSS	5,6/3	Operates below INTELSAT V-A frequencies
337.0°E (23.0°W)	18 Jan 1980 11669	FLTSATCOM 3	US-Government	FSS	UHF,8/UHF,7	IFRB: 23.0°W ARII/A/48/1561, ADD-1/1587
337.5°E (22.5°W)	19 Nov. 1978 15391	NATO III	NATO	FSS	20a,8/2.3,7	On 12/26/85 drifting at 0.04°E and incl. 1.68° incl. 4.06°
338.4°E (21.6°W)	25 May 1977 10024	INTELSAT IV-A (F-4)	INTELSAT	FSS	6/4	IFRB: 21.5°W, FLTSAT B (EATL) (INTELSAT IVA ATL 1)

TABLE 1 (continued). IN-ORBIT GEOSTATIONARY COMMUNICATIONS SATELLITES FOR YEAR END 1986

Subsatellite Longitude[a]	Launch Date Object/Catalog Number[b]	Satellite Designation	Country or Organization	Service	Frequency Up/Down-Link (GHz)	Remarks
342.0°E (18.0°W)	Apr 1976 08808	NATO I-A	NATO	FSS	8/7	
344.0°E (16°W)	30 Jun 1983 14160	GORIZONT 7	USSR	FSS	6/4	
345.0°E (15.0°W)	10 Nov 1984 15384	LEASESAT F-1	US-Government		UHF	
345.1°E (14.9°W)	19 Feb 1976 8697	MARISAT F-1	US-COMSAT General	MMSS,FSS	UHF 1,6b,6 UHF 1,5a,4	Spare, but only UHF transponder used IFRB: 15°W ARII/A/7/1101 ARII/C/33/1254
348.0°E (12.0°W)	Nov 1979	DSCS II	US-Government	FSS	UHF,8/UHF,7	IFRB: 12°W (USGCSS 2 ATL) ARII/C/153
349.6°E (10.4°W)	14 Jun 1980 11841	GORIZONT 4	USSR	FSS	6,8/4,7	IFRB: 11°W STATSIONAR 11 in coordination ARII/C/877/1737
352.0°E (8°W)	04 Aug 1984 15159	TELECOM 1-A	France	FSS	2,6,8,14a/2, 4,7,12a,12b,12c	IFRB: 8°W in coordination ARII/A/268 ARII/C/84/1611
355.0°E (5.0°W)	08 May 1985 15678	TELECOM 1-B	France	FSS	2,6,8,14a/2, 4,7,12a,12b,12c	IFRB: 5°W ARII/A/269 ARII/C/472
356.2°E (3.8°W)	29 Jan 1976	INTELSAT IV-A (F-2)	INTELSAT	FSS	6/4	IFRB: 4°W, INTELSAT IVA ATL 2 in coordination ARII/A/65 ARII/C/121
357.0°E (3.0°W)	12 Mar 1983 13878	EKRAN 10	USSR	FSS	6/UHF	Incl. 3.75°
358.3°E (1.7°W)	06 Dec 1980 12089	INTELSAT V (F-2)	INTELSAT	FSS	6,14a/4,11	IFRB: 1°W, (INTELSAT V CONT 4) Incl. 0.034° ARII/A/83 ARII/C/593
359.0°E (1.0°W)	Jun 1986 07547	SKYNET 4A (2B)	UK	FSS	6/4	IFRB: 1°W ARII/A/336 ARII/C/182

[a]The list of satellite longitudes was compiled from the best information available.
[b]Space objects that can be tracked are assigned an object/catalog number which is used by NASA and others.

TABLE 2. PLANNED GEOSTATIONARY COMMUNICATIONS SATELLITES AS OF YEAR END 1986

Subsatellite Longitude[a]	Launch or In-Use Date/ Period of Validity[b]	Satellite Designation	Country or Organization	Service	Frequency Up/Down-Link (GHz)	Remarks
1.0°E	Sep 1986	GDL 5	Luxembourg	FSS/BSS	6b,12e,14a 11.7,12b,12c	ARII/C/612/1657
3.0°E	198?	TELECOM 1-C	France	FSS/BSS	6b,8,14/4, 7,12b,12c	ARII/A/29/1339 ARII/C/116/ADD-2 ARII/C/157/1598 ARII/C/131/1594 ARII/C/116/ADD-2/1643 AR14/D/28/1669
3.0°E	30 Sept 1991/10	TELECOM 2-C	France	FSS MMSS	6,14/4,12b,12c 8/7 2/2.2	ARII/A/326/1745
5.0°E	198?	TELE-X	Norway, Sweden	FSS/BSS	2,6,30a,17,20a/2, 12a,12b,20d	ARII/A/27/1535 ARII/C/446/1644
6.0°E	Mar 1986/10[c]	SKYNET 4B	UK	FSS/MMSS	UHF,45/7,UHF	AR14/C/82/1677 ARII/C/183/ADD-1/1652 ARII/C/589/1652 ARII/C/183/1611
7.0°E	1987	F-SAT1	France	FSS	2,14a,12b,12c,20d	AR/II/C/568/1648 AR/II/A/79/1587 AR/II/C/566-567/1648
8.0°E	31 Dec 1987/20	STATSIONAR 18	USSR	FSS/BSS	6a,6b,6/ 4a	ARII/A/219/1686 ARII/C/911/1749 ARII/C/911/CORR-1/1756
8.0°E	31 Dec 1987/20	GALS 7	USSR	FSS	8/7	ARII/A/238/1693 ARII/C/913/1750 ARII/C/913/ADD-1/A56
8.0°E	31 Dec 1987/20	VOLNA 15	USSR	AMSS	UHF,1.6e/ UHF,1.5c	ARII/A/241/1693
8.0°E	08 Aug 1990/20	TOR-8	USSR	FSS/AMSS/ LMSS/MMSS	43, 45, 20b	ARII/A/285/1710
10.0°E	1986	APEX	France	BSS/FSS	6,30a/2,4,20b, 39,40	ARII/C/1583-584/1651 ARII/A/62/1578 AR14/C/79/1676
12.0°E	1982/20	PROGNOZ 2	USSR	SRS	14a,2	SPA-AA/317/1471
13.0°E	31 Dec 1987/7	ITALSAT	Italy	FSS	30a/2,20b,39,40	ARII/A/151/1633 ARII/C/827/1697

TABLE 2 (continued). PLANNED GEOSTATIONARY COMMUNICATIONS SATELLITES AS OF YEAR END 1986

Subsatellite Longitude[a]	Launch or In-Use Date/ Period of Validity[b]	Satellite Designation	Country or Organization	Service	Frequency Up/Down-Link (GHz)	Remarks
13.0°E	1984	EUTELSAT I-2	France/EUTELSAT	FSS/BSS	14a/11,12a,12b,12c	SPA-AJ/328/1492 ARII/A/61/1578, 1589 & 1582 ARII/C/445/1644 AR14/C/51/1669 ARII/D/71/1700
13.0°E	31 Oct 1989/15	EUTELSAT II-13E	France/EUTELSAT	STS	2/2	ARII/A/306/1732
14.0°E	Unknown	Nigerian National System	Nigeria	FSS	6/4	SPA-AA/2091346
15.0°E	1986	AMS I	Israel	FSS	6,14a/4,11	ARII/A/39/1554 ARII/B/30/1593
15.0°E	Dec 1990/20	STATSIONAR 23	USSR	FSS	6/4a	ARII/A/318/1740
15.0°E	31 Dec 1990/20	TOR 12	USSR	FSS/AMSS/ MMSS/LMSS	43, 45 20b	ARII/A/309/1736
15.0°E	1986	AMS 2	Israel	FSS	6,14a/4,11	ARII/A/39/1554
15.0°E	31 Dec 1990/20	GALS 12	USSR	FSS	8/7	ARII/A/313/1740
16.0°E	1987	SICRAL I-A	Italy	FSS	8,14a,45/7,12b, 12c,20b,44	ARII/A/44/1588
16.0°E	31 Jan 1986/11	EUTELSAT I-4	France/EUTELSAT	FSS/STS	14a/11, 11,12b 12c	ARII/A/218/1685 ARII/C/874/ADD-1/ CORR-1/1762/1737
17.0°E	Unknown	SABS	Saudi Arabia	BSS	14a/12b,12c	SPA-AA/235/1387
17.0°E	1988	SABS I-2	Saudi Arabia	BSS	14a,14a/12b,12a	ARII/A/125/1616
19.0°E	Sep 1986	GDL 6	Luxembourg	FSS/BSS	6b,14a/11,12	ARII/A/94/1594/ ADD-1/1708
20.0°E	Unknown	Nigerian National System	Nigeria	FSS	6/4	SPA-AA/209/1346
20.0E	Feb 1982	SIRIO 2	France/SIRIO		1,3	SPA-AJ/424/1515
22.0°E	1987	SICRAL I-B	Italy	MMSS/FSS	UHF,8,14a,45/7, 12b,12c,20b	ARII/A/45/1557 ARII/A/45/1588
23.0°E	31 Dec 1987/20	STATSIONAR 19	USSR	FSS/BSS	6a,6b,4a	ARII/A/220/1686 ARII/C/916/1752 ARII/C/917/1952 ARII/C/1917 CORR-1/1756

TABLE 2 (continued). PLANNED GEOSTATIONARY COMMUNICATIONS SATELLITES AS OF YEAR END 1986

Subsatellite Longitude[a]	Launch or In-Use Date/ Period of Validity[b]	Satellite Designation	Country or Organization	Service	Frequency Up/Down-Link (GHz)	Remarks
23.0°E	31 Dec 1987/20	GALS 8	USSR	FSS	8/7	ARII/A/239/16930 ARII/C/914/1750 ARII/C/914/ADD-1/1756
23.0°E	31 Dec 1987/20	VOLNA 17	USSR	FSS	UHF,1.6e/UHF,1.5c	ARII/A/242/1693
23.0°E	01 Aug 1990/20	TOR 7	USSR	FSS/MSSS LMSS/AMSS	43,45,20b	ARII/4/284/1710
23.5°E	1987	DFS 1	Germany	FSS	2,14,30/11,12b,12c, 20b	ARII/A/40/1556 ARII/C/696-697/1670 ARII/C/774/1681 ARII/C/779/1681
26.0°E	31 Dec 1988/20	ZOHREH 2	Iran	FSS	14a/11	SPA-AA/164/1278 SPA-AJ/76/1303
28.5°E	1987	DFS 2	Germany	FSS	2,14/11,12b,12c, 20d,30	ARII/A/41/1556
32.0°E	1987/10	VIDEOSAT 1	France	FSS	14a/2,12b,12c	ARII/A/80/1588 ARII/C/574/1650 ARII/C/580/1650 AR14/C/781/1676
34.0°E	31 Dec 1988/20	ZOHREH 1	Iran	FSS	14a/11	SPA-AA/163/1278 A/296/ADD-1/1728
35.0°E	Unknown	PROGNOZ 3	USSR	SRS	-/4a/2	SPA-AA/318/1471
35.0°E	1 Aug 1990/20	TOR 2	USSR	FSS/AMSS/ LMSS/MMSS	43,45,20b	ARII/A/279/1710
35.0°E	Jun 1988/20	STATSIONAR D-3	USSR	FSS	6b/4b	ARII/A/195/1675
35.0°E	31 Dec 1985/20	VOLNA 11	USSR	AMSS	UHF,1.6d/UHF,1.5c	AR/II/A/150/1631
35.0°E	Dec 1984/20	GALS 6	USSR	FSS	8/7	AR/II/C/109/1578
36.0°E	31 Oct 1989/15	EUTELSAT II-36E	France/EUTELSAT	STS	2/2	ARII/A/307/1732
38.0°E	1986	PAKSAT 1	Pakistan	FSS	14a/11,12b,12c	ARII/A/90/1592
40.0°E	31 Dec 1986/20	LOUTCH 7	USSR	FSS	14a/11	ARII/A/270/CORR-1/1707
40.0°E	10 Oct 1984/20	STATSIONAR 12	USSR	FSS	4a	ARII/C/878/1737
41.0°E	Unknown	ZOHREH 4	Iran	FSS	14a/11	SPA-AA/203/1330
41.0°E	1986	PAKSAT 2	Pakistan	FSS	14a/12b,12c	ARII/A/91/1592
45.0°E	Unknown	VOLNA 3	USSR	MMSS	UHF,1.6b/1.5a,UHF	SPA-AA/274/1425

TABLE 2 (continued). PLANNED GEOSTATIONARY COMMUNICATIONS SATELLITES AS OF YEAR END 1986

Subsatellite Longitude[a]	Launch or In-Use Date/ Period of Validity[b]	Satellite Designation	Country or Organization	Service	Frequency Up/Down-Link (GHz)	Remarks
45.0°E	Unknown	LOUTCH P2	USSR	FSS	14a/11	SPA-AA/178/1289 SPA-AJ/122/1340
45.0°E	Jun 1988/20	STATSIONAR D4	USSR	FSS	6a/4b	ARII/A/196/1675
45.0°E	1980	GALS 2	USSR	FSS	8/7	SPA-AJ/112/1335 SPA-AA/154/1262
45.0°E	31 Dec 1990/20	VOLNA 3n	USSR	MMSS	1.6b/1.5a	ARII/A/249/1697
45.0°E	1 Aug 1990/20	TOR 3	USSR	FSS/AMSS MMSS/LMSS	43,45, 20b	ARII/A/280/1710
47.0°E	31 Dec 1988/20	ZOHREH 3	Iran	FSS	14a/11	SPA-AA/165/1278
53.0°E	Unknown	LOUTCH 2	USSR	FSS	14a/11	SPA-AJ/85/1318 Leased to Intersputnik
53.0°E	1 Aug 1987/10	SKYNET 4C	UK	FSS/MMSS	UHF,8, 45/UHF	ARII/B/45/1626 ARII/A/84/ADD-1/1597 ARII/A/84/1588 ARII/C/870/1737/867
53.0°E	1 Jun 1989/15	MORE 53	USSR	MMSS/FSS	1.6b,6b/1.5a,1.5b,4	ARII/A/185/1662
57.0°E	1988	INTELSAT VI (IND 2) INTELSAT V (IND 3)	INTELSAT INTELSAT	FSS	6a,6b,6,14/4a,4,11	ARII/A/72/1584
57.0°E	1985	INTELSAT V-A (IND 2)	INTELSAT	FSS	6,14a/4,11	ARII/A/68/1580
58.0 (302.0°W)	1 Aug 1990/20	TOR 13	USSR	TSS/LMSS	43,45/20b	ARII/A/310/1736
58.0 (302.0°)	Jun 1988/20	STATSIONAR 24	USSR	AMSS/MMSS FSS	6/4a	ARII/4/319 Corr-1/1760
58.0	31 Dec 1990/20	GALS 13	USSR	FSS	8/7	ARII/A/B14/1740
58.0	31 Dec 1990/20	VOLNA 4	USSR	MMSS/FSS	1.6b/1.5a	SPA-AA/172/1286
60.0°E	1988	INTELSAT VI	INTELSAT	FSS	6a,6b,6,14/4a,4,11	ARII/A/71/1584
64.5°E	Unknown	MARECS (IND 1)	INMARSAT (F)	MMSS	1.6b,6b/1.5a, 4	SPA-AJ/243/1432
64.5°E	1989/15	INMARSAT IOR	INMARSAT (G)	MMSS/AMSS	1.6b,1.6c,1.6d/ 6b,/4a	ARII/A/178/1644 ARII/C/846/1706

TABLE 2 (continued). PLANNED GEOSTATIONARY COMMUNICATIONS SATELLITES AS OF YEAR END 1986

Subsatellite Longitude[a]	Launch or In-Use Date/ Period of Validity[b]	Satellite Designation	Country or Organization	Service	Frequency Up/Down-Link (GHz)	Remarks
64.5°E	31 Jan 1990/15	INMARSAT IOR-11	INMARSAT	MMSS/AMSS/ FSS/STSS	1.6b,1.6c,1.6d/ 1.5b,1.5c 6b,4a,4	ARII/A/293/1713
65.0°E	April 1983/1	SIRIO	Italy	FSS	1,11,12,17/18	ARII/C/601/1655
66.0°E	1986	INTELSAT V (IND 4)	INTELSAT	FSS	6,14a/4,11	SPA-AA/253/1419
66.0°E	1 July 1987/10	INTELSAT MCS (IND D-Spare)	INTELSAT	MMSS/FSS	6b,1.6b/1.5a,4	SPA-AA/275/1425 ARII/C/857/1735
66.0°E	1989	INTELSAT V-A 66E	INTELSAT	FSS	6,14a/4,11	
69.0°E	31 Dec 1990/20	GALS 14	USSR	FSS	8/7	ARII/A/315/1740 ARII/A/315/CORR-1/1760
69.0°E	Dec 1986/20	STATSIONAR 20	USSR	FSS	6/4a	ARII/A/316/1740
70.0°E	1985/86	STW 2	China, Peoples Republic of	FSS	6/4	SPA-AA/142/1255
72.0°E	Dec 1984/10	FLTSAT A (IND)	USA	FSS/MMSS	UHF,8/UHF,7	ARII/A/100/ADD-1/ 1652, A/100/1605
73.0°E	Unknown	MARECS (IND 2)	INMARSAT (F)	MMSS	1.6b,6b,/1.5a, 4	ARII/D/3/1551

74.0°E (286.0°W)	31 July 1990/20	INSAT METEO	India	BSS/FSS MET AIDS logical	UHF,6,6b/4b, 0.4c/-	ARII/A/262/1702
74.0°E	July 1990/20	INSAT II-C	India	BSS/FSS MET AIDS	UHF,6b/4b, 0.4c/-	ARII/A/262/1702 RES 33/A/7/1702
75.0°E	31 Dec 1986/10	FLTSATCOM B (IND)	USA	FSS/MMSS	45/20d	ARII/A/52/1561 AR/II/A/52/ADD-1/1587
76.0°E	31 Dec 1986/15	GOMS	USSR	MMSS/FSS	30a/7,1.6f, 20a,20b	ARII/A/205/1678
77.0°E	Oct 1989/20	SSRD 2	USSR	FSS	14c,15,14b/11, 13,12e	ARII/A/188/1672
80.0°E	Unknown	POTOK 2	USSR	FSS	6/4	ARII/A/179/1645 SPA-AA/345/1485
80.0°E	Dec 1986/20	STATSIONAR 13	USSR	FSS	6/4a	ARII/C/599/1655
80.0°E	31 Dec 1987/20	LOUTCH 8	USSR	FSS	14a/11,6/4a	ARII/A/271/CORR-1/1707
81.5°E	1 Jun 1990/10	FOTON 2	USSR	FSS	6b/4b	ARII/A/236/1692

TABLE 2 (continued). PLANNED GEOSTATIONARY COMMUNICATIONS SATELLITES AS OF YEAR END 1986

Subsatellite Longitude[a]	Launch or In-Use Date/ Period of Validity[b]	Satellite Designation	Country or Organization	Service	Frequency Up/Down-Link (GHz)	Remarks
83.0°E	Jan 1989/15	INSAT I-D	India	FSS/STSS/ MET AIDS	6b/4 UHF 0.4c/-	ARII/A/126/1617 RES 33/A/3/ADD-1-10/ ARI4/C/91/1682 ARII/C/860/1735
83.0°E	Jan 1990/20	INSAT II-A	India	FSS/MMSS	6,6b,4,4b	ARII/A/260/1702 RES 33/A/5/1702
85.0°E	Unknown	LOUTCH P3	USSR	FSS	14a/11	SPA-AA/179/1289 SPA-AJ/123/1340
85.0°E	1 Aug 1990/20	TOR 4	USSR	FSS/AMSS/ MMSS/LMSS	43,45,20b	ARII/A/281/1210
85.0°E	1980	GALS 3	USSR	FSS	8/7	SPA-AJ/112/1335 SPA-AA/154/1262
85.0°E	Jun 1988/20	STATSIONAR D5	USSR	FSS	6/4b	ARII/A/197/1675
85.0°E	Unknown	VOLNA 5	USSR	MMSS	UHF,1.6b/1.5a,UHF	SPA-AJ/100/1329 SPA-AA/173/1286
85.0°E	31 Dec 1990/20	VOLNA 5M	USSR	FSS	1.6b/1.5a	ARII/A/250/1697
85.0°W	31 Dec 1989/10	NAHUEL 2	Argentina	FSS	14a,6/12,4	ARII/C/204/1677 ARII/A/204/1677
87.5°E (272.5°)	15 Mar 1988	CHINASAT 1	PRC	FSS	6/4	ARII/A/255/1702
89.0°W	30 Jun 1990/10	CONDOR B	Andean	FSS	6/4	ARII/A/209/1679
90.0°E (270.0°W)	Unknown	LOUTCH 3	USSR	FSS	14a/11	SPA-AJ/86/1318
90.0°E	1 Jun 1989/15	MORE 90	USSR	MMSS	1.6b,6b/1.5a,1.5b,4	ARII/A/154/1562
90.0°E	Unknown	VOLNA 8	USSR	MMSS	UHF,1.6b/1.5a,UHF	SPA-AA/289/1445 ARII/C/15/1589
93.5°E	Mar 1990/20	INSAT II-B	India	FSS/BSS MET AIDS	6,6b/UHF 0.4c/-	ARII/A/261/1702 RES 33/A/6/261/1702
93.5°E	1986/18	INSAT I-C	India	FSS/STS MET AIDS	UHF,6/4,6/4a 6b/4, 0.4c/-	SPA-AJ/231/1429 ARII/C/851/1708 ARII/C/852-856/1708
95.0°E	1985/20	CSDRN	USSR	SRS	14b/14d,11,13	SPA-AA/342/1484 (May have been launched as COSMOS 1700)
95.0°E	July 1984/20	STATSIONAR 14	USSR	FSS/BSS	6/UHF	SPA-AJ/311/1469

TABLE 2 (continued). PLANNED GEOSTATIONARY COMMUNICATIONS SATELLITES AS OF YEAR END 1986

Subsatellite Longitude[a]	Launch or In-Use Date/ Period of Validity[b]	Satellite Designation	Country or Organization	Service	Frequency Up/Down-Link (GHz)	Remarks
96.5°E	31 Dec 1988/20	LOUTCH 9	USSR	FSS	14a/11	AR11/A/272/CORR-1/1707
97.0°E	30 Apr 1989/10	STSC 2	CUBA	FSS	6/4	AR11/A/268/1706 AR11/A/268/1723
98.0°E	15 Mar 1989/10	CHINASAT 3	PRC	FSS	6/4	AR11/A/257/1702
99.0°E	Unknown	STATSIONAR-T	USSR	FSS/BSS	6/UHF	RES-SPA2-3-AA10/1426 SPA-AJ/316/1473
99.0°E	Unknown	STATSIONAR-T2	USSR	FSS/BSS	6/UHF	SPA-AJ/316/1473
103.0°E	31 Dec 1988/20	STATSIONAR 21	USSR	FSS/BSS	5a, 6, 6b 4a,4,	AR11/A/244/1692 AR11/C/905/1748 AR11/C/906/1748 AR11/C/905/ADD-1/1752
103.0°E	April 1986	STW 2	China	FSS	6/4	AR11/A/245ADD-1/1712
103.0°E	31 Dec 1988/20	LOUTCH 5	USSR	FSS	14a/11	AR11/A/243/1694
110.0°E	1 Jun 1990	BS-3	Japan	FSS	14a/12c,12b	AR11/A/334/1750
110.5°E	31 Dec 1988/10	CHINASAT 11	China	FSS	6/4	AR11/A/25b/1702
118.0°E ±0.5°	Jun 1989	PALAPA B-3	Indonesia	FSS	6/4	AR11/A/157/1637
124.0°E	31 Dec 1988	SCS-1b	Japan	CM/TM/FSS	12c,30a,14a,20a, 20b, 12b, 12c	AR11/A/274/1708
128.0°E	1984/20	STATSIONAR 15	USSR	FSS	6/4a	SPA-AA/273/1425 SPA-AJ/3071469
128.0°E	1 Jun 1990/20	GALS 10	USSR	FSS	8/7	AR11/A/247/1695 AR11/C/919/1753
128.0°E	Dec 1988/13	SCS-1B	Japan	FSS	-/12c,30a,14a/20a, 20b,12b,12c	AR11/A/274/1708
128.0°E	Unknown	VOLNA 9	USSR	FSS/BSS MMSS	UHF,1.60b/1.5a,UHF 1,2,11,34	
128.0°E	30 Jun 1988/13	SCS-1a	JAPAN	FSS	14a/12c,30a,20a, 20b,12b,12c	AR11/A/273/1708
128.0°E	1 Aug 1990/20	TOR 6	USSR	FSS/LMSS AMSS/MMSS	43,45,20b	AR11/A/283/1710
128.0°E	Jun 1988/20	STATSIONAR-D6	USSR	FSS	6a/4b	AR11/A/198/1675
128.0°E	31 Dec 1990/20	VOLNA 9M	USSR	MMSS/FSS	1.6b/1.5a	AR11/A/251/1697

TABLE 2 (continued). PLANNED GEOSTATIONARY COMMUNICATIONS SATELLITES AS OF YEAR END 1986

Subsatellite Longitude[a]	Launch or In-Use Date/ Period of Validity[b]	Satellite Designation	Country or Organization	Service	Frequency Up/Down-Link (GHz)	Remarks
130.0°E	Unknown	ETS 2	Japan	Experi-mental		
130.0°	July 1990/20	PROGNOZ 5	USSR	SRSS	2/4a	ARII/A/275/1709
130.0°E	Dec 1984/20	GALS 5	USSR	FSS	8/7	ARII/C/108/1578 ARII/C/28/1561 SPA-AA/339/1480
130.0°E	1 Aug 1990	TOR 10	USSR	FSS/MMSS/ AMSS/LMSS	43,45,20d,20b	ARII/A/290/1711
132.0°E	March 1988/10	CS-3A	Japan	FSS	6,30a,20a,20b	ARII/A/212/1680
136.0°E	30 Jun 1988/10	CS-3B	Japan	FSS	6,30a,20a,20b	ARII/A/213/1680
140.0°E	Aug 1984	GMS 3	Japan	FSS	2,4a/UHF,1.6m,1.6n	ARII/C/474/1648 ARII/A/54/1563
140.0°E	Unknown	LOUTCH 4	USSR	FSS	14a/11	SPA-AJ/87/1318
140.0°E	1 Jun 1984	MORE 140	USSR	MMSS	1.6b,6b/1.5a,4	ARII/A/186/1662
140.0°E	Unknown	VOLNA 6	USSR	FSS/BSS	4a	
145.0°E (215.0°W)	31 Dec 1987/20	STATSIONAR 16	USSR	FSS	6b,6,4a	ARII/A/76/1593 & 1586 ARII/C/850/CORR-2/1728 ARII/C/849/CORR-2/1728 ARII/C/849/1707
150.0°E	Unknown	CSE	Japan	FSS	14a/12a	AR533/6/3/1639 AR533/6/3/164 ARII/C/177/1606
150.0°E	1 Aug 1987/5	ETS-V	Japan	MMSS/FSS/ STS/AMSS Experi-mental	6/5 6 1.6d,1.6e/1.5c	ARII/A/217/1685 ARII/C/923/1754/920
150.0°E	31 Dec 1987/12	JCSAT 1	Japan	FSS	14a/12b,12c	ARII/A/253/1700
154.0°E	30 Apr 1988/12	JCSAT 2	Japan	FSS	14a/12b,12c	ARII/A/254/1700
164.0°E	1986/10	AUSSAT 3	Australia (OTC)	FSS/BSS	14a,12b,12c	RES 33/C/5/1643 RES 33/C/5/1647-III
164.0°E	1986/10	AUSSAT PAC III	Australia (OTC) South Pacific Region	FSS	14a/12b,12c	Adv. Publication 5/85 ARII/A/215/1684
166.0°E	July 1990/20	PROGNOZ 6	USSR	SRS	2/4a	ARII/C/941/1763

TABLE 2 (continued). PLANNED GEOSTATIONARY COMMUNICATIONS SATELLITES AS OF YEAR END 1986

Subsatellite Longitude[a]	Launch or In-Use Date/ Period of Validity[b]	Satellite Designation	Country or Organization	Service	Frequency Up/Down-Link (GHz)	Remarks
166.0°E	31 Dec 1988/15	GOMS 2	USSR	MMSS/FSS	30a/7,1.6f,20a,20b	ARII/A/207/1578
167.0°E	Jun 1985/20	PACSTAR I	Papua, New Guinea	FSS	14a,6b,12a,12b,4a	ARII/A/200/1676
167.0°E	Oct 1989/20	SSRD 2	USSR	FSS	14c,15,14b/11, 13,12c	ARII/A/187/1672
167.0°E	10 Sept 1990/15	PACSTAR A-1	Papua, New Guinea	AMSS/MMSS	1.6,1.6e/1.5c	ARII/A/331/1749
172.0°E	Dec 1986/10	FLTSAT B (W PAC)	USA	FSS/MMSS	45/20d	ARII/A/51/1561 ARII/A/51/ADD-1/1587
173.0°E	Jan 1987/10	INTELSAT V-A (PAC 1)	INTELSAT	FSS	6,14a/4,11	ARII/A/65/1580
174.0°E	Dec 84?/10	INTELSAT V (PAC 1)	US-INTELSAT	FSS	6,14a/4,11	SPA-AJ/376/1511 Notified
174.0°E	Jan 1987/10	INTELSAT V-A (PAC 1)	US-INTELSAT	FSS	6,14a/4,11	ARII/C/680/1668
174.0°E	Jan 1987/10	INTELSAT IV-A (PAC 1)	INTELSAT	FSS	6/4	Notified
175.0°E	Dec 1987/10	USGCSS 3 (W PAC)	USA	FSS/MMSS LMSS/STS	8/7,2,8/7	ARII/266/ADD-1/1730/ 1706. See also Table 1.
175.0°E	10 Sept 1990/15	PACSTAR A-2	Papua, New Guinea	AMSS/MMSS	1.6d,1.6e/1.5c	ARII/A/332/1749
177.0°E (79°E)	Jan 1986/10	INTELSAT V (PAC 2)	US-INTELSAT	FSS	6,14a/4,11	ARII/A/81/1588/ 66/1580 ARII/C/681/1668 SPA-AA/255/1419 ARII/C/590/1652
177.0°E	Jan 1987/10	INTELSAT V-A (PAC 2)	US-INTELSAT	FSS	6/14a/4,11	ARII/A/66/1580 ARII/C/678/1668
179.0°E	Dec 1984/10	INTELSAT V (PAC 2)	US-INTELSAT	FSS	6,14a/4,11	SPA-AJ/377/1511
179.5°E	31 Oct 1989/15	INMARSAT POR-1	UK/INMARSAT	MMSS/AMSS/ FSS/STS	1.6b,1.6c,1.6d/ 1.5b,1.5c 6g/4a 6,4	ARII/A/329/1747
180.0°E (180.0°W)	Jan 1985/10	INTELSAT V (PAC 3)	US-INTELSAT	FSS	6,14a/4,11	ARII/C/682/1668

TABLE 2 (continued). PLANNED GEOSTATIONARY COMMUNICATIONS SATELLITES AS OF YEAR END 1986

Subsatellite Longitude[a]	Launch or In-Use Date/ Period of Validity[b]	Satellite Designation	Country or Organization	Service	Frequency Up/Down-Link (GHz)	Remarks
180.0°E (180.0°W)	1991/10	INTELSAT V-A (PAC 3)	INTELSAT	FSS	6,14a/4,11	ARII/
180.0°E (180.0°W)	1 Jul 1963/10 Jan 1986	INTELSAT MCS PAC A	USA	MMSS/FSS	1.6b/1.5a 6b/4a	SPA-AJ/477/1577 ARII/C/859/1735
182.0°E (178.0°W)	1 Jul 1990/10	USASAT 13K	USA	FSS	6/4	ARII/C/945/1763
185.0°E (175.0°W)	Jun 1985/20	PACSTAR 2	Papua, New Guinea	FSS	14,6b/12a,12b,4a	ARII/A/201/1676
189.0°E (171.0°W)	1985/15	TDRS WEST	USA-NASA/ SPACECOM	SRS	2,14d,14b/2,13	SPA-AA/232/1381 ARII/C/47/1568
190.0°E (170.0°W)	Jun 1988/20	STATSIONAR D2	USSR	FSS	6/4b	ARII/A/194/675
190.0°E (170.0°W)	1 Aug 1990/20	TOR 5	USSR	FSS/AMSS/ LMSS/MMSS	43,45,20b	ARII/A/282/1710
190.0°E (170.0°W)	Unknown	LOUTCH P4	USSR	FSS	14a/11	SPA-AA/180/1289 SPA-AJ/124/1340
190.0°E (170.0°W)	Unknown	STATSIONAR 10	USSR	FSS	6/4	SPA-AJ/64/1280
190.0°E (170.0°W)	Unknown	VOLNA 7	USSR	MMSS	UHF,1.6b/1.5a,UHF	SPA-AA/175/1286
190.0°E (170.0°W)	1980/20	GALS 4	USSR	FSS	8/7	SPA-AJ/114/1335 SPA-AA/156/1262
190.5°E (169.5°W)	1 Jun 1990/10	FOTON 3	USSR	FSS	6b/4b	ARII/A/237/1692
192.0°E (168.0°W)	Unknown	POTOK 3	USSR	FSS	6/4	SPA-AA/346/1485
200.0°E (160.0°W)	1985	ESDRN	USSR	SRS	14d,14b,10,11,13	SPA-AA/343/1484
201.0°E (159.0°W)	July 1990/20	PROGNOZ 7	USSR	SRS	2/4a	ARII/A/277/1709 ARII/C/942/1763
214.0°E (146.0°W)	1985	AMIGO 2	Mexico	BSS	17,20a/12b,12a	RES 33/A/2/1560
214.0°E (146.0°W)	Jun 1990/10	USASAT 20C (AURORA 2)	USA	FSS	6/4	ARII/A/259/1702

TABLE 2 (continued). PLANNED GEOSTATIONARY COMMUNICATIONS SATELLITES AS OF YEAR END 1986

Subsatellite Longitude[a]	Launch or In-Use Date/ Period of Validity[b]	Satellite Designation	Country or Organization	Service	Frequency Up/Down-Link (GHz)	Remarks
215.0°E (145.0°W)	Dec 1984/10	FLTSATCOM A (PAC)	USA	FSS/MMSS	UHF,8/UHF,7	ARII/A/181/1652
215.0°E (145.0°W)	Unknown	ILHUICAHUA 4	Mexico	FSS	6,14a/4,12a	ARII/A/25/1533
215.0°E (145.0°W)	1 Dec 1990/20	VOLNA 2M	USSR	MMSS	1.6e,1.6d/1.5a, 1.5c	ARII/A/252/1697
216.0°E (144.0°W)	Jun 1990/10	USASAT 20-B (WESTAR 7)	USA	FSS	6/4	ARII/A/258/1702
217.0°E (143.0°W)	Dec 1982/10	US SATCOM V	USA	FSS	6/4	ARII/D/104/1724
218.0°E (142.0°W)	1987/10	USASAT 11-C (WESTAR B)	USA	FSS	14a/12a	ARII/III/1609
219.0°E (141.0°W)	Dec 1989/10	USASAT 17-C (Galaxy 4)	USA	FSS	6/4	ARII/A/228/1687
219.0°E (141.0°W)	Unknown	ILHUICAHUA 3	Mexico	FSS	6,14a/4,12a	ARII/A/24,1533
223.0°E (137.0°W)	Dec 1989/10	USASAT 17-B (Spacenet 4)	USA	FSS	6/4	ARII/A/227/1687
225.0°E (135.0°W)	31 Dec 1986/10	USGCSS 3E PAC	USA	STS	2/3	SPA-AA/349/1493 ARII/C/406-408/169
224.0°E (136.0°W)	Jan 1990/10	USASAT 16-D (GSTAR 3)	USA	FSS	14a/12a	ARII/A/225/1687
226.0°E (134.0°W)	Jan 1990/10	USASAT 16-C	USA	FSS	14/11	ARII/A/224/1687
226.0°E	Jan 1990/10	USASAT 11-D (Hughes Galaxy)	USA	FSS	14a/11	ARII/A/120/1615
230.0°E (130.0°W)	Jun 1987/10	USASAT 10-D (Galaxy B)	USA	FSS	14a/12a	ARII/A/108/1609
230.0°E (130.09°W)	1 Oct 1991/15	ACS 3	USA	AMSS	1.6d,1.6c/1.5c	ARII/A/303/1723
230.0°E (130.0°W)	31 Dec 1987/10	USRDSS West	USA	FSS/RDSS	1.6a,6b/25	ARII/A/176/1641
234.0°E (126.0°W)	15 Sep 1987/10	USASAT 10-C	USA	FSS	14a/12a	ARII/A/107/1609
234.0°E (126.0°W)	31 Oct 1985/10	USASAT 20-A	USA	FSS/STS	6/4	ARII/A/304/1730

TABLE 2 (continued). PLANNED GEOSTATIONARY COMMUNICATIONS SATELLITES AS OF YEAR END 1986

Subsatellite Longitude[a]	Launch or In-Use Date/ Period of Validity[b]	Satellite Designation	Country or Organization	Service	Frequency Up/Down-Link (GHz)	Remarks
234.0°E (126.0°)	Sep 1987/10	USASAT 10-C	USA	FSS	14a/11	ARII/A/107/1609
236.0°E (124.0°W)	15 Sep 1986/10	USASAT 10-B	USA	FSS	14a/12a	ARII/A/106/1609
238.0°E (122.0°W)	15 Jan 1987/10	USASAT 10-A (SBS 5)	USA	FSS	14a/12a	ARII/A/105/1609 ARII/C/883/1741 ARII/C/616 ARII/C/617-624/1658 ARII/C/616/1658 AR30/A/4/1567 ARII/A/10/ADD-1/1548 ARII/A/10/1525
246.0°E (114.0°W)	Unknown	TELESAT D2	Canada-Telesat (ANIK)	FSS	6/4	SPA-AA/358/1500
249.5°E (110.5°W)	31 Mar 1991/12	TELESAT E-B	Canada-Telesat	FSS	6b,14a/4,12a	ARII/A/323/1744 ARII/A/323/CORR-1/1750
251.0°E (109.0°W)	Unknown See Remarks	TELESAT C3	Canada-Telesat	FSS	14a/12a	ARII/C/737-738/1674 AR14/C/101/1686
252.0°E (108.0°W)	Nov 1986/10	ANIK D2	Canada	FSS	6/4	ARII/C/960/1764
252.5°E	31 Mar 1991/12	TELESAT E-A	Canada-Telesat	FSS	6b,14a/4.12a	ARII/322/1744 ARII/A/322/CORR-1/1750
253.5°E (106.5°W)	31 Dec 1987/10	MSAT	Canada	FSS/MMSS	UHF/UHF-EHF	ARII/A/55/1563 AR14/C/32/1663 ARII/C/797-811/1689 ARII/A/56/1563 AR14/C/33/1663 ARII/A/56/ADD-1/1678 AR14/C/37/1664 ARII/C/797-811/1689
255.0°E (105.0°W)	Nov 1984/10	FLTSATCOM A (E PAC)	USA	FSS/MMSS	UHF,8/UHF,7	ARII/A/98/ADD-1/1652 ARII/A/98/1605
259.0°E (101.0°W)	Dec 1989/10	USASAT 17-A	USA	FSS	6/4	ARII/A/226/1687
259.0°E (101.0°W)	31 Jan 1990/10	USASAT 16-B	USA	FSS	14a/12a	ARII/A/223/1687
260.0°E (100.0°W)	10 Sep 1990/15	ACS I	USA	AMSS	1.6d,1.6e/1.5c	ARII/4/301/1723
260.0°E (100.0°W)	30 Sep 1987/10	USRDSS Central	USA	FSS/RDSs	1.6a,6b/2,5	ARII/A/175/1641
260.0°E (100.0°W)	10 Aug 1989/10	ACTS	US-NASA	FSS	30a/20b	ARII/A/321/1944 ARII/A/321/ADD-1/1753
267.0°E (93.0°W)	Jan 1990/10	USASAT 16-A	USA	FSS	14a/12a	ARII/A/222/1687

TABLE 2 (continued). PLANNED GEOSTATIONARY COMMUNICATIONS SATELLITES AS OF YEAR END 1986

Subsatellite Longitude[a]	Launch or In-Use Date/ Period of Validity[b]	Satellite Designation	Country or Organization	Service	Frequency Up/Down-Link (GHz)	Remarks
269.0°E (91.0°W)	April 1988/10	WESTAR VI-S	US-Western Union	FSS	6/4	ARII/C/962/1765 ARII/C/963/1765
263.0°E (970.0°W)	April 1989/10	STSC 2	Cuba	FSS	6/4	ARII/A/268/1706
271.0°E (89.0°W)	June 1990/10	CONDOR B	ANDEAN Countries	FSS	6/4	ARII/A/209/1679
265.0°E						
271.5°E (88.5°W)	Sep 1985/10	USASAT 12-D	USA	FSS	6/4	ARII/A/124/1615
271.5°E (88.5°W)	Feb 1984/10	SPACENET III	USA	FSS	14a,6/4,1a	ARII/C/834/1699
273.0°E (87.0°W)	14 Oct 1985 15 Jun 1985/10	USASAT 9-B	US-RCA USA	FSS	14a/12a	Under Construction ARII/A/102
275.0°E (85.0°W)	15 Mar 87/10	USASAT 9-C	USA	FSS	14a/12a	ARII/A/103/1609
275.0°E (85.0°W)	Dec 1989/10	NAHUEL II	Argentina	FSS	6/4 14a/11	ARII/C/204/1677
277.0°E (83.0°W)	1988	STSC I	Cuba	FSS	6/4	ARII/A/58/1578, Note 83.0°W occupied by USASAT 7B or SATCOM IV
277.0°E (83.0°W)	Jan 1987/10	USASAT 9-D (RCA-B)	USA	FSS	14a/11	ARII/A/104/1609
279.0°E (81.0°W)	Dec 1986/10	USASAT 7-D (ASC *2)	USA	FSS	6,14a/4,12a	ARII/C/50/1568 Was 79.0°W ARII/A/12/1525 ARII/C/257/1623
280.0°E (80.0°W)	Jun 1989/10	NAHUEL I	Argentina	FSS	14a,6/12,4	ARII/A/203/1677
281.0°E (79.0°W)	1985	TDRS Central	USA-NASA/SPACECOM USA-SYSTEMAT. GEN	SRS FSS	2,14d,14b/2,13a 6/4	SPA-AA/233/1381
281.0°E (79.0°W)	Jan 1987/15	TDRS C2	USA-NASA/ SPACECOM	SRS	2,14d,14b/2,13	ARII/B/166/1750 ARII/A/265/1704
281.0°E (79.0°W)	15 Mar 1987	USASAT 11-A	USA	FSS	14a/12a	ARII/A/109/1609
281.0°E (790.0°W)	Oct 1987/10	USASAT 12-A	USA	FSS/STS	6/4	ARII/C/896/898/ADD-1/ 1752
282.5°E (77.5°W)	June 1990/10	CONDOR A	Andean Countries	FSS	6/4	ARII/A/208/1679
283.0°E (77.0°W)	15 Jun 1987/10 27 Nov 1985	USASAT 11-B (Fedex-A)	USA RCA	FSS	14a/12a	ARII/A/110/1609 Under Construction

TABLE 2 (continued). PLANNED GEOSTATIONARY COMMUNICATIONS SATELLITES AS OF YEAR END 1986

Subsatellite Longitude[a]	Launch or In-Use Date/ Period of Validity[b]	Satellite Designation	Country or Organization	Service	Frequency Up/Down-Link (GHz)	Remarks
284.0°E (76.0°W)	Sep 1983/7	USASAT 12C	USA	FSS	6/4	ARII/C/907/1748
284.6°E	1986	SATCOL 1-A	Colombia	FSS	6/4	SPA-AA/322,323/1474
(75.4°W)	1986	SATCOL 1-B	Colombia	FSS	6/4	ARII/C/79/1573
285.0°E (75.0°W)	1986	SATCOL 2	Colombia	FSS	6/4	SPA-AJ/127/1343 SPA-AA/324/1474 ARII/C/811/1573
285.0°E (75.0°W)	Jan 1990/10	USASAT 18-A	USA	FSS	14a/11	ARII/A/230/1687
286.0°E (74.0°W)	Jan 1985/10	USASAT 7-A	USA	FSS	6/4	SPA-AA/312/1465
287.0°E (73.0°W)	Jan 1990/10	USASAT 18-B	USA	FSS	14a/11	ARII/A/231/1687
288.0°E (72.0°W)	June 1986/10	USASAT 8-B	USA	FSS	6/4	ARII/A/37/1553
288.0°E (72.0°W)	11 Oct 1990/15		USA	AMSS	1.6d/1.5c,1.6e	ARII/A/302/1723
288.0°E (72.0°W)	30 Jun 1990/10	CONDOR C	Andean	FSS	6/4	ARII/A/210/1679
289.0°E (71.0°W)	Jan 1990/7	USASAT 18-C	USA	FSS	14a/11	AP30/A/60/1748
282.3°E (77.5°W)	30 Jun 1990/10	CONDOR A	Andean Countries	FSS	6/4	ARII/A/208/1679
290.0°E (69.0°W)	1985	USASAT 7-C (Spacenet 2)	USA	FSS	6/4	ARII/A/1525 FCC: 69.0°W
290.0°E (70.0°W)	30 Jun 1987/10	USRDSS East	USA	FSS/RDSS	1.6a,6b 5.1a	ARII/A/174/1641
290.0°E (70.0°W)	Dec 1986/10	FLTSAT-B (W ATL)	USA-Government	FSS/MMSS	UHF,8/UHF,7	ARII/A/41/ADD-1/1587
293.0°E (67.0°W)	Late 1987	USASAT 8-A (SATCOM 6)	USA (RCA)	FSS	6/4	ARII/C/394/1629 A/36/1553/1629
294.0°E (66.0°W)	30 Jun 1989/10	USASAT 15-D	USA	FSS	14a/12a	ARII/A/165/1637 FCC: 67.0°W
296.0°E (64.0°W)	1988/10	USASAT 15-C	USA	FSS	14a/12a	
296.0°E (64.0°W)	1986/10	USASAT 14-D	USA	FSS	6/4	ARII/C/99/1576
298.0°E (62.0°W)	1988/10	USASAT 15-B (SBS 6)	USA	FSS	14a/11,12a	ARII/A/163/1637
299.0°E (61.0°W)	1989/10	USASAT 14-C	USA	FSS	6/4	ARII/A/160/1637
300.0°E (60.0°W)	01 Jan 1986/10	INTELSAT IBS 300.0°E	INTELSAT	FSS	6b,14a/4a, 11a,12b,12c	ARII/A/167/1638

TABLE 2 (continued). PLANNED GEOSTATIONARY COMMUNICATIONS SATELLITES AS OF YEAR END 1986

Subsatellite Longitude[a]	Launch or In-Use Date/ Period of Validity[b]	Satellite Designation	Country or Organization	Service	Frequency Up/Down-Link (GHz)	Remarks
300.0°E (60.0°W)	31 Dec 1988/10	USASAT 15-A	USA	FSS	14a/12a	ARII/A/162/1637
300.0°E (60.0°W)	Dec 1989/10	USASAT 17-D	USA	FSS	6/4	ARII/A/229/1687
300.0°E (60.0°W)	Jan 1986/10	INTELSAT V-A	US-INTELSAT	FSS	6,14a/4,11	ARII/A/166/1638
302.0°E (58.0°W)	1987/10	USASAT 8-C	USA	FSS	6/4	ARII/A/38/1553
302.0°E (58.0°W)	30 Jul 1988/10	USASAT 13-E (ISI)	USA	FSS-INT'L	14a/11,12a,12b,	ARII/A/136/1620
303.0°E (57.0°W)	30 Sep 1987/10	USASAT 13-H (PANAMSAT I)	USA	FSS	6b/4,11	ARII/A/177/1643
304.0°E (56.0°W)	01 Apr 1986/10	INTELSAT V-A 304.0°E	INTELSAT	FSS	6,14a/4,11	ARII/A/168/1638
304.0°E (56.0°W)	01 Apr 1986/10	INTELSAT IBS 304E	INTELSAT	FSS	6b,14a/4a, 11,12b,12c	ARII/A/169/1638
304.0°E (56.0°W)	30 Jul 1988/10	USASAT 13-D (ISI)	USA	FSS	6/4	ARII/C/246/1620
305.0°E (55.0°W)	31 Dec 1988/10	USASAT 14-B	USA	FSS	6/4	ARII/A/159/1637
305.0°E (55.0°W)	31 Mar 1989	INMARSAT AOR-WEST	INMARSAT	MMSS/AMSS	1.6b,1.6c,1.6d/ 1.5b,1.5c	ARII/A/328/1747
307.0°E[d] (53.0°W)	1986	INTELSAT IBS 307E	INTELSAT	FSS	6b,14a/4,11,12a	Under construction
307.0°E[d] (53.0°W)	April 1988/10	INTELSAT V-A CONTINENTAL 1	US-INTELSAT	FSS	6,14a/4,11	ARIIC/674/1667 ARII/A/115/1609
307.5°E (52.5°W)	31 Dec 1986/10	USGCSS PH3 (W ATL)	USA	STS	2/2	ARII/C/904/1746
310.0E (50.0°W)	1985	INTELSAT IV-A (ATL 2)	INTELSAT	FSS	6/4	ARII/C/140/1596
310.0°E (50.0°W)	1986	INTELSAT V-A CONTINENTAL 2	INTELSAT	FSS	6,14a/4,11	ARII/A/74/1586
310.0°E (50.0°W)	1986	INTELSAT IBS 310E	INTELSAT	FSS	6b,14a/4,11,12	ARII/A/129/1617 ADD-1/1628 ARII/C/706/1673
310.0°E (50.0°W)	Jun 1986/10	INTELSAT V CONTINENTAL 2	US-INTELSAT	FSS	6,14a/4,11	ARII/A/74/1586 ARII/C/594/1660
310.0°E (50.0°W)	30 Dec 1987/10	USASAT 13-C (ORION)	USA	FSS-INT'L	14a/11	ARII/A/134/1618 ARII/C/748/1675
310.0°E	July 1989	INTELSAT VI 310E	INTELSAT	FSS	6b/4,6,6b,14a/4a, 4,11	ARII/A/287/1711 ARII/A/287/ADD-1/1724

TABLE 2 (continued). PLANNED GEOSTATIONARY COMMUNICATIONS SATELLITES AS OF YEAR END 1986

Subsatellite Longitude[a]	Launch or In-Use Date/ Period of Validity[b]	Satellite Designation	Country or Organization	Service	Frequency Up/Down-Link (GHz)	Remarks
313.0°E (47.0°W)	Aug 1990	USASAT 13-J	USA	FSS	6/4	ARII/A/263/1703 ARII/C/944/1763
313.0°E (47.0°W)	30 Sep 1987/10 (ORION)	USASAT 13-B	USA	FSS	14a/11	ARIIA/133/1618
315.0°E (45.0°W)	1 Jan 1988/10	USASAT 13-F (CYGNUS)	USA	FSS-INT'L	14a,12a/11,12b,12c	ARII/A/154/1635 ADD-1/1714
315.0°E (45.0°W)	Jan 1989/10	USASAT 13-I (PANAMSAT II)	USA	FSS	6/4,11	ARII/A/199/1675 ARII/C/866/1736
316.5°E (43.5°W)	31 Dec 1988/10	VIDEOSAT 3	France	FSS	14a,2/11,12b,12c	ARII/A/148/1631 ARII/C/766/1678 ARI4/C/110/1698
317.0°E (43.0°W)	01 Jun 1988/10	USASAT 13-G (CYGNUS)	USA	FSS-INT'L	14a/12a,11,12b,12c	ARII/A/155/1635
(42.5°W)	Dec 1986/10	USGCSS 3 MID-ATL	USA	FSS/MMSS LMSS/STS	8/7 2/7	ARII/A/140/1622
319.0°E (41.0°W)	31 Dec 1988/10	USASAT 14-A (TDRS I)	USA	FSS	6/4	ARII/A/158/1637
319.5°E (40.5°W)	1 Apr 1986/10	INTELSAT V-A	INTELSAT	FSS	6,14a/4,11	ARII/A/127/1617
319.5°E (40.5°W)	1 Apr 1986/10	INTELSAT IBS	INTELSAT	FSS	6a,14a/4a,11, 12b,12c	ARII/A/130/1617 ARII/A/130/ ADD-1/1628) ARII/C/707/1673
322.5°E (37.5°W)	1987/10	VIDEOSAT 2	France	FSS	14a/2,12b,12c	ARII/A/86/1589 ARII/C/727/1673 ARI4/C/76/1676
322.5°E (37.5°W)	Jun 1988/10	USASAT 13-A (ORION)	USA	FSS	14a/11,4a	ARII/132/1618 ARII/C/746/1675
325.5°E (34.5°W)	1987	INTELSAT V-A (ATL 3)	INTELSAT	FSS	6,14a/4,11	ARII/A/63/1580
325.5°E (34.5°W)	1 May 1989/15	INTELSAT VI	INTELSAT	FSS	6b/4b,6/6b, 14a,4,4a,11	ARII/A/288/1711 ARII/A/288/1724
327.0°E (33.0°W)	30 Nov 1991	Skynet 4D	U.K.	FSS/MMSS	UHF,8,45 UHF,7	ARII/A/333/1749
329.0°E (31.0°W)	1986	UNISAT 1 ATL	U.K.-BRITISH TELECOM	FSS	14a,11,12b,12a,12c	ARII/A/26/1534 (See next entry)

TABLE 2 (continued). PLANNED GEOSTATIONARY COMMUNICATIONS SATELLITES AS OF YEAR END 1986

Subsatellite Longitude[a]	Launch or In-Use Date/ Period of Validity[b]	Satellite Designation	Country or Organization	Service	Frequency Up/Down-Link (GHz)	Remarks
329.0°E (31.0°W)	30 Jun 1986/10	UNISAT I	U.K.	FSS/BSS	17,20a,14a,14b/12b, 12c,2,4,12d,12e	ARII/C/576/1650 ARII/A/23/1532
329.0°E (31.0°W)	01 Jan 1987/10	INTELSAT V-A (ATL 6)	INTELSAT	FSS	6,14a/4,11	ARII/A/119/1611 ARII/A/119/ ADD-1/1628 ARII/A/119/ ADD-2/1638
392.0°E (31.0°W)	Dec 1987/12	EIRESAT I	Ireland	FSS/BSS	13/11	ARII/A/182/1656
329.0°E (31.0°W)	01 Jan 1987/10	INTELSAT V (ATL 6)	INTELSAT	FSS	6,14/4,11	ARII/A/118/1611
332.5°E (27.5°W)	Oct 1987/15	INTELSAT VI 332.5E	INTELSAT	FSS	6a,6b,/14a/4a,4,11	ARII/A/70/1584 ARII/C/628/1658, ADD-1/1713
333.5°E (26.5°W)	Dec 1982/20	GALS I	USSR	FSS	8/7	SPA-AJ/365/1508 SPA-AJ/111/1335 SPA-AA/153/1262
333.5°E (26.5°W)	31 Dec 1987/20	VOLNA 13	USSR	AMSS	UHF,1.6e/UHF,1.5c	ARII/A/240/1693
333.5°E (26.5°W)	31 Dec 1987/20	STATSIONAR 17	USSR	FSS/BSS	6b,5e,6/4a,4	ARII/A/219/1686 ARII/C/910/1749 ARII/C/910/ADD-1/1756
333.5°E (26.5°W)	Jun 1988/20	STATSIONAR 01	USSR	FSS	6a/4b	ARII/A/193/1675
333.5°E (26.5°W)	1 Aug 1990/20	TOR 1	USSR	FSS/AMSS/ MMSS/LMSS	43,45/4,20b	ARII/A/278/1710
334.0°E (26.0°W)	1 Aug 1988/15	INMARSAT AOR-CENTRAL	UK	AMSS/MMSS/ FSS FSS STS	1.6b,1.6c,1.6d/1.5b, 1.5c,6.4,6b,4a	ARII/A/152/1634 ARII/C/843/1706
335.0°E (25.0°W)	Unknown	LOUTCH P1	USSR	FSS	14a/11	SPA-AA/177/1289
335.0°E (25.0°W)	1 Aug 1990/20	TOR 9	USSR	FSS/LMSS AMSS/MMSS	43,45,20b	ARII/A/289/1711
335.0°E (25.0°W)	Unknown	STATSIONAR 8	USSR	FSS	6/4a	SPA-AJ/62/1280
335.0°E (25.0°W)	Dec 1990/20	VONA 1-M	USSR	MMSS	1.6b/1.5a	ARII/A/248/1697

TABLE 2 (continued). PLANNED GEOSTATIONARY COMMUNICATIONS SATELLITES AS OF YEAR END 1986

Subsatellite Longitude[a]	Launch or In-Use Date/ Period of Validity[b]	Satellite Designation	Country or Organization	Service	Frequency Up/Down-Link (GHz)	Remarks
335.0°E (25.0°W)	31 Dec 1987	VOLNA 1-A	USSR	MMSS	UHF,1.6b/1.5a, UHF 1.6d,1.6e UHF 1.5c	SPA-AA/169/1286
335.0°E (25.0°W)	1 Jun 1990/20	GALS 9	USSR	FSS/ AMSS/LMSS	8/7	A/291/1712 ARII/A/246/1695 ARII/C/918/1752 ARII/C/918/CORR-1/1756
335.5°E (24.5°W)	Oct 1987/15	INTELSAT VI 335.5E	INTELSAT	FSS	6,14a/4,11	ARII/A/69/1584 ARIIC/627/1658, ADD-1/1713
336.0°E (24.0°W)	Unknown	PROGNOZ 1	USSR	SRS	2/4a	SPA-AA/316/1471
336.0°E (24.0°W)	31 Dec 1988/15	INMARSAT AOR-CII	INMARSAT	MMSS/AMSS	1.6b,1.6c,1.6d/ 1.5b,1.5c	ARII/A/292/1713 ARII/A/292/ADD-1/1760
				FSS	6/4	
				STS	6b/4a	
337.0°E (23.0°W)	Unknown	MARECS (ATL 2)	France	FSS/MMSS	1.6b,6, UHF/1.5a,4a,UHF	SPA-AJ/241/1432 SPA-AA/219/1351 ARII/D/3/1551
338.5°E (21.5°W)	1 Jun 1986/10	INTELSAT MCS (ATL C)	USA	MMSS/FSS	1.6b/1.5a	ARII/C/858/1735

338.5°E (21.5°W)	1987	INTELSAT V (ATL 5)	INTELSAT	FSS	6,14a/4,11	SPA-AA/252/1419
338.5°E (21.5°W)	01 Jan 1989/10	INTELSAT V-A 338.5E	INTELSAT	FSS	6,14a/4,11	ARII/A/781/1682 ARII/A/180/1645 SPA-AA/48/1161 SPA-AA/65/1170
340.0°E (20.0°W)	Jan 1989/10	GDL 4	Luxembourg	FSS/BSS	6b,12a,14/11,12b,12c	ARII/A/92/1594/ ADD-1/1708 ARII/C/610CORR-1/1744 ARII/C/611/CORR-1/1744 1657
341.0°E (19.0°W)	Jun 87/10	TDF 1	France	BSS	17/12b,12c	ARII/A/57/1570 ARII/C/107/1578 ARII/C/741/1674 ARII/C/124/1592 RR1042/2/1521
341.0°E (19.0°W)	1985	L-SAT	ESA (France)	BSS/FSS	14a,30a/12b,12a 20b	SPA-AA/308/1463 ARII/A/33/1544 ARII/A/88/1590 ARII/A/57/1570 ARII/C/124/1592

TABLE 2 (continued). PLANNED GEOSTATIONARY COMMUNICATIONS SATELLITES AS OF YEAR END 1986

Subsatellite Longitude[a]	Launch or In-Use Date/ Period of Validity[b]	Satellite Designation	Country or Organization	Service	Frequency Up/Down-Link (GHz)	Remarks
341.0°E (19.0°W)	1987	TV-SAT	Federal Republic of Germany	BSS	17a,20a,17/20a, 2,12a,12e,2	SPA-AA/311/1464 SPA-AA/325/1474 SPA-AA/366/1526 AR14/C/4/1550 AR11/C/608/1656 AR11/C/609/1656
341.0°E (19.0°W)		L-SAT	France	BSS	17/20a	AR11/C/6/1554 AR11/A/308/1463 AR11/C/782/1682 AR14/D/23/1707
	01 Jul 1986/10	L-SAT	France (30/20 GHz)	FSS/FSS	30a/20a	AR11/C/232/1619 AR11/A/32/1544 AR11/A/32ADD-1/1716
	01 Jul 1986/10	L-SAT (14,139/12 GHz)	France	BSS/FSS	14a,13,12b,12c	AR11/C/174/1605 AR11/C/174/ ADD-1/1643 SPA-AA/337/1479 AR11/A/88/1590
340.0°E (19.0°W)	Dec 1988/10	TDF 2	France	FSS	17/12a	AR11/A/216/1684
341.0°E (19.0°W)	01 Jul 1986/10	L-SAT	France	BSS/FSS	2/2	AR11/C/176/1605 AR11/A/33/1544
341.0°E (19.0°W)	1986	HELVESAT I	Switzerland	BSS	17,20a,18/12b,12a, 2	SPA-AA/365/1512
341.0°E (19.0°W)	1986	SARIT	Italy	BSS/FSS	17a,18h/2, 13,30a/20b	SPA-AA/360/1505 SPA-AA/371/1547 AR11/294/1716
341.0°E (19.0°W)	1986	LUX-SAT	Luxembourg	BSS	17a/12b,12a,17, 12a,12e,20a	AR11/A/20/1529
341.5°E (18.5°W)	1987	INTELSAT V-A	INTELSAT (ATL 4)	FSS	6,14a/4,11	AR11/A/64/1580
341.5°E (18.5°W)	Jul 1986/10	INTELSAT IBS (341.5°E)	INTELSAT	FSS	6,14a/4,11,12a, 12b,12c	Under construction by Ford Aerospace; replaces INTELSAT VA above
342.0°E (18.0°W)	15 Oct 1989	SATCOM II	BELGIUM	FSS	8/7	SPA-AJ/137/1355 SPA-AA/144/1257
343.5°E (16.5°W)	01 Jan 1986/10	INTELSAT V (343.5°E)	INTELSAT	FSS	6,14a/4,11	AR11/A/172/1639 AR11/C/758/1677
343.5°E (16.5°W)	Jan 1986/10	INTELSAT V-A (343.5°E)	INTELSAT	FSS	6,14a/4,11	AR11/A/170/1638 AR11/A/751/1677

TABLE 2 (continued). PLANNED GEOSTATIONARY COMMUNICATIONS SATELLITES AS OF YEAR END 1986

Subsatellite Longitude[a]	Launch or In-Use Date/ Period of Validity[b]	Satellite Designation	Country or Organization	Service	Frequency Up/Down-Link (GHz)	Remarks
343.5°E (16.5°W)	01 Jul 1986/10	INTELSAT IBS (343.5°E)	INTELSAT	FSS	6a,14a/4a,11d,11, 12d	ARII/A/171/1638 ARII/C/754/ ADD-1/1731
344.0°E (16.0°W)	01 Jun 1987/20	WSDRN	USSR	FSS/SRS	14d,14b,11,13	ARII/C/67/1570 SPA-AA/341/1484
344.0°E (16.0°W)	17 Oct 1989/20	ZSSRD 2	USSR	FSS/STS/SRS	11,12b,12c/13d 14b,14d	ARII/A/189/1672 ARII/C/850/1740/880
345.0°E (15.0°W)	Nov 1984/10	FLTSATCOM A (ATL)	USA-Government	FSS/MMSS	UHF,8/UHF,7	ARII/A/97/ADD-1/1652 ARII/97/1605 : 23°W
345.0°E (15.0°W)	1 Aug 1988/15	INMARSAT AOR-EAST	UK	MMSS/FSS/ AMSS	1.6b,1.6c, 1.6d/1.5a,1.5c 6/4,6b,4a	ARII/A/153/1634
345.0°E (15.0°W)	01 Jun 1990/10	FOTON 1	USSR	FSS	6b/4b	ARII/A/235/1692
345.0°E (14.0°W)	31 Dec 1987/15	GOMS 1	USSR	MMSS/FSS	8,30a/7,1.6f, 20a,20b	ARII/A/206/1578
345.0°E (14.0°W)	01 Jun 1989/15	MORE 14	USSR	MMSS	1.6b,6b/1.5a,4a	ARII/A/183/1662

346.0°E (14.5°W)	Unknown	LOUTCH 1	USSR	FSS	14a/11	SPA-AA/157/1262 SPA-AJ/84/1318
346.0°E (14.0°W)	1980/10	VOLNA 2	USSR	MMSS	1.6b/1.5a	SPA-AJ/97/1329 SPA-AA/170/1286: 14°W
346.0°E (14.0°W)	31 Dec 1982/20	STATSIONAR 4	USSR	FSS	6/4	SPA-AJ/336/1494 SPA-AA/92/1197 AR/A/C/875/1737
346.5°E (13.5°W)	Unknown	POTOK 1	USSR	FSS	-/4	SPA-AA/344/1485
347.5°E (12.5°W)	Unknown	MAROTS-B	France	MMSS	1.6b,UHF/1.5a,UHF	SPA-AA/204/133
348.0°E (12.0°W)	Early 1988/10	HIPPARCOS	France	FSS/SRS	2/2	ARII/A/138/1621 ARII/A/138/ADD-1/1636 ARI4/C/64/1673
348.0° (12.0°W)	July 1984/10	USGCSS 3 ATL	USA	FSS/MMSS LMSS/STS	8/7 2/7 6/4	ARII/C/451/1645
352.0°E	Sep 1991/10	Telecom 2A	France	FSS/BSS	6b,12e,12b,12c, 14a/11,12b,12c	ARII/A/324/1745
349.0°E (11.0°W)	1986	F-SAT 2	France	FSS	2,14a,30a/12b, 12c/20d	ARII/C/466/1647 ARII/A/73/1586 ARII/C/467-468/1647 ARI4/C/71/1675

TABLE 2 (continued). PLANNED GEOSTATIONARY COMMUNICATIONS SATELLITES AS OF YEAR END 1986

Subsatellite Longitude[a]	Launch or In-Use Date/ Period of Validity[b]	Satellite Designation	Country or Organization	Service	Frequency Up/Down-Link (GHz)	Remarks
349.0°E (11.0°W)	31 Dec 1986/20	LOUTCH 6	USSR	FSS	14a/11	AR11/A/269/1728
335.0°E (5.0°W	Sep 1991/10	Telecom 2B	France	FSS	2/4/6,7	AR11/A/325/1745
356.0°E (4.0°W)	01 Jul 1987/10	INTELSAT V CONT 3	INTELSAT	FSS	6,14a/4,11	AR11/A/112/1609
356.0°E (4.0°W)	01 Jul 1986/10	INTELSAT V-A CONT 3	INTELSAT	FSS	6,14a/4,11	AR11/A/116/1609 AR11/A/116/ ADD-1/1628 AR11/C/675/1667
357.0°E (3.0°W)	Dec 1990/20	TOR II	USSR	FSS/LMSS MSS/MMSS	43,45/20b	AR11/A/308/1736
357.0°E (3.0°W)	Dec 1990/20	STATSIONAR 22	USSR	FSS	6/4	AR11/A/317/1740
357.0°E (3.0°W)	31 Dec 1990/20	GALS II	USSR	FSS	8/7	AR11/A/312/1740
359.0°E (1.0°W)	Jan 1985/10	INTELSAT V CONT 4	INTELSAT	FSS	6,14a/4,11	AR11/A/83/1588 AR11/C/593/1652
359.0°E (1.0°W)	01 Jan 1987/10	INTELSAT V-A CONT 4	INTELSAT	FSS	6,14a,4,11	AR11/A/117/1609 AR11/117/ ADD-1/1628 AR11/117/ ADD-2/1638 AR11/A/117/ ADD-2/1638
359.0°E (1.0°W)		SKYNET 4A	UK	FSS/MMSS	UHF,44/7,UHF	

[a]The list of satellite longitudes was compiled from the best information available.
[b]The period of validity is the number of years over which the frequency assignments of the space stations are to be used. Typical periods range from 10 to 20 years.
[c]A 2- to 3-year delay possible due to shuttle launch delays.
[d]Either CONTINENTAL I or INTELSAT IBS will be operated at this location.

TABLE 3. FREQUENCY CODES FOR ALLOCATED BANDS, SERVICES, AND ITU REGIONS

Code	Service	Link Direction, ITU Region[1]		Allocated Frequency Band (GHz)
0.1	MSS[2]	Up[3]		0.12145-0.12155
0.2	MSS	Up[3]		0.24295-0.24305
0.3a	MSS	Up	Down	0.235-0.322
0.3b	MSS	Up	Down	0.3354-0.3999
0.4a	LMSS,MMSS	Up[4]		0.4055-0.406
0.4b	MSS	Up[3]		0.406-0.4061
0.4c	Met Aids	Up		0.402-0.403
0.6	LMSS,MSS (sec[5])	Up (sec) 2		0.608-0.614
0.7	BSS (CR[6,7])			
0.8	LMSS,MMSS	Up	Down 2,3[8]	0.806-0.89
0.9	LMSS,MMSS	Up MSS	Down 3[8]	0.942-0.96
1.5a	MMSS		Down	1.530-1.544
1.5b	MMSS,AMSS		Down[9]	1.544-1.545
1.5c	AMSS		Down	1.545-1.559
1.6a	AMSS	Up	Down	1.610-1.6265
1.6b	MMSS	Up		1.6265-1.6455
1.6c	MSS	Up[9]		1.6455-1.6465
1.6d	AMSS	Up		1.6465-1.660
1.6e	AMSS	Up		1.660-1.6605
1.6f	SRS	Passive (No direction given)		1.6605-1.6684
2		(See Tables 1 and 2)		Various frequencies in the 2.0 to 2.99-GHz range
2.6a	FSS		Down 2,3	2.5-2.535
2.6b	FSS		Down 2	2.535-2.655
2.6c	FSS	Up 2,3	Down 2	2.655-2.69
2.6d	BSS (CR)		Down	2.5-2.69
4	FSS		Down	3.7-4.2
4a	FSS		Down	3.4-4.2
4b	FSS		Down	4.5-4.8
5	AMSS	Up	Down	5.0-5.25
6	FSS	Up		5.925-6.425
6a	FSS	Up 1		5.725-5.85
6b	FSS	Up		5.85-7.075
7	FSS		Down	7.25-7.75
7a	MSS		Down	7.25-7.375

TABLE 3 (continued). FREQUENCY CODES FOR ALLOCATED BANDS, SERVICES, AND ITU REGIONS

Code	Service	Link Direction, ITU Region[1]		Allocated Frequency Band (GHz)
8	FSS	Up		7.9-8.4
8a	MSS	Up		7.9-8.025
11	FSS	Up 1	Down	10.7-11.7
12a	FSS		Down 2	11.7-12.2
12b	FSS	Up 1	Down 1,3	12.5-12.7
12c	FSS	Up 1,2	Down 1,3	12.7-12.75
12d	BSS		Down 1,3	11.7-12.2
12e	BSS		Down 1,2	12.2-12.5
12f	BSS (CR)		Down 2,3	12.5-12.7
12g	BSS (CR)		Down 3	12.7-12.75
13	FSS	Up		12.75-13.25
13a	SRS	Up		13.25-14.0
14a	FSS	Up		14.0-14.5
14b	FSS	Up		14.5-14.8
14c	LMSS[7] (sec)	Up		14.0-14.5
14d	SRSS (sec)	Up		14.8-15.35
15	AMSS	Up	Down	15.4-15.7
17	FSS	Up		17.3-17.7
20a	FSS	Up	Down	17.7-18.1
20b	FSS		Down	18.1-21.2
20c	MSS (sec)		Down	19.7-20.2
20d	MSS		Down	20.2-21.2
23	BSS		Down 2,3	22.5-23.0
27	FSS	Up 2,3		27.0-27.5
30a	FSS	Up		27.5-31.0
30b	MSS (sec)	Up		29.5-30.0
30c	MSS	Up		30.0-31.0
39	FSS		Down	37.5-40.5
40	MSS		Down	39.5-40.5
42	BSS		Down	40.5-42.5
43	FSS	Up		42.5-43.5
45	MSS	Up	Down	43.5-47.0
48	FSS	Up		47.2-49.2
50a	FSS	Up		49.2-50.2
50b	FSS	Up		50.4-51.4
50c	MSS (sec)	Up		50.4-51.4
84	BSS		Down	84.0-86.0

[1]If the allocation to the service is confined to one or more ITU Regions, the region(s) are identified by number(s) placed after the link direction.
[2]In all cases, MSS includes LMSS, MMSS, and AMSS.
[3]Emergency positioning indicator beam only.
[4]Canada only.
[5]sec = secondary allocation.
[6]CR = community reception, TV only.
[7]This allocation is covered by footnote 693 in the allocation tables.
[8]Norway, Sweden.
[9]Distress/safety.

Codificador circunvolucional y descodificador de umbral programable

J. S. SNYDER

Abstracto

Se presenta una nueva arquitectura de codificador y descodificador para la corrección de errores, que emplea las funciones de almacenamiento de datos en memoria de acceso libre (RAM) y la generación de señales de control en memoria de lectura solamente, programable por el usuario (PROM), en lugar de la estructura tradicional de registro de desplazamiento. El descodificador de umbral utiliza una lógica programable para emitir el patrón de síndromes y las señales para la corrección de errores. El códec programable es de un diseño estandarizado menos complejo, y puede cambiar los parámetros del código y las condiciones de la interfaz con tan solo modificar los componentes programables.

Se describe una aplicación experimental en que el códec programable mejora la proporción de errores en los bitios de canales de modulación por impulsos codificados (PCM) a 64 kbit/s en el sistema de acceso múltiple por distribución en el tiempo a 120 Mbit/s de INTELSAT, mediante el uso eficaz de un método de codificación para la protección contra errores desigual. Esta aplicación ofrece diferentes grados de corrección de errores a los bitios que se encuentran dentro de un multibio PCM, a fin de permitir una transmisión fiable de datos digitales por los canales PCM telefónicos.

Author Index, CTR 1986

The following is a cross-referenced index of articles that appeared in the *COMSAT Technical Review* in 1986. The code number at the end of each entry is to be used for ordering reprints from Corporate Records, COMSAT Corporation, 22300 Comsat Drive, Clarksburg, Maryland 20871-9475.

*INTELSAT author.
†Non-COMSAT author.

ONUFRY, M., and Engelman, S. J., "Subjective Evaluation of the INTELSAT TDMA/DSI System," *COMSAT Technical Review*, Vol. 16, No. 1, Spring, pp. 239–251 [CTR86/304].

PALMER, L. C., "A Comparison of Three MAC TV Transmission Formats," *COMSAT Technical Review*, Vol. 16, No. 2, Fall, pp. 375–423 [CTR86/308].

PARKER, H. L., see Barnett, J. S. [CTR86/299].

PONTANO, B. A., see Campanella, S. J. [CTR86/303].

RIDINGS, R. P., Bomar, J. F., and Khoo, F. L.,* "TDMA Traffic Terminal Verification and Testing," *COMSAT Technical Review*, Vol. 16, No. 1, Spring, pp. 127–151 [CTR86/301].

ROACH, P. W.,* see Trusty, P. A. [CTR86/302].

ROTHERMICH, E. W., and Williams, S. T., "Synthesized C-Band Down-Converter," *COMSAT Technical Review*, Vol. 16, No. 2, Fall, pp. 467–480 [CTR86/312].

SANDRIN, W. A., and Fang, D. J.,† "Multipath Fading Characterization of L-Band Maritime Mobile Satellite Links," *COMSAT Technical Review*, Vol. 16, No. 2, Fall, pp. 319–338 [CTR86/306].

SCHMITT, C. H., "Geostationary Satellite Log," *COMSAT Technical Review*, Vol. 16, No. 1, Spring, pp. 253–298 [CTR86/305].

SIDDIQI, S., see Sorbello, R. M. [CTR86/307].

SORBELLO, R. M., Zaghloul, A. I., Lee, B. S., Siddiqi, S., and Geller, B. D., "20-GHz Phased-Array-Fed Antennas Utilizing Distributed MMIC Modules," *COMSAT Technical Review*, Vol. 16, No. 2, Fall, pp. 339–373 [CTR86/307].

THORNE, C. R., see Barnett, J. S. [CTR86/299].

TRUSTY, P. A., King, C. A., and Roach, P. W.,* "Generation of Burst Time Plans for the INTELSAT TDMA System," *COMSAT Technical Review*, Vol. 16, No. 1, Spring, pp. 153–205 [CTR86/302].

VAIDYANATHAN, H., "New Anode Catalyst for the Negative Electrode of the Nickel-Hydrogen Battery," *COMSAT Technical Review*, Vol. 16, No. 2, Fall, pp. 459–466 [CTR86/311].

WEINREICH, D. E., see Jones, M. E. [CTR86/300].

WILLIAMS, S. T., see Rothermich, E. W. [CTR86/312].

ZAGHLOUL, A. I., see Sorbello, R. M. [CTR86/307].

*INTELSAT author.

†Non-COMSAT author.

Index of 1986 Publications by COMSAT Authors

The following is a cross-referenced index of publications by COMSAT authors for 1986, not including papers published in the *COMSAT Technical Review*. Copies of these publications may be obtained by contacting the COMSAT authors at COMSAT Corporation, 22300 Comsat Drive, Clarksburg, MD 20871-9475.

AGARWAL, A., see Chitre, D. M.

AJOSE, S. O., and Hung, H-L. A., "A 19-GHz FET Amplifier," *International Journal of Electronics*, Vol. 60, No. 3, March 1986, pp. 331–337.

ALLISON, J. F., Chang, W. H., Holdeman, L. B., and Smith, T., "Microlithographic Techniques for High-Speed GaAs Field-Effect Transistors," *Solid State Technology*, Vol. 29, No. 6, June 1986, pp. 169–175.

ALLNUTT, J. E.,* and Rogers, D. V., "System Implications of 14/11-GHz Path Depolarization, Part II: Reducing the Impairments," *International Journal of Satellite Communications*, Vol. 4, No. 1, January–March 1986, pp. 13–17.

ARNDT, R. A., "Photovoltaics for Satellites," *PV International*, Vol. 4, No. 7, October 1986, p. 9.

ASSAL, F., see Gupta, R.

BENET, C. A., Wickham, M., and Balzer, J., "The COMSAT Attitude and Orbit Control System Flight Simulator" (Abstract), International Telemetering Conference, Las Vegas, NV, October 1986, Paper 86–0804, *Proc.*, Vol. 22, p. 37.

CAMPANELLA, S. J., Pontano, B. A., and Kao, T., "Economics of Multiple Beam Satellites," 7th International Conference on Digital Satellite Communications, Munich, FRG, May 1986, *Proc.*, pp. 479–487.

CHANG, W. H., see Allison, J. F.

CHITRE, D. M., Chong, H. Y., Agarwal, A., Colella, R.,† and Mills, K. L.,† "A Joint COMSAT/NBS Experiment on Transport Protocol," 7th International Conference on Digital Satellite Communications, Munich, FRG, May 1986, *Proc.*, pp. 351–357.

CHITRE, D. M., and Sen, A., "Reliable Data Transfer via Satellite," 7th International Conference on Digital Satellite Communications, Munich, FRG, May 1986, *Proc.*, pp. 333–341.

CHITRE, D. M., and Sen, A., "ISDN Protocols and Satellites," IEEE International Conference on Communications, Toronto, Canada, June 1986, *Conf. Rec.*, pp. 1077–1083.

CHONG, H. Y., see Chitre, D. M.

DIFONZO, D. F., "Satellite Communications: Passage to Middle Age?" (Abstract), APS International Symposium, Philadelphia, PA, June 1986, *Digest*, p. 500.

*INTELSAT author.

†Non-COMSAT author.

DIMOLITSAS, S., and Lister, P. F.,† "Waveform Preserving Encoders for the Compression of EEG Data," *Signal Processing*, Vol. 10, No. 2, June 1986, pp. 439–454.

DUNLOP, J. D., and Beauchamp, R.,† "Hydrogen/Nickel Oxide Battery: Individual Cells in a Common Pressure Vessel (ICPV)," 170th Meeting of the Electrochemical Society, San Diego, CA, October 1986, *Extended Abstracts*, p. 85.

DUNLOP, J. D., see Vaidyanathan, H.

FANG, R. J. F., "A Coded 8-PSK System for 140-Mbit/s Information Rate Transmission Over 80-MHz Nonlinear Transponders," 7th International Conference on Digital Satellite Communications, Munich, FRG, May 1986, *Proc.*, pp. 305–313.

FANG, R. J. F., "Design of a Digital Flexible Mobile Transceiver," 37th Congress of the International Astronautical Federation, Innsbruck, Austria, October 1986, New York: Pergamon Press, Paper No. IAF-86-335.

FEIGENBAUM, I. A., "Reliability of Commercial Communications Satellite Systems," *IEEE Journal of Selected Areas in Communications*, Vol. SAC-4, No. 7, October 1986, pp. 1034–1038.

FEIGENBAUM, I. A., "Reliability of Surface-Mount Technology," 18th International SAMPE Conference, Seattle, WA, October 1986, *Proc.*, pp. 287–296.

FREEMAN, D. K., see Zaghloul, A. I.

GROSSMAN, M., see Taylor, D.

GUPTA, R., Potukuchi, J., and Assal, F., "Ground-Based Failure Diagnostic/Monitoring Schemes for SS-TDMA Satellites," 7th International Conference on Digital Satellite Communications, Munich, FRG, May 1986, *Proc.*, pp. 393–400.

HEMMATI, F., "A New Property for PN Sequences" (Abstract), 3rd SIAM Conference on Discrete Mathematics, Clemson, SC, May 1986, *Final Program*, p. 821.

HEMMATI, F., "A Versatile Viterbi Processor for Decoding Variable Gain/Rate Convolutional Codes," 7th International Conference on Digital Satellite Communications, Munich, FRG, May 1986, *Proc.*, pp. 361–367.

HOLDEMAN, L. B., and Morell, N., "Erosion Profile of a Radio Frequency Planar Magnetron Sputtering Target With Aperture Shield," *Journal of Vacuum Science and Technology A*, Vol. 4, No. 1, January/February 1986, pp. 137–138.

HOLDEMAN, L. B., see Allison, J. F.

HUNG, H-L. A., "Microwave Devices," *Handbook of Modern Electronics and Electrical Engineering*, C. Belove, ed., New York: Wiley-Interscience, 1986, pp. 553–603.

HUNG, H-L. A., see Ajose, S. O.

HYDE, G., and Mahle, C. E., "Commercial Satellite Communications Systems: Year 2000," IEEE International Conference on Communications, Toronto, Canada, June 1986, *Conf. Rec.*, Vol. 2, pp. 808–812.

KAO, T., see Campanella, S. J.

†Non-COMSAT author.

KELLY, W. H., and Reisenweber, J. H., "Experimental and Flight Determination of the Solar Absorptance for an OSR Radiator as a Function of Incidence Angle," 16th Intersociety Conference on Environmental Systems, San Diego, CA, July 1986, Paper 860978, *Proc.*, p. 177.

KELLY, W. H., see Wise, P. C.†

KNIGHT, I. N., ed., "Special: Maritime Mobile Services," *ITU Telecommunication Journal*, Vol. 53, No. 6, June 1986, pp. 317–342.

KNIGHT, I. N., and Neibert, M. T., "An Overview of Satellite Transmission Issues and the ISDN," IEEE International Conference on Communications, Toronto, Canada, June 1986, *Conf. Rec.*, pp. 1073–1076.

KOEPF, G. A., Peters, R.,* and Marshalek, R. G., "Analysis of Burst Error Occurrence on Optical Intersatellite Link (ISL) Design," Optical Technologies for Communication Satellite Applications, Los Angeles, CA, January 1986, *Proc. SPIE*, Vol. 616, pp. 129–136.

KOEPF, G.,† see Marshalek, R. G.

LEE, Y. S., Srinivas, D. N., and Gordon, G.,† "Flight Data-Based Communications Spacecraft Reliability Assessment," AIAA 11th Communication Satellite Systems Conference, San Diego, CA, March 1986, Paper 86–0711, *A Collection of Technical Papers*, pp. 621–626.

LIPKE, D. W., see Sandrin, W. A.

MAHLE, C. E., see Hyde, G.

MARSHALEK, R. G., and Koepf, G., "Comparison of Optical Technologies for Intersatellite Links," Optical Technologies for Communication Satellite Applications, Los Angeles, CA, January 1986, *Proc. SPIE*, Vol. 616, pp. 29–48.

MARSHALEK, R. G., see Koepf, G.†

MORELL, N., see Holdeman, L. B.

NEIBERT, M. T., see Knight, I. N.

PALMER, L. C., and Shenoy, A., "Simulation of TV Transmission Over the Communications Satellite Channel," *IEEE Transactions on Communications*, Vol. COM-34, No. 2, February 1986, pp. 188–199.

PAUL, D., "1986: A Year of Transition for Fiber Optics Technology," Annual Review of Fiber Optic Technology and Markets, R. Mack and A. Tebo, eds., *Laser Focus*, Vol. 22, No. 10, October 1986, pp. 104–114.

PAUL, D., "Fiber Optic Communications Systems: Year 2000," IEEE International Conference on Communications, Toronto, Canada, June 1986, *Conf. Rec.*, Vol. 2, pp. 813–819.

PAUL, D., "Reliability Considerations in Fiber Optic Systems Design," Fiber/Lase '86: Conference on Reliability Considerations in Fiber Optic Applications, Cambridge, MA, September 1986, *Proc. SPIE*, Vol. 717, D. K. Paul, ed., pp. 134–146.

PONTANO, B. A., see Campanella, S. J.

POTUKUCHI, J., see Gupta, R.

*INTELSAT author.

†Non-COMSAT author.

REISENWEBER, J. H., see Kelly, W. H.

ROGERS, D. V., and Allnutt, J. E.,* "System Implications of 14/11-GHz Path Depolarization, Part I: Predicting the Impairments," *International Journal of Satellite Communications*, Vol. 4, No. 1, January–March 1986, pp. 1–11.

ROGERS, D. V., see Allnutt, J. E.*

SANDRIN, W. A., and Lipke, D. W., "A Satellite System for Aeronautical Data Communications," AIAA 11th Communication Satellite Systems Conference, San Diego, CA, March 1986, Paper 86-0602, *A Collection of Technical Papers*, pp. 12–17.

SAYEGH, S. I., "A Class of Optimum Block Codes in Signal Space," *IEEE Transactions on Communications*, Vol. COM-34, No. 10, October 1986, pp. 1043–1045.

SEN, A., see Chitre, D. M. (two papers).

SHARMA, S. P., see Wise, P. C.†

SHENOY, A., see Palmer, L. C.

SMITH, T., "Beyond-Punchthrough Current in GaAs MESFET's," *IEEE Electron Device Letters*, Vol. EDL-7, No. 3, March 1986, pp. 188–189.

SMITH, T., see Allison, J. F.

SRINIVAS, D. N., see Lee, Y. S.

TAYLOR, D.,† and Grossman, M., "The Effect of FEC on Packet Error Performance in a VSAT Network." IEEE Global Telecommunications Conference, Houston, TX, December 1986, *Digest*, pp. 1475–1478.

VAIDYANATHAN, H., and Dunlop, J. D., "Capacity Maintenance for INTELSAT VI Nickel-Hydrogen Cells," 21st Intersociety Energy Conversion Engineering Conference, Washington, DC, August 1986, *Proc.*, Vol. 3, pp. 1560–1564.

WEINREICH, D. E., "Transmission and Performance Quality Standards for Satellite Links in the ISDN," IEEE International Conference on Communications, Toronto, Canada, June 1986, *Conf. Rec.*, pp. 34.3.1–34.3.4.

WISE, P. C.,† Raisch, J.,† Kelly, W., and Sharma, S. P., "Thermal Design Verification of a High-Power Direct Broadcast Satellite," AIAA/ASME 4th Joint Thermophysics and Heat Transfer Conference, Boston, MA, June 1986, Paper No. AIAA-86-1339.

WOLEJSZA, C. J., "Simulation and Design of a Simple Burst Demodulator for a Random-Access TDMA Packet Terminal," 7th International Conference on Digital Satellite Communications, Munich, FRG, May 1986, *Proc.*, pp. 683–689.

ZAGHLOUL, A. I., and Freeman, D. K., "Phased Array Synthesis for Shaped Beams Using Power Matrix Technique," AP-S International Symposium, Philadelphia, PA, June 1986, *Digest*, pp. 177–180.

ZAKS, C., and Anderson, S.,† "Aeronautical Satellite Data Link Measurement Over the North Atlantic: Test Results," 7th International Conference on Digital Satellite Communications, Munich, FRG, May 1986, *Proc.*, pp. 557–563.

*INTELSAT author.

†Non-COMSAT author.